AD___________________

Award Number: W81XWH-04-1-0590

TITLE: Constrained Adaptive Beamforming for Improved Contrast in Breast Ultrasound

PRINCIPAL INVESTIGATOR: William F. Walker, Ph.D.

CONTRACTING ORGANIZATION: University of Virginia
Charlottesville, VA 22904

REPORT DATE: June 2007

TYPE OF REPORT: Final

PREPARED FOR: U.S. Army Medical Research and Materiel Command
Fort Detrick, Maryland 21702-5012

DISTRIBUTION STATEMENT: Approved for Public Release;
Distribution Unlimited

The views, opinions and/or findings contained in this report are those of the author(s) and should not be construed as an official Department of the Army position, policy or decision unless so designated by other documentation.

REPORT DOCUMENTATION PAGE

Form Approved
OMB No. 0704-0188

Public reporting burden for this collection of information is estimated to average 1 hour per response, including the time for reviewing instructions, searching existing data sources, gathering and maintaining the data needed, and completing and reviewing this collection of information. Send comments regarding this burden estimate or any other aspect of this collection of information, including suggestions for reducing this burden to Department of Defense, Washington Headquarters Services, Directorate for Information Operations and Reports (0704-0188), 1215 Jefferson Davis Highway, Suite 1204, Arlington, VA 22202-4302. Respondents should be aware that notwithstanding any other provision of law, no person shall be subject to any penalty for failing to comply with a collection of information if it does not display a currently valid OMB control number. **PLEASE DO NOT RETURN YOUR FORM TO THE ABOVE ADDRESS.**

1. REPORT DATE *(DD-MM-YYYY)*
01-06-2007

2. REPORT TYPE
Final

3. DATES COVERED *(From - To)*
1 Jun 2004 – 31 May 2007

4. TITLE AND SUBTITLE
Constrained Adaptive Beamforming for Improved Contrast in Breast Ultrasound

5a. CONTRACT NUMBER

5b. GRANT NUMBER
W81XWH-04-1-0590

5c. PROGRAM ELEMENT NUMBER

6. AUTHOR(S)

William F. Walker, Ph.D.

E-Mail: bwalker@virginia.edu

5d. PROJECT NUMBER

5e. TASK NUMBER

5f. WORK UNIT NUMBER

7. PERFORMING ORGANIZATION NAME(S) AND ADDRESS(ES)

University of Virginia
Charlottesville, VA 22904

8. PERFORMING ORGANIZATION REPORT NUMBER

9. SPONSORING / MONITORING AGENCY NAME(S) AND ADDRESS(ES)
U.S. Army Medical Research and Materiel Command
Fort Detrick, Maryland 21702-5012

10. SPONSOR/MONITOR'S ACRONYM(S)

11. SPONSOR/MONITOR'S REPORT NUMBER(S)

12. DISTRIBUTION / AVAILABILITY STATEMENT
Approved for Public Release; Distribution Unlimited

13. SUPPLEMENTARY NOTES – Original contains colored plates: ALL DTIC reproductions will be in black and white.

14. ABSTRACT

Ultrasonic imaging plays an important role as an adjunct to mammography, with an emergingrole in breast cancer screening. Ultrasound's real-time nature, lack of ionizing radiation,and relative comfort for the patient make it an attractive imaging choice. Unfortunately,ultrasound image quality is often limited.We hypothesize that bright scatterers seriously degrade ultrasound images by introducingimage clutter. In the breast bright off-axis echoes may originate from Cooper's ligaments,structured glandular tissue, calcification, fat-soft tissue interfaces, or other structures. We initially proposed using a variant of the Frost Adaptive Beamformer to reduce clutter,but discovered that this technique is non-optimal for our application. Extensive literaturereview led us to modify the Spatial Processing Optimized and Constrained algorithm (SPOC) toyield the Time-Domain Optimized Near-field Estimator (TONE). In simulations and phantomexperiments this technique yields dramatic improvements in resolution and contrast. We havealso developed alternate methods of image formation (LCLS and QCLS).

15. SUBJECT TERMS
Imaging, Ultrasound, Diagnosis, Non-Invasive

16. SECURITY CLASSIFICATION OF:			**17. LIMITATION OF ABSTRACT**	**18. NUMBER OF PAGES**	**19a. NAME OF RESPONSIBLE PERSON** USAMRMC
a. REPORT U	**b. ABSTRACT** U	**c. THIS PAGE** U	UU	158	**19b. TELEPHONE NUMBER** *(include area code)*

Table of Contents

Introduction……………………………………………………………..……….…..4

Body…………………………………………………………………………………6

- **Summary of Third Year Progress……………………………………6**
- **A Metric for Assessing Beamformer Performance………………7**
- **Conventional Beamformer Optimization…………….……………..….7**
- **The FIR Beamformer ……….……………………………………….….8**
- **TONE Progress…………………………..………………………..……10**
- **Diffuse Target TONE (dTONE)……….…...……………………..……15**
- **Simulation Tool Development…………………………………………16**
- **Experimental Platform Development……………………………..….17**
- **Corporate Interactions……………………………….…………………..18**

Key Research Accomplishments……………………………………….………19

Reportable Outcomes…………………………………………………………...20

Conclusions……………………………………………………………………..21

References………………………………………………………………………22

Appendices………………………………………………………………………24

Introduction:

Ultrasonic imaging currently plays an important role as an adjunct to mammography [1, 2]. Ultrasound's real-time nature, lack of ionizing radiation, and relative comfort for the patient make it an attractive choice for applications which include the differentiation of fluid filled cysts and solid masses, differentiation of benign and malignant lesions, and guidance of needle and core biopsy procedures. Recent studies have even shown the potential of ultrasound as a screening tool, especially for pre-menopausal women whose radio-dense breast tissue seriously limits x-ray mammography [3]. In both differential diagnosis and screening applications however, ultrasound image quality is limited, with high levels of background clutter representing a significant problem in many patients.

While the cause of high background clutter and poor breast image quality has not been determined with certainty, it is widely held that acoustic velocity inhomogeneities in breast tissue cause defocusing of the acoustic beam. This distortion manifests itself through mainlobe broadening and increasing sidelobe levels. Numerous researchers, including the Principal Investigator, have suggested that this problem, known as phase aberration, might be corrected through the application of compensating time delays [4-6], a combination of delay and amplitude corrections [7], or other more complex techniques [8-10]. While proposed phase aberration correction methods have been shown to have great potential in *ex vivo* or other non real-time environments, there has been limited evidence of significant clinical image improvement. The development of a real-time phase aberration correction system at the GE Global Research Center has shown that real-time phase correction is possible, however *in vivo* results using 1.5-D arrays show contrast improvements of only about 3 dB in the abdomen [11, 12]. This unimpressive outcome may result from imperfect algorithm optimization, or perhaps a lower level of *in vivo* phase aberration than previously suspected. This latter hypothesis is supported by recent phase aberration measurements performed at Duke University which indicate *in vivo* phase aberrations of only ~25ns RMS (Root Mean Squared) with a 3.5 mm FWHM (Full Width at Half Maximum) [13]. The limited improvements of real-time phase correction, coupled with low measured aberrations, suggest that phase aberration may not represent the major source of breast image degradation.

If phase aberration is not the primary factor limiting breast image quality, then what is? We hypothesize that localized bright scatterers seriously degrade ultrasound images by introducing broad image clutter. Figure 1 shows single channel Radio Frequency (RF) echo data obtained from calcifications in the thyroid of a human subject at Duke University. A focused transmit beam was used and RF data was acquired from each element in a 1.5-D array consisting of approximately 1000 elements. Figure 1 shows data from one row of this array after application of geometrically determined focal delays. At least three clear waveforms are visible in this data set, with each probably resulting from a single calcification. Although summation across channels to form an RF image line would amplify the echo coming from directly in front of the array, it would not entirely eliminate the two other visible targets. These non-focal targets would appear in this image line as clutter, reducing image contrast. In addition to the three dominant calcification waveforms, the data set also includes echoes from background speckle. These background echoes also include discernable off-axis scatterers that undoubtedly generate further clutter in the image. Note that the thyroid data presented in figure 1 is similar in appearance to breast data obtained at Duke. In the breast bright off-axis echoes may originate from Cooper's ligaments, highly structured glandular tissue, calcification, fat-soft tissue interfaces, or other tissue structures.

The presence of bright off-axis scatterers and the image degradation that they cause is not surprising. It is well known that the acoustic reflectivity of targets within the body covers many orders of magnitude. It is precisely for this reason that manufacturers employ aggressive apodization to reduce sidelobe levels in diagnostic ultrasound. It has also been argued that harmonic imaging is effective at improving image quality because it further reduces sidelobe levels and therefore reduces the spatial spread of bright targets. The detrimental impact of bright scatterers on ultrasound image quality is recognized in experimental data, physical intuition, and years of experience in ultrasound system design.

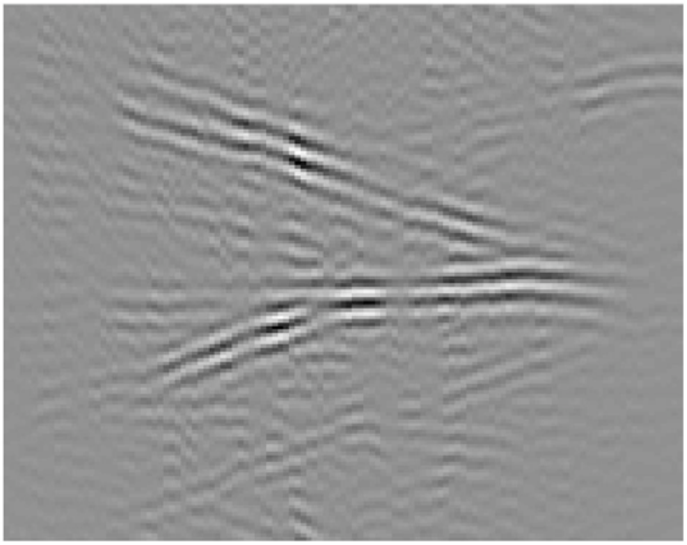

Figure 1: Single channel data obtained *in vivo* from a human thyroid. At least three bright scatterers (likely microcalcifications) are visible. While one target lies near the focus, the other two are off-axis and will contribute clutter to this image line. Off-axis targets are also visible within the speckle generating background echoes. (Data courtesy Gregg Trahey, Duke University.)

The impact of a few bright targets in an otherwise dim image has been well studied in both RADAR and SONAR. In SONAR the detection of an intentionally stealthy submarine among many noisy ships requires separating out a signal that is orders of magnitude below the signals from other nearby targets. A broad variety of adaptive beamforming algorithms have been developed for this scenario. It is the goal of this research project to evaluate the potential applicability of these methods in medical ultrasound.

Body:

Summary of Third Year Progress:

As described in our prior progress reports, we have successfully modified the Spatial Processing Optimized and Constrained (SPOC) algorithm [14, 15] to operate on near-field, broadband signals. In the process of writing about this modified algorithm it became clear that our significant changes to SPOC really made it a new algorithm, deserving a new name. Thus we have come to call our algorithm TONE for Time Domain Optimized Near-field Estimator. We have just had our first peer-reviewed paper describing TONE accepted for publication in IEEE Transactions on Medical Imaging [16].

During the past year we have worked to address one of the apparent limitations of the TONE algorithm. Although TONE is able to achieve super-resolution, it seems to have some difficulty when the actual targets do not lie at the exact locations of the hypothetical targets in the reconstruction. In this scenario TONE may generate a large cloud centered about the true target location in the reconstructed image. To counteract this problem we intentionally use a target model in which the response of the system to a single "target" actually consists of the response to a number of closely spaced targets. In our early experience, the use of diffuse target functions improves image contrast, reduces artifacts, and smoothes the image, making it much easier to interpret. We present initial results from diffuse target TONE or dTONE below.

While the main focus of this grant has been the development and evaluation of adaptive beamforming (i.e. TONE) we continue to explore the limits of optimization of conventional beamforming. In the past year we have adapted the CLS beamformer design method (developed under this grant) to design not only for single element weights (apodization), but to design for channel dependent FIR filters. While a natural evolution of our prior work, this technique really represents a new architecture for ultrasound beamformers. This new FIR beamformer architecture seems to offer a number of advantages over conventional beamforming. First, it is capable of improving both image contrast and resolution, a simultaneous optimization that is normally considered impossible. We have assessed this capability in wire target experiments and in simulated cyst images, achieving positive results that suggest high potential for clinical impact. Secondly, the FIR beamformer seems to be intrinsically robust to phase aberration. In extensive simulations, an aberrated FIR beamformer outperforms an unaberrated conventional beamfomer. Thus, this algorithm may effectively solve the long-standing problem of phase aberration in medical ultrasound. We have just submitted a paper describing this work [17].

Both TONE and CLS require accurate models of the imaging system response. While these responses can be determined experimentally or predicted theoretically, computer simulations represent the best long-term solution because of their potential for high accuracy and rigor. We have just published our novel spline-based simulation tool DELFI [18]. We have placed this tool on the MathWorks User Community where it has been downloaded over 210 times since February. We are currently modifying the implementation of the algorithm to improve accuracy and speed execution. We are also working with PocketSonics Inc. to implement a version of this software on the PlayStation 3 (PS3) to enable highly detailed simulation within a reasonable computational budget.

As our work on algorithm development and evaluation continues, we have also endeavored to perform high quality experiments to evaluate these algorithms. While we have gained tremendous control and built a powerful set of tools for the Sonix RP system, the transducers available for this system have not approached the state of the art for breast imaging. Thus, while the electronics and control are excellent for our intended studies, the poor transducers unacceptably corrupt our experiments. In the past few months we have acquired and characterized a high frequency linear array (15-6L) made by Philips. This array is among the best in the world for shallow, small parts imaging. We have already mapped the elements of this array and are in the process of designing a new interconnect system that will enable transparent operation with the Sonix RP.

We have filed a US Patent application covering TONE and dTONE, to encourage commercial implementation and speed clinical implementation. Early licensing discussions have been positive. We have also filed a provisional patent application on the FIR Beamformer and two companies are already in licensing discussions.

A Metric for Assessing Beamformer Performance:
The literature in ultrasound imaging, as well as SONAR and RADAR, is littered with novel beamforming strategies, new apodization functions, and "optimal" imaging strategies. Unfortunately traditional measures of beamformer quality, such as Full Width at Half Maximum (FWHM) of the beamplot are not well suited to quantify the performance of medical ultrasound imaging systems, where true point targets are rare, but diffuse targets are common. This disparity has meant that many algorithms that appear promising for point target imaging are not useful in clinical settings. Some time ago we realized that a new measure of beamformer performance was needed; one that was more in tune with clinical problems.

We have derived a novel metric for quantifying ultrasound image quality. Unlike traditional measures, such as the Rayleigh resolution, which quantify point target resolution, our metric quantifies the contrast of an anechoic cyst as a function of cyst radius. Cystic contrast is a much more relevant parameter for medical ultrasound where point targets are rare and of little clinical importance. Our paper describing this new metric was published in April 2007 [19].

While the Cystic contrast metric published this year is of tremendous value in comparing imaging systems and in guiding the design of imaging systems, it is still limited in one manner. This metric only tracks the impact of electronic noise through a Signal to Noise Ratio (SNR) on the summed echo signal. This makes it awkward to compare the impact of apodization on SNR directly, as the current metric does not explicitly consider the SNR on individual beamformer channels. We are now developing a new cystic resolution metric that considers individual channel SNR, and therefore allows direct comparison across various apodization functions. This metric allows the designer to identify "optimal" apodizations that incorporate both realistic propagation physics and the impact of electronic noise. In our early work with this metric we have identified a tradeoff between idealized image contrast and electronic noise; a tradeoff that we have not seen considered explicitly elsewhere. We anticipate submitting a paper on this new metric and its implications later this year.

Conventional Beamformer Optimization:
While the TONE and dTONE algorithms (described in detail below) offer tremendous improvements in resolution and contrast, their high computational cost presents a challenge to short-term, real-time implementation. Further, while we know that these algorithms significantly outperform existing beamformers, we do not know that such conventional delay and sum beamformers are "optimal" in the sense of achieving the best possible contrast or resolution. Thus, to offer a better chance of short-term technology gains and to provide a true benchmark for comparison, we have developed two novel techniques for optimizing conventional delay and sum beamformer performance. These techniques, termed Linear Constrained Least Squares (LCLS) and Quadratically Constrained Least Squares (QCLS) optimization design optimal beamformer weights using slightly different mathematical criterion. LCLS minimizes the point spread function energy outside a given cyst radius while maintaining a constant gain at the center of the cyst. This technique yields a closed form solution that makes best use of the element responses, regardless of system non-idealities including limited element angular response, near field variations, and finite bandwidth. The second technique, QCLS, also minimizes the point spread function energy outside a given cyst radius, but constrains the energy within the cyst radius. This technique effectively optimizes the cystic contrast metric and therefore should optimize image quality. The theoretical underpinnings and simulation validation of these techniques are described in two papers published in IEEE Transactions on Ultrasonics, Ferroelectrics, and Frequency Control in February of this year [20, 21].

The FIR Beamformer:

The LCLS and QCLS design techniques are guaranteed to yield optimal apodization profiles for a given imaging system, however with only one parameter to adjust on each beamformer channel, we found that the optimal performance was not always much better than conventional apodization. As we reflected upon this, we wondered if it was possible to define a beamformer architecture wherein we could adjust multiple parameters on each channel and thereby achieve greater gains in performance. The beamfomer architecture we envisioned is shown below in figure 2. The upper panel depicts a conventional delay and sum beamformer where the parameters W, X, and Y are the designed apodizations. The lower panel depicts the new FIR beamfomer architecture in which a 3 tap FIR filter is placed on each beamformer channel, after the delay stage. (Note that the abbreviation FIR stands for Finite Impulse Response.) In this beamformer the parameters A, B, C, … N, and O are designed in the numerical optimization.

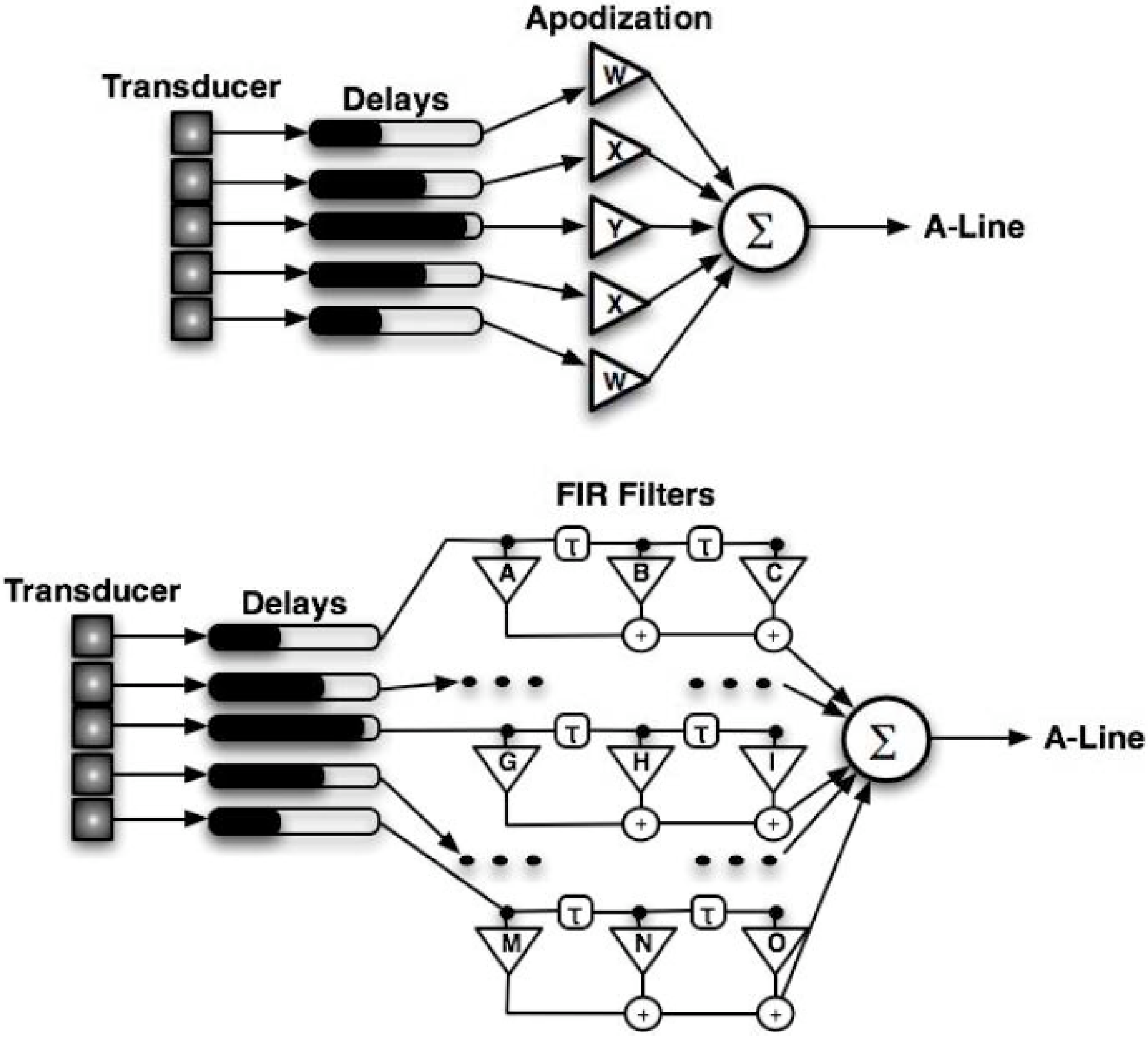

Figure 2: Conventional and FIR beamformer architectures. The upper panel depicts a conventional delay and sum beamfomer with a single adjustable apodization value per channel. The lower panel depicts the novel FIR beamformer architecture in which multiple weights are applied to each channel. In this particular realization three filter taps are used on each channel, although there is no theoretical limit to the number of taps that can be applied.

This greater degree of flexibility afforded the FIR beamformer yields dramatic, and robust increases in performance. In our current design methodology we simply apply the QCLS design method, but design for find multiple, temporally delayed apodization profiles to obtain channel dependent FIR filter coefficients. Because this method forms FIR filters on each channel it is able to effectively perform frequency dependent beamforming to achieve optimal broadband results. Figure 3 shows significant experimental improvements in lateral resolution and contrast achievable with the FIR beamformer. Note that the FIR beamformer achieves both a narrower mainlobe and a lower sidelobe level than conventional beamforming. These benefits have a significant impact on cystic contrast, improving cystic contrast by over 10 dB.

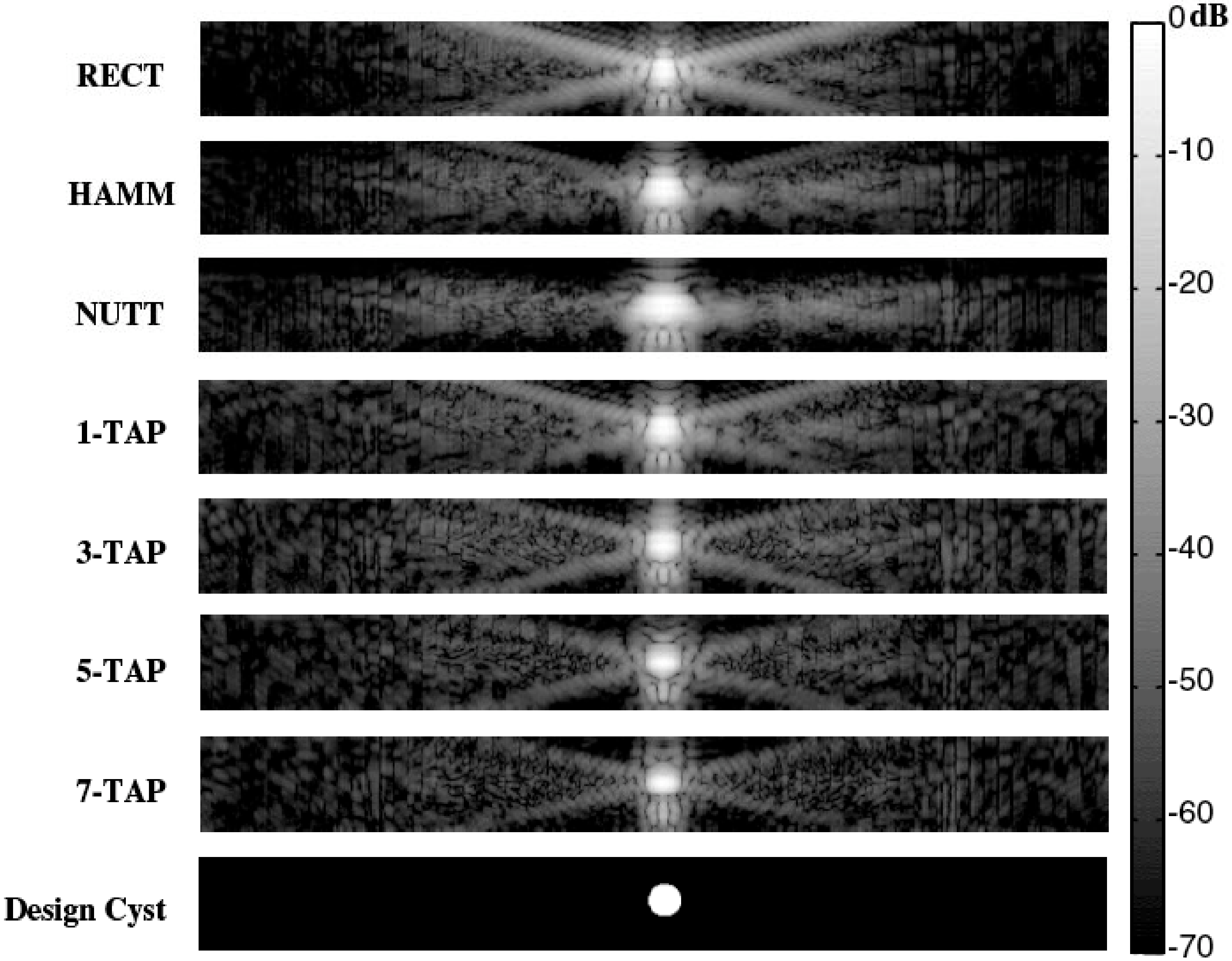

Figure 3: Experimental 2D PSFs with different receive apodization functions applied. Each image is 0.2 cm axially by 1.95 cm laterally. All images were envelope detected and log compressed to 70 dB. The conventional windows' PSFs suffer from high sidelobes and wide mainlobes. The multi-tap FIR-QCLS apodization functions progressively reduce the total sidelobe energy while maintaining a tight mainlobe in the spatial PSFs. The design cyst is shown for reference.

We further assessed the performance improvements of the FIR beamformer by convolving the experimentally obtained point spread functions with simulated cysts within a speckle generating background. The simulated images, shown below in figure 4, show an appreciable improvement in cystic contrast with FIR beamforming.

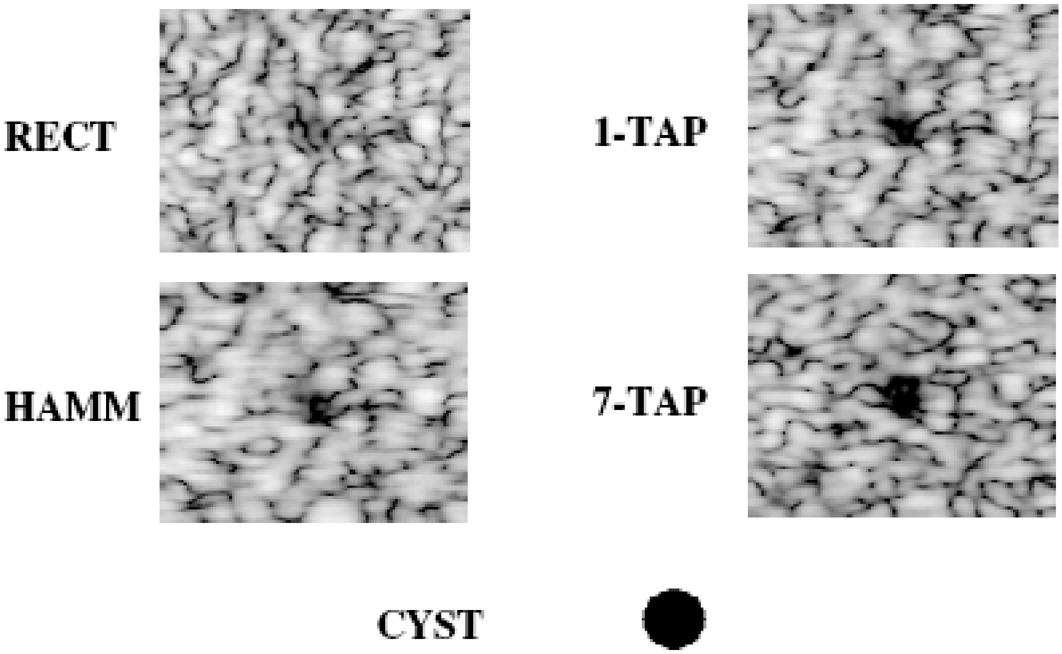

Figure 4: Simulated B-mode images of a 1.0 mm diameter cyst embedded in speckle using the experimental PSFs. All images are log compressed to 30 dB and show a 5 mm by 5 mm area surrounding the anechoic cyst. The 1.0 mm diameter cyst is shown for reference.

TONE Progress:

The region of tissue to be imaged region (the region of interest or ROI), is subdivided into a collection of hypothetical targets at arbitrary positions, as shown in figure 5. Finer target placement yields finer final image resolution but entails higher computational costs. For each hypothetical target in the ROI, we model the signal received by the array for that specific point (i.e., the spatial responses). These spatial responses can be determined using a theoretical model, computational model, or can be extracted from experimental data. For every hypothetical target, the spatial impulse response is a matrix of dimensions TxN, where T is the number of samples in the time dimension and N is the number of elements in the array. After the spatial impulse responses for all the hypothetical targets have been calculated, these responses are reshaped to form an array manifold matrix $\underline{V}$ of dimensions NTxLP, where L and P are the numbers of hypothetical sources in the range and lateral dimensions, respectively. The observation model then becomes:

$$\underline{x} = \underline{V}\,\underline{f} \qquad (1)$$

where $\underline{x} = [\underline{x_1} \;\; \underline{x_2} \cdots\cdots \underline{x_N}]^T$ is the data received by the N-element array and $\underline{f}$ is the LPx1 target amplitude vector, whose elements are the amplitudes of the hypothetical targets located in the ROI. $\underline{x}$ is a NTx1 vector that is obtained by concatenating the Tx1 channel data $\underline{x_i}$. Given $\underline{x}$ and $\underline{V}$, TONE matches the received data $\underline{x}$ to the signal model to solve for the position and intensity of the real sources (i.e., the $\underline{f}$ vector). If there is no real source at a particular location within the ROI, then the element of $\underline{f}$ that corresponds to that location should be zero. Mathematically, this is accomplished by solving the following maximum a posteriori (MAP) optimization problem:

$$\begin{aligned} &Cost \quad function: \quad \sum_{l=1}^{LP} \ln\left|f_l\right|^2 \\ &subject \quad to: \quad \underline{x} = \underline{V}\,\underline{f} \end{aligned} \tag{2}$$

where f_l are elements of $\underline{f}$. A solution for the MAP optimization problem is found using the following iterative procedure described by K. W. Lo.

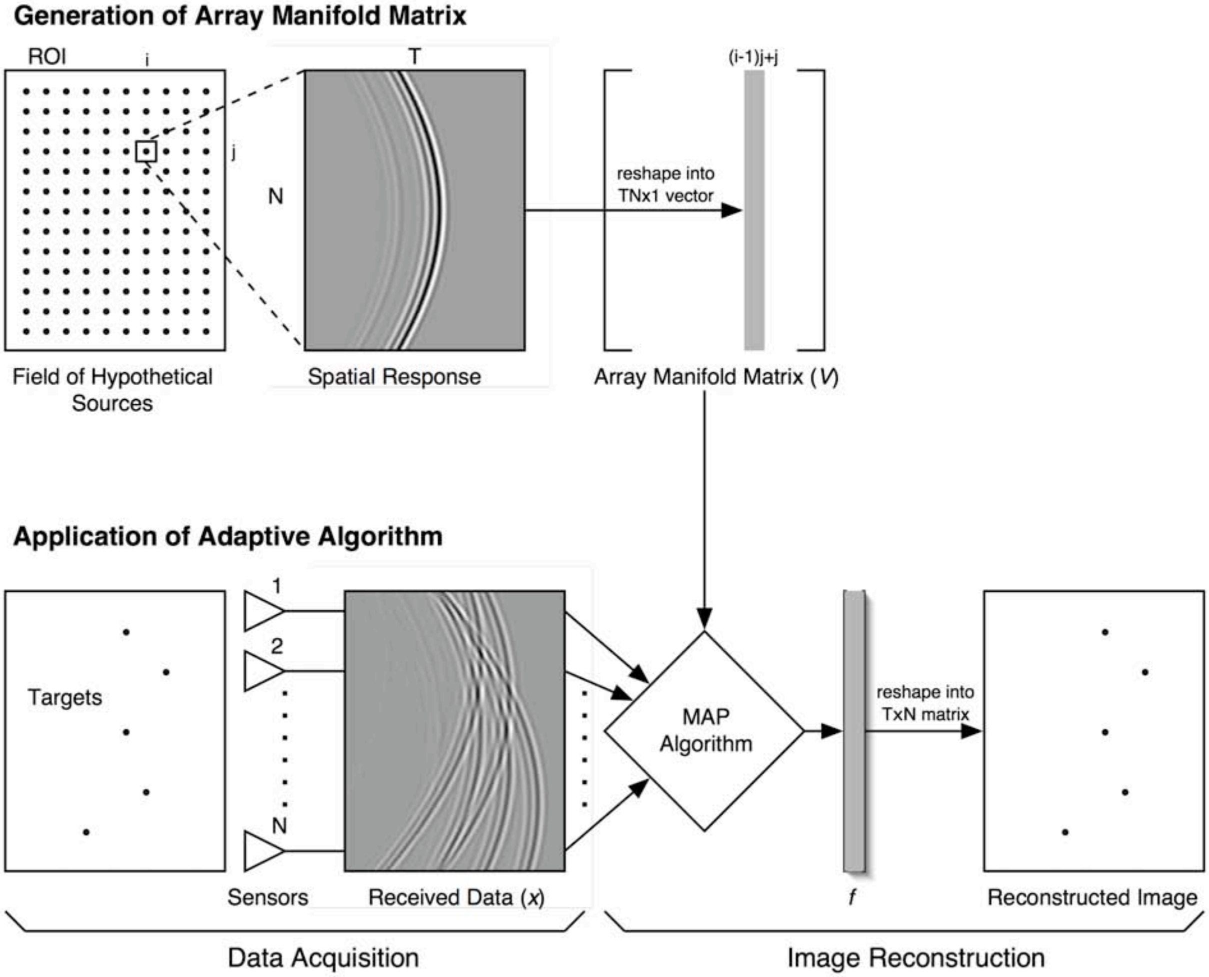
Generation of Array Manifold Matrix
ROI
i
j
T
N
(i-1)j+j
reshape into TNx1 vector
Field of Hypothetical Sources
Spatial Response
Array Manifold Matrix (V)
Application of Adaptive Algorithm
Targets
1
2
N
MAP Algorithm
reshape into TxN matrix
Sensors
Received Data (x)
f
Reconstructed Image
Data Acquisition
Image Reconstruction

Figure 5. Schematic diagram of TONE.

A series of computer simulations were performed in Matlab to test the potential of TONE. These simulations and their results are described in detail below.

Single Point Target Simulations

A point target was placed directly in front of the transducer at a depth of 20.1mm. We simulated a 33 element linear array operating at 5 MHz with element spacing of 150µm. Signals were sampled at 40 MHz. Plane wave transmission was used for conventional beamforming and SPOC. Conventional beamforming was applied on the received RF data using Hann apodization and dynamic receive focusing. For SPOC, we discretized the image region as a setof hypothetical targets separated 20µm in range and 100µm in azimuth.

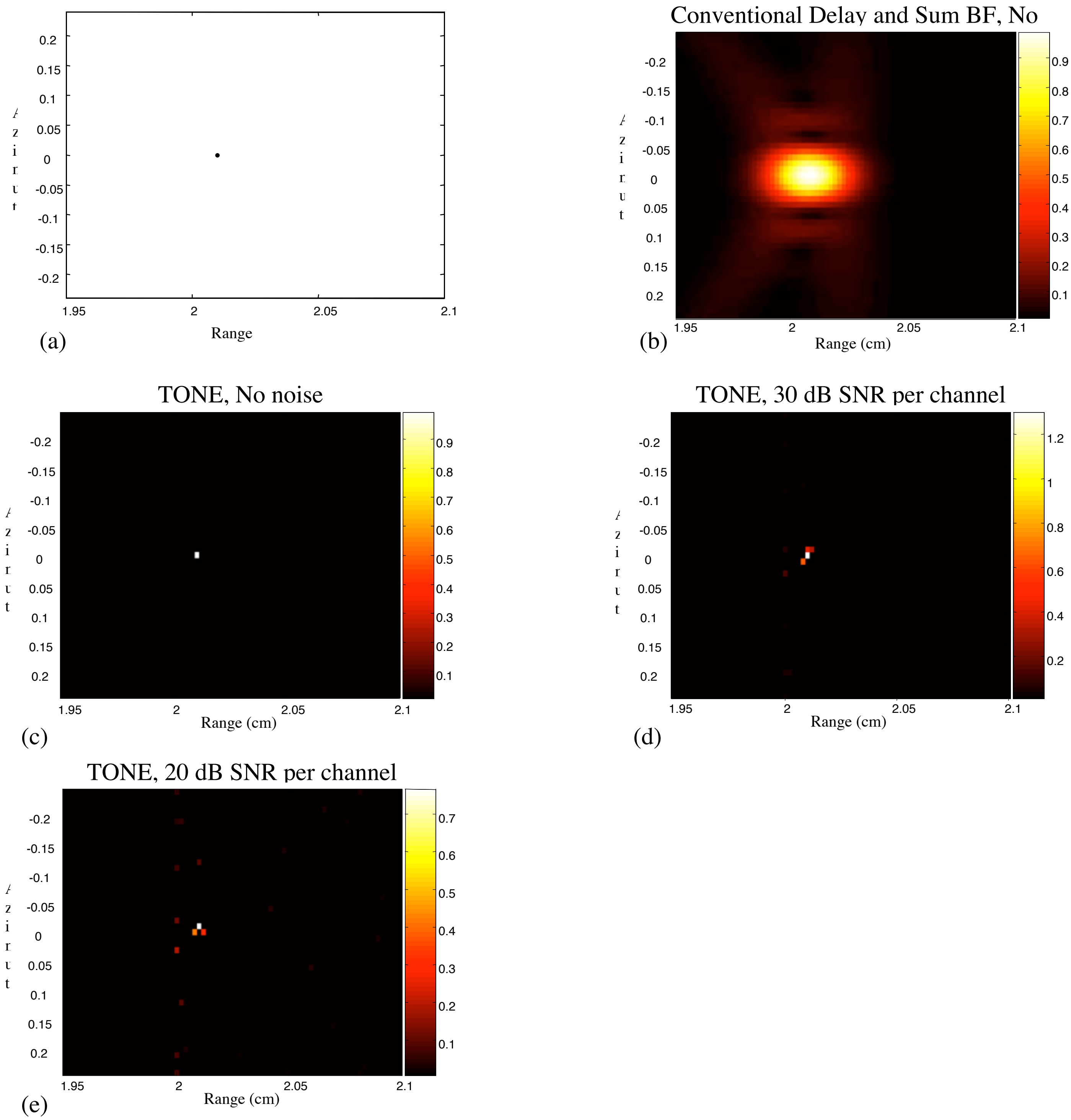

Figure 6. Point target simulations. The point target is depicted in (a); (b) shows conventional delay-and-sum beamforming, whereas images (c) to (e) show SPOC with different levels of electronic noise.

Multiple Point Target Simulations

A series of point targets were distributed within a 4x5mm region in range and azimuth, respectively. In this case, we simulated a 33 element linear array operating at 5 MHz with element spacing of 150µm. The final sampling frequency was set at 40 MHz. A plane wave was used on transmit for both conventional beamforming and TONE. Conventional beamforming was applied on the received RF data using Hann apodization and dynamic receive focusing.

For TONE, we discretized the image region in a set of hypothetical target locations separated 20μm in range and 120μm in azimuth. The positions of the points were chosen so that some, but not all coincide with the positions of the hypothetical targets. Results are encouraging in that they show TONE is robust to differences between true target location and model target location.

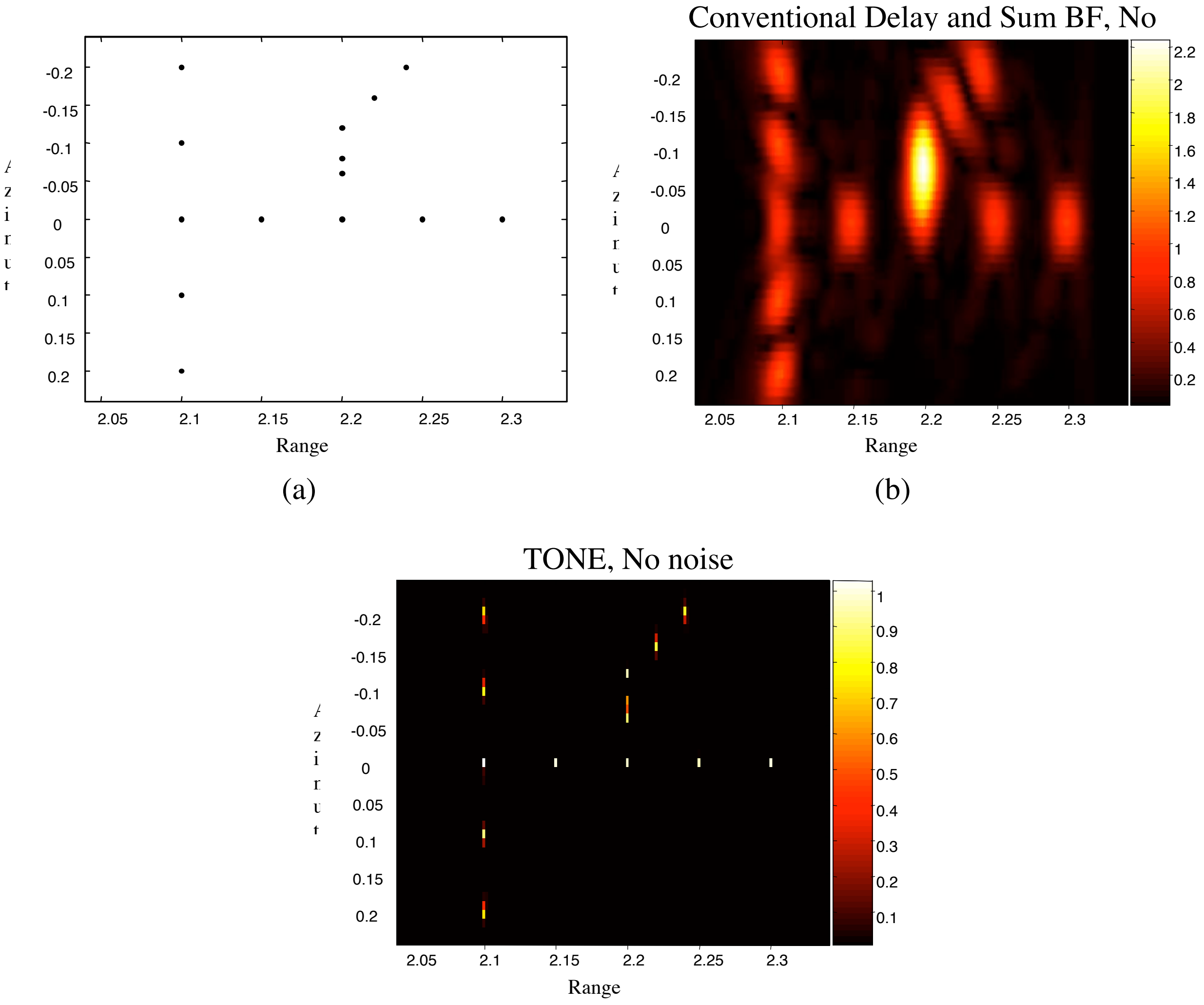

(a)

(b)

(c)

Figure 7. Results obtained simulating a series of wire targets. The wires are depicted in (a); (b) shows conventional delay-and-sum beamforming, whereas (c) show TONE.

Anechoic Cyst Simulation

A 1mm radius anechoic cyst was placed in front of the array and surrounded by ultrasonic scatterers randomly distributed within the image region. Scatterer amplitudes followed a Gaussian distribution with zero mean and standard deviation of one. Simulation methods are the same of those described in the previous section, except that the hypothetical source sampling was reduced to 100μm in azimuth. Again, the positions of the scatterers do not necessarily coincide with the position of the hypothetical sources. Results indicate that SPOC is robust in the presence of large numbers of targets placed at intervals closer than the conventional resolution.

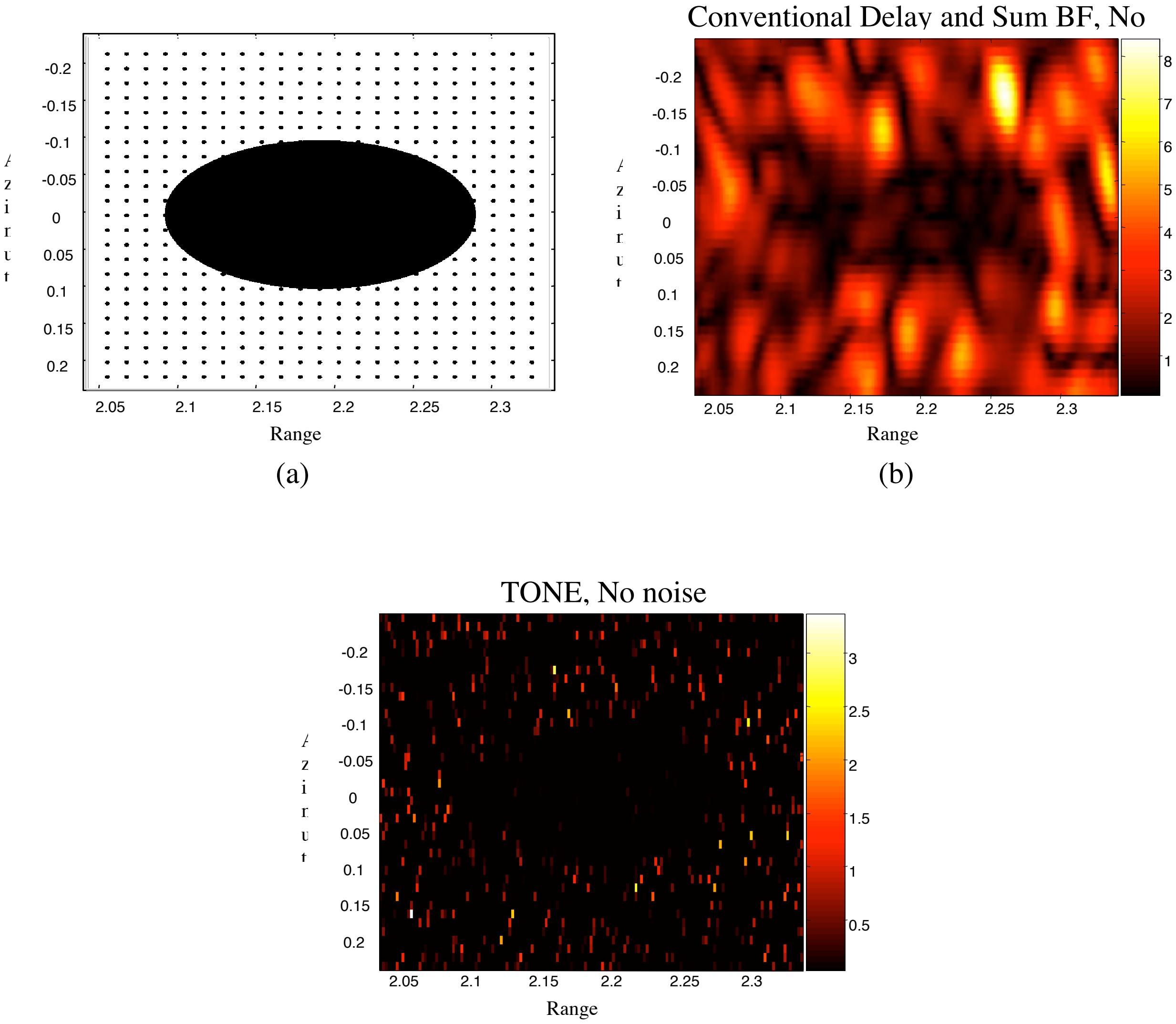

(a) (b)

(c)

Figure 8. Results obtained simulating an anechoic cyst surrounded by scatterers. The cysts is depicted in (a); (b) shows conventional delay-and-sum beamforming, whereas (c) show TONE.

Experimental results

We also performed a series of experiments using a commercially available Philips SONOS 5500 imaging scanner and a series of 5 wires suspended in a water tank. The wires are 20µm in diameter and spaced roughly 2mm apart. The top panel of figure 5 shows the image generated by the Philips scanner, whereas the bottom panel shows the TONE reconstructed image. In the case of TONE we discretized the image region in a series of hypothetical targets separated by roughly 20µm in both range and azimuth. Results indicate that TONE can perform robustly with real experimental data. Further work is ongoing to test TONE in excised tissues.

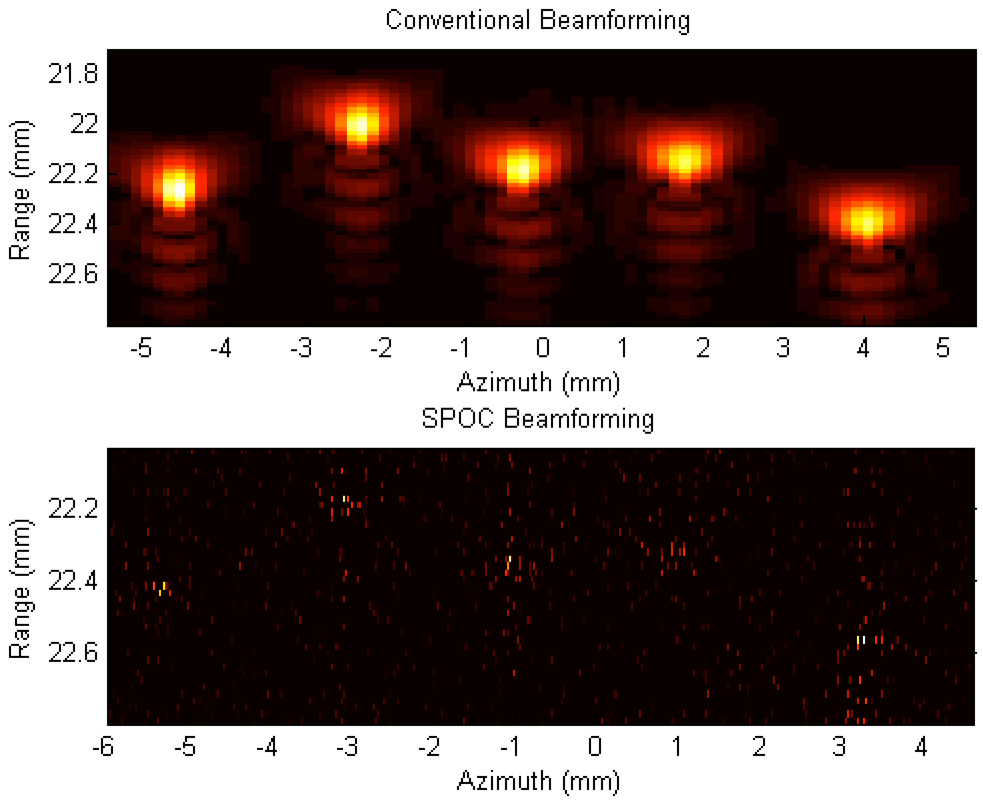
Conventional Beamforming

SPOC Beamforming

Figure 9. Comparison between conventional beamforming (top) and TONE [formerly called SPOC] (bottom) on a set of 5 wires suspended within a water tank. The wires are 20µm in diameter.

Diffuse Target TONE (dTONE):

One of the limitations of TONE is that it assumes that the imaged targets lie at discrete locations within the body, an assumption that is clearly not true in practice. While the impact of this assumption can be mitigated to some extent by more finely sampling the hypothetical target grid, this approach is extremely costly computationally. Further, in our experience it is not clear that the costs incurred result in a significantly better image. Because of the coherent nature of echo summation, a true target lying between two hypothetical target locations might be best modeled by TONE using a large cloud of scatterers spread over a large region of the reconstructed image. This is both unsightly and not useful. To deal with both of these issues we have developed a new variant of TONE called diffuse target TONE or dTONE.

dTONE reconstructs the image in exactly the same manner as TONE, but by using a slightly array manifold matrix $\underline{V}$ it is able to robustly account for targets that do not lie precisely on the reconstruction grid. dTONE alters the array manifold matrix by assuming that the signal from one hypothetical target really originates from a diffuse, amplitude weighted group of targets centered about the hypothetical target location. This approach is more computationally costly in the formulation of the problem, i.e. computation of the array manifold and later eigenvalue decompositions, but has absolutely no impact on the computational cost of the reconstruction. Since we anticipate that the array manifold formation and eigenvalue decompositions will be performed offline, this algorithm represents an elegant way to improve performance. When we reconstruct a dTONE image we represent the targets from each hypothetical location using a bi-cubic spline. This approach yields a smoother and more pleasing image. An experimental dTONE image is compared with a TONE image below in figure 10. The dTONE image has less clutter and is visibly smoother.

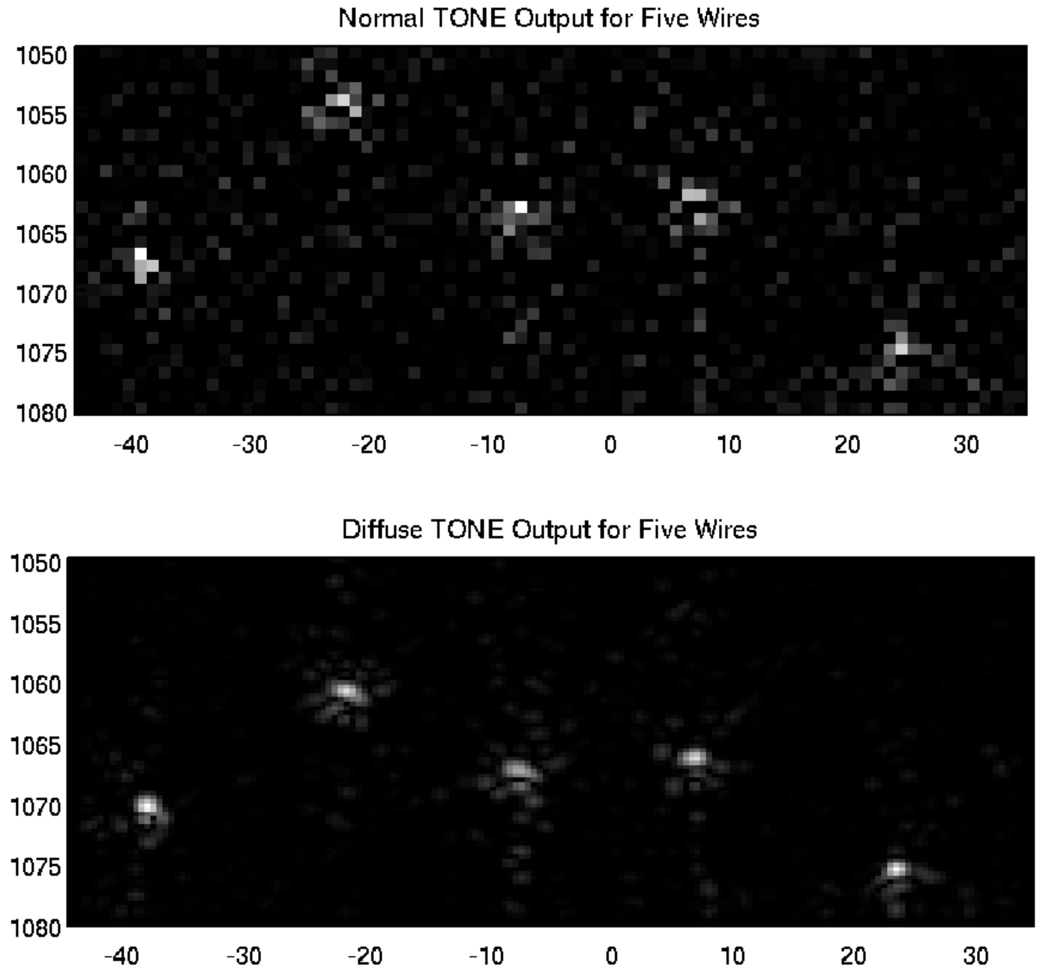

Figure 10. Comparison between experimentally formed TONE and dTONE images.

Simulation Tool Development:

The performance of TONE depends greatly upon the quality of the system model it applies. In our initial simulations we modeled the system using analytical methods, or using the well known FIELD program written by Jørgen Jensen. Unfortunately FIELD is quite slow when computing full 3D spatial impulse responses. Further, because FIELD works entirely on sampled data sets it is prone to artifacts from undersampling. We have implemented the Tupholme-Stepanishen method (the core approach used in FIELD) in a new piece of code we call DELFI. The DELFI code uses cubic spline representations of the transmitted pulse, and the transmit and receive spatial impulse responses. This approach avoids the potential sampling difficulties of FIELD. It is also significantly faster at computing space-space-space responses at an instant in time. These sort of responses are critical in much of our research and the 25 fold increase in speed for DELFI is of great significance. Our paper describing the DELFI code was published this May [18]. Some results from this paper are shown below in figure 11. Note that for space-space responses DELFI is significantly faster to achieve a given accuracy level. For space-time responses DELFI is somewhat slower, but can achieve high accuracy at significantly lower sampling rates. We placed the final version of our DELFI code on the Mathworks web site just after our paper was accepted for publication. This code has been downloaded over 200 times since then.

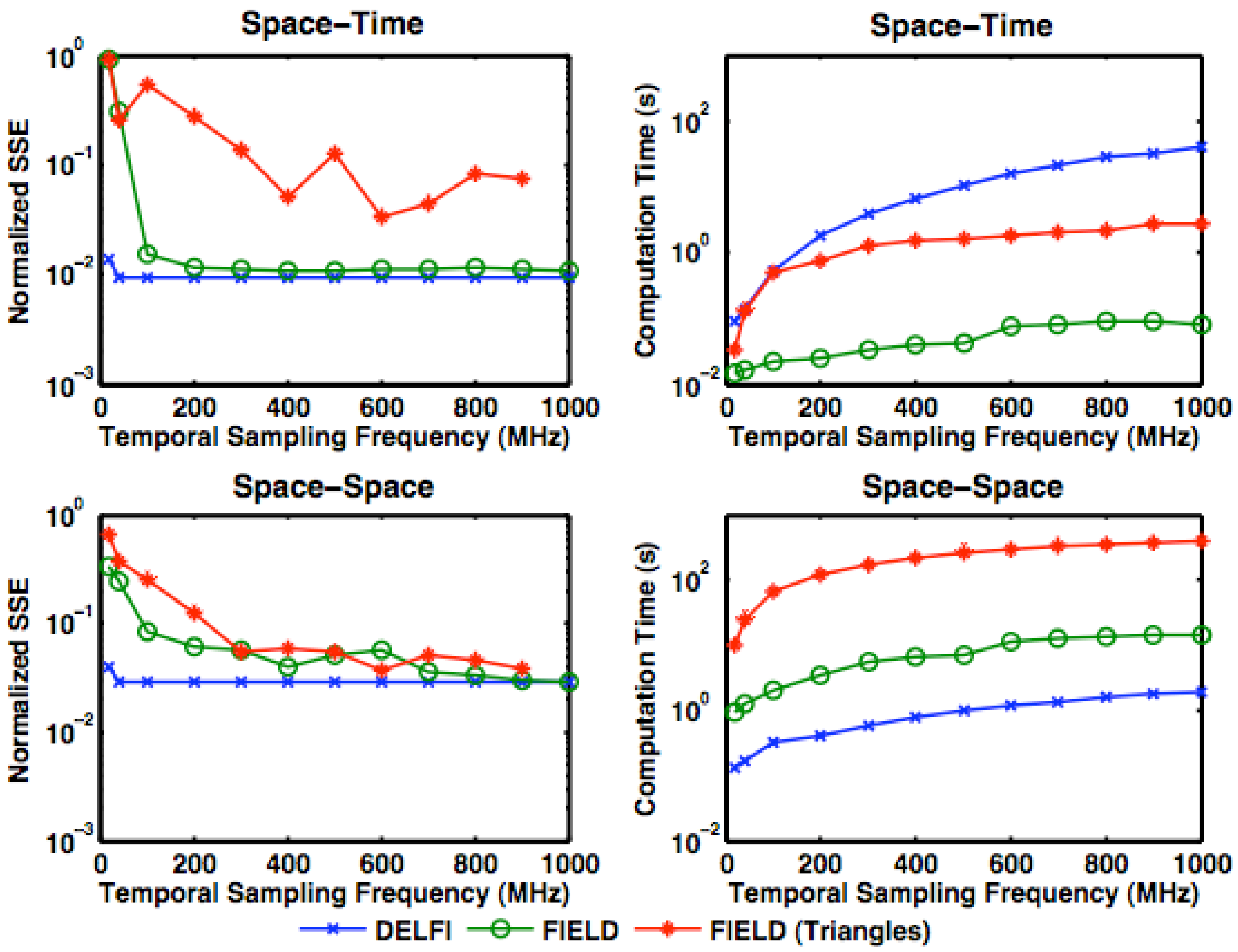

Figure 11: Simulation results comparing the speed and accuracy of DELFI and FIELD (both rectangular and triangular computational elements) for space-space and space-time responses. Note the high accuracy achieved for DELFI at even low sampling rates.

While DELFI is a powerful and computationally efficient tool, the cost of performing detailed simulations of 2D transducer arrays still requires the use of massive computer clusters or even supercomputers. Our team is now collaborating with a local startup (PocketSonics, Inc. in which the PI is a founder) to port the DELFI code to the PlayStation 3. The Cell Processor used by the PS3 represents an ideal low cost platform for these embarrassingly parallel simulations. While this project requires a significant algorithmic change to enable implementation with single precision floating point arithmetic, we are hoping to get prototype software running this summer.

Experimental Platform Development:

As we near the end of the life of this grant we have shifted our experimental work almost entirely to the Ultrasonix Sonix RP. The Sonix RP is a highly programmable research platform built around a clinical ultrasound imaging system. We acquired this system in June 2006 and have since implemented a broad range of tools:

* Python scripting interface for Ultrasonix, to allow interactive control of all transmit/receive sequences without recompilation, for rapid experiment turnaround.
* Synthetic receive control - ability to receive single element RF data on successive transmits.
* Synthetic transmit control - ability to transmit on single elements.

* Automated full synthetic transmit/receive, this lets us capture full synthetic data sets from a 128-element transducer in 30 seconds.
* Automated transducer characterization in conjunction with hydrophone.
* Matlab interface for execution and analysis of simple sequences in a single script.
* Automated averaging of repeatedly captured data to improve SNR.

While we have made tremendous progress in developing tools for system control and data acquisition, our experimental progress is hampered by the poor quality of the transducer arrays currently sold for the Sonix RP. These transducers exhibit poorer element angular response, poorer element spacing, and poorer bandwidth than state of the art transducers. To circumvent this limitation we are integrating a Philips linear array probe with the Sonix RP. This array is at the state of the art for small parts imaging and when integrated, will be recognized by the Sonix RP as native and thus available for real-time imaging and programmed data acquisition.

Another experimental system, not described in the original proposal, is a fully custom system developed in a collaboration with two other investigators at the University of Virginia (John A. Hossack and Travis N. Blalock.) A second generation of this system is being assembled. This second generation system will utilize a 3600 element 2D array and will operate at a 5.0 MHz center frequency. Data from all channels will be acquired in parallel in real-time, however only four real samples will be acquired by each channel. Although the data acquisition of this system is certainly limited in some ways, we believe that this system will provide an excellent testbed for TONE. In the coming months as this system becomes operational we will acquire data to test the viability of TONE on 2D arrays.

Corporate Interactions:
Our work on TONE has great potential, but presents great challenges. We have been assisted in these efforts through a number of valuable corporate interactions.

Our experimental work was originally aided through technical support and equipment donations from Philips Medical Systems. Our transition to the Sonix RP system has of course been supported by UltraSonix.

TONE is extremely challenging to implement computationally and we have worked closely with Interactive Supercomputing to test the algorithm. They have provided technical support to enable the transition of our algorithms to their Star-P MATLAB parallelization software. Interactive Supercomputing has also provided us with free CPU cycles on their high-end cluster.

One of the most exciting corporate collaborations in this project has been our ongoing interaction with InnerVision Medical Technologies. InnerVision is currently developing an ultrasound platform that has both the data acquisition capabilities and computational capabilities to implement TONE clinically. The University of Virginia Patent Foundation is actively negotiating licensing terms with InnerVision and both sides have indicated that they expect to achieve a mutually agreeable conclusion in the next few months.

Transition of DELFI to the PS3 with the support of PocketSonics Inc.

Key Research Accomplishments:

- Developed and published a new metric to quantify ultrasound beamformer performance
- Currently developing another new metric that accurately combines the effects of cystic contrast resulting from the system point spread function and noise on individual beamformer channels.

- Developed and published two new methods for optimizing beamformer apodization functions (LCLS and QCLS design methods.)

- Developed a new ultrasound beamformer architecture (FIR beamformer) that achieves dramatic improvements in image contrast and resolution.

- Developed, tested, and published (accepted) a new adaptive beamformer, the TONE algorithm.

- Developed and have begun testing a variant of TONE, dTONE which yields smoother images with higher contrast and fewer artifacts.

- Developed and published a new approach to ultrasound simulation (DELFI).

- Developed extensive experimental tools for imaging and data acquisition using the Sonix RP.
- Currently integrating a high frequency linear array probe with the Sonix RP to improve image and data quality.

- Built and expanded collaborations with numerous corporations including Philips Medical Systems, UltraSonix, InnerVision, and PocketSonics.
- Active licensing negotiations ongoing.

Reportable Outcomes:

Papers:

Guenther, D.A., and W.F. Walker, "Broadband Optimal Contrast Resolution Beamforming," submitted to IEEE Trans. Ultrason. Ferroelec. Freq. Contr., May 2007.

Viola, F., M.A. Ellis, and W.F. Walker, "Time-Domain Optimized Near-Field Estimator for Ultrasonic Imaging: Initial Development and Results," accepted to IEEE Trans. Med. Imaging.

Ellis, M., D.A. Guenther, and Walker, W.F., "A Spline-Based Approach for Computing Spatial Impulse Responses," IEEE Trans. Ultrason. Ferroelec. Freq. Contr., vol. 54, no. 5, pp. 1045-1054, May 2007.

Ranganathan, K. and W.F. Walker, "Cystic Resolution: A Performance Metric for Ultrasound Imaging Systems," IEEE Trans. Ultrason. Ferroelec. Freq. Contr., vol. 54, no. 4, pp. 782-92, March 2007.

Guenther, D.A., and W.F. Walker, "Optimal Apodization Design for Medical Ultrasound using Constrained Least Squares. Part I: Theory," IEEE Trans. Ultrason. Ferroelec. Freq. Contr., vol. 54, no. 2, pp. 332-42, Feb. 2007.

Guenther, D.A., and W.F. Walker, "Optimal Apodization Design for Medical Ultrasound using Constrained Least Squares. Part II: Results," IEEE Trans. Ultrason. Ferroelec. Freq. Contr., vol. 54, no. 2, pp. 343-58, Feb. 2007.

Conference Abstracts:

K. Owen and W.F. Walker, "A Novel Method for Designing and Fabricating Single Piston Transducers with Extended Depth of Field," submitted to the 2007 IEEE Ultrasonics Symposium.

M.A. Ellis, F. Viola, and W.F. Walker, "Diffuse Targets for Improved Contrast in Beamforming Adapted to Target," submitted to the 2007 IEEE Ultrasonics Symposium.

D.G. Guenther and W.F. Walker, "Optimal Contrast Resolution Beamforming," submitted to the 2007 IEEE Ultrasonics Symposium.

D.A. Guenther and W.F. Walker, "Receive Channel FIR Filters for Improved Contrast in Medical Ultrasound," 2007 SPIE Medical Imaging Symposium.

F. Viola, M.A. Ellis, and W. F. Walker, "Near-Field, Broadband Adaptive Beamforming for Ultrasound Imaging," Fortieth Annual Asilomar Conference on Signals, Systems, and Computers, Pacific Grove, California, USA, 2006.

M.A. Ellis and W.F. Walker, "Piecewise-Linear Approximation for Improved Accuracy in Near-Field Ultrasound Simulation," 2006 IEEE Ultrasonics Symposium.

F. Viola, M.A. Ellis, and W.F. Walker, "Ultrasound Imaging with Beamforming Adapted to Target," 2006 IEEE Ultrasonics Symposium.

D.A. Guenther, Ranganathan, K. and W.F. Walker, "Design of Apodization Profiles Using a Cystic Resolution Metric for Ultrasound," 2005 IEEE Ultrasonics Symposium.

Viola, F. and W.F. Walker, "Adaptive Signal Processing in Medical Ultrasound Beamforming," 2005 IEEE Ultrasonics Symposium.

Viola, F., and W.F. Walker, "Adaptive Beamforming for Medical Ultrasound Imaging," U.S. Dept. of Defense Breast Cancer Research Program Era of Hope 2005 Meeting, June 2005.

Patent Activity:

"System and Method for Adaptive Beamforming for Image Reconstruction and/or Target/Source Localization," W.F. Walker and F. Viola, U.S. Patent Application filed September 19, 2006.

"An Improved Ultrasound Beamformer Using Channel Dependent FIR Filters," G.A. Guenther and W.F. Walker, provisional patent filed October 2, 2006.

"System and Method for Application of a Resolution Metric and Design for Apodization Profiles for Optimal Cystic Contrast," D.A. Guenther and W.F. Walker, patent disclosure filed September, 2005. (abandoned)

"Adaptive Beamformiong for Medical Ultrasound Imaging," F. Viola, and W.F. Walker, patent disclosure filed 2005. (superceded by full application)

Software:

DELFI – A cubic spline based code for simulating spatial impulse responses. Available for download at:
http://www.mathworks.com/matlabcentral/fileexchange/loadFile.do?objectId=13970
Downloaded 227 times as of June 18, 2007.

Conclusions:

As we enter the final months of this grant (a no-cost extension has been requested), we feel that we have made some significant advances that offer a real potential for clinical impact. We will be pursuing follow on funding to evaluate TONE, dTONE, and QCLS in human tissues. We are hopeful that this work will advance the state of the art in breast cancer detection and diagnosis.

References:

[1] V. Jackson, "Management of solid breast nodules: what is the role of sonography?," ***Radiology*****, vol. 196, pp. 14-15, 1995.**

[2] V. P. Jackson, "The Role of US in Breast Imaging," ***Radiology*****, vol. 177, pp. 305 - 311, 1990.**

[3] T. M. Kolb, J. Lichy, and J. H. Newhouse, "Comparison of the Performance of Screening Mammography, Physical Examination, and Breast US and Evaluation of Factors that Influence Them: An Analysis of 27,825 Patient Evaluations," ***Radiology*****, vol. 225, pp. 165-175, 2002.**

[4] M. O'Donnell and S. W. Flax, "Phase aberration correction using signals from point reflectors and diffuse scatters: measurements," ***IEEE Trans. Ultrason. Ferroelec. Freq. Contr.*****, vol. 35, pp. 768-774, 1988.**

[5] M. O'Donnell and S. W. Flax, "Phase aberration measurements in medical ultrasound: human studies," ***Ultrasonic Imaging*****, vol. 10, pp. 1-11, 1988.**

[6] L. Nock, G. E. Trahey, and S. W. Smith, "Phase aberration correction in medical ultrasound using speckle brightness as a quality factor," ***JASA*****, vol. 85, pp. 1819-1833, 1989.**

[7] S. Krishnan, P.-C. Li, and M. O'Donnell, "Adaptive Compensation of Phase and Magnitude Aberrations," ***IEEE Transactions on Ultrasonics Ferroelectrics & Frequency Control*****, vol. 43, pp. 44-55, 1996.**

[8] L. M. Hinkelman, D.-L. Liu, R. C. Waag, Q. Zhu, and B. D. Steinberg, "Measurement and correction of ultrasonic pulse distortion produced by the human breast.," ***Journal of the Acoustical Society of America*****, vol. 97:3, pp. 1958-1969, 1995.**

[9] G. Ng, P. D. Freiburger, W. F. Walker, and G. E. Trahey, "A technique for adaptive imaging in the presence of distributed aberrations," presented at IEEE Ultrasonics Symposium, Seattle, Washington, 1995.

[10] Q. Zhu and B. D. Steinberg, "Correction of multipath interference using clean and spatial location diversity," presented at IEEE International Ultrasonics Symposium, Seattle, Washington, 1995.

[11] K. Rigby, E. Andarawis, C. Chalek, B. Haider, W. Hinrichs, R. Hogel, W. Leue, M. Angle, B. McEathron, S. Miller, S. Peshman, M. Peters, L. Thomas, S. Krishnan, and M. O'Donnell, "Realtime Adaptive Imaging," presented at IEEE Ultrasonic Symposium, 1998.

[12] K. Rigby, C. Chalek, B. Haider, R. Lewandowski, M. O'Donnell, L. Smith, and D. Wildes, "Improved in vivo Abdominal Image Quality Using Real-Time Estimation and Correction of Wavefront Arrival Time Errors," presented at IEEE Ultrasonics Symposium, 2000.

[13] R. Gauss, G. Trahey, and M. Soo, "Wavefront Estimation in the Human Breast," presented at SPIE Medical Imaging, 2001.

[14] R. Bethel, B. Shapo, and H. V. Trees, "Single Snapshot Spatial Processing: Optimized and Constrained," presented at Sensor Array and Multichannel Signal Processing Workshop Proceedings, 2002.

[15] K. W. Lo, "Adaptive Array Processing for Wide-Band Active Sonars," ***IEEE Journal of Oceanic Engineering*****, vol. 29, pp. 837-846, 2004.**

[16] F. Viola, M. A. Ellis, and W. F. Walker, "Time-Domain Optimized Near-Field Estimator for Ultrasonic Imaging: Initial Development and Results," ***IEEE Transactions on Medical Imaging*****, in press.**

[17] D. A. Guenther and W. F. Walker, "Broadband Optimal Contrast Resolution Beamforming," ***IEEE Transactions on Ultrasonics Ferroelectrics & Frequency Control*****, submitted 2007.**

[18] M. A. Ellis, D. A. Guenther, and W. F. Walker, "A Spline-Based Approach for Computing Spatial Impulse Responses," ***IEEE Transactions on Ultrasonics Ferroelectrics & Frequency Control*****, vol. 54, pp. 1045-54, 2007.**

[19] K. Ranganathan and W. F. Walker, "Cystic Resolution: A Performance Metric for Ultrasound Imaging Systems," *IEEE Transactions on Ultrasonics Ferroelectrics & Frequency Control*, vol. 54, pp. 782-92, 2007.

[20] D. A. Guenther and W. F. Walker, "Optimal Apodization Design for Medical Ultrasound using Constrained Least Squares. Part II: Results," *IEEE Transactions on Ultrasonics Ferroelectrics & Frequency Control*, vol. 54, pp. 343-58, 2007.

[21] D. A. Guenther and W. F. Walker, "Optimal Apodization Design for Medical Ultrasound using Constrained Least Squares. Part I: Theory," *IEEE Transactions on Ultrasonics Ferroelectrics & Frequency Control*, vol. 54, pp. 332-42, 2007.

Manuscript submitted for publication in IEEE Transactions UFFC May 29th, 2007

Broadband Optimal Contrast Resolution Beamforming

Drake A. Guenther and William F. Walker
Dept. of Biomedical Engineering, University of Virginia
dag2m@virginia.edu

ABSTRACT

This paper proposes a novel receive beamformer architecture for broadband imaging systems that uses unique finite impulse response (FIR) filters on each channel. The conventional delay-and-sum (DAS) beamformer applies receive apodization by weighting the signal on each receive channel prior to beam summation. Our proposed FIR beamformer passes the focused receive radio frequency (RF) signals through multi-tap FIR filters on each receive channel prior to summation. The receive FIR filters are constructed to maximize the contrast resolution of the system's point spread function (PSF). We describe an array pattern synthesis technique that utilizes *a priori* knowledge about the imaging system to model the transmit/receive PSF. The broadband FIR beamformer produces PSFs with narrower mainlobe widths and lower sidelobe levels than PSFs produced by the conventional DAS beamformer.

We present simulation results showing that FIR filters of modest tap lengths (3-7) can yield marked improvement in image contrast and point resolution. Specifically we show that 7-tap FIR filters can reduce sidelobe and grating lobe energy by 30dB and improve contrast resolution by as much as 20dB compared to conventional apodization profiles. We investigate the effects of phase aberration and show simulation results that the multi-tap FIR beamformer outperforms the conventional DAS beamformer by 8 to 12 dB even in the presence of aberration characterized by a root-mean-square strength of 28 ns and a full-width at half-maximum correlation length of 3.6 mm. We show experimental results wherein multi-tap FIR filters decrease sidelobe energy in the resulting 2D PSF while achieving a narrow mainlobe. We also show results where the FIR beamformer improves the contrast to noise ratio (CNR) in simulated B-mode cyst images by more than 4 dB. Our algorithm has the potential to significantly improve ultrasound beamforming in any application where the system response is well characterized. Furthermore, this algorithm can be used to increase contrast and resolution in one-way beamforming systems such as acousto-optic and opto-acoustic imaging.

INTRODUCTION

Weighting individual receive channels can significantly change the sensitivity and resolution of the delay-and-sum (DAS) beamformer. Conventional apodization functions like the rectangular, Bartlett, and Hamming windows offer a tradeoff between the beamformer spatial impulse response's mainlobe width and sidelobe levels [1]. Because receive channel weighting changes the shape of the overall system PSF, apodization greatly affects the contrast and resolution of the final output image. The rich history of array pattern synthesis includes volumes about the design and optimization of apodization functions. For example, Nuttall produced a window that minimized the maximum sidelobe level [2] and Er *et al.* derived techniques to achieve array patterns that minimized the mean squared sidelobe energy [3]-[5]. Adams developed an algorithm to calculate a window that achieved the optimal tradeoff between peak sidelobe level and total sidelobe energy [6]. He also plotted peak sidelobe level versus sidelobe energy to easily visualize and compare the performance of different windows. Cox *et al.* determined the optimal weighting function that maximized array gain in the presence of white noise to achieve “superdirectivity” [7]. The latter required assumptions about the noise field statistics. Almost all of the previously mentioned optimal beamforming techniques share a common goal: to increase sensitivity and directivity of the beamformer. The apodization functions are “optimal” given certain performance criterion. However, these previous methods are limited in their application to general broadband beamforming systems since they rely upon far-field, narrowband assumptions.

Docolo and Moonen thoroughly described designing apodization functions for broadband, nearfield beamformers using eigenfilters and a total least squares error criterion [8]. Korompis *et al.* developed a broadband beamformer with maximum energy and arbitrary spatial and frequency constraints [9]. Both of these methods provided novel design procedures for synthesizing broadband array patterns, but their applicability to conventional ultrasound is limited since the algorithms were intended for synthesizing beampatterns for communications and passive microphone arrays, not for constructing pulse-echo beampatterns for imaging low echogenicity targets.

Conventional ultrasound imaging systems use delay-and-sum beamforming strategies and apply dynamic receive apodization to control f/# with depth, decrease sidelobes, and to suppress edge effects resulting from a finite aperture size. Optimal apodization design techniques like [8] and [9] above have only recently been applied to medical ultrasound. Schwann *et al.* [10] used an assortment of resolution criteria to optimize frequency-dependent receive apodization. Ranganathan and Walker [11] used a minimum sum squared error technique to develop apodization functions for arbitrary system design. Their method is useful in aiding the design of prototype systems, but suffers from the lack of a quantitative measure detailing how system performance changes with respect to a deviation in system parameters. Our group previously described an aperture design method using constrained least squares to produce spatial impulse responses that maximized contrast resolution according to a general cystic resolution metric [12], [13]. This method utilizes *a priori* information about the system in order to optimize the beamformer's spatial impulse response characteristics. Therefore, whereas the DAS beamformer is considered data independent, this method incorporates system characteristics to improve the DAS beamformer's performance.

In this work we replace the dynamic receive aperture weights with dynamic finite impulse response (FIR) filters. The FIR filters on each channel are unique, and the filter weights are chosen to maximize contrast resolution. A simplified depiction of the conventional DAS beamformer and the proposed multi-tap FIR beamformer is shown in figure 1. Note that apodization is applied in both architectures after the dynamic focal delays have been applied, thus all RF data coming into the apodization portion of the beamformer are focused. The proposed multi-tap FIR beamformer increases system complexity, but should be relatively easy and inexpensive to implement in modern system hardware.

The proposed beamformer architecture using FIR filters on each receive channel is well known and utilized in the RADAR signal processing literature [14]-[16]. Furthermore, dynamic FIR filters have been used extensively to increase sensitivity and directivity in adaptive RADAR array processing [17], [18]. Our proposed FIR beamformer is different from these earlier approaches in that our beamformer is data independent and the filter tap weights are completely deterministic given the *a priori* system model. Furthermore, we are not limited by nearfield, narrowband assumptions and do not require estimation of the receive signal second order statistics. The FIR beamformer utilizes our previous apodization design method that optimizes the weights of the conventional DAS beamformer to maximize contrast resolution [12]. In this paper we extend that algorithm to calculate the optimal weights for the FIR filters utilizing a general cystic resolution metric. Our beamformer can be readily adapted to existing commercial architectures and also offers the potential to significantly improve the point resolution and contrast of one-way beamforming systems [19]-[21], some novel passive ultrasound systems [22]-[24], as well as improve performance of the spatial matched filter beamformer [25].

THEORY

Our goal is to determine optimal dynamic filter tap weights for the receive FIR beamformer depicted in figure 1. We model a pulse-echo broadband imaging system; however, the algorithm can be adapted to model a passive, receive only system as well as a narrowband/farfield array processor. The proposed beamformer is specially suited for medical ultrasound since it maximizes contrast resolution of anechoic targets, but applies to general array pattern synthesis since it produces PSFs with narrow mainlobes and low sidelobes.

A. Linear algebra formulation of the spatial point spread function

The sensitivity field for a transducer during pulse-echo imaging can be expressed as the product of a propagation matrix, *S*, and a set of aperture weightings, *w*. The propagation matrix uses superposition to describe the contribution of each transducer element at each field point at an instant in time. For our formulation, *S* is a function of the transmit aperture weights, the excitation pulse, and the individual element impulse responses of the transmit and receive elements. Focusing on transmit and/or receive using our formulation is accomplished by adjusting the instant in time at which to capture the spatial response for an individual element. We refer the reader to [12] for a more detailed analysis of the linear algebra formulation of the PSF and present a brief review of the major results below.

The two way pulse echo propagation matrix, *S*, for a fixed transmit aperture and a *n* element focused receive aperture at a total number of *p* points in three dimensional space is:

$$S = \begin{bmatrix} s_{1,1} & s_{1,2} & \cdots & s_{1,n} \\ s_{2,1} & . & \cdots & . \\ \vdots & \vdots & \ddots & \vdots \\ s_{p,1} & . & \cdots & s_{p,n} \end{bmatrix}, \tag{1}$$

where $s_{i,j}$ is the contribution of the *j*th receive element at the *i*th point in three dimensional space. The receive aperture weighting function, w, for each of the *n* elements used on receive can be written in vector form as:

$$w = \begin{bmatrix} w_1 & w_2 & w_3 & \cdots & w_n \end{bmatrix}^T, \tag{2}$$

where T denotes the vector transpose operation. Using (1) and (2), we can now write the complete two-way pulse echo system PSF, P, as follows:

$$P = Sw, \tag{3}$$

the propagation matrix multiplied by the receive weighting vector. Note that this results in the one dimensional column vector, P, of length p the total number of points in three-dimensional space where the system PSF is measured.

To expand our formulation to include receive channel FIR filters, we recognize that the final spatial PSF of the FIR beamformer is a linear superposition of multiple dynamically focused 2-way PSFs. We create a new propagation matrix, S_{FIR}, which is a simple combination of the propagation matrices associated with each dynamic receive focus. The number of propagation matrices included corresponds to number of FIR filter taps, k.

$$S_{FIR} = \left[S_{z1}, S_{z2}, S_{z3}, \ldots S_{zk}\right] = \begin{bmatrix} s_{z1,1,1} & s_{z1,1,2} & \cdots & s_{z1,1,n} & \cdots & s_{zk,1,1} & s_{zk,1,2} & \cdots & s_{zk,1,n} \\ s_{z1,2,1} & \cdot & \cdots & \cdot & \cdots & s_{zk,2,1} & \cdot & \cdots & \cdot \\ \vdots & \vdots & \ddots & \vdots & \cdots & \vdots & \vdots & \ddots & \vdots \\ s_{z1,p,1} & \cdot & \cdots & s_{z1,p,n} & \cdots & s_{zk,p,1} & \cdot & \cdots & s_{zk,p,n} \end{bmatrix},$$

(4)

where $s_{zk,i,j}$ is the contribution of the jth element at the ith point in space for the kth receive focus (tap). Adequate spatial and temporal sampling of the three dimensional PSF yields huge propagation matrices, and therefore for this paper we have limited our analysis to two spatial dimensions, azimuth and range, and assume a temporal sampling rate of 40 MHz for the FIR filters. The receive FIR filter taps, w_{FIR}, can also be written in vector form as:

$$w_{FIR} = \left[w_{z1,1} \quad w_{z1,2} \quad w_{z1,3} \quad \cdots \quad w_{z1,n} \cdots \; w_{zk,1} \; w_{zk,2} \quad w_{zk,3} \quad \cdots \quad w_{zk,n} \quad \right]^T, \tag{5}$$

where $w_{zk,j}$ is the weight applied for the kth receive focus (tap) on the jth receive element. Using (4) and (5), the complete two-way pulse echo system PSF for the receive channel FIR beamformer using k-taps on each channel is written as follows:

$$P_{FIR} = S_{FIR} w_{FIR} \quad . \tag{6}$$

B. Algorithm for computing the FIR filter taps

The cystic resolution metric described in [26] quantifies the contrast at the center of an anechoic cyst embedded in a speckle generating background. Note that this metric measures contrast at a specific point in space (the center of the cyst) at an instant in time. This is a different parameter than the overall cystic contrast computed from a B-mode image [27]. We refer to the cystic resolution metric's result as a "point contrast" to avoid this confusion. From [28] the point contrast of the center of a cyst relative to the background, neglecting electronic noise, is defined as:

$$C = \sqrt{\frac{E_{out}}{E_{tot}}} \quad , \tag{7}$$

where E_{out} is the PSF energy outside the cyst and E_{tot} is the total PSF energy. The contrast resolution metric identifies the contribution of specific points in the PSF to the overall contrast. Note that if all of the PSF energy lay within the cyst, C would be 0, indicating the best possible contrast. On the other hand, if most of the PSF energy lies outside the cyst, C approaches a value of 1. Therefore, when we present contrast curves as a function of cyst radius, a more negative dB value indicates better performance.

The FIR filter design algorithm uses the above cystic resolution metric to formulate a least squares minimization problem with a quadratic constraint. We call the resulting weights quadratically constrained least squares (QCLS) apodization profiles [12]. Our algorithm utilizes the linear algebraic representation of the PSF presented above. If we describe the PSF for all spatial points in the final image, we can develop a full set of optimal dynamic receive aperture weights for the FIR receive beamformer in figure 1.

We can optimize contrast according to (7) by minimizing the ratio of PSF energy outside a specified cyst boundary to the total PSF energy. This is equivalent to minimizing the ratio of PSF energy outside the cyst to PSF energy inside the cyst:

$$\min_{w} \left\| S_{out} w \right\|^2 \quad \text{subject to the quadratic constraint } \left\| S_{in} w \right\|^2 = 1 \ , \tag{8}$$

where $\left\| \bullet \right\|^2$ denotes the square of the ℓ^2-norm, S_{out} is the propagation matrix for all the spatial points of the PSF lying outside the cyst boundary, and S_{in} is the propagation matrix for all the spatial points of the PSF lying inside the cyst boundary. Note that the quadratic constraint minimizes the ratio of PSF energy outside the cyst to PSF energy inside the cyst. Drawing upon [28], the optimal receive aperture weighting satisfying the quadratic constraint is the eigenvector, w_{eig}, corresponding to the minimum eigenvalue resulting from the generalized eigenvalue decomposition problem of $S_{out}^T S_{out}$ and $S_{in}^T S_{in}$. One of the main advantages of the QCLS technique is that no matrix inversion is required to solve for the optimal apodization profile. The generalized eigenvalue problem [29] for a matrix pair (*A*, *B*) both *n* by *n* matrices, is finding the eigenvalues, λ_k, and the eigenvectors, $x_k \neq 0$, such that:

$$Ax_k = \lambda_k B x_k . \tag{9}$$

SIMULATION RESULTS

A. Comparing the FIR and the DAS Beamformers

We simulated a 64 element 150 µm pitch 1D linear array operating at 6.5MHz and 75% fractional bandwidth in DELFI [30], a custom ultrasound simulation tool that can be downloaded from the Mathworks MATLAB (The Mathworks, Inc., Natick, MA) file exchange website (www.mathworks.com/matlabcentral). All calculations were performed on an IBM Intellistation Z Pro (Processor speed 2.80 GHz, 4.00 Gb RAM, IBM Corporation, Armonk, NY). In general an FIR-QCLS apodization profile took less than three minutes of CPU time to calculate with the longer filters requiring more computation time.

Spatial PSFs were calculated in a 2D plane, azimuth and range, at an instant in time corresponding to a particular receive focus. We investigated the ability of our algorithm to produce optimal PSFs when using different FIR filter lengths and different receive focal depths. We investigated FIR tap lengths ranging from 1-tap to 7-taps and compared these results to PSFs produced using the DAS beamformer with conventional apodization functions applied. In order to investigate the FIR beamformer with multiple taps on each channel we had to acquire multiple spatial PSFs. We assumed a receive sampling frequency of 40 MHz for the FIR beamformer and a speed of sound of 1545 m/s. Therefore, the receive focus of every PSF coming into the FIR beamformer is separated by 19.3 μm in the axial direction. We acquired 7 focused, spatial PSFs centered around one predetermined focal depth in order to have the spatial PSFs required to calculate the unique 1, 3, 5 and 7-tap FIR filters. For instance to calculate the 3-tap FIR filters for the FIR beamformer with a receive focus at 2.0 cm, we used the receive element spatial PSFs that had receive foci of 1.99807 cm, 2.00000 cm, and 2.00193 cm. We then specify a cyst size, for instance a 300 μm radius, in order to identify the spatial points that lie outside the cyst and inside the cyst to populate the propagation matrices. With these propagation matrices, the weights are calculated according to the QCLS algorithm previously described.

Note that cyst size is an important parameter in the QCLS apodization design method: specifying the propagation matrices in equation (8) and implicitly defining mainlobe size in the resulting PSF. PSFs constructed with QCLS profiles designed for larger cysts will naturally have a large mainlobe. We routinely refer to "design cyst size" to differentiate between QCLS profiles. Every design cyst size will produce a different, optimal QCLS profile, yet experience shows that the general shape of the QCLS weights remains similar over a range of cyst sizes. Furthermore, we can produce a set of apodization profiles to achieve optimal contrast at every cyst size. When analyzed with the cystic resolution metric, plotting cystic contrast versus cyst size, this set of QCLS apodization profiles will generate a lower bound on cystic contrast for the FIR and DAS beamformer given the specified system characteristics. Since scanning through all the different apodization profiles would not be realistic in a real-time clinical setting, it is interesting to see how an apodization profile designed for a specific cyst size performs over a range of cyst sizes.

To illustrate this important point, figure 2 shows cystic point contrast curves for the 5-tap FIR beamformer with a receive focus at 2.0 cm (also the transmit focus). Cystic contrast is computed using equation 7 with the PSF centered in the middle of the cyst and plotted as a function of cyst size (from 0.1 mm to 1.0 mm in radius). The dashed line represents the cystic contrast lower bound for this particular beamformer at this receive focal depth. This lower bound is constructed by calculating the cystic contrast for the optimal apodization profile at each cyst size. We also plot the contrast curves for the 5-tap QCLS apodization profiles corresponding to a design cyst radius of 100 μm, 500 μm, and 1000 μm. For each design cyst radius the contrast curve touches the lower bound at that cyst size, and contrast performance suffers away from the design cyst size. We have found that the QCLS profile around the "knee" of the lower bound curve offers good performance over a large working range of cyst sizes. For example, in figure 2 the 500 μm contrast curve achieves better contrast than the 1000 μm curve for the smaller cyst sizes and also outperforms the 100 μm curve for the larger cyst sizes. The 100 μm and 1000 μm curves show that operating at the extremes (really small cysts or really large cysts) will produce optimal contrast at the specific design size, but performance is seriously degraded at other cyst sizes. For the remainder of the simulations we use a 400 μm design cyst radius for the QCLS profiles unless otherwise noted.

We find that excellent performance with the FIR beamformer can be achieved with a modest filter tap length. In figure 3 we show cystic point contrast curves for the DAS and FIR beamformer with a receive focus at 2.0 cm. The dashed vertical line shows the design cyst radius. It is interesting to note that for this particular system and operating conditions conventional receive apodization functions like the Hamming and Nuttall window perform worse than using no apodization (rectangular window). Although the Hamming and Nuttall PSFs have lower sidelobes, the cystic resolution metric shows that the lower sidelobes do not outweigh the resulting increase in mainlobe width. The 1-tap QCLS profile on the other hand lowers sidelobe levels, maintains a narrow mainlobe, and outperforms all the conventional apodization functions for a range of cyst sizes. More compelling results presented in figure 3 are the dramatic increases in cystic resolution when using the multi-tap FIR beamformer. The 3-tap FIR beamformer improves contrast resolution by 10 dB, the 5-tap by 15 dB, and the 7-tap by more than 20 dB. Using longer tap lengths (9, 11, 13, etc.) improved contrast a few more dB over the 7-tap curve but suggests that there is a limit to the increase in cystic contrast achievable by the FIR beamformer.

We investigated the effects of receive focal depth on the FIR beamformer. In figure 4 we show results corresponding to a 64 element receive aperture dynamically focused at 1.0 cm, 2.0 cm (transmit focus), and 3.0 cm. The top row of figures plots the integrated lateral beamplots when using different apodization windows. The beamplots were calculated by integrating the energy of the different spatial PSFs in range. We compare our FIR-QCLS windows against conventional windows such as the rectangular, Hamming, and Nuttall windows. We only show results comparing the QCLS windows with the rectangular window since the Hamming and Nuttall windows performed worse than the rectangular window at all receive depths. We calculated FIR-QCLS windows using a design cyst radius of 0.4 mm with 1-tap, 3-taps, 5-taps, and 7-taps per channel. Notice the marked reduction of the sidelobe levels for the higher tap FIR-QCLS beamplots. Some lateral beamplots show sidelobe level reduction of 30 dB compared to the beamplot for a rectangular window. The bottom row of plots in figure 4 show the cystic point contrast curves. In general contrast improves when increasing the number of taps on each receive channel, however the biggest jump in contrast improvement between tap lengths occurs between three taps and one tap. The FIR-QCLS windows show cystic resolution improvements greater than 10 dB for a wide range of cyst sizes. The FIR-QCLS weights computed for the 1.0 cm and 2.0 cm dynamically focused data achieve contrast improvements of 20 dB over the conventional windows for cysts larger than 0.4 mm. In general we see similar trends at all three dynamic receive focal depths. The contrast improvement decreases at ranges deeper than the transmit focus.

Figure 5 shows the calculated FIR-QCLS weights for the data dynamically focused at 2.0 cm. These weights were computed for a design cyst radius of 0.4 mm. The 1-tap and 3-tap FIR-QCLS weights are mostly smooth Gaussian like functions across the aperture, except at the endpoints where discontinuities appear. The 5-tap and 7-tap weights are much more variant and discontinuous. It is interesting to note that the FIR-QCLS weights take on negative values, a phenomenon never seen in conventional windows like the Hamming or Nuttall window. The weights also invert in time on some channels. Although the weights computed from the FIR-QCLS algorithm are always real, this inversion in time suggests that a 180° phase shift between consecutive time samples reduces sidelobe energy in the PSF.

B. Robustness of the FIR beamformer in the presence of phase aberration

Receive channel focal delays in the DAS beamformer are calculated assuming a propagation speed of sound in tissue. Conventional systems assume a sound velocity of 1540 m/s, however actual sound velocities in human tissue vary between human subject and tissue type [31]. Differences in the assumed sound speed cause wavefront distortion, amplitude variation, and phase variation of the ultrasound beam. These distortions or phase aberrations adversely affect the quality of *in vivo* images. Numerous researchers have applied adaptive imaging techniques to restore the phase coherence of the receive echoes by compensating for these tissue induced aberrations. Nearly two decades of research has been spent on developing algorithms and methods for not only correcting but also estimating aberration in human tissue [31]-[37].

Phase aberration will degrade the DAS beamformer's PSF, reducing the contrast and resolution of the output image. Therefore, it is important to investigate the affects of phase aberration on our proposed FIR beamformer architecture. Recent literature indicates that phase aberrations in the breast can be modeled as a nearfield thin phase screen characterized by a root mean square (RMS) amplitude strength of 28 ns and a full-width at half-maximum (FWHM) correlation length of 3.6 mm [35], [36]. We performed a series of simulations whereby aberrations were used to distort the PSF resulting from the FIR beamformer. Specifically we used data from 100 realizations of a one dimensional 28 ns RMS, 3.6 mm FWHM correlation length aberrator in order to get decent statistics. Each aberrator distorted the instant in time at which each receive channel's spatial response was calculated. Note that the same aberration would apply to all the spatial PSFs required for the input into the FIR beamformer.

Figure 6 shows how the simulated PSFs for different receive apodization profiles are affected by phase aberration. For each apodization function, the left figure shows the unaberrated 2D PSF with a receive focus of 2.0 cm and the right figure shows the same PSF that has been aberrated. The 0.4 mm design cyst radius QCLS apodization profiles were used for all FIR beamformer PSFs. All spatial PSFs are a 6 mm (lateral) by 2 mm (axial) range around the focus. The absolute value of each PSF was calculated and then log compressed to 60 dB for visualization. The aberration profile used for this particular realization is also shown. It is clear that the aberrator raises sidelobe levels and distorts the mainlobe for every PSF. It is interesting that the FIR beamformer PSFs maintain a narrow mainlobe and low sidelobe levels even in the presence of aberration. Furthermore, the sidelobe energy in the aberrated FIR beamformer PSFs continually decreases as tap length increases.

Figure 7 summarizes the data from the aberration simulations. Phase aberration can "steer" the ultrasound beam, which can spatially shift the PSF. In order to be consistent when applying the resolution metric, cystic contrast was computed after centering the cyst at the maximum of each aberrated PSF. The plot on the left shows the unaberrated and aberrated cystic point contrast curves for the rectangular and 7-tap PSFs. Also shown is the lower bound (LB) contrast curve for the 7-tap FIR beamformer. The errorbars show +/- 1 standard deviation about the mean. Aberration degrades the cystic point contrast performance for both apodization functions: the 7-tap PSF by 7 dB and the rectangular PSF by 2 dB. However, the 7-tap aberrated PSF outperforms the unaberrated rectangular PSF by 10 dB. The Hamming and Nuttall window performed worse than the rectangular window and are not shown in this plot for clarity. The plot on the right in figure 7 shows the mean cystic contrast for each aberrated PSF relative to the rectangular window. The 0 dB point on the y-axis indicates the aberrated rectangular window's mean cystic contrast for each cyst size. A more positive dB value indicates better performance than the rectangular window, and errorbars are +/- 1 standard deviation. We only show the Hamming, Nuttall, 1-tap, and 7-tap plots to reduce clutter in the image. It is interesting to note that the Hamming and Nuttall windows achieve worse cystic point contrast compared to the rectangular window over almost the entire range of investigated cyst sizes. The 1-tap QCLS weights in the presence of aberration still improve contrast for the smaller cyst sizes but perform worse than the rectangular, Hamming, and Nuttall window for the large diameter cysts. The 7-tap QCLS weights maintain 10-15 dB cystic point contrast improvements compared to the rectangular window for a large range of cyst sizes. These results show that the FIR beamformer is robust to relatively strong phase aberration errors. Furthermore even the aberrated FIR beamformer outperforms the phase corrected DAS beamformer. These simulation results suggest that the FIR beamformer can dramatically improve the contrast resolution of ultrasound images and is robust in the presence of phase aberration.

EXPERIMENTAL RESULTS

We investigated the ability of our algorithm and novel receive beamformer architecture to improve the spatial PSF characteristics of an Ultrasonix Sonix RP ultrasound scanner (Ultrasonix Medical Corp., Richmond, BC, Canada). The Sonix RP system has a software development kit (SDK) named TEXO that enables low level scanner control with the ability to acquire single channel RF data sampled at 40 MHz with 12 bit precision. We have also created a Python™

programming language interface to the TEXO SDK that allows us to create customized pulse sequences without the need to recompile the system C code. Utilizing our Python™ interface with the TEXO SDK we can acquire a full set of synthetic receive aperture data from a 64 element transmit aperture and 64 element receive aperture in fractions of a second. In order to measure the 2D PSF required for our algorithm, we imaged a 20 μm steel wire in a tank full of deionized water. We electronically scanned the transmit aperture across the array while mechanically moving the array using a 3-axis positioning system (Newport Motion Controller MM3000, Newport Co., Irvine, CA) in order to achieve azimuthal spatial sampling of 75 μm and axial spatial sampling of 50 μm. We interpolated the data in MATLAB using cubic splines to achieve 25 μm azimuthal sampling and 12.5 μm axial sampling. We acquired a 1.95 cm (azimuth) by 0.2 cm (range) by 3000 time sample dataset to characterize the 3D spatio-temporal PSF. The entire experiment required 29 hours to execute, resulting in over 10 Gbytes of raw, averaged RF data. The water temperature remained relatively constant over the course of the experiment, ranging between 21.6-22.4 ^{o}C.

We used the L14-5 128 element linear probe excited with a 1 cycle 6.67 MHz pulse. The transmit aperture consisted of 64 elements focused at 4.0 cm in range (f/2). We acquired 64 receive elements synthetically and averaged each receive signal 100 times to improve electronic SNR. The receive data was digitally bandpass filtered in MATLAB using a 101 order bandpass filter with cutoff frequencies at 4 and 8 MHz. An experimental 2D spatial PSF was formed by sampling the interpolated 3D spatio-temporal PSF for each receive element according to a dynamic receive profile for a particular receive focus.

The log compressed, envelope detected experimental 2D PSFs dynamically focused at 2.0 cm are shown in figure 8. 2D PSFs are shown for conventional apodization functions and 1-tap, 3-tap, 5-tap and 7-tap FIR-QCLS windows designed for a cyst radius of 0.35 mm. The design cyst radius is shown for reference. All images are log compressed to 60 dB. Notice the progressive reduction of PSF energy in the sidelobe regions when using the multi-tap FIR-QCLS design. The 7-tap FIR-QCLS PSF has superior axial and lateral resolution compared to the other PSFs. Figure 9 shows the experimental integrated lateral beamplots and contrast curves. The FIR-QCLS weights reduce sidelobe levels, lower the total PSF energy outside the mainlobe, and decrease mainlobe width. For clarity, only the 1-tap and 7-tap QCLS plots are shown. The contrast curves for the rectangular, Hamming, Nuttall, 1-tap QCLS and 7-tap QCLS experimental PSFs are shown on the right of figure 9. The FIR-QCLS PSFs show increases in cystic resolution compared to the conventional windows. Specifically, the 7-tap apodization profile improved contrast by 7 dB compared to the Hamming window, by 10 dB compared to the rectangular window, and by 12 dB compared to the Nuttall window over a range of cyst sizes. Furthermore, the 7-tap curve achieves the best contrast for all cyst sizes investigated. The QCLS weights for the multi-tap FIR filters are shown in figure 10. They show similar characteristics to the weights computed in the simulations including discontinuities at the edges of the aperture as well as inversion in time.

According to the contrast curves for the simulations and experiments, the FIR beamformer improves cystic contrast. However, results from the cystic resolution metric will not necessarily translate to improved lesion detectability in B-mode images, since the metric only specifies the point contrast at the center of the cyst. Therefore it is desirable to analyze detectability in B-mode images. We simulate B-mode ultrasound images and calculate a contrast to noise ratio (CNR) defined as:

$$CNR = 10\log_{10}\left(\frac{\langle I_{cyst}\rangle}{\langle I_{speck}\rangle}\right), \tag{10}$$

where $\langle I_{cyst}\rangle$ and $\langle I_{speck}\rangle$ are the mean signal intensity values for image regions inside the cyst and outside the cyst, respectively. A similar equation was proposed in [38] for lesion detectability for log compressed B-mode images. We simulated B-mode images of cysts embedded in a speckle generating background by performing a 2-dimensional convolution of a target function and an experimental PSF. Note that this assumes shift invariance of the PSF over the image region, which is a reasonable assumption over the small, simulated axial and lateral ranges. We simulate 1000 different speckle generating backgrounds to get good statistics on lesion contrast as computed by equation 10. We formed B-mode images of cyst sizes ranging from 0.1 mm to 1.75 mm in radius using the rectangular, Hamming, Nuttall, 1-tap QCLS, and 7-tap QCLS experimental PSFs. A representative realization of the simulated B-mode images for all the different PSFs is shown in figure 11. All images are enveloped detected and log compressed to 30 dB. These images show a 5 mm by 5 mm region surrounding a 0.5 mm radius cyst. The QCLS weights were designed for a 0.35 mm radius. The cyst in the image made using the rectangular apodized PSF is corrupted with clutter from the PSF's high sidelobes. The speckle size is finer than the other images due to the PSF's narrow mainlobe. The Nuttall PSF image has much larger speckle size due to the large mainlobe width, which severely blurs the cyst. The Hamming and the 1-tap QCLS PSFs produce similar images, with the 1-tap PSF arguably reducing the clutter inside the cyst to a greater degree. The 7-tap PSF clearly outperforms all the conventional windows, reducing clutter inside the cyst and sharpening the cyst boundary. We show the actual cyst size for comparison.

In figure 12 we plot cyst CNR computed from (10) as a function of cyst radius. We plot the mean values computed over the 1000 trials. A more negative contrast value indicates better performance. We show two plots, one corresponding to a computed contrast at a cyst size that is the same size as the imaged cyst (100% plot on the left) and the other computed assuming a smaller cyst (70% plot on the right). We use a smaller cyst in order to reduce edge effect corruption in the CNR calculations. Contrast improves with increasing cyst radius for all windows. Computing contrast with the true cyst size results in a 2 dB improvement in B-mode CNR for the 7-tap PSF. Computing contrast with 70% of the true cyst size results in a 4-10 dB CNR improvement over the conventional windows. These results reinforce the qualitative improvements seen in the B-mode images of figure 11.

DISCUSSION

We have presented a novel receive beamformer architecture where conventional apodization is replaced with FIR filters on each channel; a system architecture prevalent in the RADAR literature but not currently employed in medical ultrasound. Schwann *et al.* suggested a similar type of architecture for ultrasound using linear phase FIR filters and also discussed the calculation of frequency dependent optimal receive apodization profiles [10]. Their simulation results showed contrast improvements, however, their multiple objective formulation required iterative procedures and made it difficult to determine an “optimal” apodization profile. Our formulation on the other hand requires no iteration and produces an optimal apodization profile (in a least squares sense) that maximizes cystic resolution. Furthermore, the improvements in system performance using the FIR-QCLS windows are easily quantified using the contrast resolution metric. Our beamformer’s mathematical formulation is similar to the broadband maximum energy array described by Korompis *et al.* which maximizes a generalized Rayleigh ratio of beampattern energies. Their algorithm uses a frequency domain far-field analysis and allows for user defined spatial and frequency constraints of the beam pattern [9]. Our QCLS algorithm is similar since it minimizes a ratio of energies, but is different in its formulation for time domain, nearfield, broadband beamforming.

The FIR filters computed from the QCLS algorithm are not linear phase but are frequency dependent given the *a priori* system operating conditions. Constraining them to be linear phase is straightforward using our formulation, however contrast improvements would decrease compared to a nonlinear phase FIR filter of the same order. The frequency response of the FIR-QCLS filters is a concern because it could reduce SNR, negating the improvements in contrast resolution. However, the initial results from the simulations and experiments do not indicate that the FIR-QCLS filters drastically change the spectra of the received data. If future results show that SNR is severely decreased, it may be possible to constrain SNR in our QCLS formulation by using techniques similar to those presented in [9] concerning the constrained maximum energy array.

Our experimental and simulation results show that we can achieve large gains in cystic contrast with a modest length FIR filter (3-7 taps). The contrast curves also indicate that the gains in contrast decrease with increasing tap length. It is natural to wonder if limits exist on the length of the FIR filters or if there exists a lower bound on contrast. Filter tap length is limited by the sampling of the A/D in the receive beamformer. As tap length increases the resulting FIR beamformer PSF incorporates PSFs that are displaced more and more axially around the particular focus. Eventually the QCLS algorithm will incorporate a PSF where most of the PSF's energy lies outside the design cyst boundary. This will tend to make the filter tap weights associated with that PSF close to 0. This effect can be seen in the 7-tap weight images of figures

5 and 10, where the first and last taps for every receive channel are smaller in magnitude than the weights for the middle taps on each channel. One could naturally increase the number of possible taps by increasing the sampling frequency of the receive A/D's. This may further enhance the contrast improvements however higher sampling frequencies will require significant changes to the receive beamformer hardware as well as increase system complexity. For this paper we assumed a sampling frequency of 40 MHz, typical for conventional systems, and will investigate higher sampling frequencies in future research.

Our experimental results do not show the same large gains in contrast (15-20 dB) and point resolution observed in the simulations. Possible causes for this disparity include: a limited element angular response on the array, poor single channel SNR, element nonuniformity across the array, and hysteresis in the motors of the 3D motion stage. All of these effects are detrimental to the FIR-QCLS algorithm. While compiling a full set of dynamic receive FIR-QCLS filters for every output image pixel is possible given the full spatio-temporal PSF dataset, to acquire such a dataset is infeasible with our current experimental setup. We are currently researching methods to improve our characterization of the system without the need to physically acquire the full 4D spatio-temporal PSF. If these solutions prove successful, we will be able to calculate the full set of receive filters and further assess the performance of our algorithm to produce optimal contrast.

Further investigation is required to examine the effects of phase aberration on the FIR beamformer, although the simulation results presented in this paper suggest that the FIR beamformer is robust to such distortion. We must investigate different system conditions and acquire *in vivo* data in order to fully appreciate the extent to which phase aberration corrupts the FIR beamformer. We point out that our PSF formulation is readily adaptable to model harmonic imaging which has been shown to reduce the detrimental effects of phase aberration [39].

Ranganathan's [26] cystic resolution metric quantifies the contrast at a single point in space at an instant in time. In this paper we use it to measure the contrast of the center of a cyst in a speckle background. The cystic resolution metric is useful for guiding system design because system parameters can be optimized in a straightforward, rigorous manner. However, the relationship between cystic resolution and lesion detectability in B-mode images remains unclear. The B-mode CNR plots in figure 12 show improvements in contrast using the 7-tap PSF as compared to the conventional windows. The 2-2.5 dB estimated for the true cyst size does not seem indicative of the qualitative improvement in detectability seen in figure 11. The 4-10 dB improvements observed when using 70% of the true cyst size indicate that edge effects were corrupting the 100% radius CNR calculations. These results suggest that even a small change in B-mode contrast can greatly improve lesion detectability for small cysts. The authors point out that more rigorous contrast-detail metrics, such as those presented in [27] and [38], were not used because these previous metrics rely upon the assumption that the cyst encompasses many resolution cells (> 20). The cysts investigated in our B-mode analysis are much smaller and do not satisfy these resolution cell requirements. We did not investigate large cyst sizes (0.5 cm – 2 cm in diameter) because the experimental contrast curves in figure 9 show that for cysts greater than 2 mm in diameter cystic contrast levels off for all the different PSFs. Furthermore, the acquired experimental PSFs are limited in range and our shift invariance assumption of the PSF becomes less valid for larger ranges. Nonetheless, figures 11 and 12 show qualitative and quantitative improvements in contrast using the FIR beamformer. We plan to perform a human observer study in order to further assess the contrast enhancements of our novel receive beamformer architecture.

The FIR beamformer presented in this paper offers large contrast improvements for a minimal increase in system complexity. Once the system response has been adequately characterized, computation of the FIR filters is straightforward and requires no iteration. Results suggest that the FIR beamformer has the potential to significantly improve contrast of anechoic lesions and improve beamforming in general with the synthesis of PSFs that have narrow mainlobes and low sidelobes. The FIR beamformer should increase contrast and resolution as well as extend the depth of field in conventional B-mode imaging. In one-way beamforming systems and other novel beamforming techniques, the FIR beamformer could increase point resolution and contrast by improving the overall system PSF.

CONCLUSION

The results presented here show that under the analyzed conditions, the FIR beamformer enhances the contrast resolution of ultrasound images. The 2D spatial PSFs produced in simulations and experiments show lower sidelobe levels and narrower mainlobes than PSFs produced with the DAS beamformer and conventional apodization windows. The FIR-QCLS algorithm appears stable across dynamic receive focal ranges and performs better in the presence of phase aberration than a phase corrected DAS beamformer. Further investigation is required to examine the effects of shift variance of the system response, varying frequency response of the channel filters, and the costs of implementation in a real system. Results suggest that filters with as few as 7 taps can offer large contrast improvements. Furthermore, FIR-QCLS apodization profiles consistently outperform conventional apodization profiles and offer significant gains in image quality with a modest increase in system complexity.

ACKNOWLEDGEMENTS

The authors would like to thank Kevin Owen for his assistance in developing the experimental control software. We thank Kris Dickie and Ultrasonix Medical Corporation for technical support. This work was supported by US Army Congressionally Directed Research Program Grant No. W81XWH-04-1-0590.

REFERENCES

[1] K. E. Thomenius, "Evolution of ultrasound beamformers," in *Proc. of the 1996 IEEE Ultrason. Symp.*, pp. 1615-1622, 1996.

[2] A. H. Nuttall, "Some Windows with Very Good Sidelobe Behavior." *IEEE Trans. Acoust., Speech, and Signal Process.*, vol. 29, no. 1, pp. 84-91, 1981.

[3] M. H. Er, "Array pattern synthesis with a controlled mean-square sidelobe level," *IEEE Trans. Signal Processing*, vol. 40, no. 4, pp. 977-981, 1992.

[4] S. L. Sim and M. H. Er, "Constrained optimization technique for general array pattern synthesis," *Electron. Lett.*, vol. 32, no. 10, pp. 861-862, 1996.

[5] M. H. Er, S. L. Sim, and S. N. Koh, "Application of constrained optimization techniques to array pattern synthesis," *Signal Processing*, vol. 34, pp. 323-334, 1993.

[6] J. Adams, "A New Optimal Window," *IEEE Transactions on Signal Processing*, vol. 39, no. 8, pp. 1753-1769, 1991.

[7] H. Cox, R. M. Zeskind, and T. Kooij, "Practical Supergain," *IEEE Trans. Acoust., Speech, and Signal Process.*, vol. 34, no. 3, pp. 393-398, 1986.

[8] S. Docolo and M. Moonen, "Design of far-field and near-field broadband beamformers using eigenfilters," *Signal Processing*, vol. 83, pp. 2641-2673, 2003.

[9] D. Korompis, K. Yao, and F. Lorenzelli, "Broadband Maximum Energy Array with User Imposed Spatial and Frequency Constraints," *Proc. of the 1994 IEEE ICASSP*, vol. 4, pp. 529-532, 1994.

[10] R. Schwann, N. Stache, and T. G. Noll, "Optimization of Frequency Dependent Receive Apodization," *Proc. of the 2005 IEEE International Ultrasonics Symposium*, vol. 4, pp. 1988-1991, 2005.

[11] K. Ranganathan and W. F. Walker, "A novel beamformer design method for medical ultrasound. Part I: Theory," *IEEE Trans. Ultrason., Ferroelect., Freq. Contr.,* vol. 50, no. 1, pp. 15-24, 2003.

[12] D. A. Guenther and W. F. Walker, "Optimal Apodization Design for Medical Ultrasound using Constrained Least Squares. Part I: Theory," *IEEE Transactions on Ultrasonics, Ferroelectrics, and Frequency Control*, vol. 54, no. 2, pp. 332-342.

[13] D. A. Guenther and W. F. Walker, "Optimal Apodization Design for Medical Ultrasound using Constrained Least Squares. Part II: Simulation Results," *IEEE Transactions on Ultrasonics, Ferroelectrics, and Frequency Control*, vol. 54, no. 2, pp. 343-358.

[14] I. Thng, A. Cantoni, and Y. H. Leung, "Derivative Constrained Optimum Broad-Band Antenna Arrays," *IEEE Trans. on Sig. Proc.*, vol. 41, no. 7, pp. 2376-2388, 1993.

[15] M. Er and A. Cantoni, "A New Approach to the Design of Broad-Band Element Space Antenna Array Processors," *IEEE Journal of Oceanic Engineering*, vol. OE-10, no. 3, pp. 231-240, 1985.

[16] H. Van Trees, *Optimum Array Processing: Part IV Detection, Estimation, and Modulation Theory.* New York, NY: John Wiley and Sons, Inc., 2002.

[17] O. L. Frost III, "An Algorithm for Linearly Constrained Adaptive Array Processing," *Proc. IEEE*, vol. 60, no. 8, pp. 926-935, 1972.

[18] B. Widrow, K. M. Duvall, R. P. Gooch, and W. C. Newman, "Signal Cancellation Phenomena in Adaptive Antennas: Causes and Cures," *IEEE Trans. on Antennas and Propagation*, vol. 30, no. 3, pp. 469-478, 1982.

[19] M. Tanter, J. Bercoff, L. Sandrin, and M. Fink, "Ultrafast Compound Imaging for 2-D Motion Vector Estimation: Application to Transient Elastography," *IEEE Transactions on Ultrasonics, Ferroelectrics, and Frequency Control*, vol. 49, no. 10, pp 1363-1374, 2002.

[20] M. Fuller *et al.*, "Portable, Low Cost Medical Ultrasound Device Prototype," *Proc. of the 2004 IEEE International Ultrasonics Symposium*, vol. 1, pp. 106-109, 2004.

[21] M. Fink, L. Sandrin, M. Tanter, S. Catheline, S. Chaffai, J. Bercoff, and J.-L. Gennisson, "Ultra High Speed Imaging of Elasticity," *Proc. of the 2002 IEEE International Ultrasonics Symposium*, vol. 2, pp. 1811-1820, 2002.

[22] S. Emelianov *et al.,* "Combined ultrasound, optoacoustic, and elasticity imaging, "*Proc. of the 2004 International Biomedical Optics Symposium*, vol. 5320, pp. 101-112, 2004.

[23] V. Kozhushko *et al.*, "Focused array transducer for two-dimensional optoacoustic tomography," *Journal Acoust. Soc. Am.*, vol. 116, no. 3, pp. 1498-1506, 2004.

[24] S. Sethuraman *et al.*, "Intravascular Photoacoustic Imaging Using an IVUS Imaging Catheter," *IEEE Transactions on Ultrasonics, Ferroelectrics, and Frequency Control*, vol. 54, no. 5, pp 978-986, 2007.

[25] K. Kim, J. Liu, and M. F. Insana, "Efficient array beam forming by spatial filtering for ultrasound B-mode imaging," *Journal Acoust. Soc. of America*, vol. 120, no. 2, pp. 852-861, 2006.

[26] K. Ranganthan and W. F. Walker, "Cystic Resolution: A Performance Metric for Ultrasound Imaging Systems," *IEEE Trans. Ultrason., Ferroelect., Freq. Contr.,* vol. 54, no. 4, pp. 782-792, 2007.

[27] S. W. Smith and H. Lopez, "A contrast-detail analysis of diagnostic ultrasound imaging," *Med. Phys.*, vol. 9, no. 1, pp. 4-12, 1982.

[28] W. H. Gander, "Least Squares with a Quadratic Constraint," Numerische Mathematik, vol. 36, pp. 291-307, 1981.

[29] G. H. Golub and C. F. Van Loan, *Matrix Computations*. 3rd ed, Baltimore: Johns Hopkins University Press, pp. 375-378, 1996.

[30] M. Ellis, D. A. Guenther, and W. F. Walker, "A Spline Based Approach for Computing Spatial Impulse Responses," *IEEE Trans. Ultrason., Ferroelect., Freq. Contr.,* vol. 54, no. 5, pp. 1045-1054, 2007.

[31] S. A. Goss, R. L. Johnston, and F. Dunn, "Compilation of empirical ultrasonic properties of mammalian tissues," *J. Acoust. Soc. Amer.,* vol. 64, no. 2, pp. 423-457, 1978.

[32] S. W. Flax and M. O'Donnell, "Phase aberration correction using signals from point reflectors and diffuse scatterers: Basic principles," *IEEE Trans. Ultrason., Ferroelect., Freq. Contr.,* vol. 35, no. 6, pp. 758-767, 1988.

[33] M. O'Donnell and S. W. Flax, "Phase aberration measurements in medical ultrasound: Human studies," *Ultrason. Imag.,* vol. 10, no. 1, pp. 1-11, 1988.

[34] D.-L. Liu and R. C. Waag, “Correction of ultrasonic wavefront distortion using backpropagation and a reference waveform method for time-shift compensation,” *J. Acoust. Soc. Amer.,* vol. 96, no. 2, pp. 649-660, 1994.

[35] R. C. Gauss, M. S. Soo, and G. E. Trahey, “Wavefront distortion measurements in the human breast,” *Proc. of the 1997 IEEE International Ultrasonics Symposium*, pp. 1547-51, 1997.

[36] A. T. Fernandez, J. J. Dahl, D. Dumont, and G. Trahey, “Array elevation requirements in phase aberration correction using an 8x128 1.75D array,” *Proc. of SPIE Medical Imaging 2002*, vol. 4687, pp. 79-90, 2002.

[37] J. J. Dahl *et al.*, “Adaptive imaging on a diagnostic ultrasound scanner at quasi real-time rates,” *IEEE Trans. Ultrason., Ferroelect., Freq. Contr.,* vol. 53, no. 10, pp. 1832-1843, 2006.

[38] P. C. Li and M. O’Donnell, “Improved Detectability with Blocked Element Compensation,” *Ultrasonic Imaging*, vol. 16, pp. 1-18, 1994.

[39] M. A. Averkiou, “Tissue Harmonic Imaging,” *Proc. of the 2000 IEEE International Ultrasonics Symposium*, vol. 2, pp. 1563-1572, 2000.

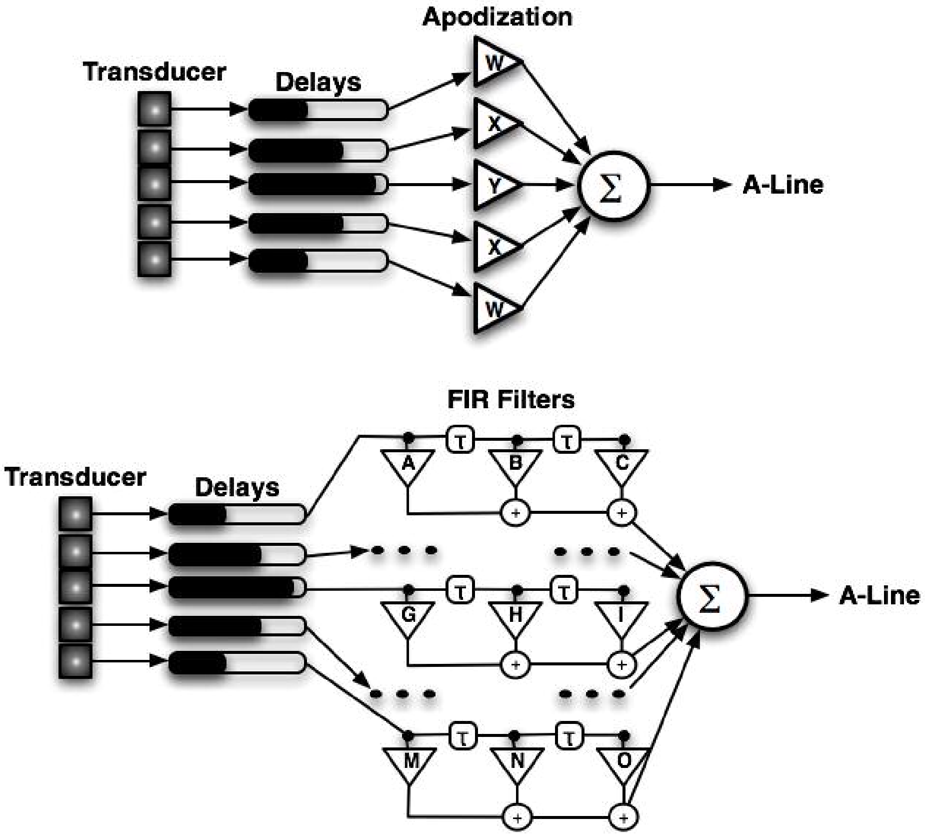
Apodization
Transducer
Delays
W
X
Y
X
W
Σ
A-Line
FIR Filters
Transducer
Delays
τ
τ
A
B
C
+
+
τ
τ
G
H
I
+
+
τ
τ
M
N
O
+
+
Σ
A-Line

Fig. 1. Receive beamformer architectures: (top) Conventional delay-and-sum beamformer (bottom) proposed FIR beamformer. The architecture depicted on the bottom shows the proposed beamformer with 3-tap FIR filters. Note that apodization is applied after dynamic receive focusing in both architectures.

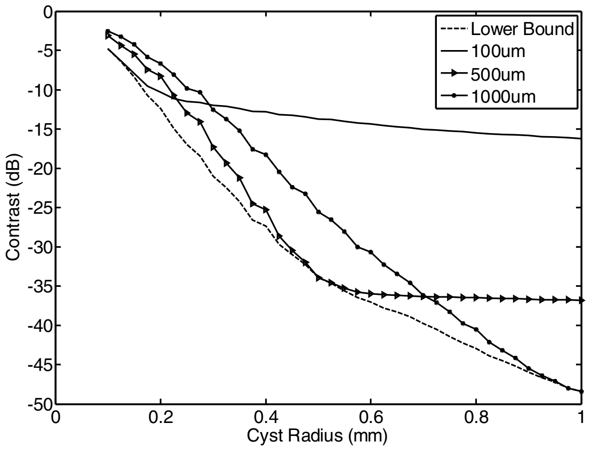

Fig. 2. Cystic contrast curves for the 5-tap FIR beamformer investigating different design cyst radii. The lower bound curve (--) is generated by computing the cystic contrast for the optimal QCLS 5-tap filter at each design cyst radius. The 100 µm design radius curve (solid line) achieves the best contrast for cysts smaller than 250µm but suffers at larger cyst sizes. The 1000 µm design radius curve (-•-) performs well over a larger range than the 100 µm curve, but has the worst contrast at cysts smaller than 300 µm. The 500 µm design radius curve offers a good tradeoff between these two operating extremes. For the most part, these trends are similar for FIR filter tap length.

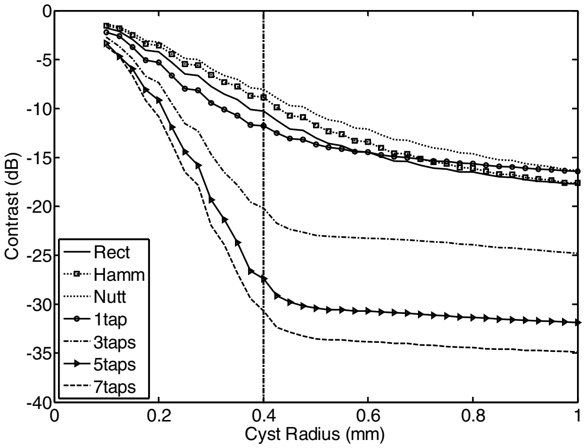

Fig. 3. Cystic contrast curves for the DAS beamformer with different conventional apodization functions and the 1-tap, 3-tap, 5-tap, and 7-tap FIR beamformer with 400 μm design cyst (dashed vertical line) apodization profiles. Data is calculated from the PSFs focused at 2.0 cm on transmit (f/2) and 2.0 cm on receive (f/2). It is interesting to note that for this particular system configuration both the Hamming and Nuttall windows degrade cystic contrast compared to the rectangular window. The reduction in sidelobe energy achieved through apodization does not outweigh the increase in mainlobe size. The 7-tap FIR beamformer improves cystic contrast by almost 20 dB.

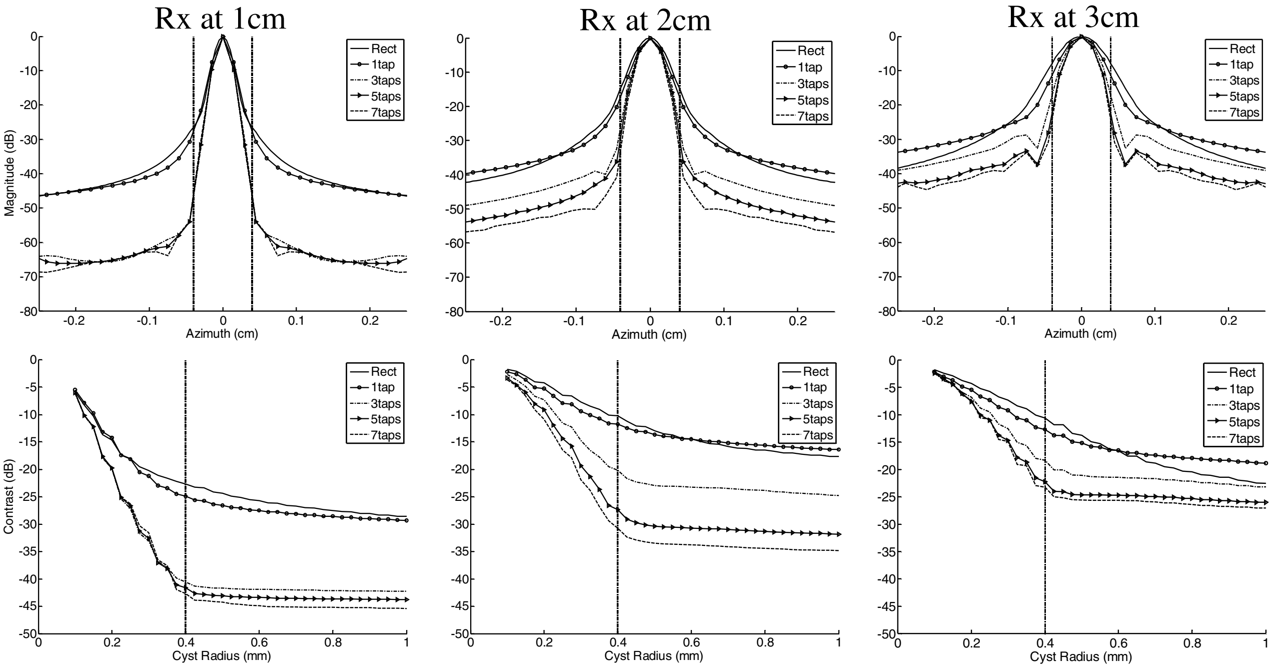

Fig. 4. Integrated lateral beamplots and cystic contrast curves comparing different apodization functions at different dynamic receive focal depths (Tx focus at 2.0 cm). FIR-QCLS weights were calculated for 1-tap, 3-tap, 5-tap, and 7-tap FIR filters with a design cyst radius of 0.4 mm (indicated as a dashed line in all plots). Notice the large reduction in sidelobe and grating lobe levels for the higher tap filters. The bottom row shows cystic contrast curves as a function of cyst radius for the simulated 2D PSFs. Cystic contrast is improved by more than 20 dB for the higher tap FIR filters at dynamic receive focal depths of 1.0 and 2.0 cm. In general longer tap filters increasingly improve contrast resolution, but the gain in contrast between two subsequent tap lengths (i.e. 1 vs. 3-taps and 3 vs. 5-taps) continually decreases.

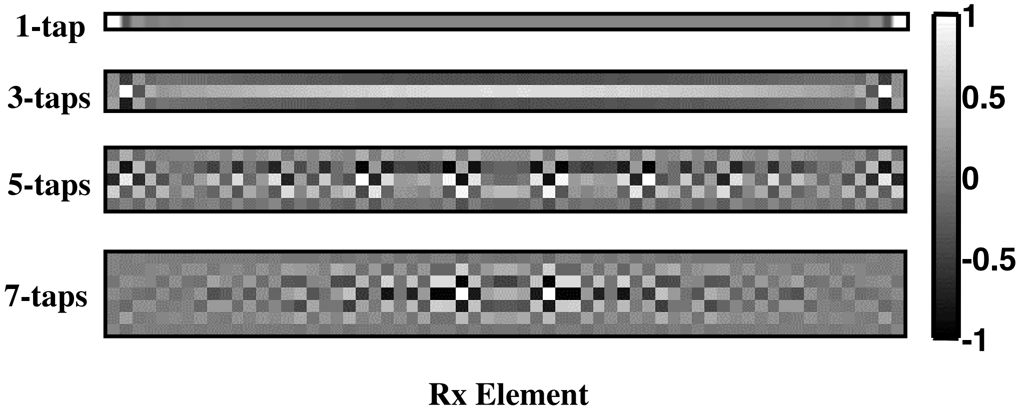

Fig. 5. FIR-QCLS weights for the multi-tap FIR filters. These weights correspond to the PSF dynamically focused at 2.0 cm in figure 4. The 1-tap and 3-tap weights are smooth curves across the receive aperture with some discontinuities at the edges. The 5-tap and 7-tap filters are more variant and discontinuous across the aperture. Notice that some weights take on negative amplitudes and the filters are not linear phase.

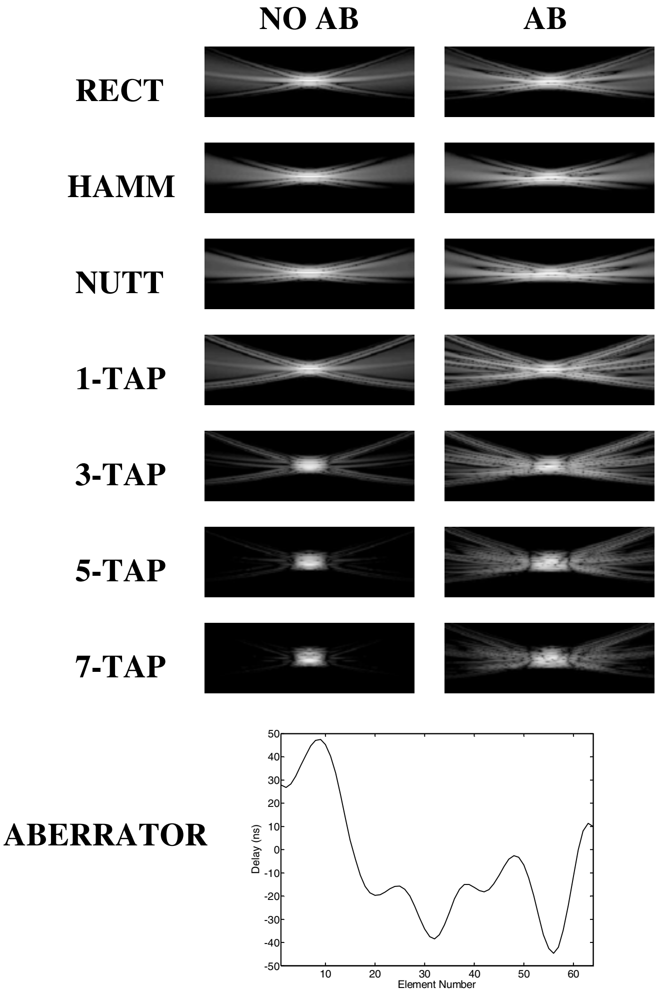

Fig. 6. Unaberrated (left) and aberrated (right) simulation PSFs for different apodization functions. All images are a 6 mm (lateral) by 2 mm (axial) area of the PSF. The absolute value of each PSF was calculated and then log compressed to 60 dB for visualization. The aberration profile (3.6 mm FWHM, 28.8 ns RMS) associated with this particular realization is also shown. The aberration distorts the mainlobe and raises sidelobe levels in all PSFs. Note that the FIR beamformer PSFs maintain relatively narrow mainlobes. The sidelobe energy in the aberrated FIR beamformer PSFs continually decreases as tap length increases.

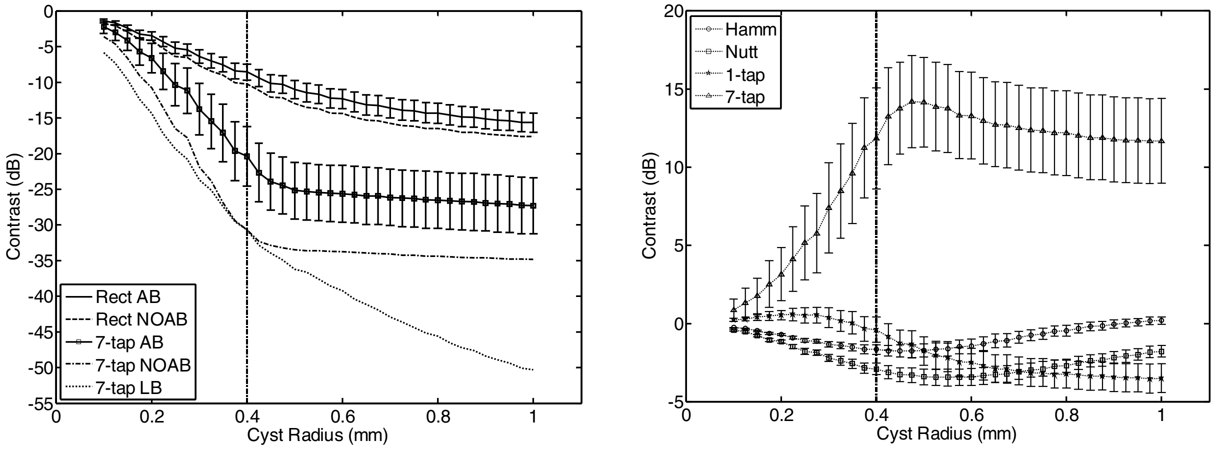

Fig. 7. Cystic contrast plots calculated using 100 realizations of a 28 ns RMS, 3.6 mm FWHM one dimensional aberrator. The plot on the left shows the contrast plots for the unaberrated and aberrated rectangular and 7-tap PSFs with a receive focus at 2.0 cm. The errorbars are +/- 1 standard deviation for the aberrated contrast plots. Also shown is the lower bound on cystic contrast for the 7-tap PSF. Note that aberration degrades the contrast performance for both the rectangular and 7-tap PSF as expected. However, even the aberrated 7-tap PSF outperforms the unaberrated rectangular PSF by almost 10 dB. The Hamming and the Nuttall windows performed worse than the rectangular window for this particular system configuration. The plot on the right shows the contrast performance for the Hamming, Nuttall, 1-tap, and 7-tap PSFs in the presence of aberration normalized to the rectangular window's contrast (0 dB for all cyst radii). A more positive contrast value indicates better cystic contrast than the rectangular window, and errorbars are +/- 1 standard deviation. Note that the Nuttall window never performs better than the rectangular window, and the Hamming window only performs better for cysts larger than 0.9 mm in radius. The 1-tap PSF outperforms the rectangular window for smaller cyst sizes. The 7-tap PSF improves cystic contrast by more than 10 dB over a range of cyst sizes. The dashed vertical lines in both plots indicate the design cyst radius.

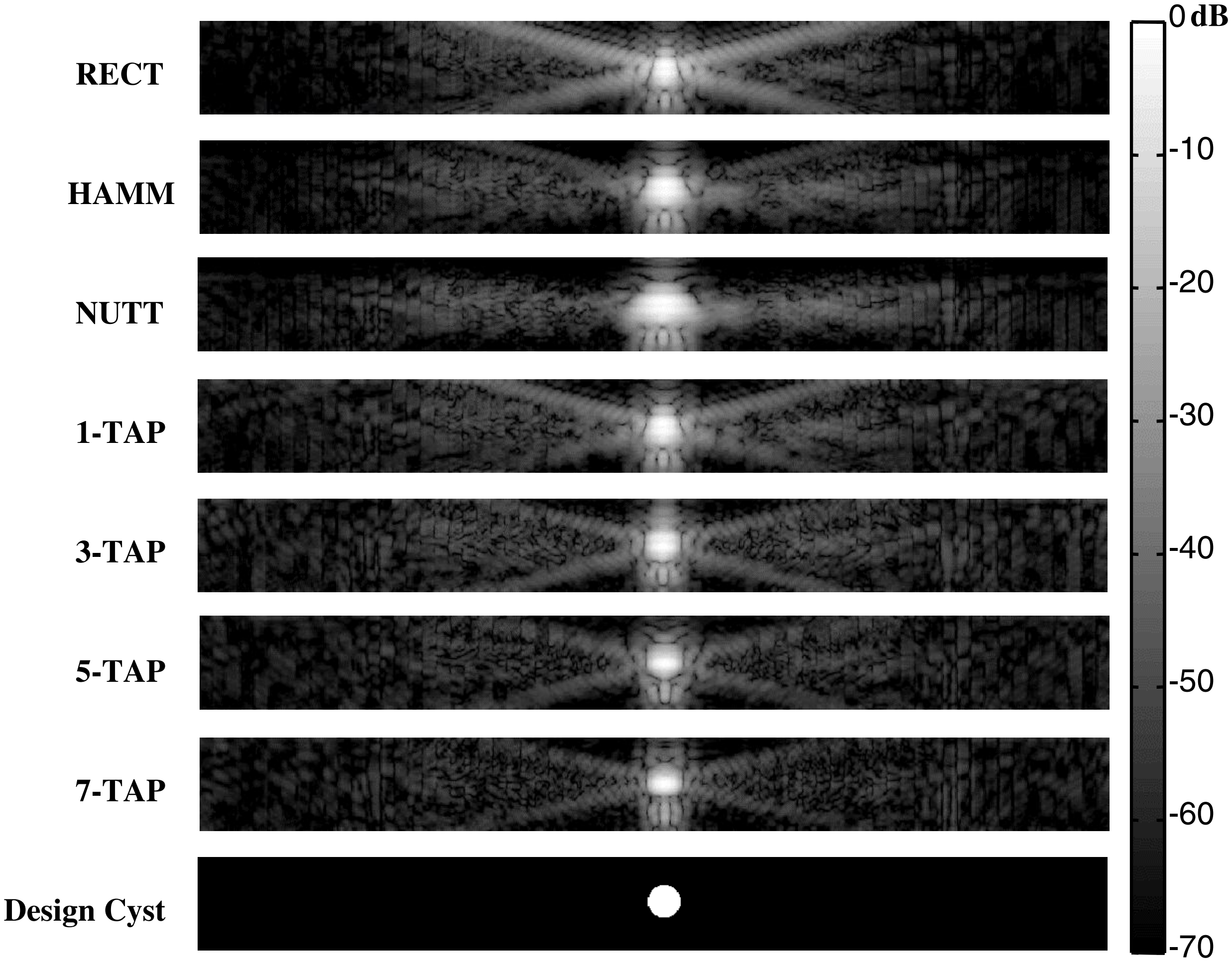
RECT
HAMM
NUTT
1-TAP
3-TAP
5-TAP
7-TAP
Design Cyst
0 dB
-10
-20
-30
-40
-50
-60
-70

Fig. 8. Experimental 2D PSFs with different receive apodization functions applied. Each image is 0.2 cm axially by 1.95 cm laterally. All images were envelope detected and log compressed to 70 dB. The conventional windows' PSFs suffer from large sidelobes and wide mainlobes. The multi-tap FIR-QCLS apodization functions progressively reduce the total sidelobe energy while maintaining a tight mainlobe in the spatial PSFs. The design cyst is shown for reference.

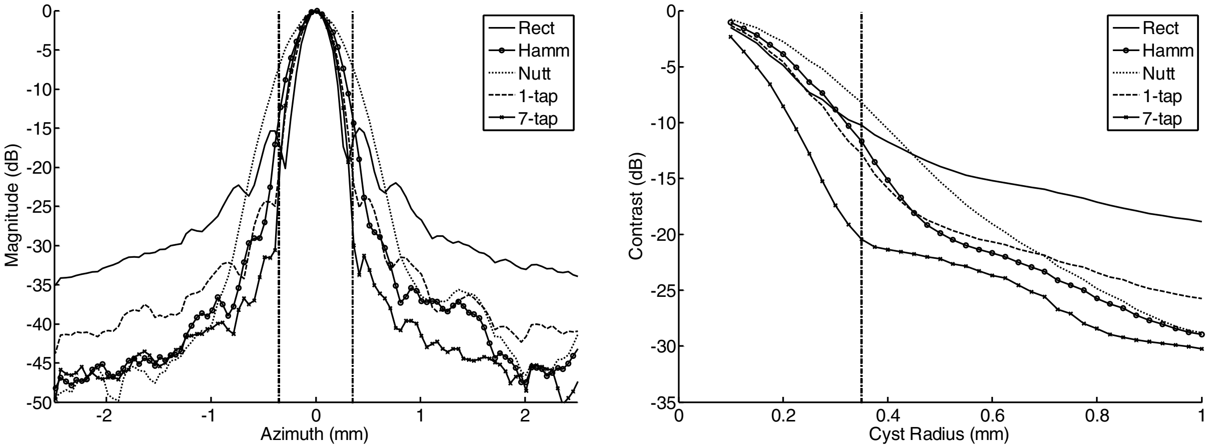

Fig. 9. Experimental integrated lateral beamplots (left) and contrast curves (right) with different receive apodization functions applied. The vertical dashed lines indicate the design cyst radius for the FIR-QCLS filters of 0.35 mm. The Hamming and Nuttall window achieve lower sidelobe levels than the rectangular apodization function but have a larger mainlobe. The 1-tap QCLS apodization function achieves a tight mainlobe, but has significant energy in the sidelobe region. The 7-tap QCLS apodization function achieves a tight mainlobe and dramatically reduces the amount of energy in the sidelobes. The Hamming, Nuttall and 1-tap QCLS functions achieve worse contrast than the rectangular function for small cyst sizes due to their mainlobe widths. The 1-tap QCLS apodization function is outperformed by the Hamming and Nuttall windows at cyst sizes greater than 0.4 mm. The 7-tap FIR-QCLS apodization function improves cystic resolution by more than 7 dB for a range of cyst sizes and achieves the best contrast at every cyst size investigated.

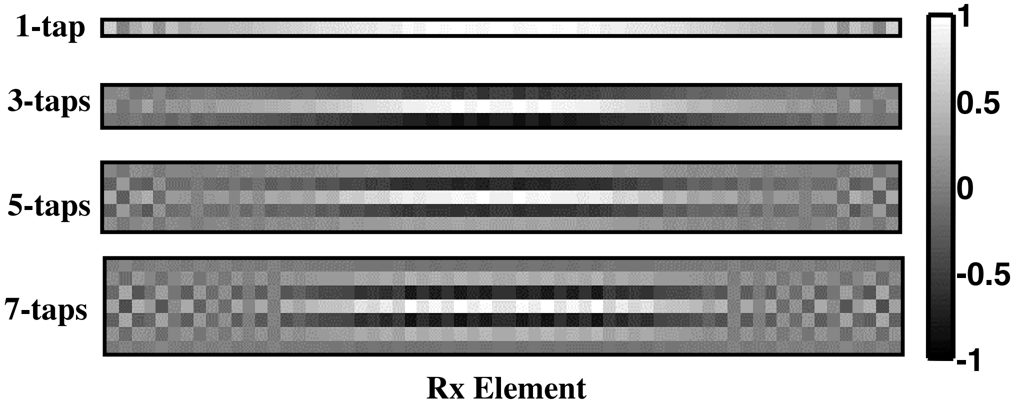

Fig. 10. Experimental FIR-QCLS weights. These weights correspond to the PSFs dynamically focused at 2.0 cm in figure 8. The weights show similar characteristics to the simulations: smooth curves across the aperture, discontinuities at the edges of the aperture, and inversion in time.

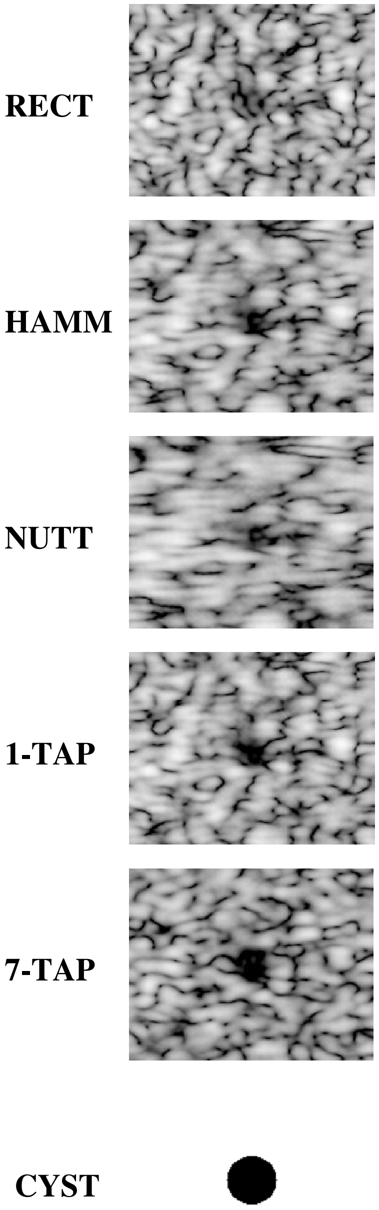

Fig. 11. Simulated B-mode images of a 1.0 mm diameter cyst embedded in speckle using the experimental PSFs. All images are log compressed to 30 dB and show a 5 mm by 5 mm area surrounding the anechoic cyst. The cyst made using the rectangular window is corrupted by clutter from the large sidelobes and the cyst made using the Nuttall window is blurred from the large mainlobe. The 1-tap and Hamming windows produce similar images with the 1-tap PSF reducing clutter inside the cyst. The 7-tap PSF image clearly outperforms the conventional windows: reducing clutter, sharpening the cyst boundary, and improving detectability. The 1.0 mm diameter cyst is shown for reference.

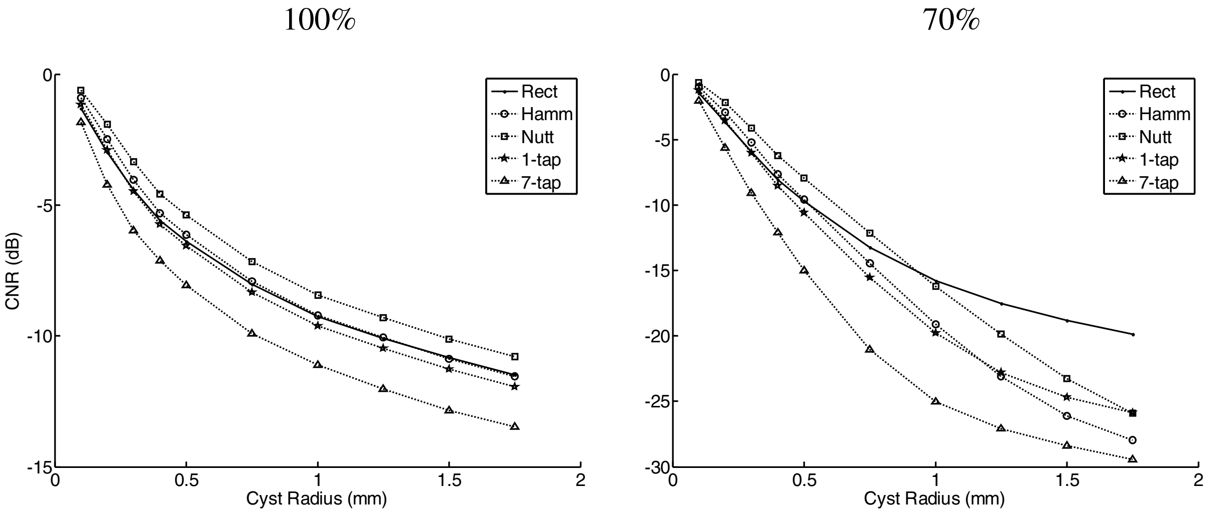

Fig. 12. Cystic CNR computed from the 1000 simulated B-mode images. CNR is computed using equation (10), and a more negative value indicates better performance. Contrast was computed using 100% (left) of the true cyst size and 70% (right) of the true cyst size. A smaller cyst size was used in order to reduce edge effects. CNR increases for increasing cyst radius from 0.1 mm to 1.75 mm. The 7-tap QCLS window achieves 2-2.5 dB contrast improvement according to the 100% plot and 4-10 dB improvement according to the 70% plot. These results reinforce the increased cyst detectability of the B-mode images in figure 7. It is interesting to note that rectangular PSF resulted in better detectability than the Hamming PSF for the smaller cyst sizes even though the B-mode images in figure 11 would suggest otherwise.

Time-Domain Optimized Near-Field Estimator for Ultrasound Imaging: Initial Development and Results

Francesco Viola, *Member IEEE*, Michael A. Ellis, and William F. Walker, *Member, IEEE*

Abstract— **For nearly four decades, adaptive beamforming (ABF) algorithms have been applied in RADAR and SONAR signal processing. These algorithms reduce the contribution of undesired off-axis signals while maintaining a desired response along a specific look direction. Typically, higher resolution and contrast is attainable using adaptive beamforming at the price of an increased computational load. In this paper we describe a novel ABF designed for medical ultrasound, named the Time-domain Optimized Near-field Estimator, or TONE. We performed a series of simulations using synthetic ultrasound data to test the performance of this algorithm and compared it to conventional, data independent, delay and sum beamforming (CBF) method. We also performed experiments using a Philips SONOS 5500 phased array imaging system. CBF was applied using the default parameters of the Philips scanner, whereas TONE was applied on per channel, unfocused data using an unfocused transmit beam. TONE images were reconstructed at a sampling of 67μm laterally and 19μm axially. The results obtained for a series of five 20μm wires in a water tank show a significant improvement in spatial resolution when compared to CBF. We also analyzed the performance of TONE as a function of speed of sound errors and array sparsity, finding it robust to both.**

***Index Terms*—Ultrasound Imaging, Beamforming, Image Reconstruction.**

I. INTRODUCTION

SENSOR arrays are used in many application fields including RADAR, SONAR, geophysics, and medical imaging. For these applications, the received data is often processed using conventional “delay-and-sum” beamforming. In this method, the output is formed by summing weighted and delayed versions of the received signals. The delays used for each sensor element are determined by the array geometry and the desired look direction. While this approach is straightforward and easy to implement, off-axis scatterers can introduce clutter, reducing the overall quality of the beamformer output. This is shown schematically and experimentally in figure 1. In panel A, an array of sensors is focused along the dotted line and a single point target is placed in the look direction, or on-axis, at a fixed distance from the array. The target reflects energy toward the array, generating a signal on each of the individual sensors. Focal delays are applied to each signal to generate the sensor/range data set shown in the right of the figure. Summation across sensors to form an image line will amplify the signal coming from the look direction. However, when a secondary target is placed off-axis, as shown in panel B, it may lie within the array’s transmit beam and therefore contribute to the received echo. This is apparent in the tilted waveforms visible in the sensor/range data set. Although summation across sensors amplifies the signal coming from directly in front of the array, it does not entirely eliminate the contribution of the off-axis target. Finally, panel C of figure 1 depicts medical ultrasound data obtained from the thyroid of a human subject (data courtesy of Gregg E. Trahey, Duke University). At least three clear waveforms (possibly due to micro-calcifications in the thyroid) are visible in this sensors/range data set. These non-focal targets would appear in this image line as clutter, ultimately reducing image contrast and resolution.

The problem of nulling the contribution of off-axis scatterers was first investigated for RADAR and SONAR systems by extending the pioneering work of Norbert Wiener. The application of Wiener filter theory to array signal processing led to the initial development of adaptive beamforming [1-3]. In ABF, the information encapsulated in the data received by an array of sensors is used to determine a set of weights that optimize the beamformer output.

For nearly four decades, a variety of adaptive beamforming algorithms have been developed, each exploiting specific properties of the received data. These algorithms are able to achieve resolution far superior to that predicted by diffraction theory, while simultaneously attaining excellent side lobe reduction. The most common approaches calculate a series of weights by minimizing the energy in the beamsum signal, subject to the constraint that the beamformer must exhibit a given response in the look-direction [4, 5]. Attenuation of off-axis targets is obtained by applying those weights to the received data. Typically, the second order statistics (i.e., the covariance matrix) of the data are used to determine the weights. These algorithms were initially applied in passive SONAR, where the use of receive only systems allowed

Manuscript received January 11, 2007. This work was supported in part by the US Army Congressionally Directed Medical Research Program in Breast Cancer grant No.W81XWH-04-1-0590.

F. Viola, M. A. Ellis, and W. F. Walker are with the Department of Biomedical Engineering, University of Virginia, Charlottesville, VA 22908 USA (Corresponding author e-mail: fv7d@ Virginia.edu).

acquisition of numerous unique statistical looks at the environment. This is not generally the case for a transmit/receive system, such as medical ultrasound.

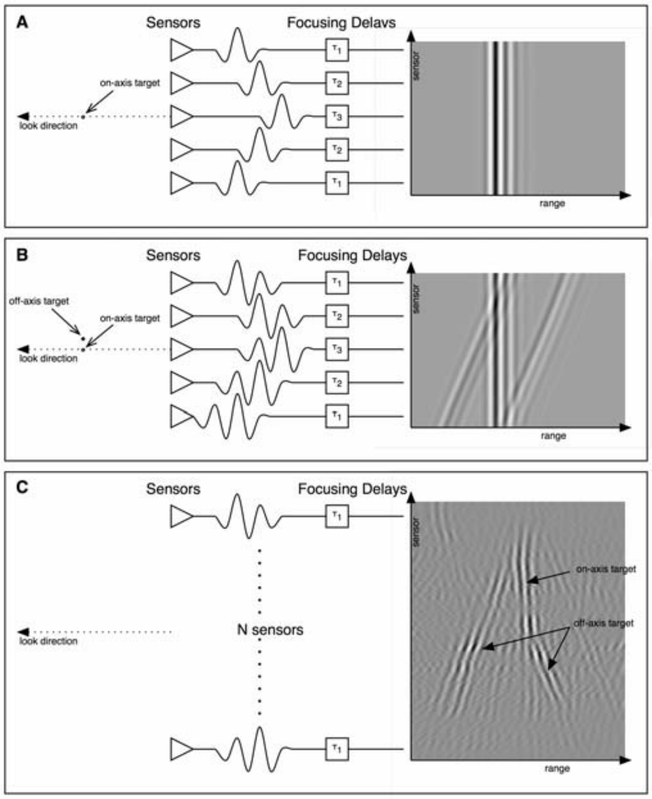

Fig. 1. Panel A: an array of sensors is focused along the look direction (dotted line) where a single point target is placed at a fixed distance from the array. The received data after focusing is depicted on the right side. Panel B: when a secondary target is placed off-axis it will corrupt the received data by introducing the tilted waveforms observed on the right hand side of this figure. Panel C: *in vivo* single channel thyroid data. The data sets clearly show the presence of bright off-axis scatterers, as evidenced by the tilted wave fronts. Data in Panel C courtesy of Gregg E. Trahey, Duke University.

Alternative ABF algorithms were simultaneously developed to utilize different properties of the received signals. Common approaches include the reduced rank beamformers [6-8]. The basic concept underlying these methods is to save computation time by calculating a reduced rank covariance matrix that only includes the strongest scatterers. Oblique projections have also been proposed to beamform the data in a subspace which is orthogonal to the space spanned by the scatterers [9, 11].

It is often the case that limited data are available, making computation of a reliable covariance matrix difficult. This could be due, for example, to non-stationary environments, fast moving targets, or transmit/receive operation. In these cases, several groups have proposed the use of a diagonal loading term to obtain a stable covariance matrix which allows solution for the optimal weights [12-15]. Diagonal loading is a common technique in array signal processing to stabilize a matrix which is ill-conditioned for inversion. Another series of adaptive algorithms has been developed which does not rely on statistical properties of the data and thus can be used on a single realization (or snapshot). These approaches are particularly well suited to pulse-echo imaging. These algorithms include techniques based on generalized eigenvalue problems [16, 17], Bayesian approaches [18-20], maximum likelihood estimators [21, 22], data-adaptive regularization [23], and minimum worst-case gain methods [24].

In medical ultrasound, bright off-axis targets can seriously degrade image quality by introducing broad image clutter, which reduces image contrast and resolution. This is confirmed in the thyroid data of figure 1C. Further, it is well known that the acoustic reflectivity of targets within the body covers many orders of magnitude [25]. The successful application of adaptive beamforming to medical ultrasound would reduce the effects of bright off-axis targets, thus improving the overall image quality. However, the unique characteristics of ultrasound data make blind application of existing adaptive beamforming algorithms unlikely to be successful. Unlike passive SONAR, for example, limited statistics are available in medical ultrasound to form a robust covariance matrix. Furthermore, on-axis and off-axis signals are strongly correlated, requiring the use of special algorithms such as the Duvall beamformer [26] or pre-processing techniques such as spatial smoothing to decorrelate signals before filtering is applied [27-31]. Lastly, ultrasound imaging is generally performed using broad-band signals in the near-field, while many adaptive beamforming techniques are specifically designed for narrow-band signals in the far-field.

In the past, several groups have applied adaptive algorithms to medical ultrasound beamforming. Mann and Walker [32, 33] showed increased resolution and contrast using a modified version of the Frost beamformer [5]. Other groups [35, 40] have applied the Capon beamformer [4] coupled with spatial smoothing to decorrelate on-axis and off-axis signals. Wang et al. [34] used synthetic transmit focusing to generate a robust covariance matrix. Although Wang's initial results are positive, the use of synthetic transmit significantly limits the application of these algorithms in real clinical environments because of potential motion artifacts and limitations of existing hardware.

In this paper we present an algorithm that is well suited for beamforming in medical ultrasound imaging. We briefly describe the algorithm, present initial results from simulations and experiments, and offer discussion and conclusions.

Note for the reader: matrices are represented using underlined upper-case italic characters such as $\underline{X}$, while vectors are represented using underlined lower-case italics such as $\underline{x}$. Superscripts H and T represent conjugate transpose and regular transpose operations, respectively.

II. TIME-DOMAIN OPTIMIZED NEAR-FIELD ESTIMATOR (TONE)

The algorithm presented here is developed from the Spatial Processing: Optimized and Constrained (SPOC) technique originally developed by Van Trees *et al.* for applications in passive SONAR [18]. We term it Time-domain, Optimized, Near-field Estimator, or TONE. TONE is particularly useful since it does not require knowledge of second order statistics and is therefore applicable with only a single realization of data. Furthermore, it does not require any pre-processing technique to be applied. This algorithm is briefly described as follows.

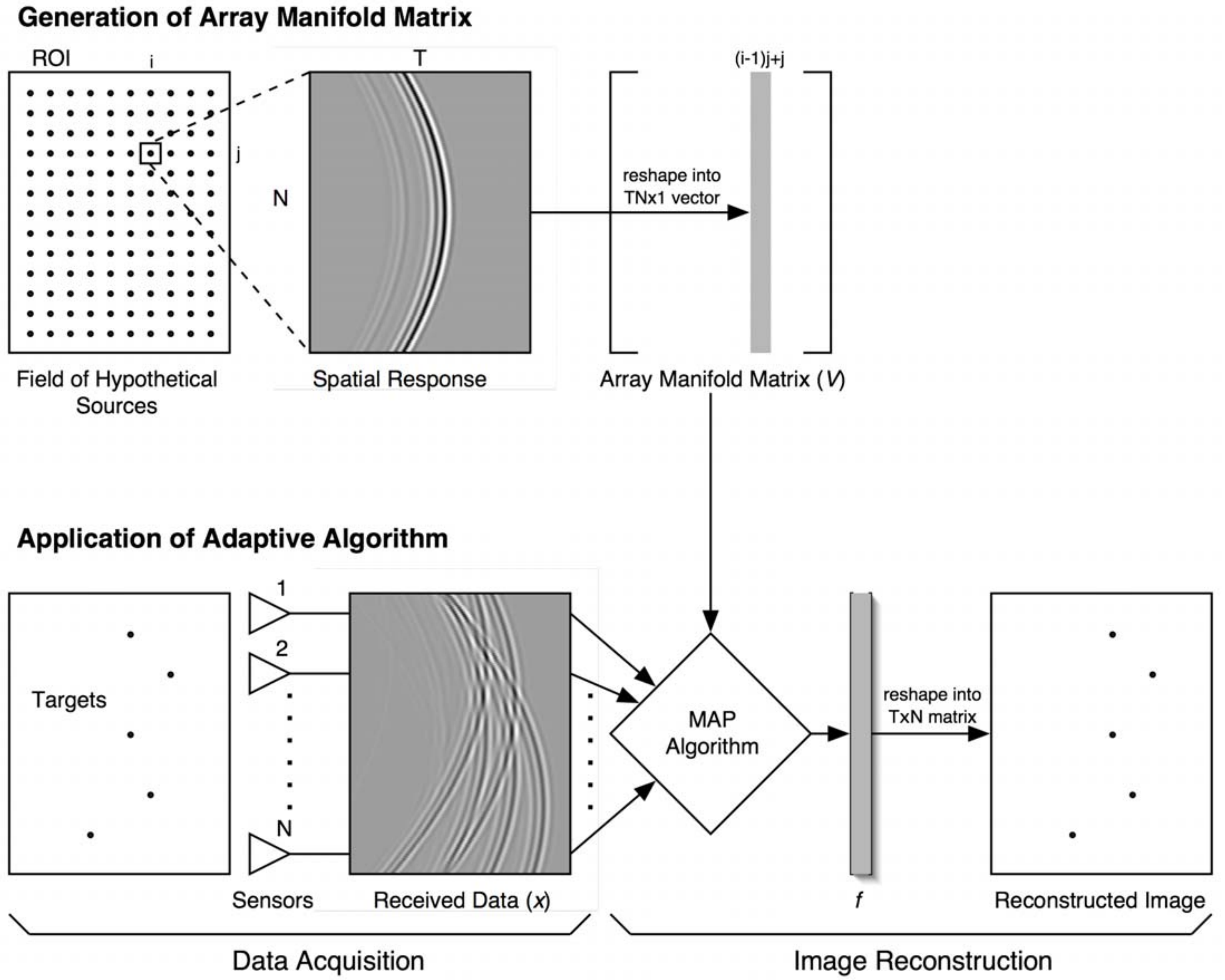
Generation of Array Manifold Matrix
ROI
i
j
T
N
(i-1)j+j
reshape into TNx1 vector
Field of Hypothetical Sources
Spatial Response
Array Manifold Matrix (V)
Application of Adaptive Algorithm
Targets
1
2
N
Sensors
Received Data (x)
MAP Algorithm
reshape into TxN matrix
f
Reconstructed Image
Data Acquisition
Image Reconstruction

Fig. 2. Schematic representation of TONE beamforming. A signal model is first generated of the field produced by a series of hypothetical targets. The sensors' output is matched to the signal model to solve for the position and intensity of the real targets. Statistics are not required and both near-field/far-field and broad/narrow band cases can be considered.

The TONE algorithm is built upon the following linear model of image formation. Similar linear model formulations have been used in medical ultrasound [41-43]. The imaging region, referred to as the region of interest (ROI), is first subdivided into a collection of hypothetical targets at arbitrary positions, as shown schematically in figure 2. Finer grid sampling yields finer final image resolution but entails higher computational costs. For each hypothetical targets in the ROI, we determine (through experiment, simulations, or theory) the signal received by the array from a target at that specific point. We refer to this two-way response as the spatial response for a particular target. For every hypothetical target, the spatial response is a matrix of dimensions TxN, where T is the number of samples in the axial, or temporal, dimension and N is the number of sensor elements in the array. Note that this formulation accommodates any array geometry. After the spatial responses for all the hypothetical targets have been determined, these responses are reshaped to form an array manifold matrix $\underline{V}$ of dimensions NTxLP, where L and P are the numbers of hypothetical targets in the range and lateral dimensions, respectively. The observation model becomes:

$$\underline{x} = \underline{V}\,\underline{f} \qquad (1)$$

where $\underline{x} = [\underline{x}_1 \;\; \underline{x}_2 \cdots\cdots \underline{x}_N]^T$ is the data received by the N-element array and $\underline{f}$ is the LPx1 target vector, whose elements are the amplitudes of the hypothetical target located in the ROI. $\underline{x}$ is an NTx1 vector that is obtained by concatenating the Tx1 channel data $\underline{x}_i$. Given $\underline{x}$ and $\underline{V}$, TONE operates on the received data $\underline{x}$ and the array manifold matrix $\underline{V}$ to solve for the position and intensity of the real targets (i.e., the $\underline{f}$ vector). In this paper we solve this under determined problem using a maximum a posteriori estimate of the target vector, as explained below. We initially consider the joint probability density function (PDF) $p(\underline{x},\underline{f})$. The maximum likelihood estimate of $\underline{f}$ is given by [39]:

$$\hat{\underline{f}} = \max_{\underline{f}} \; p(\underline{x},\underline{f}) \tag{2}$$

Note that the estimate of $\underline{f}$ is obtained by constraining the problem such that the observation model in equation (1) is satisfied. That is to say, $\underline{x} = \underline{V}\hat{\underline{f}}$. The joint PDF in (2) can be rewritten using the conditional PDF $p(\underline{x}/\underline{f})$ and the marginal density $p(\underline{f})$ as follows:

$$\hat{\underline{f}} = \max_{\underline{f}} \; p(\underline{x},\underline{f}) = \max_{\underline{f}} \; p(\underline{x}/\underline{f})p(\underline{f}) \tag{3}$$

which is referred to as the maximum a posteriori (MAP) estimate of $\underline{f}$. Note that the conditional PDF $p(\underline{x}/\underline{f})$ is equally likely for every $\underline{f}$ that satisfies the observation model described in equation (1). Thus equation (3) reduces to the following:

$$\hat{\underline{f}} = \max_{\underline{f}} \; p(\underline{f}) \tag{4}$$

Furthermore, we assume that the marginal PDF $p(\underline{f})$ is known a priori and mathematically expressed as a zero-mean Gaussian distribution. That is to say that the targets follow a Guassian amplitude distribution. The constraint imposed by the observation model (1) on equation (4) assures that the trivial solution $\hat{\underline{f}} = 0$ (which is the maximum likelihood solution for a zero-mean Gaussian pdf) is not obtained for non zero target distribution. Thus, the MAP problem becomes:

$$\begin{aligned} &Cost \quad function: \;\; \min_{\underline{f}} \sum_{l=1}^{LP} \ln|f_l|^2 \\ &subject \quad to: \;\; \underline{x} = \underline{V}\,\underline{f} \end{aligned} \tag{5}$$

where f_l are elements of $\underline{f}$. A solution for the MAP optimization problem is found using the following iterative procedure [18, 36]:

1. Perform an eigen-decomposition of the matrix $\underline{V}^H\underline{V} = \underline{P}\underline{\Lambda}\underline{P}^H$, where $\underline{P}$ contains the eigenvectors and $\underline{\Lambda} = diag(\lambda_1,\ \lambda_2,\ \cdots,\ \lambda_{LP})$ contains the eigenvalues in descending order. Note that the maximum rank of $\underline{V}^H\underline{V}$ is NT, therefore there will be at least LP-NT zero eigenvalues.
2. Divide the eigenvalues into two groups: non zero $(\lambda_1,\ \lambda_2,\ \cdots,\ \lambda_{fix})$, and zero $(\lambda_{fix+1},\ \lambda_{fix+2},\ \cdots,\ \lambda_{LP})$.
3. Decompose the eigenvector matrix $\underline{P}$ into $\underline{P}_{free}$ and $\underline{P}_{fix}$, corresponding to the non zero and zero eigenvalues, respectively.
4. Compute $\underline{x}'_{fix} = (\underline{V}\underline{P}_{fix})^H \underline{x}$.
5. Compute $\underline{f}'_{fix} = \underline{\Lambda}^{-1}_{fix}\underline{x}'_{fix}$, where $\underline{\Lambda}^{-1}_{fix} = diag(\lambda_1^{-1},\ \lambda_2^{-1},\ \cdots,\ \lambda_{fix}^{-1})$.
6. Initialize $\underline{f}'_{free}$ to zero.
7. Compute $\underline{f} = \underline{P}_{fix}\underline{f}'_{fix} + \underline{P}_{free}\underline{f}'_{free}$.
8. Compute the diagonal matrix $\underline{T} = diag(|f_1|^2,\ |f_2|^2,\ \cdots,\ |f_{LP}|^2)$.
9. Compute $\underline{f}'_{free} = (\underline{P}^H_{free}\underline{T}\underline{P}_{fix})(\underline{P}^H_{fix}\underline{T}\underline{P}_{fix})^{-1}\underline{f}'_{fix}$.
10. Repeat steps 7-9 until $\underline{f}'_{free}$ has converged.
11. The target amplitudes are given by step 7.

The original SPOC algorithm of Van Trees was developed for applications in passive SONAR, assuming narrow-band signals received from the far-field. In this application, the received data $\underline{x}$ is simply an N element vector of the complex demodulated signals received on each channel. Since passive SONAR assumes narrow-band signals, this received data consists of only a single complex sample on each channel. The signal from a single far-field target received by a uniformly spaced linear array takes on the form of a discretely sampled complex exponential. The array manifold matrix for this application thus consists of a set of Q columns, each of which is an N sample complex exponential of a different frequency (Q is the number of hypothetical targets placed in the far-field). In medical ultrasound, the received signals are near-field and broad-band, and this requires a significantly different signal model. Hypothetical targets are now distributed over the range (P) and lateral (L) dimensions of the ROI. Furthermore, time records of length T are necessary to fully capture the broad-band nature of the signals. Given an N element linear array, the array manifold matrix is thus of dimensions NTxLP, as described above.

It is also possible to formulate a signal model in the frequency domain. In this case, the algorithm is applied to every frequency bin and the array manifold matrix is constructed using complex exponential signals with different phases. Although both the frequency and time domain approaches are possible, in this paper we use the time domain approach because it more fully captures the intrinsic complexity of the data.

Extension to 3D data sets simply requires distribution of hypothetical targets over a volume and three dimensional spatial responses to form the array manifold matrix. The mathematical formulation is the same of that used in equation (1) except that the dimensions of $\underline{V}$ are now NTZ by LPQ, where Z and Q are the number of samples and the number of hypothetical targets in the third dimension, respectively (the dimensions of $\underline{f}$ and $\underline{x}$ also change accordingly).

I. SIMULATION METHODS

Computer simulations were performed to compare the performance of TONE to conventional delay-and-sum beamforming. All calculations were performed in MATLAB (MathWorks Inc., Natick, MA), and utilized synthetic ultrasound signals.

A. Resolution

For this set of simulations, we modeled a 32 element linear array operating at 5 MHz with roughly 70% fractional bandwidth (BW) and 150μm element pitch. The array response was modeled using DELFI, an ultrasound system simulation tool recently developed in our lab [44]. The radio frequency (RF) data were sampled temporally at 40MHz. We simulated two ideal point targets in front of the array at a depth of 20mm and reconstructed the image in a region 1mm axially by 2mm laterally. The points were separated by a distance of 50μm, 60μm, 90μm, 150μm, 300μm, and 1500μm to demonstrate the lateral resolution limits of TONE. Hypothetical targets were placed axially every 20μm and laterally every 40μm. Transmission was simulated by firing on all 32 elements simultaneously. This simulates a plane wave transmit and allows for a more computationally efficient and compact description of the ROI. For, all the simulations presented in this paper, the array manifold matrix $\underline{V}$ was obtained by simulating with DELFI the responses at the locations of each hypothetical target. Doing so allowed for the consideration of both angular sensitivity and attenuation. The same target distributions were also processed using the conventional delay and sum beamforming; in this case we used a fixed focused transmit and dynamic focusing on receive.

B. Point Targets

A series of point targets were distributed within a 4x5mm region in range and azimuth, respectively. Elevation slice thickness was not considered in this set of simulations. In this case, we simulated a 32 element linear array operating at 5MHz with 150μm element pitch. Also in this case, the sampling frequency was set at 40MHz. In the case of TONE, a plane wave was simulated by transmitting on all 32 elements. Conventional beamforming was applied using fixed focus transmit and dynamic receive focusing. For TONE, we discretized the image region into a series of hypothetical targets separated 20μm in range and 120μm in azimuth. The positions of the points were chosen so that none coincided with the positions of the hypothetical targets.

C. Anechoic Cyst

A 1mm radius anechoic cyst was simulated in front of the array and surrounded by ultrasonic scatterers randomly distributed within the image region. Roughly 4,000 scatterers were placed within the ROI, providing more than the typical 15 scatterers per resolution cell needed to generate fully developed speckle [38]. Scatterers' amplitudes followed a Gaussian distribution with zero mean and standard deviation of one. Simulation methods are the same as those described in the previous section, except that the hypothetical target sampling was reduced to 100μm in azimuth. The positions of the scatterers do not necessarily coincide with the position of the hypothetical targets. Furthermore, as for the simulated wires, elevation effects were not considered.

D. Algorithm Robustness

The simulations previously described were performed under ideal, noiseless conditions. Additional simulations were performed to test the robustness of TONE to various level of noise. We used the same simulation parameters as for the resolutioF simulation with 90μm separation, except that Gaussian noise was added to each receive channel. In order to mimic RF data after the bandpass filtering step, the noise was bandpass filtered using a 101-tap FIR filter to match the bandwidth of the received RF signals before summation. We analyzed the cases of 30dB, 20dB, and 10dB per channel signal-to-noise ratios (SNR) before filtering.

II. EXPERIMENTAL METHODS

Experiments were performed using a Philips SONOS 5500 imaging system employing a 6MHz linear array. The target consisted of a set of five 20μm diameter stainless steel wires (California Fine Wire Company, Grover Beach, CA) suspended in a water tank at room temperature. The wires were placed at a distance of roughly 2.2cm from the transducer's face. The imaging system was programmed to transmit on all 128 elements simultaneously to simulate a plane wave. The received data was obtained by stepping sequentially through each of the 128 receive channels. Received data was filtered using a 100-tap FIR filter with pass-band between 3 and 11MHz before beamforming. TONE was applied on a 32-processor SGI Altix server with the aid of the Star-P parallel computing platform (Interactive Supercomputing, Inc.). In all the experiments described here, the ROI was sampled with hypothetical targets placed every 19μm axially (which corresponds to the temporal sampling rate of the system) and every 67μm laterally (one half of the element pitch). The array manifold matrix was constructed as follows. The reference waveform was obtained by measuring the response from a single steel wire in water (elevation effects were ignored). For every hypothetical target location within the ROI, the reference waveform was re-interpolated and delayed using the corresponding geometrical delay profile. No attempt was made to incorporate element angular response, attenuation, or spatial variations in the transmit beam in the array manifold matrix.

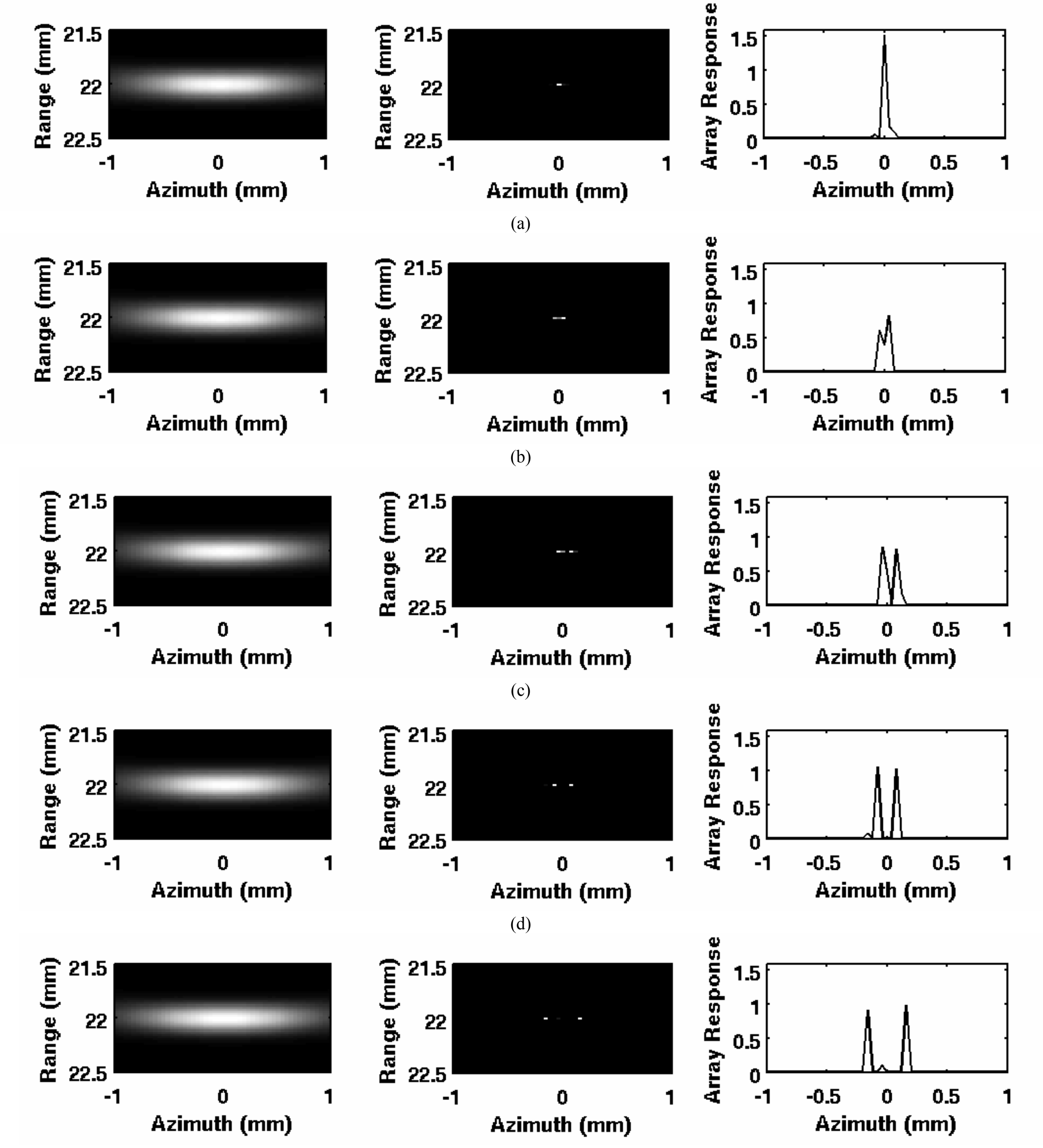

(a)

(b)

(c)

(d)

(e)

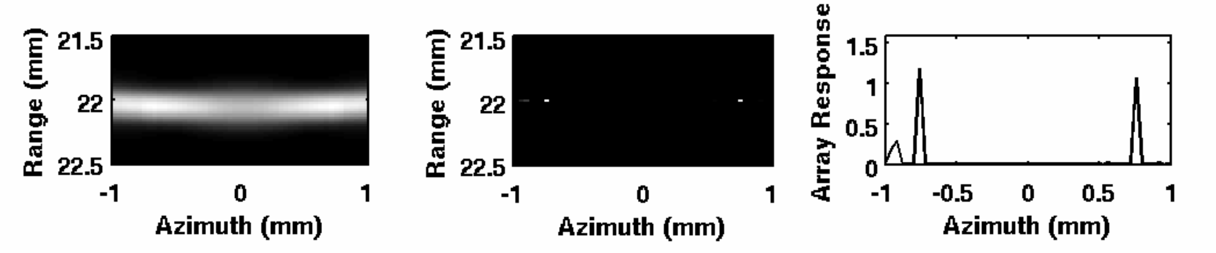

(f)

Fig. 3. Simulated lateral resolution of TONE for a 32 element linear array operating at 5MHz with 70% bandwidth. Hypothetical targets were placed every 20μm axially and every 40μm laterally. The left panels show the output images from a CBF, the central panels show the output image from TONE, and the right panels show axially integrated TONE images. Set (a) shows the case where the point targets are separated by 50 μm; (b), (c), (d), (e), and (f) correspond to point target separations of 60 μm, 90 μm, 150 μm, 300 μm, and 1500 μm respectively. Note that TONE lateral resolution is a function of the hypothetical target sampling.

I. RESULTS

Figure 3 shows the results given by TONE for two ideal point targets with varying amounts of separation. For these simulations, the hypothetical targets are placed every 20μm axially and every 40μm laterally. None of the ideal point targets are aligned with any of the hypothetical targets. Although the two point targets are indistinguishable with only 50μm of separation, they become resolvable with 60μm of separation and are fully resolved with 90μm of separation. This is nearly an order of magnitude improvement in resolution as compared to CBF with a 32 element linear array operating at 5 MHz with 150μm element pitch. It is important to note that the final resolution of TONE is strongly dependent upon the hypothetical target sampling. This suggests that a finer sampling than that used here would yield even finer resolution. Nonetheless, resolution is significantly improved using TONE, as demonstrated in figure 3. Furthermore, the results of these simulations suggest the following. In current ultrasound imaging there exists a trade off between spatial resolution and penetration depth. While higher frequencies produce images with higher spatial resolution, image depth is limited by the frequency dependent tissue attenuation. Since TONE's final resolution is dependent upon hypothetical target sampling, it should be possible to use lower frequencies to increase penetration without sacrificing image resolution.

Point targets simulation results are presented in figure 4. The top panel shows the spatial distribution of the points within the ROI. The points' spacing ranged between 1mm and 200μm in both dimensions. The middle panel of this figure depicts results obtained using conventional beamforming. Hann apodization was used on receive and dynamic receive focusing was applied. While some discrete points are detectable using this beamforming scheme, many are unresolved. The last image of figure 4 shows the TONE beamformed set of points. As figure 4 clearly indicates, TONE produces results with higher contrast and resolution when compared to the conventional technique. Nearly all the targets are clearly detectable, even when they do not lie at hypothetical target locations.

As stated above, simulations were performed using a 32-element aperture and a simulated plane wave on transmit. The use of a plane wave allowed for an easier and more compact description of the array manifold matrix, while the choice of the aperture size was dictated by the compromise between performance and computational complexity. Obviously, the use of a larger aperture will generate better images for the delay-and-sum beamformer. However, the improvement achieved through these conventional methods will still produce results that are inferior to those observed for TONE.

Figure 5 depicts the results from the anechoic cyst phantom simulation. The cyst has a 1mm radius and is surrounded by scatterers. A schematic of the cyst phantom is shown in the top panel of this figure. The second and third panels show the conventional and TONE beamformed images, respectively. The conventional method provides enough resolution and contrast to detect the presence of an anechoic region, even though the shape and size of the original cyst is completely lost. In the case of TONE, the shape of the anechoic cyst is preserved and a series of point scatterers are visible surrounding the cyst.

It is noticeable from figure 5 that the scatterers estimated using TONE do not correspond with the scattering map presented in the top panel of the figure. One possible explanation could be that hypothetical targets were placed too coarsely throughout the ROI. A finer sampling grid will yield a more dense distribution of point scatterers. It is also important to recall that amongst the infinite solutions of the underdetermined reconstruction, TONE converges toward the solution that minimizes the energy of the signal vector $\underline{f}$, as expressed by equation (4). We also analyzed the amplitude histogram of the scatterers determined by TONE and found that they follow the expected zero mean Gaussian distribution.

Additional simulations were performed to evaluate the robustness of the algorithm to additive noise. For this set of simulations, we analyzed the performance of TONE using both RF and In-phase/Quadrature (IQ) data. We have found empirically that complex demodulated IQ data yields the best results when applying TONE. This could be explained by the fact that RF signals possess higher frequency content than IQ signals. This implies that when a mismatch occurs between the model (i.e., the array manifold matrix) and the actual data, in this case due to the addition of noise, the RF signals degrade faster than the IQ. The cost in this case is that IQ data occupy twice the memory required for RF signals since there is one real and one imaginary sample for every original RF sample. In figure 6 we show the results of the simulations when IQ data is used. In this figure, each panel corresponds to a different level of noise that was added to achieve a desired SNR.

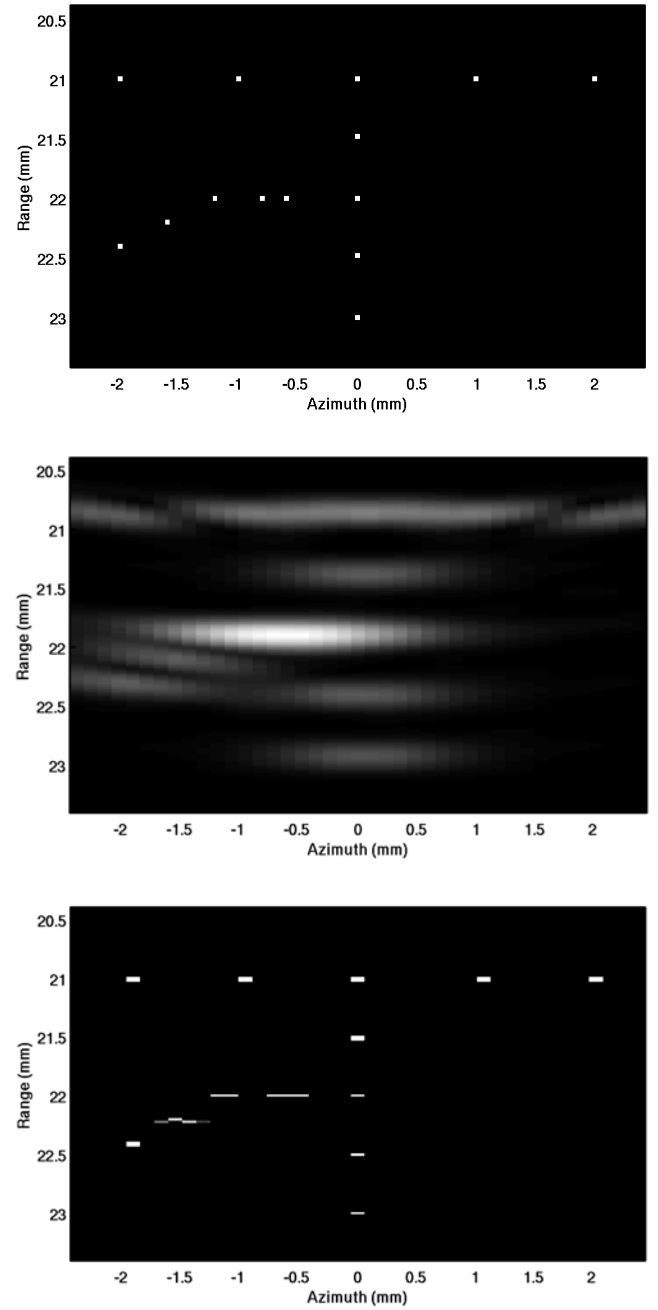

Fig. 4. Simulated point targets. The top panel shows the spatial configuration of the wire targets. The second and third panels show the results obtained with conventional beamforming and TONE, respectively. Images are displayed on a linear brightness scale.

Panel (a) shows the ideal case, when no noise is added to the RF data and the two point targets are clearly visible at a depth of 22mm. In panel (b), bandlimited Gaussian noise was added in order to achieve a "per channel" SNR of 30dB. In this case, a cloud of scatterers forms surrounding the original point targets. As the SNR is decreased to 20dB (c) and 10dB (d) per channel, the cloud expands and covers a larger region. As expected, performance deteriorates as noise increases even though the original point target is accurately detected by TONE.

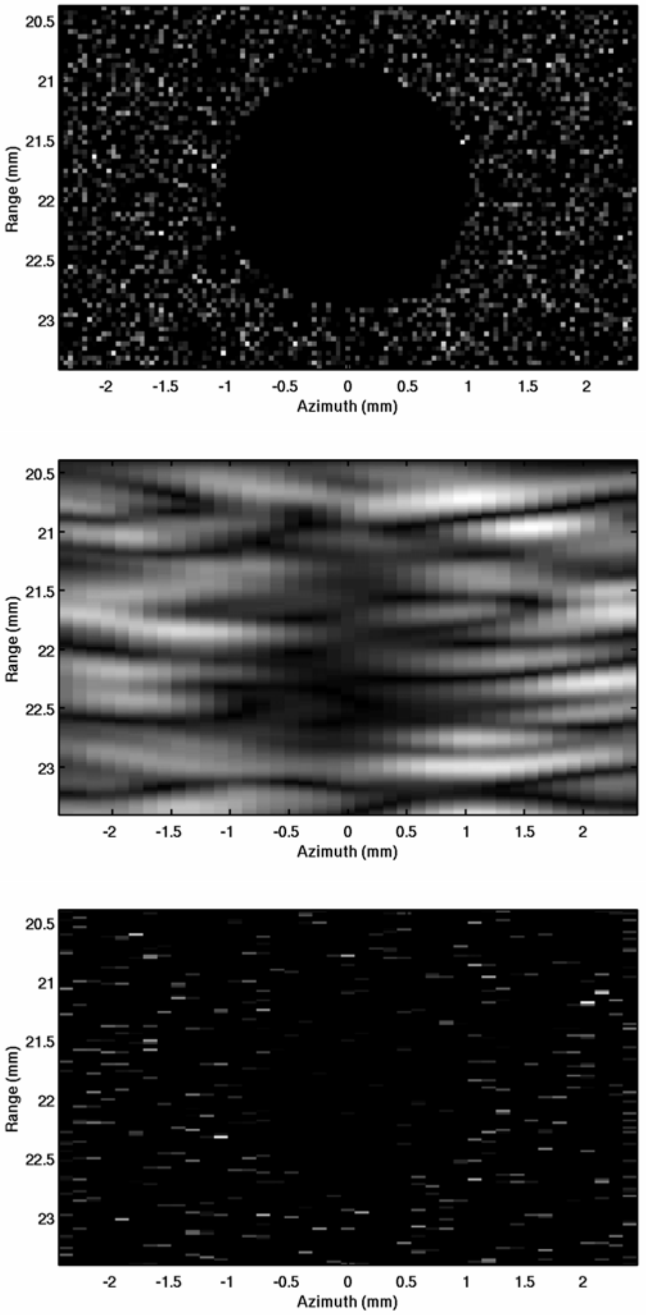

Fig. 5. Simulated anechoic cyst in a speckle generating background. The top panel shows the spatial configuration of the anechoic cyst and the surrounding scatterers. The second and third panels show the results obtained with conventional beamforming and TONE, respectively. Images are displayed on a linear brightness scale.

Experimental results are presented in figures 7 through 9. The top panel of figure 7 shows the conventional B-mode image of the five wires output by the Philips SONOS imaging system, whereas the bottom panel shows the TONE reconstructed image. This result is similar to that obtained in figure 4 for simulated point targets. Although the five wire targets are clearly resolved by TONE, a small cloud of scatterers is visible around them. This is most likely due to noise and imperfection of the array manifold matrix used to reconstruct the imaging field. As stated above, the manifold matrix was generated by simply delaying and re-interpolating the response obtained from a single steel wire. More sophisticated models could be generated which would include, for example, the effects of element angular sensitivity. Furthermore, the current formulation of TONE is derived for a plane wave transmission. This was approximated in the experiments presented here by transmitting simultaneously on all 128 elements.

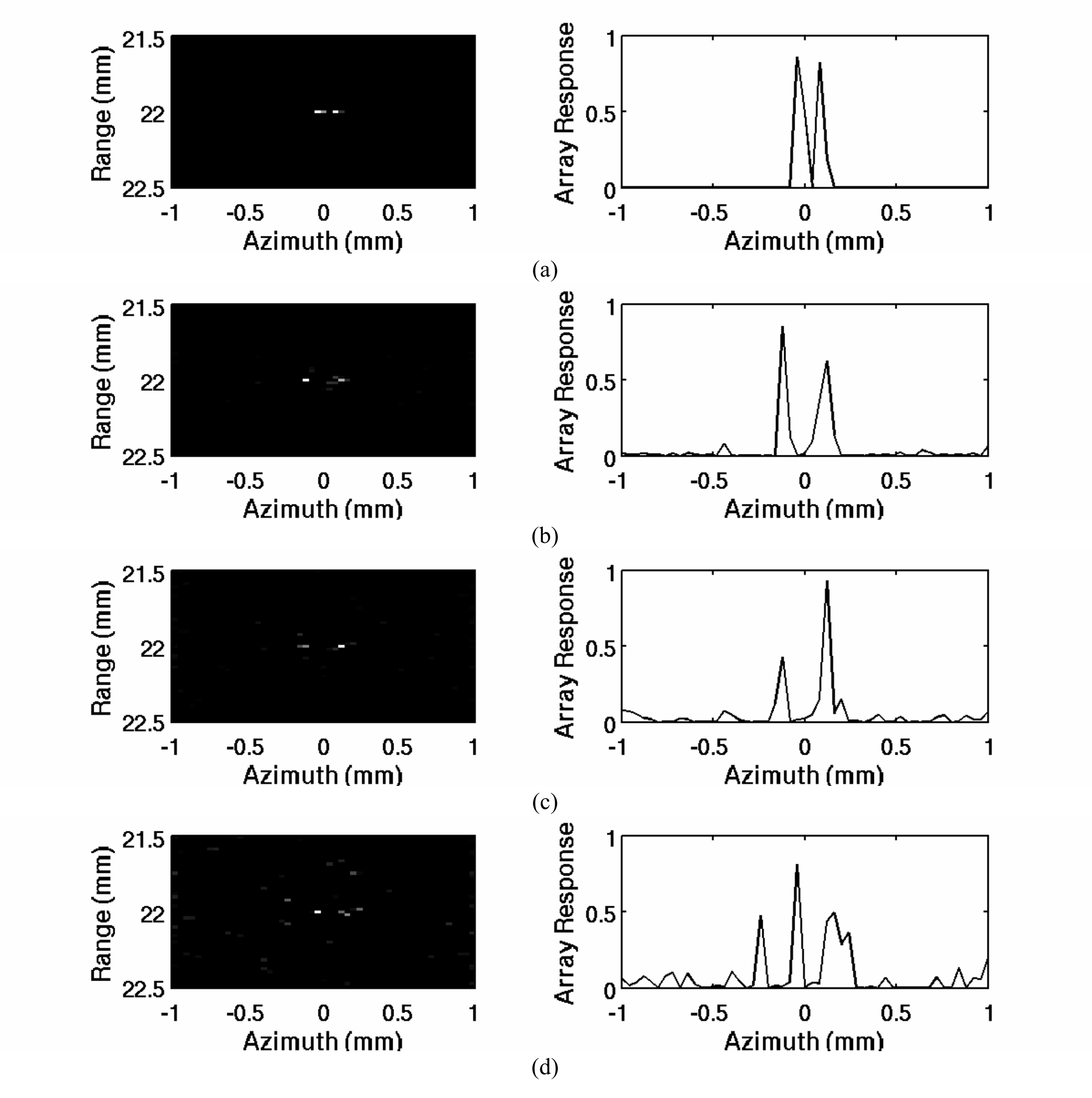

Fig. 6. Simulated robustness of TONE to additive noise. The additive noise was filtered to match the bandwidth of the received signals. Complex demodulated signals were used to generate this set of figures. The left panels show the images generated by TONE while the right panels show their respective axially integrated images. Set (a) shows the ideal case when no noise is added; (b), (c), and (d) correspond to "per channel" SNR levels of 30dB, 20dB, and 10dB, respectively. Images are displayed on a linear brightness scale.

We have also analyzed the performance of TONE as a function of mismatched speed of sound. In this case the array manifold matrix was constructed using a speed of sound that differs from the assumed true value of 1480m/sec. Results obtained for errors of 15m/s and 30m/s are shown in the top and bottom panels of figure 8, respectively. Obviously, as error increases performance starts to deteriorate. However, these results are significant since most adaptive beamforming algorithms rapidly degrade when ideal conditions are not met.

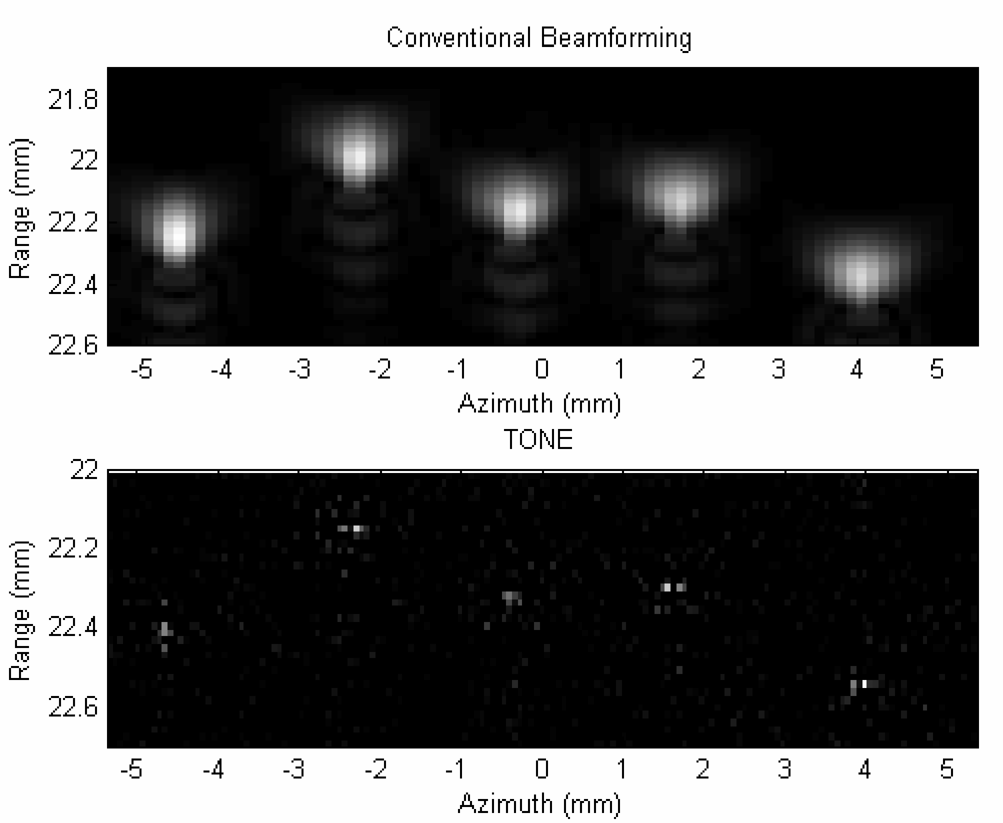

Fig. 7. Experimental comparison of conventional beamforming (top) and TONE beamformed (bottom) images of a set of five 20µm diameters stainless steel wires suspended in a water tank. In the case of TONE hypothetical targets were placed every 19µm axially and every 67µm laterally. Images are displayed on a linear brightness scale.

Finally, we investigated the behavior of TONE with missing receive channels. While the images shown in figures 7 and 8 were generated using the full 128 channels provided by the SONOS (135µm pitch), figure 9 shows the results obtained when the number of channels is reduced to 64, 32, 16, 8, 4 and finally 2 (equally spaced channels using the full aperture). The corresponding element pitches are 270µm, 540µm, 1.08mm, 2.43mm, 5.67mm, and 17.15mm respectively. This figure suggests that TONE performance is not affected by variations in channel number/pitch dimensions. While applying conventional beamforming on 8 receive channels with 2.43mm pitch would result in massive grating lobes, this figure shows that TONE remains almost unaffected. The five wires are also detectable when only 4 receive channels are used for the reconstruction, but the reconstruction fails when only 2 receive channels are used. We hypothesize that in the case of 2 channels, the received data does not hold sufficient information about the spatial responses of the actual scatterers within the ROI therefore disrupting the reconstruction process. It also appears from this figure that using 16 or fewer channels reduces the amount of clutter around the wires. In this case we hypothesize that there are two main factors to consider. First, by reducing the number of receive channels, small errors in the definition of the spatial responses become less significant compared to the case of the full aperture (or to the case of higher channel count). However, reducing channel count will eventually diminish the available information, as shown in the bottom panel for 2 channels. Nonetheless, the result presented in this figure could be important for two-dimensional arrays that rely on sparsity to reduce channel count.

I. DISCUSSION

The results presented in this paper show that under the analyzed conditions TONE outperforms conventional delay-and-sum beamforming. TONE assumes an observation model based superposition of spatial responses as indicated by equation (1). This model is then used to formulate a MAP algorithm that finds the distribution and amplitude of hypothetical targets that matches the observed data with minimal target energy. It is important to note that even though TONE uses such linear model, it is possible to model effects such as attenuation and non-linear propagation by simply redefining each of the columns (i.e., the spatial responses) of the array manifold matrix. In other words, the individual spatial responses can be constructed *ad hoc* to model any particular imaging scenario; TONE assumes that the received data set can be modeled as the superposition of those individual responses and that the first Born approximation regarding secondary scattering is satisfied. Furthermore, while other linear models have been described that specifically include the effects of noise [42, 43], these effects were not included in the work presented here. We are currently working toward extending the mathematical formulation of TONE to specifically include the contribution of noise.

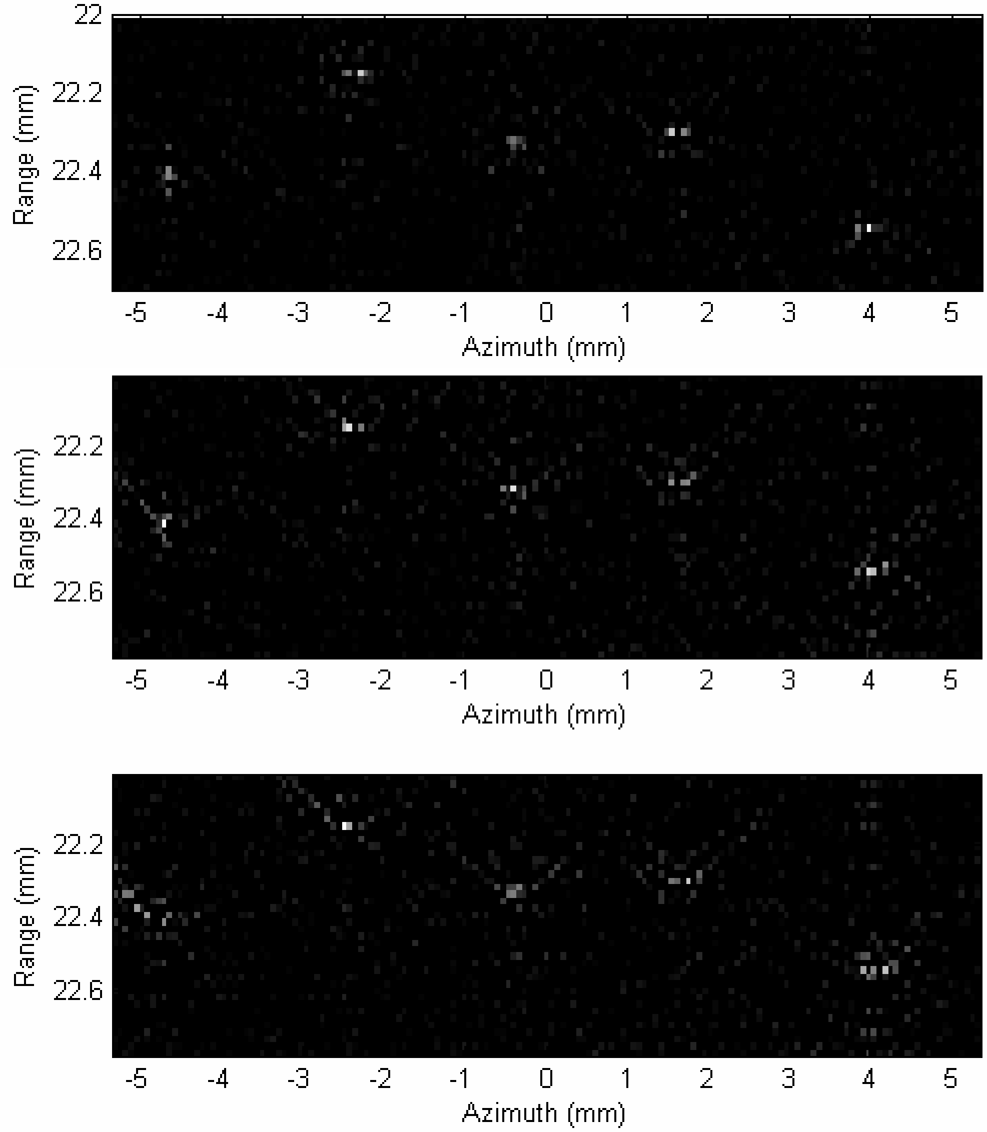

Fig. 8. Experimental assessment of sensitivity to errors in speed of sound. TONE beamformed images of the five steel wires with no error (top), 15m/s (middle), and 30m/s (bottom) mismatch in speed of sound. Images are displayed on a linear brightness scale.

The experimental TONE images shown in this paper reveal small amounts of clutter surrounding the wire targets, which causes a reduction in the effective contrast of the images. One possible cause for this clutter is the sparseness of the grid of hypothetical targets. Unless the point target lies exactly on one of the hypothetical targets, it is not possible for TONE to perfectly match the data to the system model. It would be logical to assume that, when the point target lies between hypothetical targets, TONE would distribute energy to the hypothetical targets directly surrounding that target. However, due to the coherent nature of the system, it is possible that the sum of many hypothetical targets in a diffuse cloud around the actual target would produce a more optimal, lower energy solution. One way to reduce this effect is to treat each hypothetical target as a diffuse set of scatterers. Instead of each column of the manifold matrix being the system response from a single target, it would instead be the system response from a weighted set of scatterers surrounding that single point target. Therefore, when a point target lies between two hypothetical targets, TONE would be more likely to distribute energy to the targets directly surrounding that target, thereby reducing clutter in the output image. Although this modification would require more computation upfront, the manifold matrix would not change in size. If we pre-compute this manifold matrix and keep it stored, there would be no change in the computation time to beamform the data.

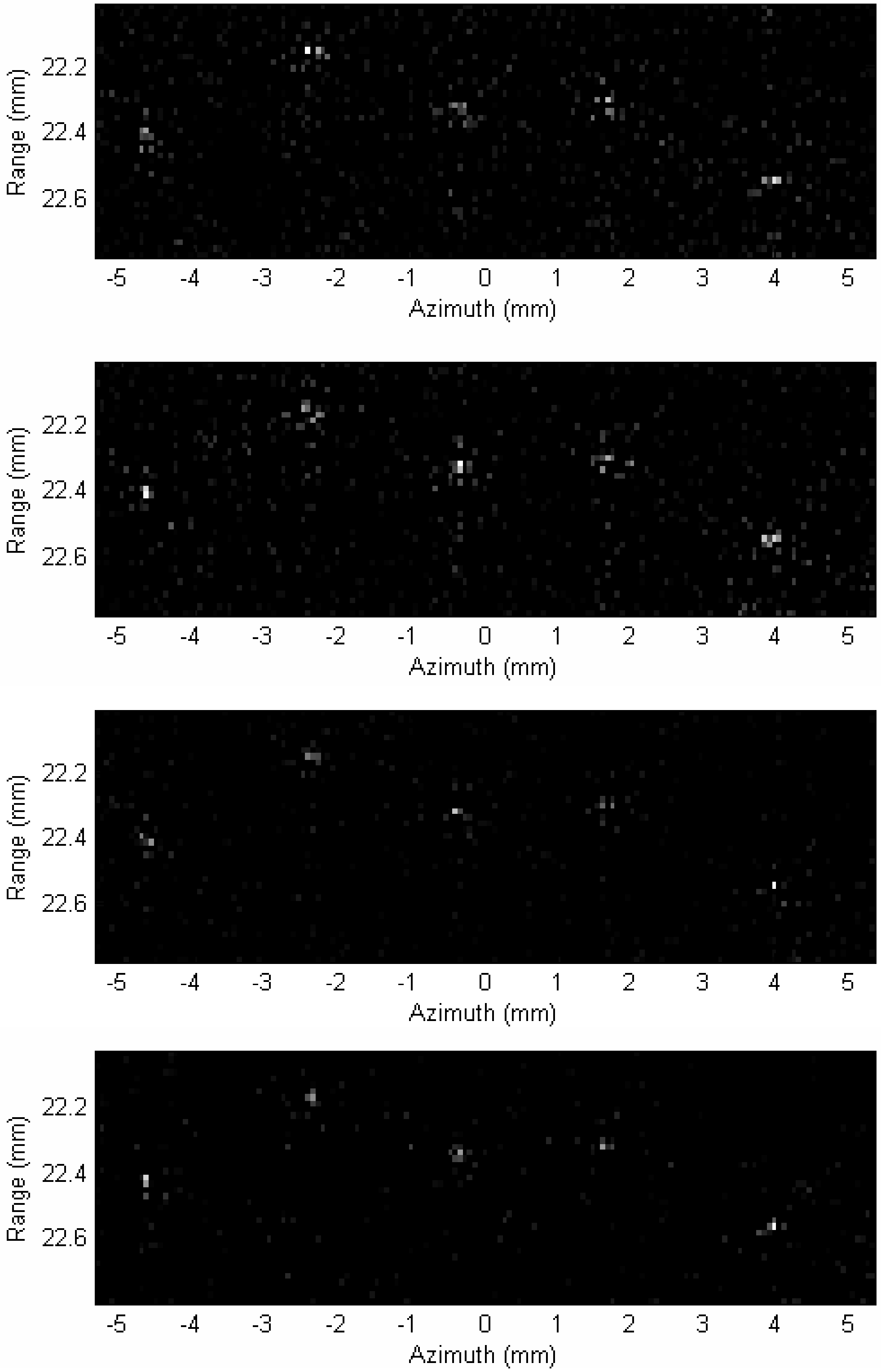
Range (mm)
22.2
22.4
22.6
-5
-4
-3
-2
-1
0
1
2
3
4
5
Azimuth (mm)
Range (mm)
22.2
22.4
22.6
-5
-4
-3
-2
-1
0
1
2
3
4
5
Azimuth (mm)
Range (mm)
22.2
22.4
22.6
-5
-4
-3
-2
-1
0
1
2
3
4
5
Azimuth (mm)
Range (mm)
22.2
22.4
22.6
-5
-4
-3
-2
-1
0
1
2
3
4
5
Azimuth (mm)

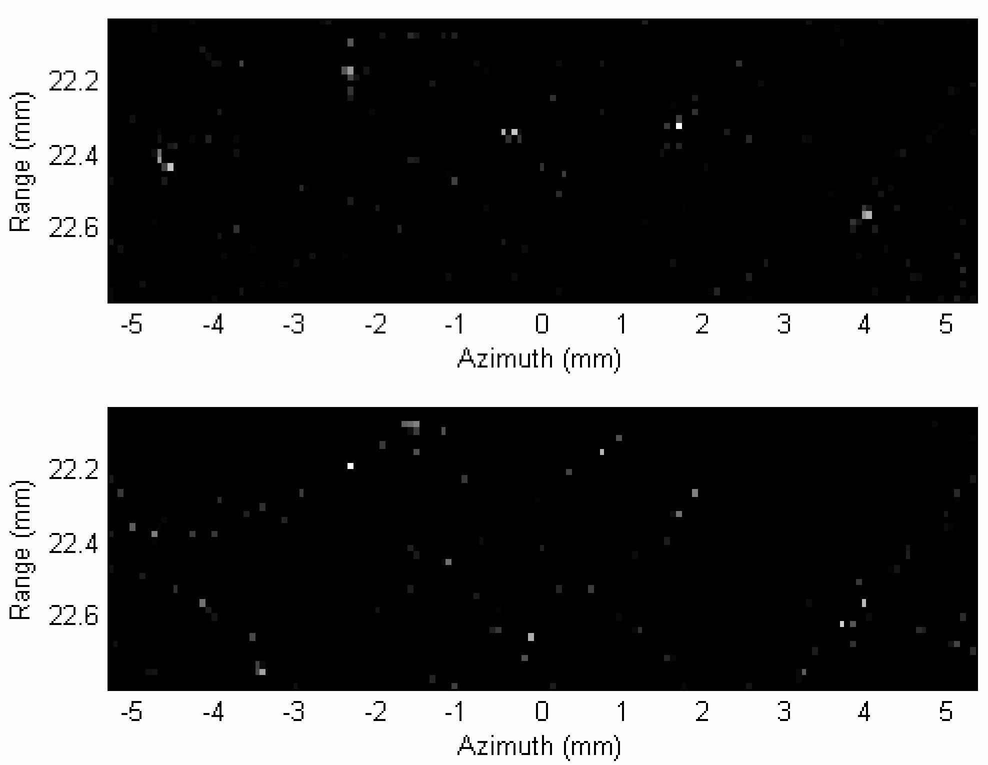

Fig. 9. Experimental assessment of sparsity. TONE beamforming of the five steel wires with (from top to bottom): 64, 32, 16, 8, 4, and 2 receive channels. Images are displayed on a linear brightness scale.

The images presented here also demonstrate increased spatial resolution of TONE when compared to conventional beamforming. While resolution in conventional beamforming is easily represented, resolution of TONE is much more complicated. We hypothesize that there is a resolution bound on TONE and other advanced beamforming algorithms that estimate the target field, similar to the bound currently available for time delay estimation. The key is that TONE is an estimation problem, not a simple beamformer. As shown in this paper, we have empirically found that sampling of the hypothetical target field, SNR, and model quality all impact apparent resolution.

Currently, the main limitation of TONE is its high computational complexity. The experimental images shown in this paper were obtained after roughly 22 minutes of computation on the high power cluster provided by Interactive Supercomputing. Furthermore, while higher spatial resolution is achieved by using finer sampling of the ROI, this also incurs higher computational complexity. In our experience, the generation of the manifold matrix and the iterative procedure to estimate $\underline{f}$ represent the most costly steps. For an image region of 1cm by 1cm and assuming a sampling grid of hypothetical targets of 20μm by 70μm, $\underline{V}$ is on the order of 64K by 71K elements for a total of 4,544M elements. However, for a given ROI and desired sampling grid, the manifold matrix can be calculated in advance and stored for later use, reducing the computational cost for most applications. Furthermore, TONE may also be applied to a given receive data set using a variety of iterative approaches to reduce the required computational complexity and data storage size. In one such approach the complete received data set is subdivided into multiple data segments that may or may not be uniformly sampled and may or may not overlap. For each received data segment, a distinct array manifold matrix would be formed to represent the responses from hypothetical targets which contribute to the specific data segment. TONE could then be applied separately to each of the data segments and their matched array manifold matrices. We are currently investigating this and other approaches.

I. CONCLUSIONS

The application of advanced beamforming methods in medical ultrasound can significantly improve overall image quality. Most of the adaptive algorithms developed for RADAR and SONAR fail when applied to medical ultrasound data. This can be attributed to some or all of the following factors: ultrasound operates in a near-field scenario, signals are broad-band, and ultrasound has limited statistical information available.

In this paper we have presented an algorithm, named TONE, which is well suited to medical ultrasound since it requires neither a far-field/narrow-band assumption nor second order statistics of the signals. Under all the simulations and experiments performed, TONE showed a significant improvement in resolution and contrast when compared to conventional, data independent beamforming.

ACKNOWLEDGMENT

We acknowledge technical support from Interactive Supercomputing, Inc. and McKee Poland from Philips Medical Systems.

REFERENCES

[1] S. Haykin, “Adaptive Filter Theory,” 4th ed., Prentice-Hall, Upper Saddle River, New Jersey, 2002.

[2] B. D. Van Veen and K. M. Buckley, “Beamforming: A Versatile Approach to Spatial Filtering,” *IEEE ASSP Magazine*, pp. 4-24, 1988.

[3] W. F. Gabriel, “Adaptive Processing Array Systems,” *Proc. IEEE*, vol. 80, no. 1, pp. 152-162, 1992.

[4] J. Capon, “High resolution frequency-wavenumber spectrum analysis,” *Proc. IEEE*, vol. 57, no. 8, pp. 1408-1418, 1969.

[5] O. L. Frost III, “An Algorithm for Linearly Constrained Adaptive Array Processing,” *Proc. IEEE*, vol. 60, no. 8, pp. 926-935, 1972.

[6] W. F. Gabriel, “Using Spectral Estimation Techniques in Adaptive Processing Antenna Systems,” *IEEE Trans. Antennas Propagat.*, vol. AP-34, no. 3, pp. 291-300, 1986.

[7] S. M. Kogon, “Experimental Results for Passive Sonar Arrays with Eigenvector-Based Adaptive Beamformers,” *Thirty-Sixth Asilomar Conference on Signals, Systems and Computers*, vol. 1, pp. 439-447, 2002.

[8] D. A. Abraham and N. L. Owsley, “Beamforming with Dominant Mode Rejection,” *Proceedings of the Oceans Conference*, pp. 470-475, 1990.

[9] H. Subbaram and K. Abend, “Interference Suppression Via Orthogonal Projections: A Performance Analysis,” *IEEE Trans. Antennas Propagat.*, vol. 41, no. 9, pp. 1187-1194, 1993.

[10] R. T. Behrens and L. L. Sharf, “Signal Processing Applications of Oblique Projection Operators,” *IEEE Trans. Signal Proc.*, vol. 42, no. 6, pp. 1413-1424, 1994.

[11] D. D. Feldman and L. J. Griffiths, “A Projection Approach for Robust Adaptive Beamforming,” *IEEE Trans. Signal Proc.*, vol. 42, no. 4, pp. 867-876, 1994.

[12] P. Stoica, Z. Wang, and J. Li, “Robust Capon Beamforming,” *IEEE Trans. Signal Proc. Letters*, vol. 10, no. 6, pp. 172-175, 2003.

[13] H. Cox, “Adaptive Beamforming in Non-Stationary Environments *Thirty-Sixth Asilomar Conference on Signals, Systems and Computers*, vol. 1, pp. 431-438, 2002.

[14] M. V. Greening and J. E. Perkins, “Adaptive beamforming for nonstationary arrays,” *J. Acoust. Soc. Am.*, vol. 112, no. 6, pp. 2872-2881, 2002.

[15] P. Gerstoft, W. S. Hodgkiss, W. A. Kuperman, H. Song, M. Siderius, and P. L. Nielsen, “Adaptive Beamforming of a Towed Array During a Turn,” *IEEE J. Oceanic Eng.*, vol. 28, no. 1, pp. 44-54, 2003.

[16] M. E. Ali and F. Schreib, “Adaptive Single Snapshot Beamforming: A New Concept for the Rejection of Nonstationary and Coherent Interferers,” *IEEE Trans, Signal Proc.*, vol. 40, no. 12, pp. 3055-3058, 1992.

[17] T. K. Sarkar, S. Park, J. Koh, and R. A. Schneible, “A Deterministic Least Squares Approach to Adaptive Antennas,” *Digital Signal Proc.*, vol. 6, pp. 185-194, 1996.

[18] R. Bethel, B. Shapo, and H. L. Van Trees, “Single Snapshot Spatial Processing: Optimized and Constrained,” *Sensor Array and Multichannel Signal Processing Workshop Proceedings*, pp. 508-512, 2002.

[19] M. Viberg and A. L. Swindlehurst, “A Bayesian Approach to Auto-Calibration for Parametric Arrays Signal Processing,” *IEEE Trans. Signal Proc.*, vol. 42, no. 12, pp. 3495-3507, 1994.

[20] B. M. Radich and K. M. Buckley, “Single-Snapshot DOA Estimation and Source Number Detection,” *IEEE Trans. Signal Proc.*, vol. 4, no. 4, pp. 109-111, 1997.

[21] E. Cekli and H. A. Cirpan, “Deterministic Maximum Likelihood Method for the Localization of Near-Field Sources: Algorithm and Performance Analysis,” *8th IEEE International Conference on Electronics, Circuits and Systems*, vol. 2, pp. 1077-1080, 2001.

[22] M.-W. Tu, I. J. Gupta, and E. K. Walton, “Application of Maximum Likelihood Estimation to Radar Imaging,” *IEEE Trans. Antennas Propagat.*, vol. 45, no. 1, pp. 20-27, 2002.

[23] D. M. Malioutov, M. Cetin, J. W. Fisher III, and A. S. Willsky, “Superresolution Source Localization Through Data-Adaptive Regularization,” *Sensor Array and Multichannel Signal Processing Workshop Proceedings*, pp. 194-198, 2002.

[24] R. T. O’Brien and K. Kiriakidis, “Single-Snapshot Robust Direction Finding,” *IEEE Trans. Signal Proc.*, vol. 53, no. 6, pp. 1964-1978, 2005.

[25] K. K. Shung and G. A. Thieme, “Ultrasonic Scattering in Biological Tissues,” CRC Press, 1993.

[26] B. Widrow, K. M. Duvall, R. P. Gooch, and W. C. Newman, “Signal Cancellation Phenomena in Adaptive Antennas: Causes and Cures,” *IEEE Trans. Antennas Propagat.*, vol. AP-30, no. 3, pp. 469-478, 1982.

[27] M. Agrawal and S. Prasad, “Robust Adaptive Beamforming for Wide-Band, Moving, and Coherent Jammers via Uniform Linear Arrays,” *IEEE Trans. Antennas Propagat.*, vol. 47, no. 8, pp. 1267-1275, 1999.

[28] Y.-L. Su, T.-J. Shan, and B. Widrow, “Parallel Spatial Processing: A Cure for Signal Cancellation in Adaptive Arrays,” *IEEE Trans. Antennas Propagat.*, vol. AP-34, no. 3, pp. 347-355, 1986.

[29] A. K. Luthra, “A Solution to the Adaptive Nulling Problem with a Look-Direction Constraint in the Presence of Coherent Jammers,” *IEEE Trans. Antennas Propagat.*, vol. AP-30, no. 5, pp. 702-710, 1986.

[30] F. Qian and B. D. Van Veen, “Partially Adaptive Beamforming for Correlated Interference Rejection,” *IEEE Trans. Signal Proc.*, vol. 43, no. 3, pp. 506-515, 1995.

[31] T.-J. Shan and T. Kailath, “Adaptive Beamforming for Coherent Signals and Interference,” *IEEE Trans. Acoust., Speech, Signal Processing*, vol. ASSP-33, no. 3, pp. 527-536, 1985.

[32] J. A. Mann and W. F. Walker, “Constrained Adaptive Beamforming: Point and Contrast Resolution,” *Proc. SPIE*, vol. 5035, 2003.

[33] J. A. Mann and W. F. Walker**, “**A constrained adaptive beamformer for medical ultrasound: initial results**,”** *IEEE Ultrasonic Symposium*, 2002.

[34] Z. Wang, J. Li, and R. Wu, “Time-Delay- and Time-Reversal-Based Robust Capon Beamformers for Ultrasound Imaging,” *IEEE Trans. Med. Imag.*, vol. 24, no. 10, pp. 1308-1322, 2005.

[35] J.-F. Synnevag, A. Austeng, and S. Holm, “Minimum variance adaptive beamforming applied to medical ultrasound imaging,” *IEEE Ultrasonic Symposium*, 2005.

[36] K. W. Lo, “Adaptive Array Processing for Wide-Band Active Sonars,” *IEEE J. Oceanic Eng.*, vol. 29, no. 3, pp. 837-846, 2004.

[37] J. A. Jensen and N. B. Svendsen, “Calculation of Pressure Fields from Arbitrarily Shaped, Apodized, and Excited Ultrasound Transducers,” *IEEE Trans. Ultrason., Ferroelect., Freq. Cont.*, vol. 39, no. 2, pp. 262-267, 1992.

[38] R. F. Wagner, S. W. Smith, J. M. Sandrik, and H. Lopez, “Statistics of Speckle in Ultrasound B-Scans,” *IEEE Trans. Sonics and Ultrason.*, vol. 30, no. 3, pp. 156-163, 1983.

[39] L. L. Scharf, “Statistical Signal Processing: Detection, Estimation, and Time Series Analysis,” *Addison Wesley*, 1991.

[40] M. Sasso and C. Cohen-Barcie, “Medical ultrasound imaging using the fully adaptive beamformer,” *Proceedings of Acoustics, Speech and Signal Processing*, 2005.

[41] R. Lavarello, F. Kamalabadi, and W. D. O’Brien, “A Regularized Inverse Approach to Ultrasonic Pulse-Echo Imaging,” *IEEE Trans. Med. Imag.*, vol. 25, no. 6, pp. 712-722, 2006.

[42] R. Stoughton and S. Strait, “Source imaging with minimum mean-square error,” *J. Acoust. Soc. Am.*, vol. 94, no. 2, pp. 827-834, 1993.

[43] F. Lingvall, “A method of improving overall resolution in ultrasonic array imaging using spatio-temporal deconvolution,” *Ultrasonics*, vol. 42, pp. 961-968, 2004.

[44] M. A. Ellis, D. A. Guenther, and W. F. Walker, “A Spline-Based Approach to Computing Spatial Impulse Responses,” *IEEE Trans. Ultrason., Ferroelect., Freq. Cont.*, vol. 54, no. 5, pp. 1045-1054, 2007.

Francesco Viola received the B.S.E. in biomedical engineering in 1999 from the Polytechnic of Milan, Milan, Italy, and the Ph.D. in biomedical engineering in 2004 from the University of Virginia, Charlottesville, VA. His dissertation work focused on acoustic radiation force imaging, elastography imaging, digital signal processing for medical ultrasound applications, and time delay estimation.

Dr. Viola is currently working in the Department of Biomedical Engineering at the University of Virginia as a research associate. His research interests include ultrasound beamforming, tissue elasticity estimation, and time delay estimation. Dr. Viola is also a co-founder of an ultrasound based startup company, HemoSonics, LLC.

Michael A. Ellis received his B.S. in Electrical Engineering in 2004 from Bucknell University, Lewisburg, PA.

After completing his B.S., he joined the Department of Biomedical Engineering at the University of Virginia, Charlottesville, VA where he is currently pursuing his Ph.D. His research interests include ultrasound beamforming, signal processing, and adaptive algorithms.

William F. Walker received the B.S.E. and Ph.D. degrees in 1990 and 1995 from Duke University, Durham, NC. His dissertation explored fundamental limits on the accuracy of adaptive ultrasound imaging.

After completing his doctoral work he stayed on at Duke as an Assistant Research Professor in the Department of Biomedical Engineering. At the same time he served as a Senior Scientist and President of NovaSon Corporation located in Durham NC. In 1997 he joined the faculty of the Department of Biomedical Engineering at the University of Virginia, being promoted to Associate Professor in 2003. He is an active founder in two ultrasound based startup companies, PocketSonics Inc. and HemoSonics LLC. His research interests include aperture domain processing, beamforming, angular scatter imaging, tissue elasticity imaging, low-cost system architectures, blood coagulation, and time delay and motion estimation.

A Spline-Based Approach for Computing Spatial Impulse Responses

Michael A. Ellis, Drake Guenther, and William F. Walker, *Member, IEEE*

***Abstract*—Computer simulations are an essential tool for the design of phased-array ultrasonic imaging systems. FIELD II, which determines the two-way temporal response of a transducer at a point in space, is the current de facto standard for ultrasound simulation tools. However, the need often arises to obtain two-way spatial responses at a single point in time, a set of dimensions for which FIELD II is not well optimized. This paper describes an analytical approach for computing the two-way, far-field, spatial impulse response from rectangular transducer elements under arbitrary excitation. The described approach determines the response as the sum of polynomial functions, making computational implementation quite straightforward. The proposed algorithm, named DELFI, was implemented as a C routine under Matlab and results were compared to those obtained under similar conditions from the well-established FIELD II program. Under the specific conditions tested here, the proposed algorithm was approximately 142 times faster than FIELD II for computing spatial sensitivity functions with similar amounts of error. For temporal sensitivity functions with similar amounts of error, the proposed algorithm was about 1.7 times slower than FIELD II using rectangular elements and 19.2 times faster than FIELD II using triangular elements. DELFI is shown to be an attractive complement to FIELD II, especially when spatial responses are needed at a specific point in time.**

I. Introduction

The design of modern, phased-array ultrasonic imaging systems relies heavily on the use of computer simulations. This is necessary because the broadband and near-field nature of most clinical imaging environments severely limits the utility of the Fraunhofer approximation [1] and other theoretical methods. Furthermore, the high degree of optimization of modern systems makes even small deviations from such theory significant. For example, if the system designer is concerned with the array sensitivity pattern down 80 dB from the main-lobe, then a deviation from theory of only 0.1% (−60 dB) will significantly affect performance and make optimization to the desired level impossible. Clearly, highly accurate simulation tools are required to guide the selection of transducer geometry, apodization, operating frequency, and other parameters.

Although most researchers and designers would agree upon the need for accurate simulation, the appropriate approach depends upon the specific problem of interest and the parameters that are most significant to that problem. For example, in cases in which details of transducer vibration and crosstalk are of interest, a computationally costly, finite-element analysis may be required to capture the most relevant behavior. For such problems, the highly optimized PZFlex (Weidlinger Associates, Inc., New York, NY) package is widely used [2]. In other cases, in which the detailed transducer response is of less interest—but the propagation medium is inhomogeneous or multiple scattering occurs—the more computationally efficient finite difference method, such as that implemented in Wave2000 (CyberLogic Inc., New York, NY), may be used [3]. Often, the motivation for adopting more computationally demanding approaches is to account for nonlinear phenomena and inhomogeneities in the simulated environment.

For the vast majority of situations, in which the system can be modeled as linear and the propagation medium can be considered homogeneous or inhomogeneities can be modeled as a near-field, thin, phase screen, Stepanishen's method [4], as implemented in Jensen and Svendsen's FIELD II program [5] has become a standard in ultrasound. This approach determines the spatial impulse response of each transmit element, convolves this with the spatial impulse response of each receive element, convolves this result with the transmitted pulse, and convolves this with the transmit and receive electromechanical impulse responses to determine the two-way temporal response at a point in space. This technique, as implemented in Jensen's code, has been highly refined over roughly a decade of development so that it is extremely efficient and available in a compiled form on a variety of computer platforms (http://www.es.oersted.dtu.dk/staff/jaj/field/). By computing the temporal signals returned from various target locations, FIELD II readily models common experimental situations.

Although the temporal response returned by FIELD II provides an excellent parallel to experiment, recent theoretical work by Zemp *et al.* [6] and Walker [7] highlights the importance of considering the full four or five dimensional system response. In a previous paper [7], we derive a method for predicting speckle correlation levels for shift variant systems using point spread functions defined as functions of three spatial dimensions and time. Although much of this detail is hidden experimentally, the consideration of the full dimensionality of the system response

---

Manuscript received August 11, 2006; accepted January 4, 2007. This work was supported in part by NIH Grant EB002348 and the US Army Congressionally Directed Research Program under Grants DAMD17-01-1-0443 and W81XWH-04-1-0590.

The authors are with the Department of Biomedical Engineering, University of Virginia, Charlottesville, VA (e-mail: mae3x@virginia.edu).

Digital Object Identifier 10.1109/TUFFC.2007.350

0885–3010/$25.00 © 2007 IEEE

yields insights and offers paths for analysis that are not apparent in the more conventional two-dimensional (space, time) view of the system. Zemp *et al.* [6] carried this concept one step further, including another dimension for image line index, thereby further clarifying system behavior. Our laboratory recently applied these frameworks to derive a general resolution metric that allows quantitative comparison of system performance, even when the individual impulse responses of those systems are very different in structure [8]. Interestingly, this new resolution metric is based upon the system response throughout space at a single instant in time; a form of the impulse response that is not naturally determined by FIELD II. Although such responses can be computed by sampling the temporal responses generated by FIELD II, this approach is extremely costly in terms of both computation and storage.

In this paper, we describe a new approach to computing spatial impulse responses that directly determines the response throughout space at a single instant in time. This approach is complementary to FIELD II, simply yielding responses in a different set of dimensions. Because results from this code are predictive of system performance and are a permutation of the data available from FIELD II, we name this code DELFI. In this paper, we describe the theoretical underpinnings of the DELFI code, describe implementation, and validate the code through comparisons with FIELD II. We discuss the relative computational efficiency of DELFI and discuss future directions for development and refinement.

II. Theory

We begin our derivation by considering the general approach used by Jensen in the FIELD II program [5]. We consider the system response for a specific transmit-receive element pair to be a four-dimensional function of space and time:

$$\begin{aligned} p(x,y,z,t) = \\ e(t) \underset{t}{*} m_t(t) \underset{t}{*} m_r(t) \underset{t}{*} h_t(x,y,z,t) \underset{t}{*} h_r(x,y,z,t), \end{aligned} \tag{1}$$

where x, y, and z are the three spatial dimensions, t is the time for a given line (proportional to range in the beamformed image), $p(x,y,z,t)$ is the system point spread function (psf), $e(t)$ is the electrical excitation of the transmit element, $m_t(t)$ and $m_r(t)$ are the electromechanical transfer functions of the transmit and receive elements, respectively, $h_t(x,y,z,t)$ and $h_r(x,y,z,t)$ are the spatial impulse responses of the transmit and receive elements, respectively, and $\underset{t}{*}$ indicates convolution in the time dimension. In typical systems the excitation and the transmit and receive electromechanical transfer functions are assumed constant for all elements of the array. Thus we can convolve these terms together before computing the overall response with little loss in generality. Performing this step we simplify (1) to yield:

$$p(x,y,z,t) = emm_{tr}(t) \underset{t}{*} h_t(x,y,z,t) \underset{t}{*} h_r(x,y,z,t), \tag{2}$$

where $emm_{tr}(t)$ is the combined effect of the excitation and the transmit and receive electromechanical transfer functions and can be represented mathematically as $emm_{tr}(t) = e(t) \underset{t}{*} m_t(t) \underset{t}{*} m_r(t)$. Although FIELD II computes expressions (1) or (2) using sampled versions of each of the component signals, we take an alternate approach instead using analytical expressions for these functions.

The utility of an analytical approach depends upon the choice of expressions used; they must be general enough to include all relevant cases, but they must be constrained in such a way to guarantee the presence of an analytical solution. Because (2) allows for consideration of most practically interesting cases and requires two convolutions [rather than the four convolutions of (1)], we build our algorithm upon this expression. Further simplification can be made by assuming that the point of interest lies in the far-field of both the transmit and receive elements. This is not an onerous assumption because cases in which the response would lie in the near-field of a physical element can be readily modeled using a superposition of computational elements for which the far-field assumption is valid. We further simplify the problem by assuming that the elements are rectangular.

Following these assumptions and once again drawing upon the methodology of Jensen [5], we recognize that the one-way spatial impulse response of an element takes on one of three functions. If the field point lies on the line perpendicular to the element face and passing through its center, the spatial impulse response as a function of time is simply a delta function, as shown in the left panel of Fig. 1. If the field point does not fulfill the first condition, but instead lies upon one of two planes passing through the element center and perpendicular to the element edges, the spatial impulse response in time is a rectangle function, as depicted in the central panel of Fig. 1. If the field point fulfills neither of these conditions, the spatial impulse response in time is a trapezoid function, as shown in the right panel of Fig. 1. These possible one-way spatial impulse responses are summarized mathematically below. Note we describe the rectangle and trapezoid functions using sums of unit step and ramp functions:

$$h_0(x,y,z,t) = A_0(x,y,z)\delta(t-t_0), \tag{3}$$

$$\begin{aligned} h_1(x,y,z,t) = {} & A_1(x,y,z)u(t-t_{1,0}) \\ & - A_1(x,y,z)u(t-t_{1,1}), \end{aligned} \tag{4}$$

$$\begin{aligned} h_2(x,y,z,t) = {} & (t-t_{2,0})A_2(x,y,z)u(t-t_{2,0}) \\ & - (t-t_{2,1})A_2(x,y,z)u(t-t_{2,1}) \\ & - (t-t_{2,2})A_2(x,y,z)u(t-t_{2,2}) \\ & + (t-t_{2,3})A_2(x,y,z)u(t-t_{2,3}), \end{aligned} \tag{5}$$

where h_0, h_1, and h_2 represent the delta, rectangle, and trapezoid spatial impulse responses, respectively, and $u(t)$ is the unit step function. The scaling functions $A_0(x,y,z)$,

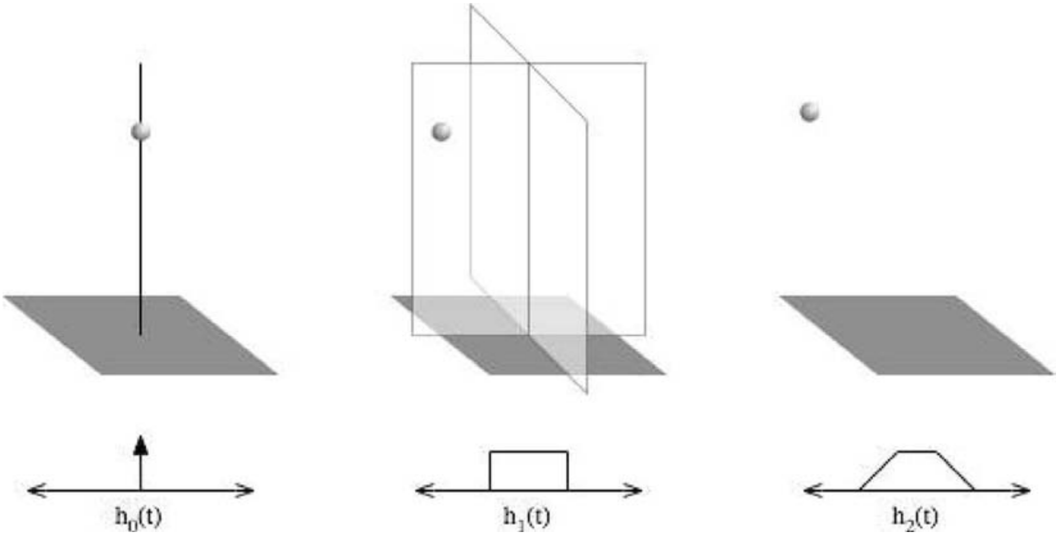

Fig. 1. Geometries for determining the one-way spatial impulse response of an individual array element. In the left panel, the field point lies on the line through the element's center and perpendicular to its face. In the center panel, the field point does not satisfy the first condition but lies on a plane that bisects the element and is perpendicular to its face. In the right panel, the field point lies at any location not satisfying either of the first two conditions.

$A_1(x,y,z)$, and $A_2(x,y,z)$ are constant at any specific spatial location and include $1/r$ spreading, scaling to account for the element size, and an obliquity factor to account for a soft transducer baffle [9], if desired. The time delay t_0 present in (3) is determined by the speed of sound and the distance from the element center to the field point. Similarly, the delays present in (4) and (5) are determined from the speed of sound and distances between the field point and the element edges and corners, respectively. It is important to note that these descriptions of the impulse response are valid only in the very far-field.

To determine the two-way response from an element pair, we must convolve the appropriate version of (3)–(5) for the receive element with the appropriate version of (3)–(5) for the transmit element. Although superficial analysis suggests that nine permutations are possible, a more careful examination reveals that, as the order of convolution is irrelevant, some of these permutations are redundant. Thus, the two-way response must fit one of the following six general expressions:

$$h_{tr} = h_t \underset{t}{*} h_r = \Big\{ h_0 \underset{t}{*} h_0 \text{ or } h_0 \underset{t}{*} h_1 \text{ or } h_0 \underset{t}{*} h_2 \text{ or } h_1 \underset{t}{*} h_1 \text{ or } h_1 \underset{t}{*} h_2 \text{ or } h_2 \underset{t}{*} h_2, \tag{6}$$

where we have dropped space and time references to simplify notation. Note that, although the simplified notation of (6) suggests that, in some cases (such as $h_2 \underset{t}{*} h_2$), the transmit and receive responses are identical, this is intended to state only that the transmit and receive responses fit the same function; they may have different delays and scaling. Substituting (3)–(5) into (6) yields a set of six possible two-way impulse responses:

$$h_{0_a} \underset{t}{*} h_{0_b} = A_{0_a} A_{0_b} \delta\left(t - t_{0_a} - t_{0_b}\right), \tag{7}$$

$$h_0 \underset{t}{*} h_1 = A_0 A_1 \sum_{j=0}^{1} (-1)^j u(t - t_0 - t_{1,j}), \tag{8}$$

$$h_0 \underset{t}{*} h_2 = A_0 A_2 \sum_{j=0}^{3} c_j (t - t_0 - t_{2,j}) u(t - t_0 - t_{2,j}), \tag{9}$$

$$\begin{aligned} h_{1_a} \underset{t}{*} h_{1_b} = A_{1_a} A_{1_b} \sum_{j=0}^{1} \sum_{k=0}^{1} (-1)^j (-1)^k (t - t_{1_a,j} \\ - t_{1_b,k}) u(t - t_{1_a,j} - t_{1_b,k}), \end{aligned} \tag{10}$$

$$\begin{aligned} h_1 \underset{t}{*} h_2 = A_1 A_2 \sum_{j=0}^{1} \sum_{k=0}^{3} (-1)^j c_k (t - t_{1,j} \\ - t_{2,k})^2 u(t - t_{1,j} - t_{2,k}), \end{aligned} \tag{11}$$

$$\begin{aligned} h_{2_a} \underset{t}{*} h_{2_b} = A_{2_a} A_{2_b} \sum_{j=0}^{3} \sum_{k=0}^{3} c_j c_k (t - t_{2_a,j} \\ - t_{2_b,k})^3 u(t - t_{2_a,j} - t_{2_b,k}), \end{aligned} \tag{12}$$

where $c_j = \{1 \text{ for } j = 0 \text{ or } 3 \text{ and } -1 \text{ for } j = 1 \text{ or } 2\}$. With each of the six possible two-way impulse responses in hand, we now can consider an appropriate analytical representation of the excitation function (including transmit and receive electromagnetic transfer functions). While a number of possible functions are attractive, we choose to represent $emm_{tr}(t)$ using cubic splines [10]. This representation is attractive because it allows arbitrary function shapes while restricting the form of the function to be no higher order than piecewise cubic polynomial. Writing this spline representation explicitly yields:

$$\begin{aligned} emm_{tr}(t) = \sum_{j=M_0}^{M_1} \left(\alpha_j + \beta_j t + \gamma_j t^2 + \delta_j t^3\right) \big(u(t - j\partial) \\ - u(t - (j+1)\partial)\big), \end{aligned} \tag{13}$$

where α_j, β_j, γ_j, and δ_j are the spline coefficients, M_0 and M_1 are the first and last spline indices, and $j\partial$ is the spline to spline interval. We now can complete an analytical expression for (2) by convolving (13) with the appropriate version of (7)–(12). Although such a convolution appears quite tedious, it can be readily performed using Laplace transforms [11]. The resulting expression is a sum of 3rd, 4th, 5th, 6th, or 7th order polynomials (multiplied by unit step functions), with the polynomial order depending upon the combination of element responses used. The analytical forms of these expressions are included in the Appendix, although for brevity's sake only one of the summands in each of (8) through (12) is presented. The final expressions can be obtained through superposition of the results from the other summands. Using these final polynomial expressions, the complete two-way response for a given transmit-receive element pair can be computed by simply summing polynomials.

III. Validation

The proposed algorithm was implemented in a C routine called as a mex file within Matlab (The MathWorks, Inc., Natick, MA). This approach allowed us to readily generate array geometries and visualize results within Matlab, while taking advantage of the increased computational efficiency of compiled C. All calculations were performed in IEEE standard double precision floating point arithmetic. All simulations were performed on an IBM x335 (IBM Corporation, Armonk, NY) with dual Intel Xeon 2.4 GHz processors (Intel, Inc., Santa Clara, CA) and 2 GB PC2100 SDRAM, running Matlab 7.2 under Red Hat Enterprise Linux 3 update 5 (Red Hat, Inc., Raleigh, NC).

The validity of the proposed algorithm was tested by comparing the two-way spatial response of a single two-dimensional (2-D) array element as predicted by DELFI, FIELD II using rectangular elements, and FIELD II using triangular elements with a "gold standard." The "gold standard" used here was the response from FIELD II using triangles, sampled at 10 GHz temporally [12]. Because FIELD II using triangular elements does not make a far-field assumption, it is a very accurate model for the true analytical response and is valid in the near-field. At a sampling rate of 10 GHz, the sharp transitions in the responses are well captured, and this method becomes a suitable "gold standard."

For all responses, the array element was modeled using a single 300×300 μm computational element. All responses also assumed a combined excitation and transmit/receive electromechanical impulse response equal to a 5.0 MHz sine multiplied by an 8-cycle Nuttall window [13]. This was achieved by windowing a sinusoid, then using the spline() command within Matlab. The system response was determined in polar coordinates over an angle of 0° to 90° (sampled at 0.45°) covering a range from 19.925 cm to 20.075 cm (sampled at 10 μm). This space is an arc of thickness 1.5 mm that exists in the plane perpendicular to the element face, passing through the element center and the center of one of the element edges. Responses were evaluated over this 2-D spatial region at a single instant in time (space-space) as well as along the 1-D spatial arc in the center of this region throughout time (space-time). Both space-space and space-time responses were evaluated over a range of temporal sampling frequencies from 20 MHz to 1 GHz. For DELFI, all points in the space-space response were computed at the time instant that centered the element response at 20 cm, and all points in the space-time response were computed by running the code repeatedly at different time points to generate a waveform at the temporal sampling frequency of interest. For both FIELD II codes, a complete response in range, azimuth, and time was computed, with the time that centered the sensitivity function at 20 cm selected for analysis in the space-space response.

Typical spatial sensitivity functions from DELFI and FIELD II using rectangular elements for the parameters given above are shown in Fig. 2. Both responses have been normalized to allow comparison. These responses are quite similar, except for a series of artifacts located about the 0° line in the FIELD II response. Although the source of this artifact is not apparent, it may result from the corrections FIELD II uses when sampling the infinite bandwidth spatial impulse responses of the array elements. Such artifacts are avoided in DELFI by evaluating a continuous time representation for the impulse response.

Simulations were performed over a range of temporal sampling frequencies from 20 MHz to 1 GHz to determine computation times and error in the responses as compared to the "gold standard." All computational times were estimated using the tic and toc commands in Matlab. The accuracy of each response was determined by computing the normalized sum squared error with respect to the "gold standard." To ensure proper alignment of the responses when measuring error, time delay estimation was performed using normalized sum squared error with splines [14].

Across the set of 12 space-space simulations, the normalized sum squared errors for DELFI ranged from approximately 1.44% to 0.14%, as shown in Fig. 3. Over the same set of conditions FIELD II errors ranged from 21.89% to 0.26% using rectangles and 21.05% to 2.02% using triangles. To achieve an error similar to that of DELFI sampled at 40 MHz, FIELD II using rectangles must be sampled at 800 MHz. Comparing computation times at these respective sampling rates, DELFI is about 142 times faster than FIELD II using rectangles. In the sampling range covered, FIELD II using triangles does not achieve an error similar to that of DELFI so such a comparison of computation times was not made. Note that these times do not include any array definitions or other housekeeping operations.

It may seem counterintuitive that FIELD II using triangles—an exact analytical solution that does not make use of a far-field approximation—should have errors as large as 21%. However, we must remember that these impulse responses have sharp transitions that must be ap-

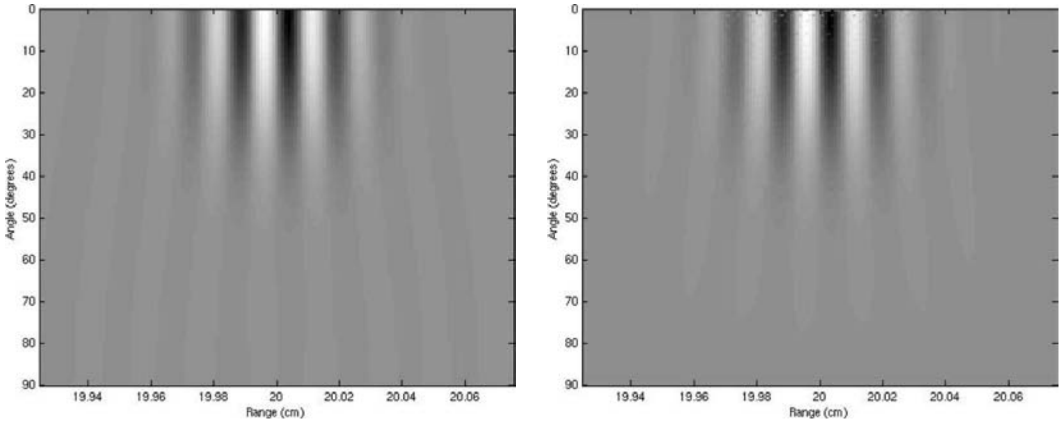

(a) (b)

Fig. 2. The spatial impulse response of a 300 μm square array element in a soft baffle for an 8 cycle Nuttall windowed 5.0 MHz transmit pulse. The left panel depicts the output of the proposed algorithm (DELFI). The right panel indicates the output of FIELD II using rectangles. Both responses have been normalized to allow easy comparison. The responses are nearly identical, with the exception of localized artifacts near the 0° line of the FIELD II response.

propriately sampled to avoid aliasing errors. The "gold-standard" is sampled temporally at 10 GHz, but here, we are considering sampling rates as low as 20 MHz, which result in large aliasing errors in the responses from FIELD II using triangles.

The default sampling rates for DELFI and FIELD II using rectangles are 40 MHz and 100 MHz, respectively. At these rates, these codes have an error of 0.16% and 1.6% and computation times of 0.1 and 5.8 seconds, respectively, for space-space simulations. So, operating at default sampling frequencies, DELFI is 58 times faster with 10 times less error than FIELD II using rectangles for space-space simulations.

For the sake of comparison, we also computed the temporal response using all three codes along the arc 20 cm from the element center, sweeping from 0° to 90° with respect to the line perpendicular to the element face and passing through its center. Across the set of 12 space-time simulations, the normalized sum squared errors for DELFI ranged from approximately 0.76% to 0.04%, as shown in Fig. 4. Over the same set of conditions, FIELD II errors ranged from 19.21% to 0.04% using rectangles and 19.18% to 0.05% using triangles. To achieve an error similar to that of DELFI sampled at 40 MHz, FIELD II using rectangles must be sampled at 400 MHz and FIELD II using triangles must be sampled at 300 MHz. Comparing computation times at these respective sampling rates, DELFI is about 1.7 times slower than FIELD II using rectangles and 19.4 times faster than FIELD II using triangles.

Again comparing DELFI and FIELD II using rectangles at their default rates, these codes have an error of 0.06% and 0.78% and computation times of 0.064 and 0.012 seconds, respectively, for space-time simulations. So, operating at default sampling frequencies, DELFI is 5.3 times slower with 13 times less error than FIELD II using rectangles for space-time simulations.

IV. Discussion

Validation of a simulation tool is not a simple task as not one method stands out as the best. As the simulation tool is designed to predict true system behavior, one might argue that comparison to experimental data would serve as the best metric. However, experimental data contains artifacts caused by many nonidealities such as element nonuniformity. Comparing simulation results to experimental data, thus, would produce errors specific to one system. A simulation tool, however, is used to predict general system behavior so such a comparison would not be useful for all readers.

Instead, we have decided to compare our simulation tool to one that is well established and makes few assumptions in computing the theoretical field from an ultrasound system. The only assumption made in FIELD II using triangles is that the element is a planar piston vibrating uniformly in an infinite rigid planar baffle into a homogeneous, nonattenuating medium. As a result, the only source of error, aside from those caused by nonidealities, is the temporal sampling frequency, as there are sharp transitions in the impulse response that must be sampled appropriately. As the purpose of a simulation tool is to help steer the decisions of ultrasound system designers by predicting general system behavior, it should be as accurate as possible without becoming too specific to any one system. Thus, FIELD II using triangles was chosen as the "gold standard" from which to determine DELFI's accuracy.

Computing the spatial impulse response of a transmit-receive element pair by convolving (13) with (7)–(12) analytically offers both advantages and disadvantages relative to the established approach using discrete time convolution. On the positive side, the analytical approach allows direct computation of the response at a single instant in time. In contrast, the conventional discrete time approach (at least as currently implemented) requires the computation of a full temporal response, even if only a single time

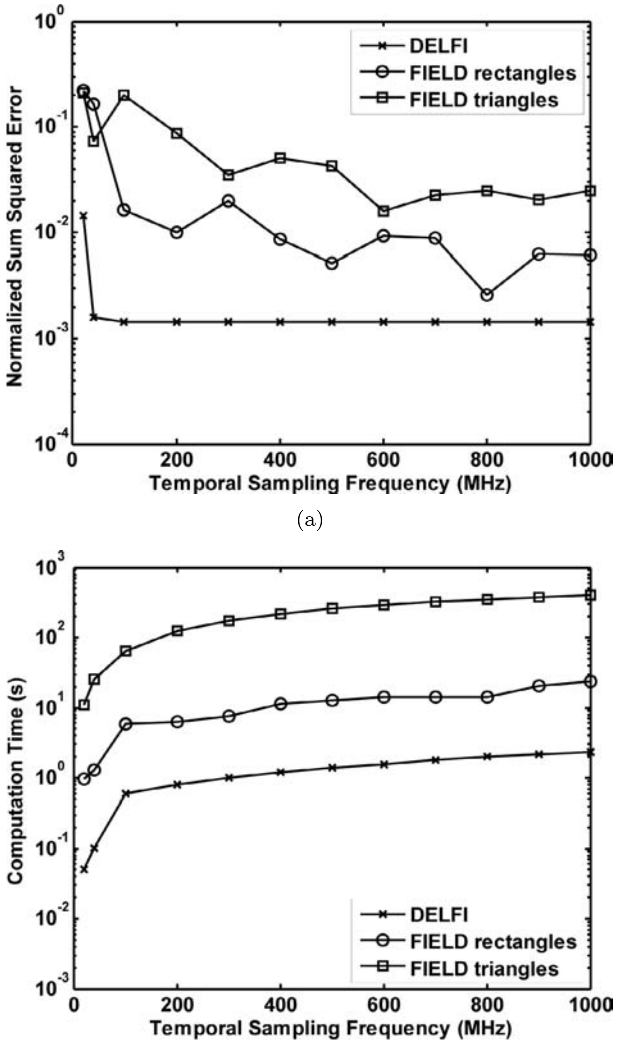

(a)

(b)

Fig. 3. Comparison of DELFI and FIELD II performance when computing space-space impulse responses over a range of temporal sampling frequencies. The top panel shows the normalized sum squared error with respect to FIELD II using triangles and sampled at 10 GHz. The bottom panel shows the computation time for each of the codes. To achieve an error similar to that of DELFI sampled at 40 MHz, FIELD II using rectangles must be sampled at 800 MHz. Comparing computation times at these respective sampling rates, DELFI is about 142 times faster than FIELD II using rectangles. In the sampling range covered, FIELD II using triangles does not achieve an error similar to that of DELFI.

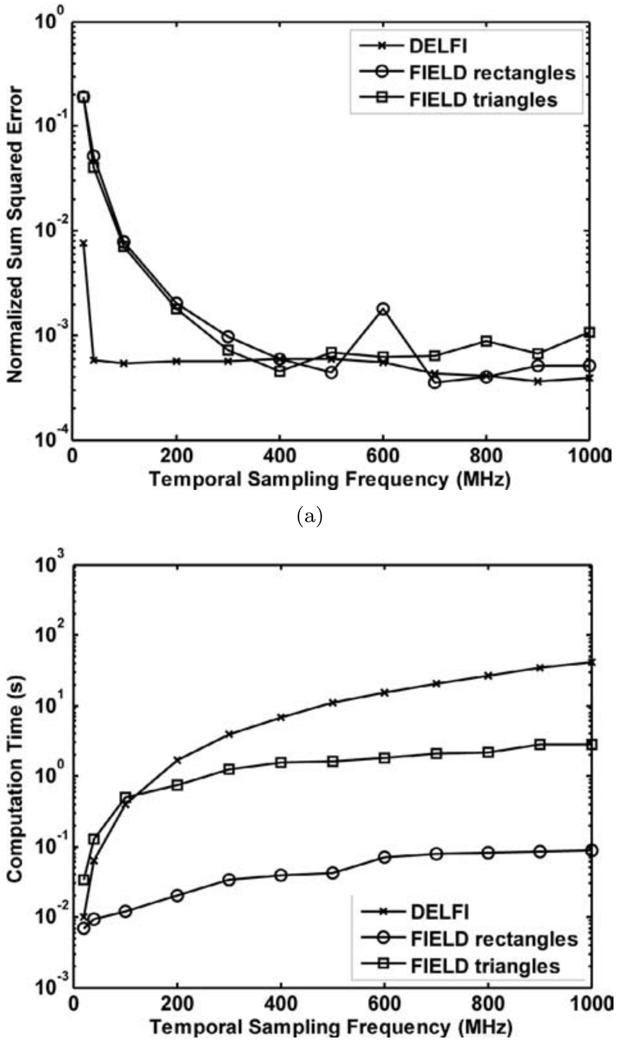

(a)

(b)

Fig. 4. Comparison of DELFI and FIELD II performance when computing space-time impulse responses over a range of temporal sampling frequencies. The top panel shows the normalized sum squared error with respect to FIELD II using triangles and sampled at 10 GHz. The bottom panel shows the computation time for each of the codes. To achieve an error similar to that of DELFI sampled at 40 MHz, FIELD II using rectangles must be sampled at 400 MHz and FIELD II using triangles must be sampled at 300 MHz. Comparing computation times at these respective sampling rates, DELFI is about 1.7 times slower than FIELD II using rectangles and 19.4 times faster than FIELD II using triangles.

point is required. An additional advantage of the analytical approach is that it yields an exact solution, at least within the numerical precision of the computer used for the calculation and within the limitations of the far-field approximation. In contrast, the discrete time approach uses under-sampled versions of the element responses and thus introduces some error. In addition, the discrete implementation makes it difficult to compute the spatial response at any exact instant in time. A relative weakness of the analytical approach is that more computation is required to determine a temporal response at a single location.

It should be noted that DELFI is, for the most part, independent of sampling frequency due to its use of an analytical solution. In Fig. 3, however, we see that the accuracy of DELFI begins to suffer at a sampling rate of 20 MHz. This artifact is due to inaccuracies in the splining of the transmitted pulse for lower sampling frequencies. Although this sampling rate meets the Nyquist criterion, the splined pulse has small errors due to it having too few spline knots. As a result, the accuracy of DELFI suffers for temporal sampling rates that are too close to the Nyquist rate.

The current DELFI code determines the result of the convolution of a single spline segment with two trapezoid functions by summing 16 7th order polynomials. This approach is computationally tedious and subject to numerical instability. Such instabilities occur only when summing the higher order polynomials evaluated at very small time differences. For example, instability occurs when the sides of the trapezoidal responses are very steep or the rectangular response is very narrow in time. To help reduce these instabilities, a minimum time difference parameter is passed into DELFI to determine how the response should be modeled. For example, if the temporal width of rectangle function is smaller than this minimum time parameter, the response will instead be modeled as a delta function. This would imply that the response would be modeled as a delta function not just along the line through the center of the element, perpendicular to its face, but in a small volume around that line as well. Increasing the minimum time parameter increases this spatial volume. The same spatial broadening occurs for the region in which the response would be modeled as a rectangle function. This approach effectively increases the error in the physical model in order to reduce the much greater numerical error.

An alternative method of implementation that would reduce both numerical instabilities and computation time is to use sums of triangles and rectangles instead of ramps and unit impulses. Using this approach, a trapezoid response would be modeled as two triangles and a rectangle, instead of as four ramp functions. This method will reduce the numerical instabilities in the code by summing polynomials of finite extent rather than those of infinite extent, as currently implemented. This change becomes especially significant with the highest order polynomials, as in (11) and (12), because they tend to saturate the dynamic range of double precision floating point numbers when they are of significant extent. Additionally, this method would provide computational savings by reducing the number of polynomials summed to form a response. The convolution of a single spline segment with two trapezoid functions would involve a summation of 9 seventh order polynomials rather than the 16 required in the current implementation. This approach could cut the computation time nearly in half, although some additional overhead would be required.

Another possible direction for improvement would begin with the recognition that the first half of this response (in time) requires only 8 polynomials for synthesis. Next, by considering the response in negative time, it is apparent that the second half of this response (again in time) also requires only 8 polynomials. Together this realization could cut computation time in half. Additional computational savings are undoubtedly possible.

Algorithmic accuracy could be enhanced by utilizing a more sophisticated model for the element impulse responses. Spline functions might prove particularly suitable for modeling complicated near-field responses [15], [16]. Alternatively, ramp functions or the triangle and rectangle functions described above could be used to form a linear approximation to the more complicated near-field responses. Because DELFI already makes use of ramp functions, such a change would not be major.

A version of DELFI that simulates one-way spatial responses, rather than two-way, also has been written. This version is less susceptible to numerical instabilities due to the use of lower order polynomials. At the time of publication, the source code for both one-way and two-way DELFI is available under a general public license on the Mathworks File Exchange (http://www.mathworks.com/matlabcentral/fileexchange) by searching for DELFI.

V. CONCLUSIONS

The DELFI code presented here uses analytical convolution of cubic spline functions with continuous time-element responses to compute the two-way spatial impulse response of ultrasound transducers. Comparison with FIELD II shows that the proposed algorithm performs comparably to existing methods. For the computation of impulse responses at a single instant in time, the proposed algorithm is about 142 times faster than FIELD II for similar error. For computing temporal responses, the proposed code is approximately 1.7 times slower than FIELD II for similar error, although further refinement may reduce this mismatch. When operating at the default sampling frequencies to generate space-space responses, DELFI is 58 times faster with 10 times less error than FIELD II. Generating space-time responses at the default sampling rates, DELFI is 5.3 times slower with 13 times less error than FIELD II. The proposed algorithm, as implemented by the DELFI code, offers an attractive complement to the well-established FIELD II program, especially when spatial responses are needed at a specific point in time.

APPENDIX A

The following equations are the analytical expressions resulting from the convolution of the two-way impulse responses (7)–(12) with the cubic spline polynomial (13). For the sake of brevity, the cubic spline polynomial is convolved with only one of the summands in (7)–(12). The final analytical expressions for the impulse responses can be obtained through superposition with the results from the other summands.

$$
\begin{aligned}
&emm_{tr}(t) \underset{t}{*} h_{0_a} \underset{t}{*} h_{0_b} = \\
&A_{0_a} A_{0_b} \sum_{j=M_0}^{M_1} \Big(\alpha_j + \beta_j \left(t - t_{0_a} - t_{0_b}\right) + \gamma_j \left(t - t_{0_a} - t_{0_b}\right)^2 \\
&\qquad + \delta_j \left(t - t_{0_a} - t_{0_b}\right)^3 \Big) \Big(u\left(t - t_{0_a} - t_{0_b} - j\partial\right) \\
&\qquad\qquad - u\left(t - t_{0_a} - t_{0_b} - (j+1)\partial\right) \Big) \qquad \text{(A1)}
\end{aligned}
$$

$$\begin{aligned}
&emm_{tr}(t) \underset{t}{*} h_0 \underset{t}{*} h_1 = \\
&\quad A_0 A_1 \sum_{j=M_0}^{M_1} \Bigg[\alpha_j\,(t-t_1) + \frac{1}{2}\beta_j\,(t-t_1)^2 \\
&\quad + \frac{1}{3}\gamma_j\,(t-t_1)^3 + \frac{1}{4}\delta_j\,(t-t_1)^4 \\
&\quad + j\partial\,(t-t_1)\Big(\beta_j + \gamma_j\,(j\partial + t - t_1) \\
&\quad + \delta_j\Big((j\partial)^2 + j\partial\,(t-t_1) + (t-t_1)^2\Big)\Big)\Bigg]u\,(t-t_1) \\
&- \Bigg[\alpha_j\,(t-t_2) + \frac{1}{2}\beta_j\,(t-t_2)^2 + \frac{1}{3}\gamma_j\,(t-t_2)^3 + \frac{1}{4}\delta_j\,(t-t_2)^4 \\
&\quad + (j+1)\partial\,(t-t_2)\Big(\beta_j + \gamma_j\,((j+1)\partial + t - t_2) \\
&\quad + \delta_j\Big(((j+1)\partial)^2 + (j+1)\partial\,(t-t_2) + (t-t_2)^2\Big)\Big)\Bigg] \\
&\quad \times u\,(t-t_2)
\end{aligned} \tag{A2}$$

where

$$\begin{aligned}
t_1 &= j\partial + t_0 + t_{10} \\
t_2 &= (j+1)\partial + t_0 + t_{10}
\end{aligned}$$

$$\begin{aligned}
&emm_{tr}(t) \underset{t}{*} h_0 \underset{t}{*} h_2 = \\
&\quad A_0 A_2 \sum_{j=M_0}^{M_1} \Bigg[\frac{1}{2}\alpha_j\,(t-t_1)^2 + \frac{1}{6}\beta_j\,(t-t_1)^3 \\
&\quad + \frac{1}{12}\gamma_j\,(t-t_1)^4 + \frac{1}{20}\delta_j\,(t-t_1)^5 \\
&\quad + j\partial\,(t-t_1)^2\left(\frac{1}{2}\beta_j + \gamma_j\left(\frac{j\partial}{2} + \frac{t-t_1}{3}\right)\right. \\
&\quad \left. + \delta_j\left(\frac{(j\partial)^2}{2} + \frac{j\partial\,(t-t_1)}{2} + \frac{(t-t_1)^2}{4}\right)\right)\Bigg]u\,(t-t_1) \\
&\quad - \Bigg[\frac{1}{2}\alpha_j\,(t-t_2)^2 + \frac{1}{6}\beta_j\,(t-t_2)^3 \\
&\quad + \frac{1}{12}\gamma_j\,(t-t_2)^4 + \frac{1}{20}\delta_j\,(t-t_2)^5 \\
&\quad + (j+1)\partial\,(t-t_2)^2\left(\frac{1}{2}\beta_j + \gamma_j\left(\frac{(j+1)\partial}{2} + \frac{t-t_2}{3}\right)\right. \\
&\quad \left. + \delta_j\left(\frac{((j+1)\partial)^2}{2} + \frac{(j+1)\partial\,(t-t_2)}{2} + \frac{(t-t_2)^2}{4}\right)\right)\Bigg] \\
&\quad \times u\,(t-t_2)
\end{aligned} \tag{A3}$$

where

$$\begin{aligned}
t_1 &= j\partial + t_0 + t_{10} \\
t_2 &= (j+1)\partial + t_0 + t_{10}
\end{aligned}$$

$$\begin{aligned}
&emm_{tr}(t) \underset{t}{*} h_{1_a} \underset{t}{*} h_{1_b} = \\
&\quad A_{1_a} A_{1_b} \Bigg[\frac{1}{2}\alpha_j\,(t-t_1)^2 + \frac{1}{6}\beta_j\,(t-t_1)^3 + \\
&\quad \frac{1}{12}\gamma_j\,(t-t_1)^4 + \frac{1}{20}\delta_j\,(t-t_1)^5 \\
&\quad + j\partial\,(t-t_1)^2\left(\frac{1}{2}\beta_j + \gamma_j\left(\frac{j\partial}{2} + \frac{t-t_1}{3}\right)\right. \\
&\quad \left. + \delta_j\left(\frac{(j\partial)^2}{2} + \frac{j\partial\,(t-t_1)}{2} + \frac{(t-t_1)^2}{4}\right)\right)\Bigg]u\,(t-t_1) \\
&\quad - \Bigg[\frac{1}{2}\alpha_j\,(t-t_2)^2 + \frac{1}{6}\beta_j\,(t-t_2)^3 \\
&\quad + \frac{1}{12}\gamma_j\,(t-t_2)^4 + \frac{1}{20}\delta_j\,(t-t_2)^5 \\
&\quad + (j+1)\partial\,(t-t_2)^2\left(\frac{1}{2}\beta_j + \gamma_j\left(\frac{(j+1)\partial}{2} + \frac{t-t_2}{3}\right)\right. \\
&\quad \left. + \delta_j\left(\frac{((j+1)\partial)^2}{2} + \frac{(j+1)\partial\,(t-t_2)}{2} + \frac{(t-t_2)^2}{4}\right)\right)\Bigg] \\
&\quad \times u\,(t-t_2)
\end{aligned} \tag{A4}$$

where

$$\begin{aligned}
t_1 &= j\partial + t_{1_a0} + t_{1_b0} \\
t_2 &= (j+1)\partial + t_{1_a0} + t_{1_b0}
\end{aligned}$$

$$\begin{aligned}
&emm_{tr}(t) \underset{t}{*} h_1 \underset{t}{*} h_2 = \\
&\quad A_1 A_2 \sum_{j=M_0}^{M_1} \Bigg[\frac{1}{3}\alpha_j\,(t-t_1)^3 + \frac{1}{12}\beta_j\,(t-t_1)^4 \\
&\quad + \frac{1}{30}\gamma_j\,(t-t_1)^5 + \frac{1}{60}\delta_j\,(t-t_1)^6 \\
&\quad + j\partial\,(t-t_1)^3\left(\frac{1}{3}\beta_j + \gamma_j\left(\frac{j\partial}{3} + \frac{t-t_1}{6}\right)\right. \\
&\quad \left. + \delta_j\left(\frac{(j\partial)^2}{3} + \frac{j\partial\,(t-t_1)}{4} + \frac{(t-t_1)^2}{10}\right)\right)\Bigg]u\,(t-t_1) \\
&\quad - \Bigg[\frac{1}{3}\alpha_j\,(t-t_2)^3 + \frac{1}{12}\beta_j\,(t-t_2)^4 \\
&\quad + \frac{1}{30}\gamma_j\,(t-t_2)^5 + \frac{1}{60}\delta_j\,(t-t_2)^6 \\
&\quad + (j+1)\partial\,(t-t_2)^3\left(\frac{1}{3}\beta_j + \gamma_j\left(\frac{(j+1)\partial}{3} + \frac{t-t_2}{6}\right)\right. \\
&\quad \left. + \delta_j\left(\frac{((j+1)\partial)^2}{3} + \frac{(j+1)\partial\,(t-t_2)}{4} + \frac{(t-t_2)^2}{10}\right)\right)\Bigg] \\
&\quad \times u\,(t-t_2)
\end{aligned} \tag{A5}$$

where

$$\begin{aligned}
t_1 &= j\partial + t_{10} + t_{20} \\
t_2 &= (j+1)\partial + t_{10} + t_{20}
\end{aligned}$$

$$
\begin{aligned}
&emm_{tr}(t) \underset{t}{*} h_{2_a} \underset{t}{*} h_{2_b} = \\
&\quad A_{2_a0}A_{2_b0} \sum_{j=M_0}^{M_1} \Bigg[\frac{1}{4}\alpha_j (t-t_1)^4 + \frac{1}{20}\beta_j (t-t_1)^5 \\
&\qquad + \frac{1}{60}\gamma_j (t-t_1)^6 + \frac{1}{140}\delta_j (t-t_1)^7 \\
&\qquad + j\partial (t-t_1)^4 \left(\frac{1}{4}\beta_j + \gamma_j \left(\frac{j\partial}{4} + \frac{t-t_1}{10} \right) \right. \\
&\quad \left. + \delta_j \left(\frac{(j\partial)^2}{4} + \frac{3j\partial (t-t_1)}{40} + \frac{(t-t_1)^2}{20} \right) \right) \Bigg] u(t-t_1) \\
&\qquad - \Bigg[\frac{1}{4}\alpha_j (t-t_2)^4 + \frac{1}{20}\beta_j (t-t_2)^5 \\
&\qquad + \frac{1}{60}\gamma_j (t-t_2)^6 + \frac{1}{140}\delta_j (t-t_2)^7 \\
&\quad + (j+1)\partial (t-t_2)^4 \left(\frac{1}{4}\beta_j + \gamma_j \left(\frac{(j+1)\partial}{4} + \frac{t-t_2}{10} \right) \right. \\
&\quad \left. + \delta_j \left(\frac{((j+1)\partial)^2}{4} + \frac{3(j+1)\partial (t-t_2)}{20} + \frac{(t-t_2)^2}{20} \right) \right) \Bigg] \\
&\qquad\qquad \times u(t-t_2) \qquad \text{(A6)}
\end{aligned}
$$

where

$$
\begin{aligned}
t_1 &= j\partial + t_{2_a0} + t_{2_b0} \\
t_2 &= (j+1)\partial + t_{2_a0} + t_{2_b0}
\end{aligned}
$$

The following equations are the analytical calculations used to determine the times for the corners of the impulse response. These times are computed as projections of the corners of the element onto the line passing through the center of the element and the field point. The resulting times must be sorted as they do not take into account which element corner is closest to the field point. The element is assumed to be a rectangle lying in the XY plane of a Cartesian coordinate system, with its center at the origin. Here, n_x is the x-coordinate of the distance from element center to field point (n_y and n_z are such distance for their respective coordinates); $w_{0,x}$ is the x-coordinate for the element center, $w_{1,x}$ is the x-coordinate for the first element corner, $w_{2,x}$ is the x-coordinate for the second element corner, etc.; and c_0 is the speed of sound in the medium.

$$
\begin{aligned}
&t_1 = \\
&t_0 + \frac{n_x (w_{1,x} - w_{0,x}) + n_y (w_{1,y} - w_{0,y}) + n_z (w_{1,z} - w_{0,z})}{\sqrt{n_x^2 + n_y^2 + n_z^2} * c_0} \\
&t_2 = \\
&t_0 + \frac{n_x (w_{2,x} - w_{0,x}) + n_y (w_{2,y} - w_{0,y}) + n_z (w_{2,z} - w_{0,z})}{\sqrt{n_x^2 + n_y^2 + n_z^2} * c_0} \\
&t_3 = \\
&t_0 + \frac{n_x (w_{3,x} - w_{0,x}) + n_y (w_{3,y} - w_{0,y}) + n_z (w_{3,z} - w_{0,z})}{\sqrt{n_x^2 + n_y^2 + n_z^2} * c_0} \\
&t_4 = \\
&t_0 + \frac{n_x (w_{4,x} - w_{0,x}) + n_y (w_{4,y} - w_{0,y}) + n_z (w_{4,z} - w_{0,z})}{\sqrt{n_x^2 + n_y^2 + n_z^2} * c_0} \\
&\hspace{20em} \text{(A7)}
\end{aligned}
$$

where

$$
t_0 = \frac{\sqrt{n_x^2 + n_y^2 + n_z^2}}{c_0}.
$$

ACKNOWLEDGMENTS

The authors would like to thank Karthik Ranganathan for his valuable feedback on this manuscript. The authors also would like to thank IBM Shared University Research Program for their technical resources and support.

REFERENCES

[1] J. W. Goodman, *Introduction to Fourier Optics*. San Francisco: McGraw-Hill, 1986.

[2] G. L. Wojcik, D. K. Vaughan, N. Abboud, and J. Mould, "Electromechanical modeling using explicit time-domain finite elements," presented at *Proc. IEEE Ultrason. Symp.*, Baltimore, MD, 1993.

[3] R. Barkman, W. Timm, S. Sakata, M. Heller, and C. C. Gluer, "Simulation of ultrasound interaction with bone structure based on 3D high-resolution-magnetic-resonance- and micro-CT-images," presented at Engineering in Medicine and Biology Society, 22nd Annual International Conference of the IEEE, Chicago, IL, 2000.

[4] P. R. Stepanishen, "Transient radiation from pistons in an infinite baffle," *J. Acoust. Soc. Amer.*, vol. 49, pp. 1629–1638, 1970.

[5] J. A. Jensen and N. B. Svendsen, "Calculation of pressure fields from arbitrarily shaped, apodized, and excited ultrasound transducers," *IEEE Trans. Ultrason., Ferroelect., Freq. Contr.*, vol. 39, pp. 262–267, 1992.

[6] R. J. Zemp, C. K. Abbey, and M. F. Insana, "Linear system models for ultrasonic imaging: Application to signal statistics," *IEEE Trans. Ultrason., Ferroelect., Freq. Contr.*, vol. 50, pp. 642–654, 2003.

[7] W. F. Walker, "The significance of correlation in ultrasound signal processing," presented at SPIE International Symposium on Medical Imaging, San Diego, CA, 2001.

[8] D. A. Guenther, K. Ranganathan, M. J. McAllister, W. F. Walker, and K. W. Rigby, "Ultrasonic synthetic aperture angular scatter imaging," in *Conf. Rec. Thirty-Eighth Asilomar Conf. Signals, Syst., Comput.*, 2004, pp. 163–167.

[9] A. R. Selfridge, G. S. Kino, and B. T. Khuri-Yahub, "A theory for the radiation pattern of a narrow strip acoustic transducer," *Appl. Phys. Lett.*, vol. 37, pp. 35–36, 1980.

[10] C. de Boor, *A Practical Guide to Splines*. Berlin: Springer-Verlag, 1978.

[11] S. Haykin and B. Van Veen, *Signals and Systems*. 2nd ed. New York: Wiley, 2003.

[12] J. A. Jensen, "Ultrasound fields from triangular apertures," *J. Acoust. Soc. Amer.*, vol. 100, pp. 2049–2056, 1996.

[13] A. H. Nuttall, "Some windows with very good sidelobe behavior," *IEEE Trans. Acoust. Speech Signal Processing*, vol. ASSP-29, pp. 84–91, 1981.

[14] F. Viola and W. F. Walker, "A spline-based algorithm for continuous time-delay estimation using sampled data," *IEEE Trans. Ultrason., Ferroelect., Freq. Contr.*, vol. 52, pp. 80–93, 2005.

[15] J. A. Hossack and G. Hayward, "Efficient calculation of the acoustic radiation from transiently excited uniform and apodised rectangular apertures," *Proc. IEEE Ultrason. Symp.*, 1993, pp. 1071–1075.

[16] J. A. Jensen, "A new calculation procedure for spatial impulse responses in ultrasound," *J. Acoust. Soc. Amer.*, vol. 105, pp. 3266–3274, 1999.

Michael Ellis received his B.S. degree in electrical engineering in 2004 from Bucknell University, Lewisburg, PA. After completing his B.S. degree, he joined the Department of Biomedical Engineering at the University of Virginia, Charlottesville, VA, where he is currently pursuing his Ph.D. degree.

His research interests include ultrasound beamforming, signal processing, and adaptive algorithms.

Drake Guenther received his B.S.E. degree in biomedical engineering in 2003 from Duke University, Durham, NC. His undergraduate research as a Pratt Fellow explored adaptive beamforming and spatial compounding in ultrasound. After completing his B.S.E. degree, he joined the Department of Biomedical Engineering at the University of Virginia, Charlottesville, VA, where he is currently pursuing his Ph.D. degree.

His research interests include ultrasound beamforming, signal processing, and angular scatter imaging.

William F. Walker (S'95-M'96) received the B.S.E. and Ph.D. degrees in 1990 and 1995 from Duke University, Durham, NC. His dissertation explored fundamental limits on the accuracy of adaptive ultrasound imaging.

After completing his doctoral work, he stayed at Duke as an assistant research professor in the Department of Biomedical Engineering. At the same time, he served as a Senior Scientist and President of NovaSon Corporation located in Durham, NC. In 1997 he joined the faculty of the Department of Biomedical Engineering at the University of Virginia, Charlottesville, VA, being promoted to associate professor in 2003. He is an active founder in two ultrasound-based startup companies, PocketSonics Inc., Charlottesville, VA, and HemoSonics LLC, Charlottesville, VA.

His research interests include aperture domain processing, beamforming, angular scatter imaging, tissue elasticity imaging, low-cost system architectures, and time delay and motion estimation.

Cystic Resolution: A Performance Metric for Ultrasound Imaging Systems

Karthik Ranganathan and William F. Walker

***Abstract*—This paper describes a metric that can be used to characterize the resolution of arbitrary broadband coherent imaging systems. The metric is particularly suited to medical ultrasound because it characterizes scanner performance using the contrast obtained by imaging anechoic cysts of various sizes that are embedded in a speckle-generating background, accounting for the effect of electronic noise. We present the theoretical derivation of the metric and provide simulation examples that demonstrate its utility. We use the metric to compare a low-cost, handheld, C-scan system under development in our laboratory to conventional ultrasound scanners. We also present the results of simulations that were designed to evaluate and optimize various parameters in our system, including the f/# and apodization windows. We investigate the impact of electronic noise on our system and quantify the tradeoffs associated with quantization in the analog to digital converter. Results indicate that an f/1 receive aperture combined with 10-bit precision and a signal-to-noise ratio (SNR) of 0 dB per channel would result in adequate image quality.**

I. Introduction

The evaluation of imaging performance is an essential task in the development of ultrasound systems, both to predict fundamental limits on quality and to optimize parameters for system design. It is possible to estimate the performance of existing systems by imaging phantoms or human subjects, but, during system design, it is necessary to be able to determine the imaging performance of a proposed system prior to construction. The ability to accurately predict performance enables system optimization and quantitative consideration of engineering tradeoffs early in the design process and significantly reduces the time and cost investment in system development. To support these goals, this paper develops a general resolution metric for comparing arbitrary imaging systems.

The most common metric used to estimate scanner performance is the beamplot, which has been adapted from radar. System resolution is usually described using a combination of the full width at half maximum (FWHM) or −6 dB beamwidth of the beamplot and the beamwidth at other levels [1]. Sidelobe and grating lobe levels are used to estimate eventual image contrast. Although widely used, there are disadvantages to using the beamplot to estimate the performance of ultrasound systems. Targets in medical ultrasound are usually weakly reflecting tissues in a scattering medium, unlike radar targets that are more often highly reflective and in a non-scattering background. Therefore, there may be scenarios in which the FWHM criterion indicates excellent performance, but actual images of tissue do not reveal important details. Vilkomerson *et al.* [2] demonstrated that the FWHM criterion sometimes provides misleading information about resolution in ultrasound systems. It is, in addition, difficult to be certain about the best levels at which to characterize and optimize the beamplot. In other words, it is difficult to decide whether to optimize the mainlobe width or sidelobe and grating lobe levels for an overall increase in image quality. As mentioned above, performance may be determined by imaging phantoms, such as in [3]. In [3], the authors describe the use of a phantom containing spherical lesions of varying sizes and contrasts to compare six automated lesion-detection algorithms and human observer studies. Imaging phantoms, however, does not provide a way to theoretically assess the performance of different hypothetical imaging systems. Although repeated image simulations can be performed to assess a wide variety of system parameters, including resolution, this approach is very computationally challenging. We need a metric that ties together resolution and contrast in a way that is relevant to diagnostic ultrasound imaging.

Vilkomerson *et al.* [2] addressed the limitations of the beamplot and proposed the concept of "cystic resolution," in which performance was quantified as the size of a void that produced a given contrast. The analysis, although novel and useful, was limited to narrowband circular apertures and neglected the axial dimension. Üstüner and Holley [4] extended cystic resolution to a three-dimensional (3-D) broadband model that addressed the above problems but did not describe its theoretical foundation or publish the model in an archival journal. The lack of a theoretical background in [4] obscures important details, resulting in a limited understanding of the formulation and its utility and drawbacks. We derive a metric identical to that in [4], extend it to include the effects of electronic noise, and present simulation results that demonstrate its utility.

II. Theory

Our goal is to derive a metric to quantify the contrast resolution of an arbitrary broadband ultrasound system. Let the point spread function (psf) of the ultrasound sys-

Manuscript received April 20, 2005; accepted October 25, 2006. This work was supported by NIH grant EB002349 and by award DAMD17-01-1-0443 from the U. S. Army Congressionally Directed Medical Research Program.

The authors are with the University of Virginia, Charlottesville, VA 22908 (e-mail: kranganathan@pocketsonics.com).

Digital Object Identifier 10.1109/TUFFC.2007.311

0885–3010/$25.00 © 2007 IEEE

tem be defined as $P(\vec{x},t)$, a function of 3-D space ($\vec{x}$) and time (t). Time in this expression is included for the propagation of the sensitivity function through tissue, and thus typically begins at transmission and ends at the completion of a single echo line. The medium scattering function is modeled as a stochastic process $N(\vec{x})$, undergoing negligible tissue motion during reception of an individual echo line and, therefore, being constant with time. We assume that the effect of electronic noise during transmit is negligible due to the high signal-to-noise ratio (SNR) on transmit, and model the electronic noise on receive as another stochastic process $E(t)$. Combining these factors, and assuming that the electronic noise is purely additive, the received signal as a function of time is:

$$S_b(t) = \int_{-\infty}^{\infty} P(\vec{x},t)N(\vec{x})d\vec{x} + E(t). \tag{1}$$

Consider the mean squared received signal $\left\langle S_b^2(t)\right\rangle$ where $\langle\rangle$ is the expected value operator:

$$\begin{aligned}\left\langle S_b^2(t)\right\rangle = &\left\langle \left[\int_{-\infty}^{\infty} P(\vec{x}_1,t)N(\vec{x}_1)d\vec{x}_1 + E(t)\right]\right.\\ &\left.\times \left[\int_{-\infty}^{\infty} P(\vec{x}_2,t)N(\vec{x}_2)d\vec{x}_2 + E(t)\right]\right\rangle,\end{aligned} \tag{2}$$

$$\begin{aligned}\left\langle S_b^2(t)\right\rangle = &\left\langle \int_{-\infty}^{\infty}\int_{-\infty}^{\infty} P(\vec{x}_1,t)P(\vec{x}_2,t)N(\vec{x}_1)N(\vec{x}_2)d\vec{x}_1 d\vec{x}_2\right\rangle\\ &+\left\langle \int_{-\infty}^{\infty}\int_{-\infty}^{\infty} P(\vec{x}_1,t)N(\vec{x}_1)E(t)d\vec{x}_1\right\rangle\\ &+\left\langle \int_{-\infty}^{\infty}\int_{-\infty}^{\infty} P(\vec{x}_2,t)N(\vec{x}_2)E(t)d\vec{x}_2\right\rangle + \left\langle E^2(t)\right\rangle.\end{aligned} \tag{3}$$

Rearranging the expected value operator to account for the fact that the scattering function and electronic noise are stochastic while the psf is deterministic yields:

$$\begin{aligned}\left\langle S_b^2(t)\right\rangle = &\int_{-\infty}^{\infty}\int_{-\infty}^{\infty} P(\vec{x}_1,t)P(\vec{x}_2,t)\left\langle N(\vec{x}_1)N(\vec{x}_2)\right\rangle d\vec{x}_1 d\vec{x}_2\\ &+\int_{-\infty}^{\infty}\int_{-\infty}^{\infty} P(\vec{x}_1,t)\left\langle N(\vec{x}_1)E(t)\right\rangle d\vec{x}_1\\ &+\int_{-\infty}^{\infty}\int_{-\infty}^{\infty} P(\vec{x}_2,t)\left\langle N(\vec{x}_2)E(t)\right\rangle d\vec{x}_2 + \left\langle E^2(t)\right\rangle.\end{aligned} \tag{4}$$

We assume that the electronic noise $E(t)$ and the scattering function $N(\vec{x})$ are uncorrelated and obtain:

$$\begin{aligned}&\left\langle S_b^2(t)\right\rangle =\\ &\int_{-\infty}^{\infty}\int_{-\infty}^{\infty} P(\vec{x}_1,t)P(\vec{x}_2,t)\left\langle N(\vec{x}_1)N(\vec{x}_2)\right\rangle d\vec{x}_1 d\vec{x}_2 + \left\langle E^2(t)\right\rangle.\end{aligned} \tag{5}$$

This expression can be simplified further by assuming that the target scattering function is a stationary, white noise process whose autocorrelation is a delta function. Applying this assumption yields:

$$\begin{aligned}&\left\langle S_b^2(t)\right\rangle =\\ &\int_{-\infty}^{\infty}\int_{-\infty}^{\infty} P(\vec{x}_1,t)P(\vec{x}_2,t)a\delta(\vec{x}_1-\vec{x}_2,t)d\vec{x}_1 d\vec{x}_2 + \left\langle E^2(t)\right\rangle,\end{aligned} \tag{6}$$

where a is a scaling factor. Performing the outermost integral in the first term yields:

$$\left\langle S_b^2(t)\right\rangle = a\int_{-\infty}^{\infty} P^2(\vec{x},t)d\vec{x} + \left\langle E^2(t)\right\rangle. \tag{7}$$

The mean squared received signal is, therefore, a function of only the 3-D psf and the electronic noise. We can now describe a mask that defines the location and size of a spherical anechoic void (cyst):

$$\begin{aligned}M(\vec{x}) &= 0,\ |\vec{x}| \le R,\\ &= 1,\ |\vec{x}| > R,\end{aligned} \tag{8}$$

where R is the radius of the cyst, and the cyst center is at the origin of the coordinate system. $M(\vec{x})$ is also independent of time because we assume no tissue motion during the acquisition.

The scattering medium with the void is represented as $N(\vec{x})M(\vec{x})$. The received signal energy is expected to be at a minimum when the beam axis coincides with the center of the void, and as much of the psf energy as possible lies in the region defined by the void. The received signal in this circumstance then can be written as:

$$S_c(t) = \int_{-\infty}^{\infty} P(\vec{x},t)N(\vec{x})M(\vec{x})d\vec{x} + E(t). \tag{9}$$

The mean squared received signal $\left\langle S_c^2(t)\right\rangle$ is given in (10) and (11) (see next page).

Since the psf and the mask are deterministic we can rearrange the expected value operator and obtain (12) (see next page).

Once again, assuming $N(\vec{x})$ is a stationary, white noise process and uncorrelated to $E(t)$, we get:

$$\begin{aligned}\left\langle S_c^2(t)\right\rangle = &\int_{-\infty}^{\infty}\int_{-\infty}^{\infty} P(\vec{x}_1,t)P(\vec{x}_2,t)M(\vec{x}_1)M(\vec{x}_2)\\ &\times a\delta(\vec{x}_1-\vec{x}_2,t)d\vec{x}_1 d\vec{x}_2 + \left\langle E^2(t)\right\rangle,\end{aligned} \tag{13}$$

$$\left\langle S_c^2(t)\right\rangle = a\int_{-\infty}^{\infty} P^2(\vec{x},t)M^2(\vec{x})d\vec{x} + \left\langle E^2(t)\right\rangle. \tag{14}$$

We define the contrast between the brightness at the center of the cyst and the brightness of the background region as:

$$\left\langle S_c^2(t)\right\rangle = \left\langle \left[\int_{-\infty}^{\infty} P(\vec{x}_1,t)N(\vec{x}_1)M(\vec{x}_1)d\vec{x}_1 + E(t)\right]\left[\int_{-\infty}^{\infty} P(\vec{x}_2,t)N(\vec{x}_2)M(\vec{x}_2)d\vec{x}_2 + E(t)\right]\right\rangle, \tag{10}$$

$$\begin{aligned}\left\langle S_c^2(t)\right\rangle = &\left\langle \int_{-\infty}^{\infty}\int_{-\infty}^{\infty} P(\vec{x}_1,t)P(\vec{x}_2,t)N(\vec{x}_1)N(\vec{x}_2)M(\vec{x}_1)M(\vec{x}_2)d\vec{x}_1 d\vec{x}_2\right\rangle \\ &+\left\langle \int_{-\infty}^{\infty}\int_{-\infty}^{\infty} P(\vec{x}_1,t)N(\vec{x}_1)M(\vec{x}_1)E(t)d\vec{x}_1\right\rangle \\ &+\left\langle \int_{-\infty}^{\infty}\int_{-\infty}^{\infty} P(\vec{x}_2,t)N(\vec{x}_2)M(\vec{x}_2)E(t)d\vec{x}_2\right\rangle + \left\langle E^2(t)\right\rangle .\end{aligned} \tag{11}$$

$$\begin{aligned}\left\langle S_c^2(t)\right\rangle = &\int_{-\infty}^{\infty}\int_{-\infty}^{\infty} P(\vec{x}_1,t)P(\vec{x}_2,t)M(\vec{x}_1)M(\vec{x}_2)\left\langle N(\vec{x}_1)N(\vec{x}_2)\right\rangle d\vec{x}_1 d\vec{x}_2 \\ &+\int_{-\infty}^{\infty}\int_{-\infty}^{\infty} P(\vec{x}_1,t)M(\vec{x}_1)\left\langle N(\vec{x}_1)E(t)\right\rangle d\vec{x}_1 \\ &+\int_{-\infty}^{\infty}\int_{-\infty}^{\infty} P(\vec{x}_2,t)M(\vec{x}_2)\left\langle N(\vec{x}_2)E(t)\right\rangle d\vec{x}_2 + \left\langle E^2(t)\right\rangle .\end{aligned} \tag{12}$$

$$\begin{aligned}C(t) &= \sqrt{\frac{\langle S_c^2(t)\rangle}{\langle S_b^2(t)\rangle}} \\ &= \sqrt{\frac{a\int_{-\infty}^{\infty} P^2(\vec{x},t)M^2(\vec{x})d\vec{x} + \langle E^2(t)\rangle}{a\int_{-\infty}^{\infty} P^2(\vec{x},t)d\vec{x} + \langle E^2(t)\rangle}}.\end{aligned} \tag{15}$$

We define the electronic SNR as a function of time:

$$\mathrm{SNR}(t) = \frac{\sigma_{\mathrm{signal}}(t)}{\sigma_{\mathrm{noise}}(t)}, \tag{16}$$

where $\sigma_{\mathrm{signal}}(t)$ and $\sigma_{\mathrm{noise}}(t)$ are the standard deviations of the signal and noise components, respectively. Note that we define the standard deviations over an ensemble of signal and noise realizations and not in time. $\sigma_{\mathrm{signal}}(t)$ can be expressed as:

$$\begin{aligned}&\sigma_{\mathrm{signal}}(t) \\ &= \sqrt{\left\langle \int_{-\infty}^{\infty} P(\vec{x}_1,t)N(\vec{x}_1)d\vec{x}_1 \int_{-\infty}^{\infty} P(\vec{x}_2,t)N(\vec{x}_2)d\vec{x}_2\right\rangle},\end{aligned} \tag{17}$$

$$\sigma_{\mathrm{signal}}(t) = \sqrt{a\int_{-\infty}^{\infty} P^2(\vec{x},t)d\vec{x}}. \tag{18}$$

$\sigma_{\mathrm{noise}}(t)$ can be expressed as:

$$\sigma_{\mathrm{noise}}(t) = \sqrt{\langle E^2(t)\rangle}. \tag{19}$$

Applying (18) and (19) to (16) yields:

$$\mathrm{SNR}(t) = \frac{\sigma_{\mathrm{signal}}(t)}{\sigma_{\mathrm{noise}}(t)} = \sqrt{\frac{a\int_{-\infty}^{\infty} P^2(\vec{x},t)d\vec{x}}{\langle E^2(t)\rangle}}, \tag{20}$$

or equivalently:

$$\left\langle E^2(t)\right\rangle = \frac{a\int_{-\infty}^{\infty} P^2(\vec{x},t)d\vec{x}}{\mathrm{SNR}^2(t)}. \tag{21}$$

Applying (21), (15) now can be modified to yield:

$$C(t) = \sqrt{\frac{a\int_{-\infty}^{\infty} P^2(\vec{x},t)M^2(\vec{x})d\vec{x} + \frac{a\int_{-\infty}^{\infty} P^2(\vec{x},t)d\vec{x}}{\mathrm{SNR}^2(t)}}{a\int_{-\infty}^{\infty} P^2(\vec{x},t)d\vec{x} + \frac{a\int_{-\infty}^{\infty} P^2(\vec{x},t)d\vec{x}}{\mathrm{SNR}^2(t)}}}. \tag{22}$$

We can simplify the expression in (22) as follows:

$$C(t) = \sqrt{\frac{\mathrm{SNR}^2(t) \int\limits_{-\infty}^{\infty} P^2(\vec{x},t)M^2(\vec{x})d\vec{x} + \int\limits_{-\infty}^{\infty} P^2(\vec{x},t)d\vec{x}}{\mathrm{SNR}^2(t) \int\limits_{-\infty}^{\infty} P^2(\vec{x},t)d\vec{x} + \int\limits_{-\infty}^{\infty} P^2(\vec{x},t)d\vec{x}}} \tag{23}$$

$$= \sqrt{\frac{1+\mathrm{SNR}^2(t)\frac{\int_{-\infty}^{\infty} P^2(\vec{x},t)M^2(\vec{x})d\vec{x}}{\int_{-\infty}^{\infty} P^2(\vec{x},t)dx}}{1+\mathrm{SNR}^2(t)}} \tag{24}$$

$$= \sqrt{\frac{1+\mathrm{SNR}^2(t)\frac{E^{\mathrm{out}}(t)}{E^{\mathrm{tot}}(t)}}{1+\mathrm{SNR}^2(t)}}, \tag{25}$$

where $E^{\mathrm{out}}(t)$ is the psf energy outside the void as a function of time:

$$E^{\mathrm{out}}(t) = \int\limits_{-\infty}^{\infty} P^2(\vec{x},t)M^2(\vec{x})d\vec{x}, \tag{26}$$

and $E^{\mathrm{out}}(t)$ is the total psf energy as a function of time:

$$E^{\mathrm{tot}}(t) = \int\limits_{-\infty}^{\infty} P^2(\vec{x},t)d\vec{x}. \tag{27}$$

Eq. (24) and (25) describe the contrast relative to background speckle obtained by an imaging system with the psf $P(\vec{x},t)$ and electronic SNR defined statistically by $\mathrm{SNR}(t)$ when imaging an anechoic cyst whose size and location are described by the mask $M(\vec{x})$. Eq. (25) can alternatively be expressed as a function of the psf energy within the cyst $E^{\mathrm{in}}(t)$, given by:

$$E^{\mathrm{in}}(t) = E^{\mathrm{tot}}(t) - E^{\mathrm{out}}(t). \tag{28}$$

Modifying (25):

$$C(t) = \sqrt{\frac{1+\mathrm{SNR}^2(t)\left(1-\frac{E^{\mathrm{tot}}(t)-E^{\mathrm{out}}(t)}{E^{\mathrm{tot}}(t)}\right)}{1+\mathrm{SNR}^2(t)}}. \tag{29}$$

Substituting (28) in (29) yields:

$$C(t) = \sqrt{\frac{1+\mathrm{SNR}^2(t)\left(1-\frac{E^{\mathrm{in}}(t)}{E^{\mathrm{tot}}(t)}\right)}{1+\mathrm{SNR}^2(t)}}. \tag{30}$$

Note that if the cyst is large enough so that the entire psf energy is contained within it, the contrast depends solely on the electronic noise. Although (24), (25), and (30) can individually completely characterize system performance for a given cyst, analysis at the instant in time when the received signal is minimum (i.e., when as much of the psf energy as possible lies within the cyst) is usually sufficient. At this single instant in time t_o, we can express the psf as a function of only 3-D space at the time of interest $P_{t_o}(\vec{x})$, and the SNR at the time of interest SNR_{t_o}. Modifying (24), the contrast at time t_o is:

$$C_{t_o} = \sqrt{\frac{1+\mathrm{SNR}^2_{t_o}\frac{\int_{-\infty}^{\infty} P^2_{t_o}(\vec{x})M^2(\vec{x})d\vec{x}}{\int_{-\infty}^{\infty} P^2_{t_o}(\vec{x})d\vec{x}}}{1+\mathrm{SNR}^2_{t_o}}} \tag{31}$$

$$= \sqrt{\frac{1+\mathrm{SNR}^2_{t_o}\frac{E^{\mathrm{out}}_{t_o}}{E^{\mathrm{tot}}_{t_o}}}{1+\mathrm{SNR}^2_{t_o}}}, \tag{32}$$

where $E^{\mathrm{out}}_{t_o}$ is the psf energy outside the cyst and $E^{\mathrm{tot}}_{t_o}$ is the total psf energy, both at time t_o. Eq. (32) also can be modified to express the contrast as a function of the psf energy within the cyst at time t_o, $E^{\mathrm{in}}_{t_o}$:

$$C_{t_o} = \sqrt{\frac{1+\mathrm{SNR}^2_{t_o}\left(1-\frac{E^{\mathrm{in}}_{t_o}}{E^{\mathrm{tot}}_{t_o}}\right)}{1+\mathrm{SNR}^2_{t_o}}}. \tag{33}$$

If we neglect electronic noise, SNR_{t_o} becomes infinite and (31) can be modified to the equation for contrast presented in [4]:

$$C_{t_o} = \sqrt{\frac{\int\limits_{-\infty}^{\infty} P^2_{t_o}(\vec{x})M^2(\vec{x})d\vec{x}}{\int\limits_{-\infty}^{\infty} P^2_{t_o}(\vec{x})d\vec{x}}} \tag{34}$$

$$= \sqrt{\frac{E^{\mathrm{out}}_{t_o}}{E^{\mathrm{tot}}_{t_o}}} = \sqrt{1-\frac{E^{\mathrm{in}}_{t_o}}{E^{\mathrm{tot}}_{t_o}}}.$$

We can compute the contrast for cysts of different sizes using one of the above expressions for cystic contrast, and characterize system performance as a function of cyst size as in [2] and [4]. This metric can be used for 4-D spatiotemporal analysis of arbitrary broadband ultrasound systems. But 3-D spatial analysis using (31) or (34) is adequate to characterize scanner performance as temporal analysis does not provide critical information. Note that, in certain cases, it is valuable to compute the metric at different cyst locations to quantify depth of field, the effect of dynamic focusing, and other factors pertaining to the shift variance of the imaging system. Note also that, although (24), (31), and (34) can be used to determine the cystic resolution of a system, we also can optimize system parameters by computing contrast as a function of cyst size and determining parameter values that maximize the contrast at the cyst sizes of interest.

III. Methods

The derived metric is useful in guiding the design and optimization of ultrasound systems. We highlight these

TABLE I
List of Default Parameters Used to Simulate Our C-Scan System.

2-D array layout	32 × 32
Pitch	635 μm (1.4λ)
Receive focus	1 cm
Receive f/#	1
Receive apodization	Nuttall window
Transmit pulse center frequency	3.3 MHz
Transmit pulse length	3 cycles weighted by a Nuttall window
Spatial window over which psf was computed	Cylindrical volume with radius 2.4 cm and height 1 cm
Spatial sampling	60 μm radially, 1 degree in angle, and 60 μm in range

applications through a series of examples drawn from our ongoing efforts to develop a low-cost, handheld, C-scan ultrasound system for use in routine procedures such as image guided needle/IV line insertion and emergency room/battlefield triage. Our system uses a fully sampled 2-D array [5] interfaced to a custom integrated circuit with transmit protection, analog conditioning, and sampling and digitizing circuitry [6]. Beamforming is implemented by complex phase rotation of in-phase/quadrature (I/Q) data that are generated by directly sampling the received RF signal [7]. Our beamforming strategy, direct sampled I/Q (DSIQ) beamforming, results in poorer image quality than might be obtained using time delays; however, the use of a fully sampled 2-D array enables dynamic focusing in elevation, which may outweigh the performance loss incurred by using DSIQ beamforming. In order to investigate such tradeoffs, we compared our current first-generation prototype system to a conventional system with a 1-D array that focused in azimuth using time delays and in elevation with a lens. The conventional system had a 128-element 1-D array with a pitch of 135 μm, which corresponds to 0.3λ, where λ is the wavelength and is 466 μm. Default parameters for our prototype system are listed in Table I. Note that the default parameters were used in all simulations unless other parameter values are specifically mentioned. Our system does not have the ability to focus or apodize on transmit, so we focused and apodized only on receive in both sets of simulations (we used all elements to transmit an unfocused plane wave). Receive apodization was implemented with 1-D and 2-D Nuttall windows [8].

We simulated our system using DELFI, a custom ultrasound simulation package developed in our laboratory. DELFI is a simulation tool for computing the two-way far-field response from rectangular transducer elements under arbitrary excitation. It uses an analytical approach to approximate the spatial impulse response of the system under consideration as the sum of polynomial functions. DELFI is currently implemented as a C routine under MATLAB (The MathWorks Inc., Natick, MA) and obtained responses, as will be described in detail in a future publication, are in excellent agreement with theory and with results obtained using Field II [9]. DELFI is unique and powerful not only because of its analytical approach, but also its efficiency; it is much more efficient than Field II when computing spatial sensitivity functions at a single instant in time. In these cases, DELFI is approximately 25 times faster than Field II with no loss in quality.

Spatial pulse-echo responses were computed by transmitting a plane wave on all elements and receiving sequentially on each element. The psfs were computed in the 3-D cylindrical volume described in Table I at two times—the time taken to propagate to the focus and back to the transducer, and a quarter period (at the center frequency) later [7]. We then combined the two psfs computed for each receive element to form a single, complex psf [7]. We implemented apodization and focusing by complex phase rotation, and we summed across elements to obtain the complete summed and focused response. Note that the desired receive f/# was implemented by including only the responses of those elements that form an aperture of the desired diameter. In other words, the f/# is calculated by including only the elements that are apodized with nonzero weights.

We used Field II to simulate the conventional system by computing the spatiotemporal response at each point in the 3-D spatial window of analysis. We applied the Hilbert transform [10] to form a complex analytic signal whose real part was the original received response and whose imaginary part was the Hilbert transform of that response. The 3-D spatial psf was constructed by summing the samples at the two-way propagation time determined by array geometry and the location of the focus. Because the conventional system uses a lens in elevation and significant portions of targets often are imaged away from the elevation focus, we computed two psfs to compare to our system—one with the elevation focus coincident with the azimuthal focus at 1 cm (21.4λ), and one with the elevation focus set to 2.8 cm (60λ). We chose to set the elevation focus at 2.8 cm because we mimicked a commercially available transducer that we use for experiments in the laboratory. Fig. 1 shows slices of the two psfs obtained with the 1-D array and focusing via time delays. Fig. 2 shows slices of the psf obtained with the 2-D array and DSIQ beamforming. We used (34) to compute the contrast for cysts of different sizes. We ignored the effects of electronic noise because noise estimates for our first generation prototype will be of limited relevance in our final system. Fig. 3 depicts the contrast as a function of cyst size for the three geometries examined.

The above application of the metric allows a direct comparison of our C-scan system to more conventional linear array based systems, a comparison that would be difficult using only the beamplot or even the psf. We also have applied the metric to quantify the often subtle differences in performance that result from changes in our system configuration. In each of the following examples, application of the metric provides clear guidance in system design.

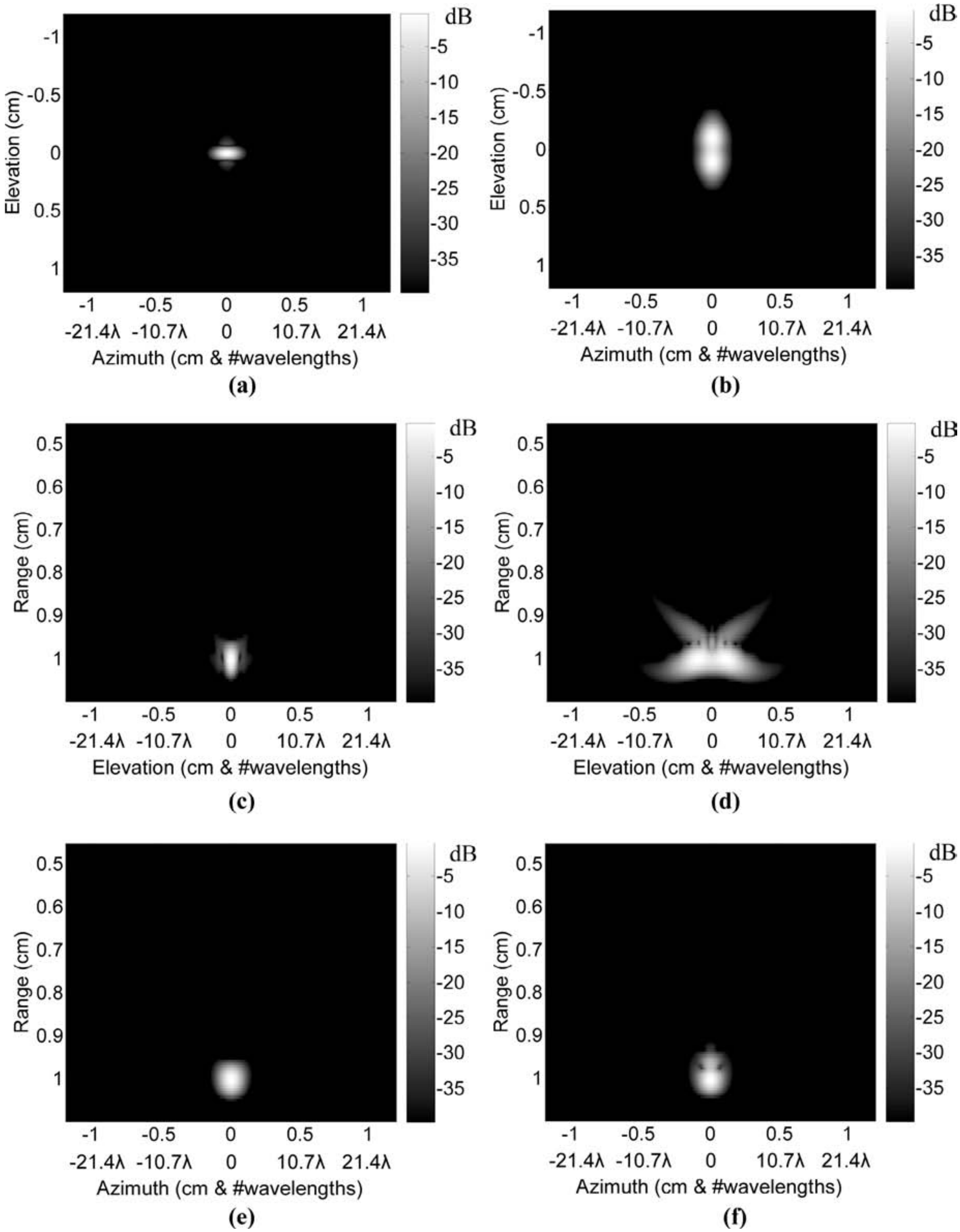

Fig. 1. Slices of the simulated 3-D spatial psf obtained for a conventional system with a 1-D array and time delay focusing. (a), (c), and (e) depict slices in azimuth-elevation, elevation-range, and azimuth-range, respectively, for the system with a coincident focus. (b), (d), and (f) depict slices in azimuth-elevation, elevation-range, and azimuth-range respectively, for the system with the elevation focus set to 2.8 cm.

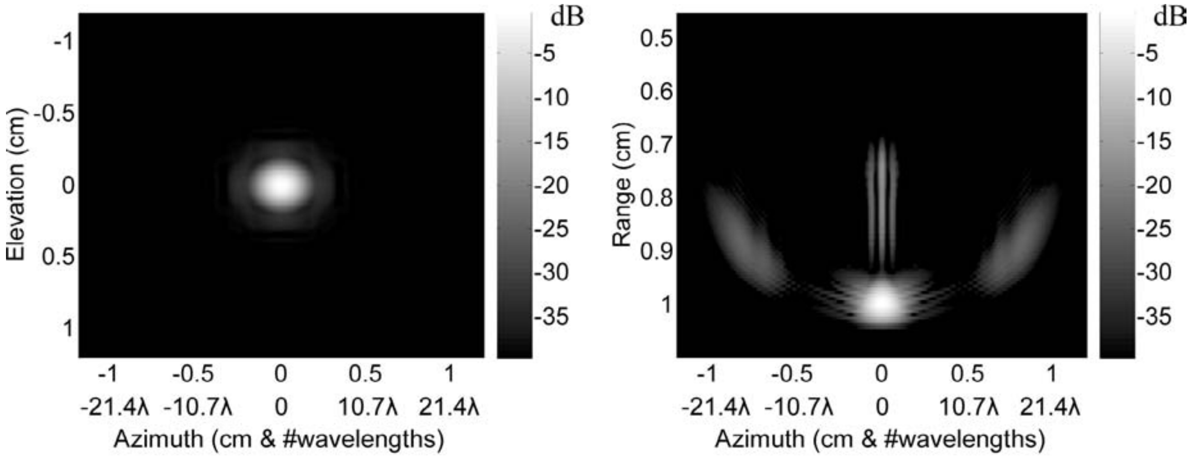

(a) (b)

Fig. 2. Slices of the simulated 3-D spatial psf obtained simulating the first generation prototype of our low-cost, C-scan system with a 2-D array and DSIQ beamforming. Relevant parameters are listed in Table I. (a) and (b) depict slices in azimuth-elevation and azimuth-range, respectively. Due to symmetry, the elevation-range slice is identical to the azimuth-elevation slice and is therefore not shown.

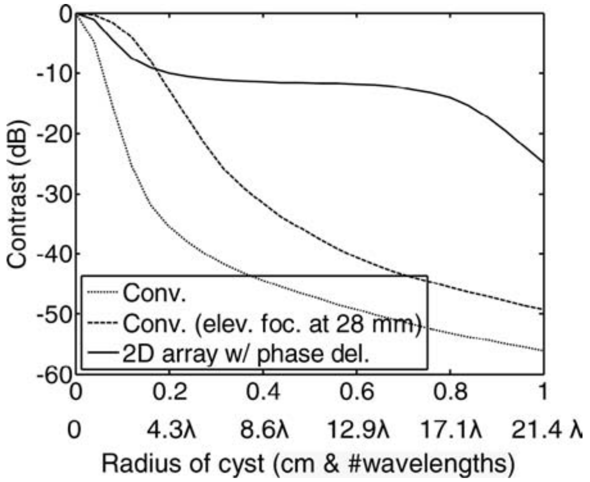

Fig. 3. Comparison of our prototype C-scan system with a conventional system. Cystic contrast was computed using (34) and is plotted as a function of cyst size.

TABLE II
SINGLE RECEIVE CHANNEL SNR VALUES USED WITH (31) TO ESTIMATE THE IMPACT OF ELECTRONIC NOISE.

Electronic SNR per channel (dB)
−10
0
10
20

TABLE III
NUMBER OF BITS USED TO REPRESENT EACH REAL VALUE TO DETERMINE THE MINIMUM PRECISION REQUIRED IN OUR SYSTEM.

Quantization (# bits)
6
8
10
12
16

Although lower electronic noise is always preferable, practical systems almost always exhibit other limitations, such as limited dynamic range, which render noise reduction beyond some threshold SNR of limited use. To determine this threshold in our system, we varied the electronic SNR per channel, as listed in Table II, computed the psf using DELFI as described above, and used (31) to compute the contrast as a function of cyst size for our prototype system. Figs. 4(a) and (b) depict the obtained contrast as a function of cyst size when receive apodization was implemented with flat and Nuttall windows, respectively.

It is well-known that digitizer quantization affects sidelobe levels [11]. State-of-the-art clinical scanners typically use 10 bits to represent each sample. However, compromises made in fabricating our 2-D array transducer and in beamforming might render 10 bits superfluous in our prototype system. We tested this hypothesis by investigating the impact of quantization on cyst contrast in an ideal scanner with no electronic noise. We quantized the single receive element responses, obtained as described above, using different precisions (Table III) and then apodized, focused, and summed the responses. Note that the precisions listed in Table III correspond to one real sample, and a full complex sample was therefore represented using twice the listed number of bits. The effect of quantization on cyst contrast is illustrated in Fig. 5.

The choice of receive f/# is an important design parameter in our system because we focus solely by phase rotation of the received data. Although larger apertures

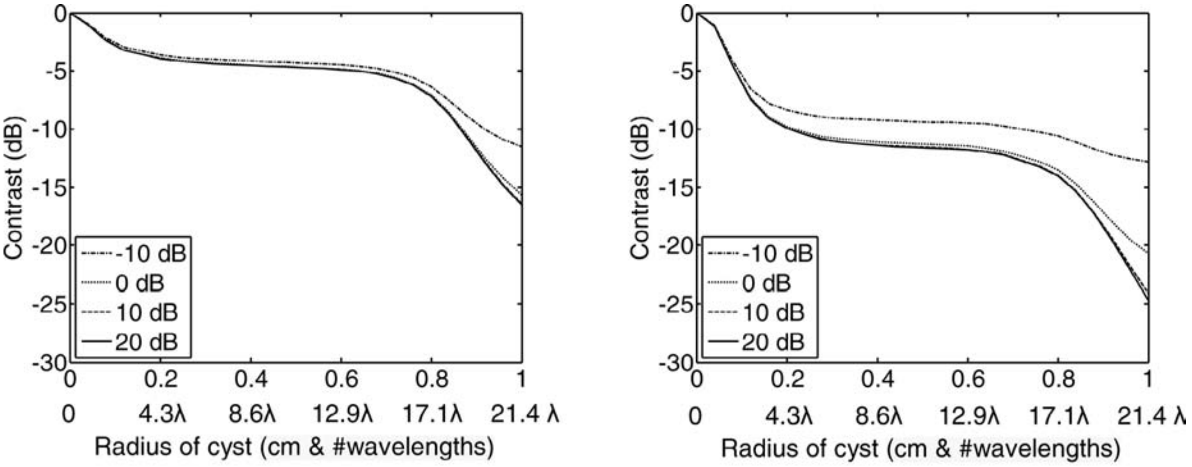

(a) **(b)**

Fig. 4. Effect of electronic noise. Contrasts were computed using (31) for the SNRs listed in Table II and are shown as a function of cyst size when receive apodization was implemented using (a) a flat window and (b) a Nuttall window.

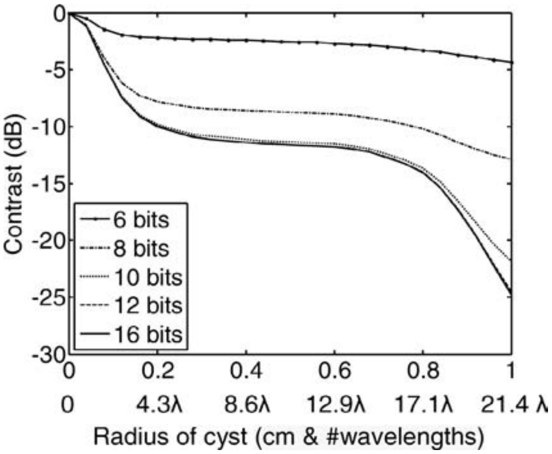

Fig. 5. Effect of quantization. Single receive element responses were quantized using different precisions (Table III) for each real sample, then apodized, focused, and summed to yield 3-D responses. Contrasts were computed using (34) and are plotted as a function of cyst size.

TABLE IV

F/#s Used on Receive to Determine the Optimal f/# for our System.

f/#
0.50
0.75
1
1.25
1.5
1.75

TABLE V

Windows Used to Determine the Impact of Receive Apodization on Cyst Contrast.

Apodization
Flat
Hann [12]
Tukey [13]
Gaussian [13]
Chebyshev (relative sidelobe attenuation of 100 dB) [14]
Nuttall [8]

improve resolution when conventional time-delay focusing is used, larger apertures might degrade image quality in our system because of the limitations of DSIQ beamforming [7]. In addition, our elements are highly directive because of our large pitch (635 μm or 1.4λ); therefore, large apertures might yield higher grating lobes. We explored the impact of f/# by computing the contrast as a function of cyst size for the f/#s listed in Table IV. Fig. 6 plots contrast as a function of cyst size for each f/# tested.

We also explored the effect of varying the apodization window on our system. We used the six windows listed in Table V. Fig. 7(a) depicts contrast as a function of cyst size for each window in a noise-free environment. Fig. 7(b) plots the obtained contrast in the presence of electronic noise with an SNR of −10 dB per channel. It is worth noting that the selection of apodization windows based solely on the presented metric might not result in the best image quality. A particular window might reduce grating lobes and sidelobes, but if it also reduces array gain, losses in sensitivity (reduction in SNR) might outweigh the contrast benefits. Table VI lists the contrasts (when imaging a cyst of radius 2.5 mm or 5.4λ) and the associated sensitivities obtained using each window. Contrasts with no electronic channel noise, and noise with an SNR of −10 dB and 0 dB per channel, are listed. The sensitivities were calculated from the peak magnitude of the psfs and are normalized

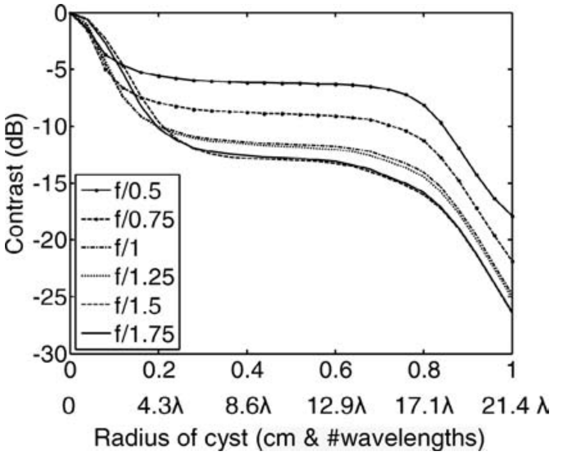

Fig. 6. Effect of f/#. Contrasts were computed using (34) and are plotted as a function of cyst size for the f/#s listed in Table IV.

to the sensitivity obtained using flat apodization. We use a cyst of radius 2.5 mm because one of the major applications envisioned for our C-scan system is image guided needle/IV line insertion in the arm, where the veins are approximately 5 mm in diameter.

IV. Results and Discussion

Fig. 1 depicts slices of the psf obtained in our control simulation of conventional ultrasound systems, with the elevation focus at the azimuthal focus (1 cm) and at 2.8 cm. We see a similar response for the two geometries in the azimuth-range plane in Fig. 1(e) and (f), but, as expected, the elevation focus plays a role in the azimuth-elevation and elevation-range planes in Fig. 1(a)–(d). We see a significant broadening of the psf in these planes when the elevation focus is moved away from the azimuthal focus.

Fig. 2 shows slices of the psf obtained for our C-scan system. The slice in the azimuth-elevation plane in Fig. 2(a) shows a broader mainlobe in azimuth than the 1-D array in Fig. 1, due to our use of only phase delays for focusing. The response is also broader in elevation when compared to the 1-D array with a coincident focus in azimuth and elevation. The benefit of a variable elevation focus becomes apparent when we compare results from our system to those from the 1-D array geometry with the elevation focus at 2.8 cm; the beam is broader in elevation in the 1-D case, as can be seen in Fig. 1(b) and (d). However, a slice of the psf obtained with the 2-D array in the azimuth-range plane reveals not only a broad mainlobe but also significant grating lobes.

Fig. 3 depicts a comparison of the three geometries described above. It can be seen that the contrast obtained with the 2-D array is much worse than with the 1-D array with coincident azimuthal and elevational foci. Recall that the metric computes the ratio of the psf energy outside the cyst to the total psf energy. Therefore, when considering the contrast curve for our system, the rightmost portion of the contrast curve (for cysts with radii greater than 4 mm or 8.6λ) is affected only by the grating lobes. However, as the size of the cyst decreases, the effects of the sidelobes (cyst radii from 1.5 to 4 mm or from 3.2λ to 8.6λ), and eventually the mainlobe (cyst radii less than 2 mm or 4.3λ), come into consideration. The effects of a larger mainlobe and grating lobes combine to limit contrast in our prototype system across cysts of all sizes. However, when we compare our system to the 1-D case with different azimuthal and elevational foci locations, we see that the mainlobe broadening in elevation in the 1-D case greatly reduces contrast for that geometry. Since one of the primary applications of our system is image-guided needle/IV line insertion, we are particularly interested in cysts of radii between 1.5 to 2.5 mm. In this range, we see that our system would generate cystic contrast that is at least comparable to the conventional system; this is an impressive conclusion considering the reductions in hardware complexity and cost of our approach.

Note that the flat region of the contrast curve (radii > 4 mm) for our system depends on the level of the grating lobes and is therefore mostly dependent on the array pitch. The array pitch in our current prototype is large due to printed circuit board fabrication limitations [5] and will be reduced significantly in the next prototype. This should, in turn, yield an overall improvement in contrast.

Fig. 4 illustrates the effect of electronic noise on receive. It can be seen, as expected, that the contrast increases with increasing SNR. The plots suggest that improving the electronic SNR much beyond 0 dB per channel will yield no noticeable improvement in image quality. Although an SNR greater than 0 dB results in better contrast for large cysts, our focus on imaging cysts of radii less than 2.5 mm makes this result of limited relevance. As we improve our element pitch and thus reduce grating lobes, the flat region of the curves will change, and we will most certainly need to reconsider the effect of SNR.

The effect of quantization can be seen in Fig. 5. Quantization noise significantly degrades the obtained contrast when less than 10 bits are used per real sample. Although these simulations did not include the effect of electronic noise, an electronic SNR as low as 0 dB per channel still should render these results valid.

Fig. 6 shows the effect of varying the f/#. We see that contrast increases with increasing f/# for large cysts. This is due to the 2-D array pitch, which results in highly directive elements and thus large grating lobes when large apertures are used. Large f/#s ($>$ f/1.5), however, result in a very broad mainlobe and reduce contrast when imaging small cysts. Fig. 6 suggests that an f/1 system would be a good compromise for imaging cysts of all sizes. Although this analysis ignores the effect of aperture size on system sensitivity, sensitivity would increase with increasing aperture size. For poor SNR environments, it may be necessary to consider the impact of SNR and f/# simultaneously.

Fig. 7 shows the contrasts obtained using different apodization windows in the presence and absence of electronic noise. Contrasts obtained using each tested apodization window for a cyst of radius 2.5 mm are listed in Ta-

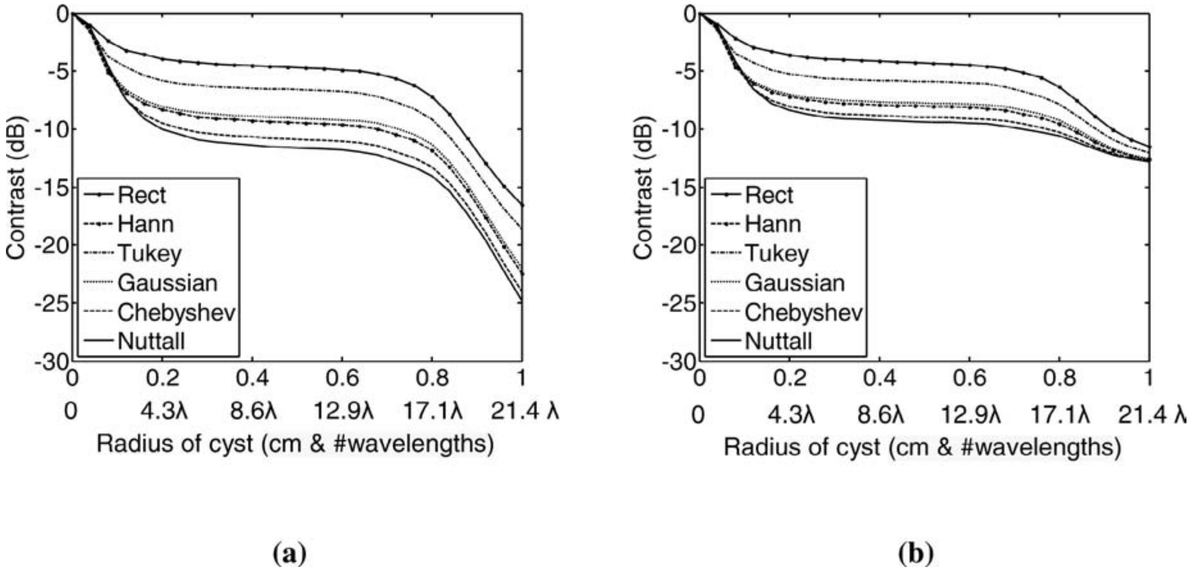

Fig. 7. Effect of apodization with (a) no electronic noise, and (b) electronic noise with SNR −10 dB per channel. Contrasts were computed using (34) in the noise-free case and (31) when noise was considered, and are plotted as a function of cyst size. Psfs obtained with each of the apodization windows listed in Table V were used to compute the shown contrast curves.

TABLE VI

Contrasts Obtained for a Cyst of Radius of 2.5 mm with Varying Amounts of Electronic Noise[1].

Window	Sensitivity (dB)	Contrast (dB) with −10 dB electronic SNR	Contrast (dB) with 0 dB electronic SNR	Contrast (dB) with no electronic noise
Rect	0	−4	−4	−4
Hann	−7	−8	−9	−9
Tukey	−2	−6	−6	−6
Gaussian	−7	−7	−8	−8
Chebyshev	−9	−8	−10	−10
Nuttall	−11	−9	−10	−11

[1] Different apodization windows were used and their associated sensitivities were normalized to the sensitivity using flat apodization. Contrasts obtained with no electronic noise, noise with an SNR of −10 dB per channel, and an SNR of 0 dB per channel are listed. Contrasts were computed using (34) in the noise-free case and (31) when noise was considered.

ble VI for various SNR values, along with the effect of the windows on system sensitivity. There is generally an inverse relationship between contrast and sensitivity. The Nuttall window maximizes contrast for all simulated noise levels, but it is also the window most affected by electronic noise. The contrast trends seen in Table VI when the noise level is varied indicate that the Hann or Tukey windows are least affected by noise because of comparatively high sensitivity. Note, however, that the Gaussian window would be a poor choice because it yields a poorer contrast for the same sensitivity as the Hann window.

As demonstrated by the above examples, the use of cystic resolution makes parameter optimization easier because a simple plot of contrast as a function of cyst size can be generated for any system. The goal of system design is then to simply maximize the contrast at the cyst size of interest, leaving no room for ambiguity. The comparison of disparate imaging systems also is straightforward because we can easily determine the system that has the better cystic resolution for a specified level of contrast. This is in stark contrast to the use of the beamplot, in which optimization is not necessarily clear. The proposed metric is also very flexible because the mask $M(\vec{x})$ can be changed to match the target of interest. We also could introduce scatterers in the region defined by the mask, as described in [2], to predict performance when imaging hypoechoic or hyperechoic lesions. Note, however, that the expressions derived in this paper for the psf energy outside and within the cyst are valid only if the mask represents an anechoic region. The major drawback of the proposed metric is that it neglects the effect of speckle statistics and size on target detectability [15]. Despite this drawback, the above metric is much better suited to characterize medical ultrasound systems than current approaches.

V. Conclusions

Existing methods to characterize ultrasound systems are limited in their utility. The beamplot is usually of limited use unless the goal is to image a bright point target. It is, in addition, difficult to decide how to optimize the beamplot to improve overall imaging performance. Contrast detail phantoms cannot be used to assess hypothetical systems without excessive computational costs. We built upon [2] and [4] to derive a metric to characterize arbitrary 3-D broadband ultrasound systems, including the effects of electronic noise. We presented simulation results that demonstrated the use of the metric in designing ultrasound systems, and we showed that it enables the straightforward optimization of any parameter that affects image quality.

References

[1] B. D. Steinberg, *Principles of Aperture and Array System Design.* New York: Wiley, 1976, pp. 40–52.

[2] D. Vilkomerson, J. Greenleaf, and V. Dutt, "Towards a resolution metric for medical ultrasonic imaging," in *Proc. IEEE Ultrason. Symp.*, 1995, pp. 1405–1410.

[3] J. M. Kofler, M. J. Lindstrom, F. Kelcz, and E. M. Madsen, "Association of automated and human observer lesion detecting ability using phantoms," *Ultrasound Med. Biol.*, vol. 3, pp. 351–359, 2005.

[4] K. F. Üstüner and G. L. Holley, "Ultrasound imaging system performance assessment," presented at 2003 AAPM Annual Meeting, 2003, San Diego, CA.

[5] E. Girard, S. Zhou, W. Walker, T. Blalock, and J. Hossack, "High element count two dimensional transducer array," in *Proc. IEEE Ultrason. Symp.*, 2003, pp. 964–967.

[6] M. I. Fuller, T. N. Blalock, J. A. Hossack, and W. F. Walker, "A portable, low-cost, highly integrated, 3-D medical ultrasound system," in *Proc. IEEE Ultrason. Symp.*, 2003, pp. 38–41.

[7] K. Ranganathan, M. K. Santy, T. N. Blalock, J. A. Hossack, and W. F. Walker, "Direct sampled I/Q beamforming for compact and very low cost ultrasound imaging," *IEEE Trans. Ultrason., Ferroelect., Freq. Contr.*, vol. 51, no. 9, pp. 1082–1094, 2004.

[8] A. H. Nuttall, "Some windows with very good sidelobe behavior," *IEEE Trans. Acoust. Speech Signal Processing*, vol. 29, no. 1, pp. 84–91, 1981.

[9] J. A. Jensen and N. B. Svendsen, "Calculation of pressure fields from arbitrarily shaped apodized and excited ultrasound transducers," *IEEE Trans. Ultrason., Ferroelect., Freq. Contr.*, vol. 39, no. 2, pp. 262–267, 1992.

[10] R. N. Bracewell, *The Fourier Transform and Its Applications.* 3rd ed. New York: McGraw-Hill, 2000, pp. 359–367.

[11] B. D. Steinberg, "Digital beamforming in ultrasound," *IEEE Trans. Ultrason., Ferroelect., Freq. Contr.*, vol. 39, no. 6, pp. 716–721, 1992.

[12] A. V. Oppenheim and R. W. Schafer, *Discrete-Time Signal Processing.* Englewood Cliffs, NJ: Prentice-Hall, 1989, pp. 447–448.

[13] F. J. Harris, "On the use of windows for harmonic analysis with the discrete Fourier transform," *Proc. IEEE*, vol. 66, no. 1, pp. 51–83, 1978.

[14] Digital Signal Processing Committee of IEEE Acoustics, Speech, and Signal Processing Society, Ed. *Programs for Digital Signal Processing.* New York: IEEE Press, 1979, Program 5.2.

[15] S. W. Smith, R. F. Wagner, J. M. Sandrik, and H. Lopez, "Low contrast detectability and contrast/detail analysis in medical ultrasound," *IEEE Trans. Ultrason., Ferroelect., Freq. Contr.*, vol. 30, no. 3, pp. 164–173, 1983.

Karthik Ranganathan received a B.E. degree in biomedical engineering in 1999 from the University of Mumbai, Mumbai, India, and a Ph.D. degree in biomedical engineering in 2005 from the University of Virginia, Charlottesville, VA. His dissertation focused on the development of ultrasound beamforming strategies for optimal image quality in state of the art systems on one hand and for low-cost systems on the other.

Dr. Ranganathan is currently at PocketSonics, Inc., which is a startup venture based in Charlottesville, VA that is focused on the development of low-cost ultrasound imaging solutions.

William F. Walker received the B.S.E. and Ph.D. degrees in 1990 and 1995 from Duke University, Durham, NC. His dissertation explored fundamental limits on the accuracy of adaptive ultrasound imaging.

After completing his doctoral work, he stayed on at Duke as an Assistant Research Professor in the Department of Biomedical Engineering. At the same time he served as a Senior Scientist and President of NovaSon Corporation located in Durham, NC. In 1997 he joined the faculty of the Department of Biomedical Engineering at the University of Virginia, being promoted to Associate Professor in 2003. He is an active founder in two ultrasound based startup companies, PocketSonics Inc., and HemoSonics LLC. His research interests include aperture domain processing, beamforming, angular scatter imaging, tissue elasticity imaging, low-cost system architectures, and time delay and motion estimation.

Optimal Apodization Design for Medical Ultrasound Using Constrained Least Squares Part I: Theory

Drake A. Guenther and William F. Walker, *Member, IEEE*

***Abstract*—Aperture weighting functions are critical design parameters in the development of ultrasound systems because beam characteristics affect the contrast and point resolution of the final output image. In previous work by our group, we developed a metric that quantifies a broadband imaging system's contrast resolution performance. We now use this metric to formulate a novel general ultrasound beamformer design method. In our algorithm, we use constrained least squares (CLS) techniques and a linear algebra formulation to describe the system point spread function (PSF) as a function of the aperture weightings. In one approach, we minimize the energy of the PSF outside a certain boundary and impose a linear constraint on the aperture weights. In a second approach, we minimize the energy of the PSF outside a certain boundary while imposing a quadratic constraint on the energy of the PSF inside the boundary. We present detailed analysis for an arbitrary ultrasound imaging system and discuss several possible applications of the CLS techniques, such as designing aperture weightings to maximize contrast resolution and improve the system depth of field.**

I. Introduction

The determination of array aperture weights that produce a synthesized beam pattern with a narrow mainlobe and low sidelobes is a classical problem with a rich history in the signal processing literature. Dolph [1] used Chebyshev polynomials to calculate aperture weights for a uniformly spaced, continuous wave linear array that achieved the minimum possible beamwidth for a given maximum sidelobe level. Taylor [2] expanded this formulation to achieve tapered sidelobes further away from the mainlobe for continuous apertures, and Villeneuve [3] applied it to discrete arrays. Nuttall [4] improved upon the Blackman-Harris window to achieve beam patterns whose maximum sidelobes are minimized. Whereas these previous papers focused on uniformly spaced arrays, Olen and Compton [5] developed an iterative procedure using an arbitrarily shaped adaptive array to produce the desired sidelobe behavior by using a recursive feedback procedure. Tseng and Griffiths [6] also produced a simple iterative algorithm that can be used to find array weights for nonuniform geometries to produce beam patterns with a given-look direction and minimum energy in the sidelobes. An interesting outcome of their methods allowed for the design of beam patterns in which the desired sidelobe response could vary with angle.

Although these previous methods produced excellent results, narrowband assumptions, computational complexities, and iterative procedures limit their applicability to general ultrasound beamformer design. Considerable gains can be made in computation time with the use of least squares methods. In fact, over the last two decades, many authors have developed constrained least squares algorithms for the design of finite impulse response (FIR) filters [7]–[10]. These methods typically minimize the error of the filter over a certain frequency band with respect to some desired filter response. For example, Selesnick *et al.* [7] described a constrained least squares approach to design FIR filters that did not require the specification of a transition band of frequencies between the passband and stopband. By setting up a minimization problem on the l^2 error of the filter's amplitude response subject to linear equality constraints, Selesnick *et al.* [7] derived filters with minimum error and devoid of Gibb's phenomenon. Other authors used least squares methods to produce eigenfilters, or filters that minimize a quadratic error measure in the passband and stopband [8]–[10]. Later in a series of papers, Er *et al.* [11]–[16] used a variety of constrained least squares techniques to synthesize arbitrary array patterns subject to different criteria such as sidelobe level and mean squared sidelobe energy. Their algorithms use linear and quadratic constraints to achieve array patterns, which are highly directional with very low sidelobes, for general array geometries.

The rich history of array pattern synthesis optimization only recently was applied to medical ultrasound imaging, and most applications have been specialized [17]–[21]. For example, Ebbini and Cain [17] proposed a method for synthesizing multiple focal regions on single transmit events for applications in hyperthermia treatment via ultrasound. Li *et al.* [18] used a total least squares method to compensate for point spread function (PSF) degradation due to "dead" array elements or elements blocked by acoustically opaque windows in the interrogated media. Recently, Wilkening *et al.* [20], [21] designed optimal FIR filters for improved image contrast in contrast agent imaging and FIR filters that increased the depth of field for dynamic receive focusing. Although insightful and useful,

Manuscript received June 5, 2006; accepted September 30, 2006.

This work was supported by US Army Congressionally Directed Research Program Grant No. W81XWH-04-1-0590.

The authors are with the University of Virginia, Department of Biomedical Engineering, Charlottesville, VA (e-mail: dag2m@virginia.edu).

Digital Object Identifier 10.1109/TUFFC.2007.247

0885–3010/$25.00 © 2007 IEEE

these methods failed to address the larger problem of general beam pattern synthesis given arbitrary arrays. Previously, our group developed a general aperture design tool, supported by rigorous theory that is applied to the design of aperture weighting functions for arbitrary system design [22], [23]. The method used a minimum sum squared error (MSSE) formulation between the system PSF and the desired or goal PSF. One strength of the approach is that it allowed for full beam optimization given system parameters obtained through theory, simulation, or experiment. The method is useful because it allows for the design of any controllable system parameter in a straightforward, rigorous, time-efficient manner. Ranganathan and Walker's [22] approach, although extremely useful in aiding the design of prototype systems, suffers from the lack of a quantitative measure detailing how system performance changes with respect to a deviation in system parameters. Furthermore, the approach offers no guidance in the selection of an appropriate goal point spread function. These shortcomings make system optimization using the MSSE approach difficult.

The method of apodization profile design presented in this paper is general enough to be applied to any coherent imaging system and is similar to many of the previous array pattern synthesis techniques using constrained least squares (CLS). For example, our linearly constrained least squares (LCLS) formulation is similar to the array pattern synthesis technique by Tseng and Griffiths [6], and our quadratically constrained least squares (QCLS) formulation is similar to the constrained eigenfilter design [8], [24]. These prior analyses were for a single carrier frequency, whereas we use a broadband formulation. Keitmann-Curdes *et al.* [25] previously developed an algorithm similar to our QCLS formulation that generated apodization profiles for ultrasound imaging with minimum sidelobe energy of the two-dimensional, space-time PSF. Recently Schwann *et al.* [26] used two different resolution criteria to design optimal frequency-dependent apodization profiles, a method whose goals are similar to ours of improving image contrast. However, their multiple objective formulation requires computationally expensive iterative methods to arrive at one Pareto optimum solution, or a solution in which further improving one objective necessarily degrades all others [27]. Further review of the differences between our LCLS and QCLS methods and the techniques mentioned above will be discussed in more detail later in this paper.

Because the ultrasound system's beam characteristics fundamentally affect the quality of the image, a great deal of effort is put into optimizing system parameters. Estimating the imaging performance of ultrasound systems is critical, both to characterize the fundamental imaging limits of the system, and to optimize image quality. It is possible to estimate the performance of existing systems by imaging phantoms or human subjects, but it is necessary during system design to be able to determine imaging performance prior to system construction. The ability to accurately predict performance enables system optimization, quantitative consideration of engineering tradeoffs, and significantly reduces the time and cost investment in system development.

Synthesis of beampatterns in diagnostic ultrasound receives a great deal of attention during system design. The system's spatial impulse response, or point spread function, characteristics will determine such parameters as point resolution and contrast in the resulting image. Thus, control over mainlobe width and sidelobe level is significant. These beam parameters are influenced by the size of the active aperture, the frequency of the ultrasound pulse, the magnitude and phase (or time delay) of the weightings applied to the active elements, and the pulse length. Because so many factors affect the characteristics of the PSF and there is no global parameter describing PSF quality, beamforming parameters usually are determined through iterative simulation and experimentation.

A quantitative resolution metric is essential to guide optimization of system parameters, including the system's PSF. The most common measure of scanner performance is the beamplot [28], which has been adapted from RADAR. The −6 dB beamwidth of the beamplot, the full width at half maximum (FWHM), and the beamwidth at other levels are used to estimate scanner resolution. Sidelobe and grating lobe levels are used to estimate eventual image contrast. Although widely used in medical ultrasound, there are scenarios in which the FWHM criterion indicates excellent performance, but actual images of tissue do not reveal important details.

Vilkomerson *et al.* [29] addressed the limitations of the beamplot and proposed the concept of cystic resolution in which performance was quantified as the size of a void that produced a given contrast. The analysis, while novel and useful, was limited to narrowband circular apertures and neglected the axial dimension. Johnson [30] further developed the contrast resolution metric to include a three-dimensional (3-D) broadband model for circular apertures and compared different imaging parameters using maximum output contrast curves versus cyst diameter. Üstüner and Holley [31] extended cystic resolution to a 3-D broadband model for arbitrary apertures, but they did not describe its theoretical foundation, resulting in a limited understanding of the formulation and its utility and drawbacks. A general cystic resolution metric was previously derived by our group [32]. This metric accounts for the effect of electronic noise and, under certain assumptions, reduces to that described in [31]. Whereas, the FWHM criterion sometimes provides misleading information about resolution in ultrasound systems, the cystic resolution metric identifies specific points in the system's PSF that can be optimized to increase image quality and performance.

This paper uses the cystic resolution metric to guide optimization of apodization profiles for coherent imaging systems. Specifically, we design optimal receive apodization profiles for a 1-D linear array; however, our theory can be applied to a 2-D array of arbitrary geometry and can be used to design one-way or two-way apodization profiles. We propose two different methods for optimal apodization design. The first algorithm minimizes the energy of the PSF outside some specified region subject to a linear constraint of the apodization weights. We call the resultant weights the LCLS apodization profile. The second algorithm minimizes the energy of the PSF outside some region subject to a quadratic energy constraint of the PSF inside the boundary. We call the resultant weights the QCLS apodization profile.

Our CLS apodization design methods return real weights and achieve a spatial impulse response with minimum sidelobe levels in a least squares sense given a specified mainlobe area. We formulate the problem starting from basic principles of acoustic wave diffraction theory and apply linear algebra techniques to represent the system PSF. We generate a least squares problem subject to either a linear or quadratic constraint in order to minimize the energy outside a given mainlobe area in the PSF. The algorithm can be applied to enhance the depth of field (DOF) in an imaging system as well as improve lesion detectability in inhomogeneous scattering media. The algorithm is arguably optimal for detecting anechoic cysts via ultrasound; however, we believe it also will improve ultrasound system performance in general imaging applications. This paper outlines the theoretical description of the constrained least squares technique for designing apodization profiles for broadband, coherent imaging systems, describes a technique for reduced computational cost, and finally discusses examples of application. Results from simulations are presented in an accompanying paper [33].

II. Theory

We present two-way broadband formulations for the LCLS and QCLS apodization design techniques. The one-way broadband formulation can be expressed in a similar manner; but we note that, in most ultrasonic imaging applications, the two-way impulse response is of greater interest. The two-way broadband formulation of the PSF incorporates the system's transmit conditions: excitation pulse, transmit apodization, element-impulse response, etc. However, the CLS algorithms, as formulated here, operating on a two-way PSF will calculate only the optimal receive apodization. In practice one could optimize the transmit apodization given the one-way PSF, then include it in the formulation of the two-way PSF optimization.

A. Linear Algebra Formulation of the Broadband Spatial Impulse Response

The acoustic pressure field emanating from a transducer during pulse-echo propagation at a single instant in time can be expressed as the product of a propagation matrix, S, and a set of aperture weightings, w. The propagation matrix uses superposition to describe the contribution of each transducer element at each field point at an instant in time. The propagation function may be derived from the Rayleigh-Sommerfeld diffraction equation derived in [34] and also may include a term relating to limited-element, angular response [35]. Alternatively, the propagation matrix may be computed via broadband simulation or estimated experimentally. For our formulation, S is a function of the transmit aperture weights, the excitation pulse, and the individual element impulse responses of the transmit and receive apertures [22].

The two-way pulse-echo propagation matrix, S, for a fixed transmit aperture and a n element receive aperture at a total number of p points in 3-D space is:

$$S = \begin{bmatrix} s_{1,1} & s_{1,2} & \cdots & s_{1,n} \\ s_{2,1} & \cdot & \cdots & \cdot \\ \vdots & \vdots & \ddots & \vdots \\ s_{p,1} & \cdot & \cdots & s_{p,n} \end{bmatrix}, \tag{1}$$

where $s_{i,j}$ is the contribution of the jth element at the ith point in space. The receive aperture weighting function, w, for each of the n elements used on receive can be written in vector form as:

$$w = \begin{bmatrix} w_1 \; w_2 \; w_3 \; \cdots \; w_n \end{bmatrix}^T, \tag{2}$$

where T denotes the vector transpose operation. Using (1) and (2), we now can write the complete, two-way pulse-echo system PSF, P, as follows:

$$P = Sw, \tag{3}$$

the propagation matrix multiplied by the receive weighting vector. Note that this results in the 1-D column vector, P, of length p the total number of points in 3-D space in which the system PSF is measured.

This formulation can be expanded to describe the PSF as a function of time. In this case, the receive weightings would be a function of element number and time, essentially forming the coefficients of a FIR filter on each receive channel. Adequate spatial and temporal sampling of the 3-D PSF yields huge propagation matrices. Therefore, for this and the accompanying paper [33] we have limited our analysis to a single instant in time and two spatial dimensions, azimuth and range. Clearly, the elevation dimension matters in planar ultrasonic B-mode images, even with acoustic lenses on linear arrays. However, restricting our analysis to two dimensions eases visualization of the algorithm while still providing meaningful results.

B. Cystic Resolution Metric

The goal of the cystic resolution metric is to quantify the contrast resolution of an arbitrary broadband ultrasound system. We refer the reader to [32] for a more detailed discussion of the derivation of the metric and highlight the meaningful results here. The metric completely characterizes the 4-D spatiotemporal contrast performance for a system imaging an anechoic void in a scattering background. However, analysis at the instant in time when the received signal is minimum (i.e., when as much of the PSF energy as possible lies within the cyst) usually is sufficient.

At this single instant in time, the PSF can be expressed as a function of 3-D space at the time of interest. The signal-to-noise ratio (SNR) also is considered at the time of interest (SNR_{t_o}). The contrast resolution at this instant in time is defined as the ratio of the rms signal received from the cyst to the rms signal received when the cyst is absent [32]:

$$C_{t_0} = \sqrt{\frac{1 + \mathrm{SNR}_{t_o}^2 \dfrac{E_{\mathrm{out}}}{E_{\mathrm{tot}}}}{1 + \mathrm{SNR}_{t_o}^2}}, \tag{4}$$

where E_{out} is the PSF energy outside the cyst and E_{tot} is the total PSF energy, both at time t_o. Eq. (4) describes the contrast at the center of an anechoic cyst embedded in a speckle-generating background obtained by an imaging system with a given PSF and electronic SNR defined statistically by SNR_{t_o}. Note that this metric quantifies the contrast at a particular point in space (the center of the cyst) and at a particular instant in time. This is different than a measure of overall cystic contrast. Overall cystic contrast is typically computed from a B-mode image and compares the signal inside the cyst to the signal of a speckle region outside the cyst [36]. Neglecting electronic noise, SNR_{t_o} becomes infinite and (4) can be modified to the equation for contrast presented in [31], which is simply the square root of the ratio of the PSF energy outside the cyst and the total PSF energy:

$$C_{t_o} = \sqrt{\frac{E_{\mathrm{out}}}{E_{\mathrm{tot}}}}. \tag{5}$$

The contrast for cysts of different sizes can be computed using the above expressions for cystic contrast, and system performance can be characterized as a function of cyst size as in [29]–[32]. Note that the best achievable contrast occurs when the cyst void encompasses the entire PSF. In this scenario, C_{t_o} in (5) would be 0. Therefore, when quantifying cystic contrast, a C_{t_o} value closer to 0, or more negative on a decibel scale, indicates better performance. This metric can be used for 4-D spatiotemporal analysis of broadband ultrasound systems, but 3-D spatial analysis using (4) or (5) is typically adequate to characterize scanner performance as temporal analysis usually does not provide critical information. Note that, in certain cases, it is valuable to compute the metric with cysts at different locations to quantify the depth of field, the effect of dynamic focusing, and other factors pertaining to the shift variance of the imaging system. Note also that, although the metric can be used to determine cystic resolution, it also can be used to optimize system parameters by computing contrast as a function of cyst size and determining parameter values that maximize the contrast at the cyst sizes of interest.

C. Linearly Constrained Least Squares Apodization Design

One conspicuous result of the above resolution metric is that cystic contrast, or our objective function, is defined in terms of the spatiotemporal PSF energy. In fact, contrast would be maximum if all the energy of the PSF lay inside the void of the cyst. Whereas beamplot details can be misleading about overall image quality, this metric considers the PSF globally to determine the impact on cystic contrast. Contrast improves when the PSF energy outside the cyst boundary is reduced or the PSF energy inside the cyst is increased. The cystic resolution metric defines a simple objective function for maximizing cystic contrast. The reader should note that different objective functions could be formulated, such as improving point contrast. But, for the discussion presented here, we focus on improving cystic contrast.

Cystic contrast is degraded by the presence of PSF energy outside the cyst. We minimize this energy by solving for the set of receive aperture weights that, when applied to the synthetic receive element responses, will yield a PSF with minimum energy outside the designated cyst boundary. Combining the above resolution metric with our linear algebra formulation of the PSF, our beam synthesis problem becomes determining the vector of weights that minimize the PSF energy outside the cyst boundary subject to a linear constraint to avoid the trivial case of all the receive weights set equal to zero. This is analogous to the problem of solving for the set of FIR filter coefficients that minimize the energy in the stopband.

Assuming the PSF is focused at the center of the cyst, the algorithm is initialized by selecting the spatial points of the PSF that lie outside the cyst boundary. We form the associated propagation matrix, S, that has as many rows as the number of points outside the cyst region and as many columns as elements in the active receive aperture. Therefore, each column of the S matrix is one focused, synthetic, receive-element response at all the spatial points outside the cyst boundary. Ranganathan and Walker's MSSE beamformer design approach outlined in [22] and [23] uses focused or unfocused aperture propagation matrices. Although imaging scenarios exist with unfocused apertures, for the CLS apodization design technique presented here, we prefocus our two-way PSFs so that the peak of the mainlobe lies in the center of the cyst boundary. This allows us to maximize the cost function in (5), cystic contrast. Using unfocused apertures is possible with the CLS formulation, but unfocused apertures typically would not be used for imaging cysts so a new cost function should be derived to reflect the system's intended application.

The CLS algorithm calculates the weights that minimize the energy in the sidelobe regions while simultaneously maintaining a peak gain at the center of the cyst. These weights are determined from the CLS problem:

$$\min_{w} \|Sw\|^2 \text{ subject to the linear constraint } C^T w = 1. \tag{6}$$

In this expression $\| \bullet \|^2$ denotes the square of the ℓ^2-norm and the row vector C^T has elements corresponding to the amplitude of each synthetic receive-element response. More specifically, C^T is a vector of the amplitudes of the receive-element responses at the focus in the center of the cyst. The expression in (6) is common in the signal processing literature, and drawing upon [37] the optimal receive aperture weightings are given by:

$$w_{\text{opt}} = (S^T S)^{-1} C [C^T \, (S^T S)^{-1} C]^{-1}, \tag{7}$$

where $(\bullet)^{-1}$ denotes the matrix inverse operation. Eq. (7) provides a simple method to calculate the receive weightings that will minimize the energy in the PSF outside a specified mainlobe region while simultaneously achieving peak gain inside the mainlobe region. The optimal receive weights minimize E_{out} in (5), so we expect to see improved cystic contrast using the LCLS apodization windows over commonly used windows such as the flat, Hamming and Nuttall [4] windows.

D. Linearly Constrained Least Squares Apodization Design with Weighting Function

In certain applications, the PSF characteristics at specific spatial positions may be more important than others because of the effects that the PSF has on point resolution and system contrast. For example, in hyperthermia applications, the ultrasonic field pattern requires high-power levels at some points while reducing the power deposition at other potential hot spots [17]. In other applications, it may be more important to reduce sidelobe levels than to precisely control the mainlobe. In these cases and others, we can incorporate a weighting function, g, that emphasizes or deemphasizes certain spatial points in the PSF during the apodization design procedure. The LCLS apodization design problem can be rewritten with the weighting function as:

$$\min_w \|g_d S w\|^2 \text{ subject to the linear constraint } C^T w = 1, \tag{8}$$

where g_d is a diagonal $p \times p$ matrix with elements of g along the 0th diagonal. The elements of g have a large value when minimizing PSF energy is important and smaller values when the PSF energy is less critical. The solution for optimal receive weightings, drawing upon [37] is:

$$w_{\text{opt}} = \left(S^T g_d^T g_d S\right)^{-1} C \left[C^T \left(S^T g_d^T g_d S\right)^{-1} C\right]^{-1}. \tag{9}$$

E. Quadratically Constrained Least Squares Apodization Design

The LCLS apodization design algorithm minimized the energy in the PSF outside a given region of the mainlobe. By doing so, the cystic contrast should improve according to (5). This analysis minimizes the numerator of (5); however, it ignores the denominator. As a result, although the energy outside the cyst will be minimized, the total PSF energy also could be decreased thus limiting cystic contrast improvements. We, therefore, develop an alternate approach in which we minimize the energy of the PSF outside a given boundary while at the same time keeping the energy of the PSF inside the boundary constant. This formulation becomes similar to the earlier beam synthesis problem of creating eigenfilters [8], [24]. In the FIR eigenfilter design case, the energy constraint on the filter coefficients is usually just the quadratic constraint $w^T w = 1$ that constrains the total energy of the filter's frequency response to be unity. However, for broadband beamformers, this constraint is meaningless, and we must devise a new formulation [24]. The modified quadratic constraint is straightforward given the cystic resolution metric. We wish to minimize E_{out} while maximizing E_{tot} in (5), and we can change E_{tot} to just the PSF energy inside the cyst boundary, E_{in}. Note that this problem can be set up as a multiple objective optimization problem [27], [38]. However, that approach does not yield an intuitive optimal solution whereas as using the cystic resolution metric does. Therefore, we choose to formulate this problem using a quadratically constrained least squares formulation:

$$\min_w \|S_{\text{out}} w\|^2 \text{ subject to the quadratic constraint } \|S_{\text{in}} w\|^2 = 1, \tag{10}$$

where $\| \bullet \|^2$ denotes the square of the ℓ^2-norm, S_{out} is the propagation matrix for all the spatial points of the PSF lying outside the cyst boundary, and S_{in} is the propagation matrix for all the spatial points of the PSF lying inside the cyst boundary. Note that the quadratic constraint essentially keeps the energy of the PSF inside the cyst constant. Drawing upon [24], [39]–[41] the optimal receive aperture weightings satisfying the quadratic constraint is the generalized eigenvector, w_{eig}, corresponding to the minimum generalized eigenvalue resulting from the generalized eigenvalue decomposition problem of $S_{\text{out}}^T S_{\text{out}}$ and $S_{\text{in}}^T S_{\text{in}}$. The generalized eigenvalue problem [39] for a matrix pair, $(A,\, B)$ both $n \times n$ matrices, is finding the eigenvalues, λ_k, and the eigenvectors, $x_k \neq 0$, such that:

$$A x_k = \lambda_k B x_k. \tag{11}$$

The number of eigenvalues, k, is dependent upon the rank of matrix B. One of the main advantages of the QCLS technique is that no matrix inversion is required to solve for the optimal apodization profile, unlike the LCLS apodization design.

F. Quadratically Constrained Least Squares Apodization Design with Weighting Function

As with the LCLS apodization design, a weighting function, g, can be added that emphasizes or deemphasizes certain regions of the PSF during the minimization process. Rewriting the QCLS apodization design problem above with the added weighting function we arrive at:

$$\min_w \|g_{\text{out}} S_{\text{out}} w\|^2 \text{ subject to the quadratic constraint } \|g_{\text{in}} S_{\text{in}} w\|^2 = 1, \tag{12}$$

where g_{out} is a diagonal $p \times p$ matrix with elements of g associated with the spatial points of the PSF outside the cyst boundary along the 0th diagonal, and g_{in} is a diagonal $q \times q$ matrix with elements of g associated with the spatial points of the PSF inside the cyst boundary along the 0th diagonal. We solve this problem by forming the Lagrangian and using the necessary conditions for a minimum:

$$L(w,\lambda) = w^T S_{\text{out}}^T g_{\text{out}}^T g_{\text{out}} S_{\text{out}} w - \lambda \left(w^T S_{\text{in}}^T g_{\text{in}}^T g_{\text{in}} S_{\text{in}} w - 1 \right), \tag{13}$$

where λ is the associated Lagrange multiplier. Following the Kuhn-Tucker conditions, a necessary condition for a minimum is that $(\partial L / \partial w) = 0$ [38]. Thus, taking the associated partial derivative of the Lagrangian with respect to the weighting vector we arrive at:

$$S_{\text{out}}^T g_{\text{out}}^T g_{\text{out}} S_{\text{out}} w = \lambda S_{\text{in}}^T g_{\text{in}}^T g_{\text{in}} S_{\text{in}} w. \tag{14}$$

Therefore, the set of optimal receive weightings satisfying (14) is again the generalized eigenvector, w_{eig}, corresponding to the minimum generalized eigenvalue resulting from the generalized eigenvalue decomposition problem of $S_{\text{out}}^T g_{\text{out}}^T g_{\text{out}} S_{\text{out}}$ and $S_{\text{in}}^T g_{\text{in}}^T g_{\text{in}} S_{\text{in}}$.

G. Reduced Computational Cost Through Symmetry Relations

The computation of CLS apodization profiles requires significant resources due to the large propagation matrices and matrix inverse operations (for the LCLS design method). In order to reduce the computational complexity of the algorithm, we take advantage of the lateral symmetry present in the system PSF for symmetric, nonsteered apertures. This symmetry means that we can use just half of the system PSF for the calculations of the optimal weightings. The propagation matrix, S, then becomes:

$$S = \begin{bmatrix} s_{1,1} & s_{1,2} \cdots & s_{1,n} \\ s_{2,1} & \cdot \;\cdots & \cdot \\ \vdots & \vdots \;\;\ddots & \vdots \\ s_{p/2,1} & \cdot \;\cdots & s_{p/2,n} \end{bmatrix}, \tag{15}$$

where S is a $(p/2) \times (n)$ matrix, consisting of the pressure field at only $p/2$ points in space for each element $[1, 2, \ldots n]$.

The symmetry of the nonsteered receive aperture is another property that can be exploited to reduce computational cost. As shown in Fig. 1, pairs of elements can be grouped together that are the same distance from the center axis of the array. Pairing is possible because these elements should have the same weights applied, assuming no beam steering and an even number of elements in the aperture. Therefore, the propagation matrix can be rewritten:

$$S = \begin{bmatrix} s_{1,1,n} & s_{1,2,n-1} \cdots & s_{1,n/2,n/2+1} \\ s_{2,1,n} & \cdot \;\cdots & \cdot \\ \vdots & \vdots \;\;\ddots & \vdots \\ s_{p/2,1,n} & \cdot \;\cdots & s_{p/2,n/2,n/2+1} \end{bmatrix}, \tag{16}$$

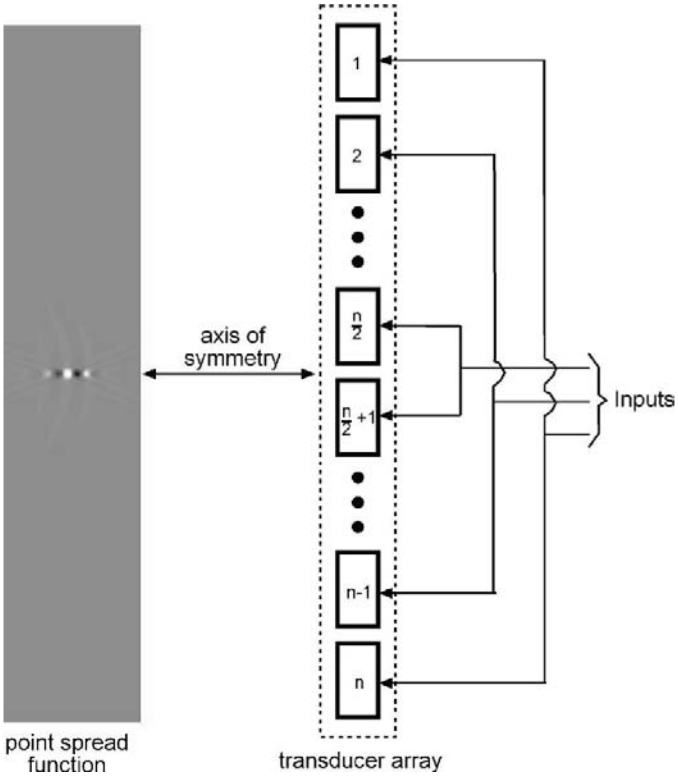

Fig. 1. Exploitation of symmetry for reduced computational cost. The aperture is symmetric about the center axis; therefore, pairs of elements that would have the same weights are grouped together. Also, the lateral symmetry in the PSF about the same center axis allows for analyzing just one-half of the PSF. This symmetry assumes a symmetric, nonsteered aperture.

where $s_{i,j,k}$ is the response at the point i in space for the element j plus the response for element k at the same point in space. The aperture weights also must be reshaped as:

$$w = \left[w_{1,n} \; w_{2,n-1} \; w_{3,n-2} \cdots w_{n/2,n/2+1} \right]^T, \tag{17}$$

where $w_{i,j}$ is the weight applied for element i and element j, respectively.

The derivation is now analogous to that in (6) and (10), and the optimal weights can be determined directly. The use of symmetry reduces the size of the propagation matrix, S, by a factor of 2 in each dimension, for a total reduction of a factor of 4 in memory requirements. The computational savings will be even greater because the necessary solution algorithms have polynomial costs as a function of matrix size.

III. Applications

Although the CLS apodization profiles discussed above were constructed to optimize cystic resolution, the techniques are general enough to be applied in wide-ranging scenarios. A few possible applications are described.

A. Improved Cystic Contrast and Improved Point Resolution

The cystic resolution metric described in [32] stated that the point contrast of an ultrasound system imaging a cyst is a function of the PSF energy. Neglecting system SNR, we note that according to (5) we can improve the contrast of a cyst in two ways. If we minimize the energy of the PSF outside the cyst boundary, the numerator in (5) decreases and contrast improves. Furthermore, if we minimize the energy of the PSF outside the cyst boundary and increase the energy of the PSF inside the cyst boundary, contrast will improve even more dramatically. The LCLS and QCLS methods described above minimize the PSF energy outside a specified boundary subject to a linear constraint on the weights or a quadratic constraint on the weights, respectively. Thus, cystic contrast will be improved by using optimal apodization profiles.

The LCLS apodization profiles produce PSFs with narrow mainlobes and minimum sidelobe energy. These profiles seem to break the governing rule of windowing in signal processing: in order to achieve lower sidelobes, the mainlobe must broaden, a result exhibited by traditional apodization functions. Therefore, the LCLS PSFs are more attractive for point imaging in general ultrasound applications, not only imaging anechoic lesions. Although the LCLS design approach improves cystic resolution, it is not truly optimal for imaging diffuse lesions and low echogenicity cysts. In these cases a broader mainlobe may be desirable. Such profiles can be designed using the QCLS approach.

B. Enhanced Depth of Field

The DOF of an ultrasound imaging system is generally defined as the axial region over which the system is in focus, or the axial region over which the system response remains similar to the PSF at the focus. Current methods to improve DOF include transmitting at a high f/#, dynamically receiving at low f/#'s, and dynamic receive apodization [42]. The implementation of these techniques lacks formal theory describing effectiveness in improving DOF. Application of the CLS algorithms at every range yields receive weightings that force the PSF at each interrogated range to have a specific mainlobe width and the lowest possible sidelobe energy outside that mainlobe. Applying dynamic receive apodization with these weightings will produce similar PSFs in range and improve the DOF.

C. Optimal Apodization for Harmonic Imaging

The linear algebra formulation of the PSF requires linear superposition on receive but places no linearity constraint on transmit. Conventionally, ultrasound imaging systems assume that the propagation of the sound pulse on transmit is linear and that the receive signal has the same frequency content as that of the transmitted pulse. However, the propagation process is substantially nonlinear, and it is possible to receive echoes whose energy content is shifted to harmonics of the fundamental transmit frequency. Imaging with these higher harmonic echoes can improve contrast and resolution in the resulting images. Our CLS techniques can be adapted to calculate receive apodization profiles that take nonlinear propagation into account. The nonlinear propagation of the transmit beam can be determined analytically, experimentally, or through simulation and substituted into the linear algebra formulation of the PSF. Assuming linear propagation on receive, the algorithm will design receive aperture functions that minimize the energy of the two-way PSF outside a specified boundary. Eq. (7) which is rewritten below, describes the relationship between the harmonic imaging scenario and the receive aperture weightings that will minimize the sidelobe energy of the PSF. Note that the propagation matrix S will have to take into account the nonlinear propagation effects of the transmit acoustic beam:

$$w_{\text{opt}} = \left(S^T S\right)^{-1} C \left[C^T \left(S^T S\right)^{-1} C\right]^{-1}.$$

D. Arbitrary PSF Shapes for General Imaging, Hyperthermia or Doppler Applications

In some scenarios, it may be more important to achieve PSFs with greater sidelobe rolloff. The weighted CLS formulations described above can achieve such system responses by incorporating a weight function that increases with distance from the mainlobe. It also is possible with the weighted CLS algorithms to design PSFs with localized areas of reduced energy. It should be noted that we focused on producing apodizations that minimized the PSF energy in the region lying outside a (typically spherical) void. This procedure was implemented in order to optimize cystic resolution. However, there is no need that the mainlobe and sidelobe regions be delineated according to the shape of a cyst. The CLS formulations can be adapted to design optimal PSFs for a variety of ultrasound applications.

In ultrasound hyperthermia procedures, during which control of the acoustic energy delivered to the tissue is of great concern [17], designing PSFs with multiple mainlobes or "hot spots" while minimizing energy transfer at other locations could improve treatment efficacy as well as shorten treatment times. It is possible with the CLS formulation to specify regions of the PSF in which delivered energy should be maximized while at the same time specifying regions in which acoustic energy should be minimized. In the LCLS design case, the linear constraint could be augmented to constrain the peak gain at a number of point locations, which would result in the C^T vector of (6) becoming a matrix whose row size corresponded to the number of hot spots. The QCLS algorithm may produce even better results for this scenario because the quadratic constraint could be modified to include all regions in which the energy of the PSF should be constant.

Many authors have considered the issue of improving the estimation of the blood flow velocity vectors by modulating the acoustic beam in the azimuthal direction using the receive apodization function and using an autocorrelation estimator to determine the lateral velocity [43],

[44]. Similar CLS formulations could be designed in order to produce apodization profiles that generate PSFs with modulation in the azimuthal direction as well as the elevation dimension. These apodization profiles may be able to produce spatial modulation frequencies higher than those previously produced, reducing the variance of the lateral motion estimates [45].

IV. Discussion

The CLS apodization design is a general formulation for designing mathematically optimal system responses. We describe formulation of this approach for a variety of imaging applications. The required propagation functions can be determined through experiments, simulations, or theory.

Implementing CLS apodization is conceptually and practically simple. Apodization weights could be precalculated and stored for the intended application, then retrieved from a look-up table during imaging. Current systems already use dynamic apodization, so implementing the CLS profiles on clinical scanners should be straightforward. However, in order for CLS apodization to be implemented on a clinical system, thorough characterization of the system is required, including the spatial variance of the impulse response. The system geometry and beamforming parameters will determine the degree of spatial variance in the impulse response, which will in turn determine whether or not this must be taken into account during optimization. Either way, once the system has been well characterized, our algorithms save a great deal of development time by obviating iterative design.

For cyst imaging, successive imaging with apodization profiles corresponding to all different design cyst radii would be impractical. The question becomes, "which apodization profiles should be used?" Simulation results, presented in an accompanying paper [33], show that CLS apodization profiles are relatively stable across a range of cyst sizes. In fact, profiles calculated for specific cyst radii outperform conventional windows at all cyst sizes. Choosing the appropriate apodization profile is straightforward when analyzed with the cystic resolution metric. Each apodization yields a contrast curve as a function of cyst radius. Therefore, choosing the optimal profile simply requires selecting the apodization that achieves a specified level of contrast for the smallest cyst, or choosing the profile that yields the best contrast for a given cyst size.

The authors have not encountered any ill-posed design cases in which the CLS algorithms become unstable. However, scenarios certainly exist, such as using an extremely large design cyst radius, where the $S_{\text{out}}^T S_{\text{out}}$ matrix becomes ill-conditioned and rank deficient because no significant amount of PSF energy lies outside the large cyst. Furthermore, because of the large propagation matrices, numerical instability due to round-off errors remains a concern. Identifying the limitations of these algorithms is an area of future work. For most practical design considerations, however, the CLS algorithms perform as expected yielding optimal apodization profiles.

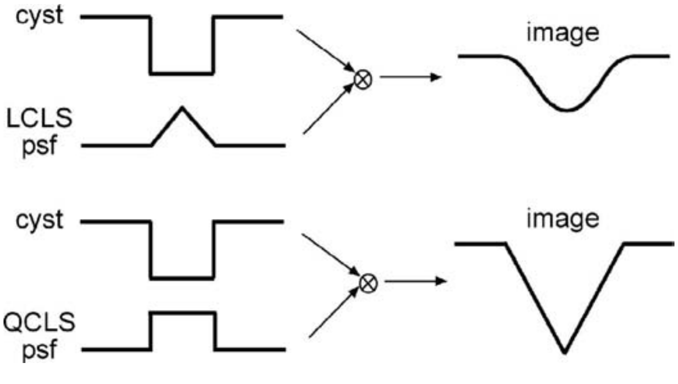

Fig. 2. One-dimensional representation of imaging a cyst with the two CLS PSFs. In the LCLS case, the resulting image of the cyst has sharper defined edges. In the QCLS case the resulting image has blurred edges but more overall contrast than the LCLS imaged cyst.

The authors acknowledge that the resolution metric, although greatly improving theoretical design considerations by accurately predicting system performance, still has some shortcomings. The most worrisome is that the metric describes contrast at a given point in space at a specific instant in time. The metric quantifies contrast of the cyst center versus the background, not the overall cystic contrast. Incorporating detection algorithms, where contrast is defined relative to a speckle region (such as those presented in [36] and [46]) may be necessary. This notion raises further questions regarding cyst detectability and observer efficiency [47]. Which cyst is easier to detect: a cyst with well-defined boundaries but low overall contrast, or a cyst with blurred edges but greater maximum contrast? A simple 1-D analysis yields some insights (Fig. 2).

If we view image formation as a simple convolution between the impulse response of the imaging system and the target function, the CLS algorithms produce two very different results. In one dimension the cyst is modeled as a rect function subtracted from a constant, i.e., (1-rect). In the LCLS case, the resulting PSF resembles a triangle function whose base corresponds to the width of the cyst. This shape stems from the implicit spatial weighting of the LCLS algorithm combined with diffraction. The linear constraint forces the PSF to peak at the center of the cyst while minimizing the PSF energy outside the cyst boundary. The resulting image of the cyst will be a smooth, inverted Gaussian-like function. Note in Fig. 2 that the resulting convolutions are not to scale with the original inputs. In the QCLS case, the cyst remains the same, but the resulting PSF somewhat resembles a rect function whose width corresponds to the size of the cyst. Just like the LCLS case, this shape arises due to the implicit spatial weighting of the algorithm and diffraction. The quadratic constraint weights the spatial points inside the boundary of the cyst equally while trying to minimize the ratio of PSF energy outside the cyst to PSF energy inside the cyst. The resulting image of the cyst will be an inverted triangle function whose negative peak is deeper than that of the smooth, inverted Gaussian resulting from the LCLS apodized PSF. It is not obvious which cyst would be more readily detectable. One has sharper edges (LCLS) but the other has a greater maximum contrast. This effect also was seen in Johnson's [30] analysis comparing Hamming and flat apodization. We hope to explore this issue through a human observer study in which detection of cysts using the CLS apodization profiles will be investigated.

The design method described here is different than that described in [22] for several reasons. First, we do not require a goal PSF in our minimization. Second, our method is considerably easier to implement for broadband imaging systems, while still taking into account the 4-D spatiotemporal nature of the PSF. Another difference is that the algorithm described by Ranganathan and Walker [22] has no constraints on the design weights that could lead to instability of the results. Our algorithm is similar to the MSSE method described by Ranganathan and Walker [22] in that it is general enough to apply to both one-way and two-way responses, continuous wave and broadband operations, and can be used to design apertures for a variety of applications. Another similarity is that the entire PSF is used to obtain a least squares solution to an overdetermined system of equations.

Our method of apodization profile design for coherent imaging systems is similar to many previously described array pattern synthesis techniques. The LCLS formulation is similar to the array pattern synthesis technique by Tseng [6]. However, we use a broadband formulation, a different linear constraint on the weights, and our algorithm does not require iterations to achieve an optimum. This QCLS formulation is similar to the constrained eigenfilter design [8], [24]; however, we use a broadband formulation and a quadratic constraint on the energy in the PSF.

Keitmann-Curdes *et al.* [25] used a formulation similar to our QCLS formulation in designing optimal apodizations in simulated ultrasound fields. However, their method minimized the energy in the sidelobes of the system response over time. The use of space-time PSFs in their model neglects the inherent shift variant properties of the imaging system and integrating the pressure field power over the time axis is not a realistic measure of the system's spatial impulse response. Schwann *et al.* [26] elegantly used two different resolution criteria to design frequency-dependent receive apodization profiles. Their resolution criteria: maximum to average ratio and the fill-in measure relate directly to cystic contrast. However, their multiple objective formulation requires computationally expensive iterative methods to arrive at one Pareto optimum solution. Furthermore, given a Pareto optimal frontier, a curve of all the Pareto optimal solutions as a function of the objectives, for the maximum to average ratio versus fill-in criteria, it is unclear as to what point on that curve is truly optimal for clinical ultrasound imaging. The contrast curves we produce using the cystic resolution metric, however, provide a straightforward approach for parameter optimization.

Our method offers an elegant path for optimizing the ultrasound system's PSF and has potential application to apodization design for many varied applications. Overall, the CLS apodization design technique has the potential to improve the contrast of anechoic legions and improve beamforming in general by forming PSFs with narrow mainlobes and low sidelobes. The technique also may aid in the design of system responses used for hyperthermia applications and Doppler signal processing. Stability of the CLS algorithms in the presence of sound speed errors as well as changing system parameters needs to be investigated. Simulation results addressing these issues for the CLS apodization design technique and its applications are described in an accompanying paper [33]. Results show that CLS apodization profiles improve cystic contrast compared to many conventional windows as well as improve DOF.

V. Conclusions

The CLS apodization design technique presented in this paper is a general beamforming method that can be used to design apertures for specific applications. It achieves mathematically optimal cystic contrast by designing mathematically optimal aperture weights for a given system. The contrast is optimized because the weights minimize the energy of the PSF outside the specified cyst boundary while either maintaining peak gain inside the cyst (LCLS) or maintaining constant PSF energy inside the cyst (QCLS). The CLS apodization design technique also has the potential to improve point resolution by forming PSFs that have narrower mainlobes and lower sidelobes than PSFs generated from conventional windows. Therefore, we believe the CLS apodization design algorithms have significant potential to improve ultrasound beamforming and can be applied in any ultrasound application in which the system response is well characterized.

References

[1] C. L. Dolph, "A current distribution for broadside arrays which optimizes the relationship between beamwidth and sidelobe level," *Proc. IRE*, vol. 34, pp. 335–348, 1946.

[2] T. T. Taylor, "Design of line source antennas for narrow beamwidth and low sidelobes," *IRE Trans. Antennas Propagat.*, vol. AP-3, pp. 16–28, 1955.

[3] A. T. Villeneuve, "Taylor patterns for discrete arrays," *IEEE Trans. Antennas Propagat.*, vol. 32, no. 10, pp. 1089–1093, 1984.

[4] A. H. Nuttall, "Some windows with very good sidelobe behavior," *IEEE Trans. Acoust. Speech Signal Processing*, vol. 29, no. 1, pp. 84–91, 1981.

[5] C. A. Olen and R. T. Compton, Jr., "A numerical pattern synthesis algorithm for arrays," *IEEE Trans. Antennas Propagat.*, vol. 38, no. 10, pp. 1666–1676, 1990.

[6] C.-Y. Tseng and L. J. Griffiths, "A simple algorithm to achieve desired patterns for arbitrary arrays," *IEEE Trans. Signal Processing*, vol. 40, no. 11, pp. 2737–2746, 1992.

[7] I. W. Selesnick, M. Lang, and C. S. Burrus, "Constrained least square design of FIR filters without specified transition bands," *IEEE Trans. Signal Processing*, vol. 44, no. 8, pp. 1879–1892, 1996.

[8] Y.-M. Law and C.-W. Kok, "Constrained eigenfilter design without specified transition bands," *IEEE Trans. Circuits Syst. II: Express Briefs*, vol. 52, no. 1, pp. 14–21, 2005.

[9] S.-C. Pei and J.-J. Shyu, "2-D FIR eigenfilters: A least-squares approach," *IEEE Trans. Circuits Syst.*, vol. 37, no. 1, pp. 24–43, 1990.

[10] P. P. Vaidyanathan and T. Q. Nguyen, "Eigenfilters: A new approach to least-squares FIR filter design and applications including nyquist filters," *IEEE Trans. Circuits Syst.*, vol. 34, no. 1, pp. 11–23, 1987.

[11] M. H. Er, "Array pattern synthesis with a controlled mean-square sidelobe level," *IEEE Trans. Signal Processing*, vol. 40, no. 4, pp. 977–981, 1992.

[12] S. L. Sim and M. H. Er, "Constrained optimization technique for general array pattern synthesis," *Electron. Lett.*, vol. 32, no. 10, pp. 861–862, 1996.

[13] M. H. Er, S. L. Sim, and S. N. Koh, "Application of constrained optimization techniques to array pattern synthesis," *Signal Processing*, vol. 34, pp. 323–334, 1993.

[14] M. H. Er, "On the limiting solution of quadratically constrained broad-band beam formers," *IEEE Trans. Signal Processing*, vol. 41, no. 1, pp. 418–419, 1993.

[15] S. L. Sim and M. H. Er, "Sidelobe suppression for general arrays in presence of element failures," *Electron. Lett.*, vol. 33, no. 15, pp. 1278–1280, 1997.

[16] B. P. Ng, M. H. Er, and C. Kot, "Linear array geometry synthesis with minimum sidelobe level and null control," *IEE Proc. Microw. Antennas Propagat.*, vol. 141, no. 3, pp. 162–166, 1994.

[17] E. S. Ebbini and C. Cain, "Multiple-focus ultrasound phased-array pattern synthesis: Optimal driving-signal distributions for hyperthermia," *IEEE Trans. Ultrason., Ferroelect., Freq. Contr.*, vol. 36, no. 5, pp. 540–548, 1989.

[18] P.-C. Li, S. W. Flax, E. S. Ebbini, and M. O'Donnell, "Blocked element compensation in phased array imaging," *IEEE Trans. Ultrason., Ferroelect., Freq. Contr.*, vol. 40, no. 4, pp. 283–292, 1993.

[19] B. Mandersson and G. Salomonsson, "Weighted least-squares pulse-shaping filters with application to ultrasonic signals," *IEEE Trans. Ultrason., Ferroelect., Freq. Contr.*, vol. 36, no. 1, pp. 109–113, 1989.

[20] W. Wilkening, B. Brendel, H. Jiang, J. Lazenby, and H. Ermert, "Optimized receive filters and phase-coded pulse sequences for contrast agent and nonlinear imaging," in *Proc. IEEE Ultrason. Symp.*, 2001, pp. 1733–1737.

[21] W. Wilkening, B. Brendel, C. Hansen, and H. Ermert, "Optimized filters for dynamic RF echo blending in multiple focal zone imaging," in *Proc. IEEE Ultrason. Symp.*, 2004, pp. 1729–1732.

[22] K. Ranganathan and W. F. Walker, "A novel beamformer design method for medical ultrasound. Part I: Theory," *IEEE Trans. Ultrason., Ferroelect., Freq. Contr.*, vol. 50, no. 1, pp. 15–24, 2003.

[23] K. Ranganathan and W. F. Walker, "A novel beamformer design method for medical ultrasound. Part II: Results," *IEEE Trans. Ultrason., Ferroelect., Freq. Contr.*, vol. 50, no. 1, pp. 25–39, 2003.

[24] S. Docolo and M. Moonen, "Design of far-field and near-field broadband beamformers using eigenfilters," *Signal Processing*, vol. 83, pp. 2641–2673, 2003.

[25] O. Keitmann-Curdes, B. Brendel, C. Marg, and H. Ermert, "Optimization of apodization based on the sidelobe pressure energy in simulated ultrasound fields," in *Proc. IEEE Ultrason. Symp.*, 2002, pp. 1677–1680.

[26] R. Schwann, N. Stache, and T. G. Noll, "Optimization of frequency dependent receive apodization," in *Proc. IEEE Ultrason. Symp.*, vol. 4, 2005, pp. 1988–1991.

[27] M. D. Intriligator, *Mathematical Optimization and Economic Theory.* Philadelphia, PA: Society for Industrial and Applied Mathematics, 2002, p. 258.

[28] B. D. Steinberg, *Principles of Aperture and Array System Design.* New York: Wiley, 1976, pp. 40–52.

[29] D. Vilkomerson, J. Greenleaf, and V. Dutt, "Towards a resolution metric for medical ultrasonic imaging," in *Proc. IEEE Ultrason. Symp.*, 1995, pp. 1405–1410.

[30] R. Johnson, "Contrast response analysis for medical ultrasound imaging," *IEEE Trans. Ultrason., Ferroelect., Freq. Contr.*, vol. 44, no. 4, pp. 805–809, 1997.

[31] K. F. Üstüner and G. L. Holley, "Ultrasound imaging system performance assessment," presented at AAPM Annu. Meeting, 2003.

[32] K. Ranganathan and W. F. Walker, "A general cystic resolution metric for medical ultrasound," *IEEE Trans. Ultrason., Ferroelect., Freq. Contr.*, submitted for publication.

[33] D. A. Guenther and W. F. Walker, "Optimal apodization design for medical ultrasound using constrained least squares. Part II: Simulation results," *IEEE Trans. Ultrason., Ferroelect., Freq. Contr.*, this issue, pp. 000–000.

[34] J. W. Goodman, *Introduction to Fourier Optics.* 3rd ed. Englewood, CO: Roberts & Company, 2005.

[35] A. R. Selfridge, G. S. Kino, and B. T. Khuri-Yakub, "A theory for the radiation pattern of a narrow-strip acoustic transducer," *Appl. Phys. Lett.*, vol. 37, no. 1, pp. 35–36, 1980.

[36] S. W. Smith, R. F. Wagner, J. M. Sandrik, and H. Lopez, "Low contrast detectability and contrast/detail analysis in medical ultrasound," *IEEE Trans. Sonics Ultrason.*, vol. 30, no. 3, pp. 164–173, 1983.

[37] L. L. Scharf, *Statistical Signal Processing: Detection, Estimation, and Time Series Analysis.* Reading, MA: Addison-Wesley, 1991.

[38] Y. Y. Haimes, *Risk Modeling, Assessment, and Management.* 2nd ed. New York: Wiley, 2004.

[39] G. H. Golub and C. F. Van Loan, *Matrix Computations.* 3rd ed. Baltimore: Johns Hopkins Univ. Press, 1996, pp. 375–378.

[40] W. H. Gander, "Least squares with a quadratic constraint," *Numerische Mathematik*, vol. 36, pp. 291–307, 1981.

[41] A. Björck, *Numerical Methods for Least Squares Problems.* Philadelphia: Society for Industrial and Applied Mathematics, 1996, pp. 203–213.

[42] K. Thomenius, "Evolution of ultrasound beamformers," in *Proc. IEEE Ultrason. Symp.*, 1996, pp. 1615–1622.

[43] J. A. Jensen and P. Munk, "A new method for estimation of velocity vectors," *IEEE Trans. Ultrason., Ferroelect., Freq. Contr.*, vol. 45, pp. 837–851, 1998.

[44] M. E. Anderson, "Spatial quadrature: A novel technique for multidimensional velocity estimation," in *Proc. IEEE Ultrason. Symp.*, 1997, pp. 1233–1238.

[45] W. F. Walker and G. E. Trahey, "A fundamental limit on delay estimation using partially correlated speckle signals," *IEEE Trans. Ultrason., Ferroelect., Freq. Contr.*, vol. 42, pp. 301–308, 1995.

[46] S. W. Smith and H. Lopez, "A contrast-detail analysis of diagnostic ultrasound imaging," *Med. Phys.*, vol. 9, no. 1, pp. 4–12, 1982.

[47] C. K. Abbey, R. J. Zemp, J. Liu, K. K. Lindfors, and M. F. Insana, "Observer efficiency in discrimination tasks simulating malignant and benign breast lesions imaged with ultrasound," *IEEE Trans. Med. Imag.*, vol. 25, no. 2, pp. 198–209, 2006.

Drake A. Guenther received his B.S.E. degree in biomedical engineering in 2003 from Duke University, Durham, NC. His undergraduate research as a Pratt Fellow explored adaptive beamforming and spatial compounding in ultrasound.

After completing his B.S.E., he joined the Department of Biomedical Engineering at the University of Virginia, Charlottesville, VA, where he is currently pursuing his Ph.D. degree. His research interests include ultrasound beamforming, signal processing, and angular scatter imaging.

William F. Walker (S'95–M'96) received the B.S.E. and Ph.D. degrees in 1990 and 1995 from Duke University, Durham, NC. His dissertation explored fundamental limits on the accuracy of adaptive ultrasound imaging.

After completing his doctoral work, he stayed at Duke as an assistant research professor in the Department of Biomedical Engineering. At the same time, he served as a Senior Scientist and President of NovaSon Corporation located in Durham, NC. In 1997 he joined the faculty of the Department of Biomedical Engineering at the University of Virginia, Charlottesville, VA, being promoted to associate professor in 2003. He is an active founder in two ultrasound-based startup companies, PocketSonics Inc., Charlottesville, VA, and HemoSonics LLC, Charlottesville, VA.

His research interests include aperture domain processing, beamforming, angular scatter imaging, tissue elasticity imaging, low-cost system architectures, and time-delay and motion estimation.

Optimal Apodization Design for Medical Ultrasound Using Constrained Least Squares Part II: Simulation Results

Drake A. Guenther and William F. Walker, *Member, IEEE*

***Abstract*—In the first part of this work, we introduced a novel general ultrasound apodization design method using constrained least squares (CLS). The technique allows for the design of system spatial impulse responses with narrow mainlobes and low sidelobes. In the linear constrained least squares (LCLS) formulation, the energy of the point spread function (PSF) outside a certain mainlobe boundary was minimized while maintaining a peak gain at the focus. In the quadratic constrained least squares (QCLS) formulation, the energy of the PSF outside a certain boundary was minimized, and the energy of the PSF inside the boundary was held constant. In this paper, we present simulation results that demonstrate the application of the CLS methods to obtain optimal system responses. We investigate the stability of the CLS apodization design methods with respect to errors in the assumed wave propagation speed. We also present simulation results that implement the CLS design techniques to improve cystic resolution. According to novel performance metrics, our apodization profiles improve cystic resolution by 3 dB to 10 dB over conventional apodizations such as the flat, Hamming, and Nuttall windows. We also show results using the CLS techniques to improve conventional depth of field (DOF).**

I. Introduction

In an accompanying paper [1], we describe two apodization design methods using a constrained least squares (CLS) formulation. The algorithms allow for the synthesis of beam patterns with a specified mainlobe width and minimum energy in the sidelobe regions. The CLS techniques express the system spatial impulse response (PSF) using a linear algebra formulation of the aperture weights and a propagation function. The propagation matrix uses superposition to describe the contribution of each transducer element at each field point at an instant in time and can be determined from experiment, simulation, or theory. The CLS formulations provide closed form solutions for the aperture weightings that minimize the energy of the PSF outside some specified boundary subject to either a linear or quadratic constraint on the weights. A brief review of the major results derived in [1] is provided below.

A. Linear Algebra Formulation of the Broadband Spatial Impulse Response

The sensitivity field for a transducer during pulse-echo imaging can be expressed as the product of a propagation matrix, S, and a set of aperture weightings, w. S can be derived from the Rayleigh-Sommerfeld diffraction equation, outlined in [2] and may include a term relating to limited element angular response [3] and frequency-dependent attenuation. The propagation matrix also can be simulated or measured experimentally. For our formulation, S is a function of the transmit aperture weights, the excitation pulse, and the individual element spatial impulse responses of the transmit and receive apertures. The two-way PSF, P, is then simply the matrix multiplication between the propagation matrix and the weight vector:

$$P = Sw. \tag{1}$$

B. Linearly Constrained Least Squares Apodization Design

In the first CLS apodization design technique, we minimize the energy of the PSF outside a certain mainlobe region subject to a linear constraint on the aperture weights. Although our formulation can account for the four-dimensional (4-D) nature of the spatiotemporal PSF, we restrict our analysis to two spatial dimensions, azimuth and range, and a single instant in time. The mainlobe region is defined by a circle of a specified radius centered at the peak of the 2-D PSF. Drawing upon [4], we can derive the least squares solution for the receive aperture weightings that produce the desired PSF:

$$w_{\text{opt}} = \left(S^T S\right)^{-1} C \left[C^T \left(S^T S\right)^{-1} C\right]^{-1}, \tag{2}$$

where the superscripts T and -1 denote the transpose and matrix inverse operations, respectively. S represents the propagation matrix for every spatial point of the PSF in which energy is to be minimized, and C is the linear constraint vector. The linear constraint, $C^T w = 1$, maintains a peak gain of the PSF at the intended focus. C has elements corresponding to the individual amplitude response of each synthetic receive element at the intended focus.

C. Quadratically Constrained Least Squares Apodization Design

The second CLS apodization design technique minimizes the energy of the PSF outside the defined mainlobe

---

Manuscript received June 5, 2006; accepted November 1, 2006.

This work was supported by US Army Congressionally Directed Research Program Grant No. W81XWH-04-1-0590.

The authors are with the University of Virginia, Department of Biomedical Engineering, Charlottesville, VA (e-mail: dag2m@virginia.edu).

Digital Object Identifier 10.1109/TUFFC.2007.248

0885–3010/$25.00 © 2007 IEEE

region, while maintaining constant energy of the PSF inside the mainlobe region. We formulate this problem as a least squares minimization subject to a quadratic constraint on the weights. This method requires the formation of two propagation matrices. The first, S_{out}, represents the propagation matrix associated with every point of the PSF in which energy is to be minimized, as in (2). The second, S_{in}, represents the propagation matrix associated with every point of the PSF lying inside the mainlobe boundary and appears in the quadratic constraint, $\|S_{\text{in}}w\|^2 = 1$, where $\| \bullet \|^2$ denotes the square of the ℓ^2-norm. Drawing upon [5] and [6], the set of optimal receive weightings for this scenario is given by the generalized eigenvector corresponding to the minimum generalized eigenvalue resulting from the generalized eigenvalue decomposition problem of $S_{\text{out}}^T S_{\text{out}}$ and $S_{\text{in}}^T S_{\text{in}}$:

$$S_{\text{out}}^T S_{\text{out}} w = \lambda S_{\text{in}}^T S_{\text{in}} w, \tag{3}$$

where the weight vector w is the generalized eigenvector and λ is the associated generalized eigenvalue.

D. Reduced Computational Cost Through Symmetry Relations

The CLS apodization design techniques can become computationally expensive rather easily due to the large propagation matrices and the computation of the matrix inverse (only for the linear constrained least squares (LCLS) design case). In order to reduce this computational complexity, we exploit the lateral symmetry of the aperture and the PSFs that arise from symmetric, nonsteered apertures [1]. Due to the symmetry relationships, we need only compute half of the aperture weights using just half of the PSF, thereby enabling more efficient computation of the apodization profiles. Note that, although the design and calculation of the weights is computationally costly, the application of the weights is trivial in modern ultrasound system hardware. Once the CLS apodization profiles have been calculated, they can be stored in a lookup table and applied as dynamic apodization with range.

All the formulas for the design methods described above are thoroughly described and derived in [1]. This paper presents results of simulations that were implemented to demonstrate the validity and stability of the LCLS and quadratic constrained least squares (QCLS) apodization design techniques.

II. Simulations

In order to test our apodization design algorithms and to highlight the utility of the cystic resolution metric [8] we performed simulations using DELFI [7], a custom ultrasound simulation tool that efficiently computes spatial pulse-echo responses. All simulations were performed under MATLAB (The Mathworks, Inc., Natick, MA). Spatial pulse-echo responses were computed by transmitting a focused wave from a fixed f/# aperture and synthetically receiving on each individual element in the array. Uniform apodization was applied on transmit. Dynamic receive focusing was used to calculate multiple PSFs at varying depths. The focal ranges on receive were 1 cm, 1.5 cm, 2 cm, 2.5 cm, and 3 cm. The PSFs were computed at the instant in time corresponding to the given receive depth and over a 2-D planar area in azimuth and range that encompassed the entire extent of the PSF.

TABLE I
Parameters Used in General CLS Apodization Design and Speed of Sound Simulations.

Parameter	Value
Number of elements	192
Element pitch	200 μm
Focus	2.0 cm
PSF window lateral sampling interval	34 μm
PSF window axial sampling interval	20 μm
Ultrasonic wave propagation speed	1545 m/s
Frequency	6.5 MHz
Fractional bandwidth	50%

TABLE II
Parameters Used in General CLS Apodization Design and F/# Simulations.

Parameter	Value
Number of elements	192
Element pitch	150 μm
Focus	2.0 cm
PSF window lateral sampling interval	25 μm
PSF window axial sampling interval	20 μm
Ultrasonic wave propagation speed	1545 m/s
Frequency	10 MHz
Fractional bandwidth	75%

We simulated two different 1-D linear arrays. The first array, whose system parameters are described in Table I, operated at 6.5 MHz center frequency with a 50% fractional bandwidth calculated as:

$$\text{Fractional BW}\,(\%) = \frac{\text{BW}}{f_c} \times 100, \tag{4}$$

where f_c is the center frequency of the transmitted pulse in megahertz and BW is the -6 dB bandwidth of the pulse also in megahertz. The array had fixed transmit focus at 2 cm (f/2). The 6.5 MHz array was used for general CLS apodization design and for the speed of sound simulations. The second array was more aggressive with a higher operating frequency of 10 MHz with a 75% fractional bandwidth. We kept the transmit focus fixed at 2 cm but used a larger f/# on transmit (f/4). This array also was used for apodization design and for the varying receive f/# simulations. The system parameters for the second array are described in Table II.

Constrained least squares apodization profiles were designed and analyzed for improvements in system performance relative to conventional apodization. All calculations were performed on an IBM Intellistation Z Pro (Processor speed 2.80 GHz, 3.00 Gb RAM, IBM Corporation, Armonk, NY). In general the CLS apodization profiles took less than two minutes of CPU time to generate, and the QCLS profiles were faster to generate than the LCLS profiles because they do not require computing a matrix inverse. The 2-D PSFs generated using DELFI [7] were used to calculate the optimal receive weights according to the CLS algorithms outlined above. CLS apodization profiles were computed for each dynamic receive response because of the spatial shift variance of the PSF with range. The sidelobe region was defined by centering a cyst of a specified radius about the mainlobe peak of the PSF. As this cyst specifies the mainlobe and sidelobe regions of the PSF, we call it the "design cyst." Cystic contrast, neglecting electronic signal-to-noise ratio (SNR), was computed according to the equation given in [8] as:

$$C = \sqrt{\frac{E_{\text{out}}}{E_{\text{tot}}}}, \tag{5}$$

where E_{out} is the energy of the PSF outside the mainlobe boundary, and E_{tot} is the entire energy of the PSF. Note that the best achievable contrast occurs when the cyst void encompasses the entire PSF. In this scenario, C in (5) would be 0. Therefore, when quantifying cystic contrast, a C value closer to 0, or more negative on a decibel scale, indicates better performance. Corresponding cystic contrast curves as a function of cyst radius were calculated for the CLS windows and compared to those for the flat, Hamming, and the Nuttall [21] windows.

To investigate the performance of the algorithms, we computed apodization profiles for a large number of design cyst radii. Specifically, we present results of LCLS and QCLS aperture weights with design cyst radii from 0.1 mm to 2.0 mm. We also computed the weights that minimized the mainlobe width for the LCLS design case in order to test the limits of this particular algorithm.

Because most commercial systems use dynamic receive focusing to improve image contrast and extend the conventional DOF, we investigated the stability of our algorithms in this scenario. We calculated PSFs at varying depths on receive (1.0 cm, 1.5 cm, 2.0 cm (Tx focus), 2.5 cm, and 3.0 cm) then applied the CLS algorithms on each PSF. The resulting aperture weights should improve DOF because the goal of applying the CLS algorithms was to make PSFs with a similar mainlobe and minimum sidelobe energy.

An important system parameter that affects image quality and contrast is the f/# used on receive. It is an important parameter for a linear array because dynamic focusing schemes that maintain constant f/# throughout the image range are limited by aperture size. We investigated the impact of f/# on our CLS apodization design algorithms by computing contrast curves as a function of cyst radius for varying f/#'s.

Errors in the assumed sound wave propagation velocity adversely affect an ultrasound system's response, potentially degrading the resulting images [9]. Because our CLS technique uses dynamic shift variant aperture weights, errors in the assumed sound speed are of great concern. Therefore, we implemented simulations in which the assumed propagation speed was underestimated by 1%, 3%, and 5%, and overestimated by 1%, 3%, and 5%. The PSFs were calculated at the instant in time corresponding to the intended transmit focus of 2 cm assuming 1545 m/s. Due to different propagation speeds through the medium, however, the PSFs shifted in range. The purpose of these simulations was to investigate the robustness of our algorithm to incorrect assumptions about the wave propagation speed.

III. Results

Optimal receive apodization profiles were computed for a linear 1-D array according to the CLS formulations discussed above. Cystic resolution curves were calculated in order to visualize and quantify the changes in system performance using the CLS windows compared to the conventional windows. Apodization profiles were computed for a range of design cyst radii from 0.1 mm to 2.0 mm. For every design cyst radius, the CLS apodization profiles resulted in PSFs that had lower energy in the sidelobe regions compared to the other windows.

Fig. 1 shows results for the 6.5 MHz simulations with a fixed transmit focus at 2 cm (f/2) and dynamic receive focus at 2 cm (f/1). The plot on the left shows an up close view of the mainlobe region of the integrated lateral beamplots using different apodization schemes. All lateral beamplots were computed by taking the square root of the energy of the 2-D PSF summed in range. The CLS profiles were designed using a cyst radius of 0.6 mm. We also used the LCLS algorithm to design an apodization profile that produces a PSF with the narrowest possible mainlobe. This beamplot is the mCLS plot in Fig. 1 designated by a □ marker. The full width at half maximums (FWHM), −6 dB beamwidths, were 264, 304, 328, 297, 301, and 190 μm for the flat, Hamming, Nuttall, LCLS, QCLS, and mCLS apodizations, respectively. The LCLS and QCLS apodization profiles had smaller −6 dB beamwidths than all but one of the conventional windows. The LCLS and QCLS lateral beamplots have decreased sidelobe levels by about 5 dB relative to the Hamming window, 12 dB below the flat apodization, and almost 16 dB below the Nuttall window. The mCLS apodization lateral beamplot has the narrowest mainlobe (20% reduction compared to the flat window) but the highest sidelobe levels. The plot on the right shows the full extent of the integrated lateral beamplots of the PSFs with notable differences in the grating lobe levels. The reduction of the sidelobe levels for the LCLS and QCLS apodization profiles did result in higher grating lobes than the Hamming and Nuttall windows, but these larger grating lobes are around −60 dB, a typical noise floor for diagnostic ultrasound imaging systems [10]. The mCLS lateral beamplot shows much larger grating lobes around −40 dB.

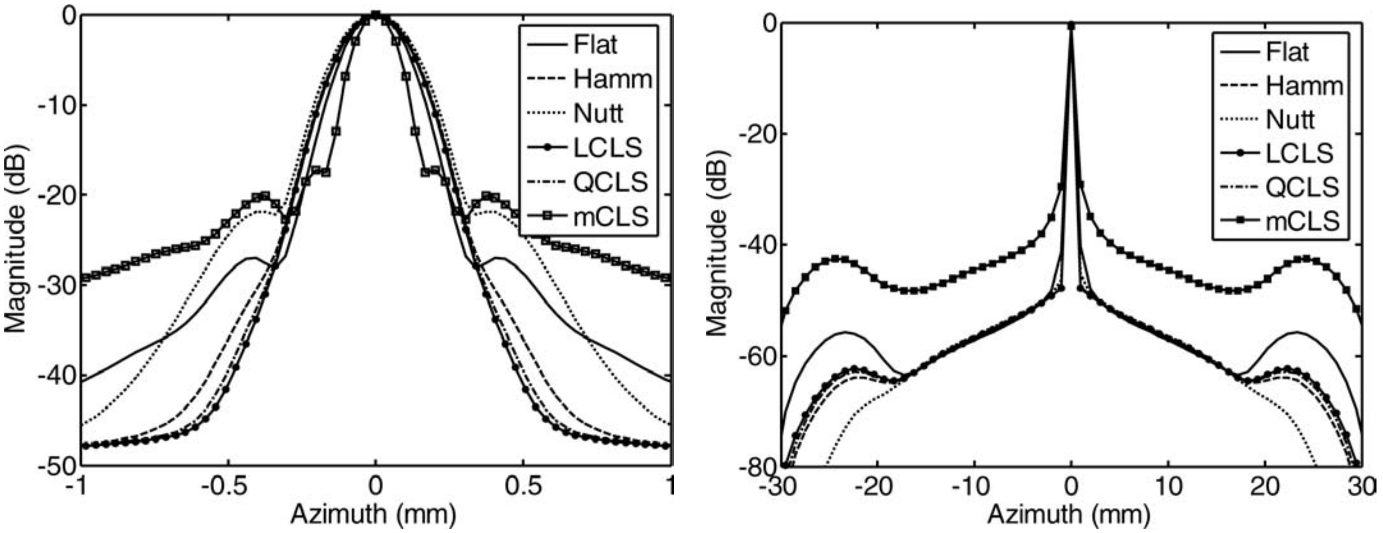

Fig. 1. Integrated lateral beamplots for different apodization schemes with the 1-D linear array operating at 6.5 MHz center frequency, fixed Tx focus at 2 cm (f/2) and dynamically focused on Rx at 2 cm (f/1). The LCLS and QCLS profiles were designed with a cyst radius of 0.6 mm. Note that the LCLS and QCLS profiles yield sidelobe levels lower than and mainlobe widths comparable to all other apodizations.

A. Effects of the Design Cyst Radius on the CLS Apodization Algorithms

Because it is unreasonable to scan through apodization profiles for every cyst radius with conventional systems, it is interesting to monitor the behavior of the CLS apodization profiles with increasing design cyst radius. Furthermore, using contrast curves we can easily compare the performance of the different apodization schemes and optimize based on required operation values. In Fig. 2 we show the performance of both the LCLS apodization windows (left column) and the QCLS apodization windows (right column) as we increase the design cyst radius from 0.2 mm to 0.8 mm in 0.2 mm steps. These simulations used the 6.5 MHz linear array conditions described in Table I. The results at different dynamic receive depths were similar so we present one set of simulation results in Fig. 2 corresponding to a dynamic receive depth of 1.5 cm. The first row of plots, panels (a) and (b), shows the contrast curves over cyst radii from 0.1 mm to 1.0 mm. For the LCLS windows, (a), we see a general trend of decreased contrast for the smaller cyst sizes when increasing the design cyst radius. At the same time, we see greatly improved contrast over a large range of cyst radii for the larger design radius curves. Overall the LCLS windows maintained relatively similar contrast curves for design cyst radii of 0.4, 0.6, and 0.8 mm. These profiles improved contrast around 5 dB relative to the flat apodization scheme across the range of larger cyst sizes (0.4 mm–1.0 mm). The QCLS contrast curves changed more than the LCLS curves across the range of design cyst radii. Each QCLS apodization profile achieved the best contrast of any window for the specific design radius; however, the QCLS profiles suffered greater losses in contrast for cyst sizes smaller than the design cyst radius compared to the LCLS profiles designed for the same cyst radius. This phenomenon can be seen easily with the 0.6 mm and 0.8 mm contrast curves where they decrease contrast by about 3 dB compared to the flat apodization for cyst radii smaller than 0.4 mm. The second row of plots in Fig. 2 shows the mainlobe region of the CLS integrated lateral beamplots. The widening of the mainlobe for the QCLS profiles is more dramatic than the LCLS profiles. This phenomenon is to be expected due to the formulation of the QCLS algorithm, which minimizes the ratio of PSF energy outside the cyst to PSF energy inside the cyst. The third row of plots, panels (e) and (f), shows the changes in the grating lobes with different design cyst radius.

The final row of plots in Fig. 2 shows the designed apodization weights for each individual element. For the most part, the CLS profiles have a typical smooth, curved shape like many of the conventional windows; however, the CLS windows' behavior at the ends of the aperture is discontinuous. These apodization profiles also show that some outer elements have negative weights and large magnitudes, a phenomenon never seen in the conventional window functions. The positive-negative discontinuity at the edges of the aperture is indeed an intriguing result. The outer elements in an aperture contribute high lateral spatial frequency content, which can sharpen the mainlobe of the overall response [11]. However, these elements also give the PSF "wings," clouds of energy outside the mainlobe region that spread in azimuth and range. Conventional apodization functions typically suppress the outer elements of an aperture to decrease this sidelobe energy. However, this reduces the high lateral spatial frequency content in the overall response. It appears that the positive-negative discontinuity at the edges of the CLS apodization functions is a novel way to sharpen the PSF's mainlobe and reduce the energy in the PSF's "wings" through destructive interference.

In the simulations that used the 10 MHz array configuration, we calculated CLS apodization profiles for a number of different cyst radii. Through this investigation we

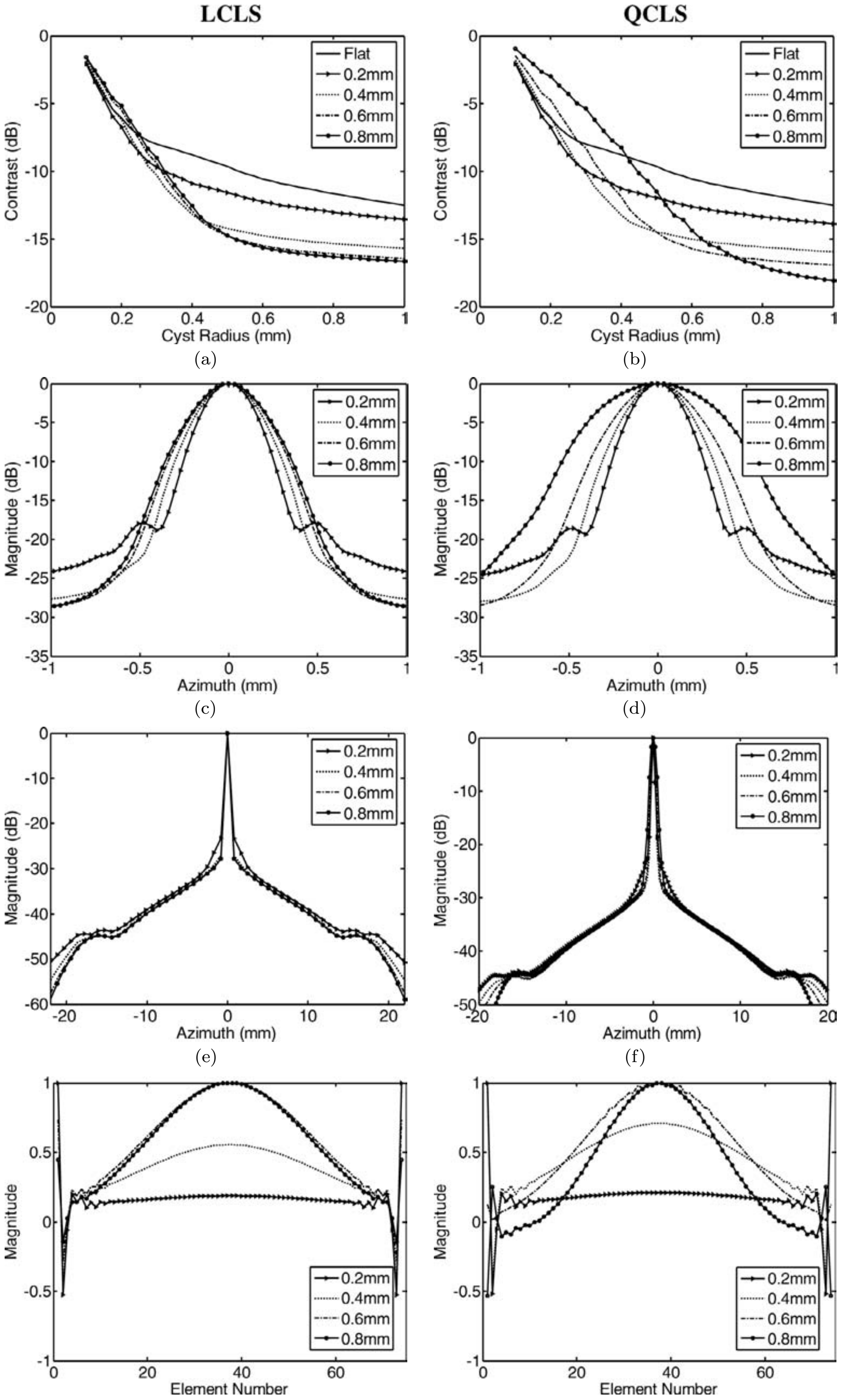

(a) (b)

(c) (d)

(e) (f)

(g) (h)

Fig. 2. Comparison of CLS apodization given different design cyst radii. The entire left column corresponds to the LCLS algorithm, and the right column corresponds to the QCLS algorithm. (a) and (b) show the associated contrast curves over a range of cyst sizes compared to the flat apodization profile. Panels (c) and (d) show the mainlobe behavior of the CLS windows. The third row, panels (e) and (f), gives the full range of the integrated lateral beamplots. (g) and (h) plot the apodization profile versus element number. Note how the mainlobe width trends with increasing design radius are indicative of the contrast performance between the two algorithms.

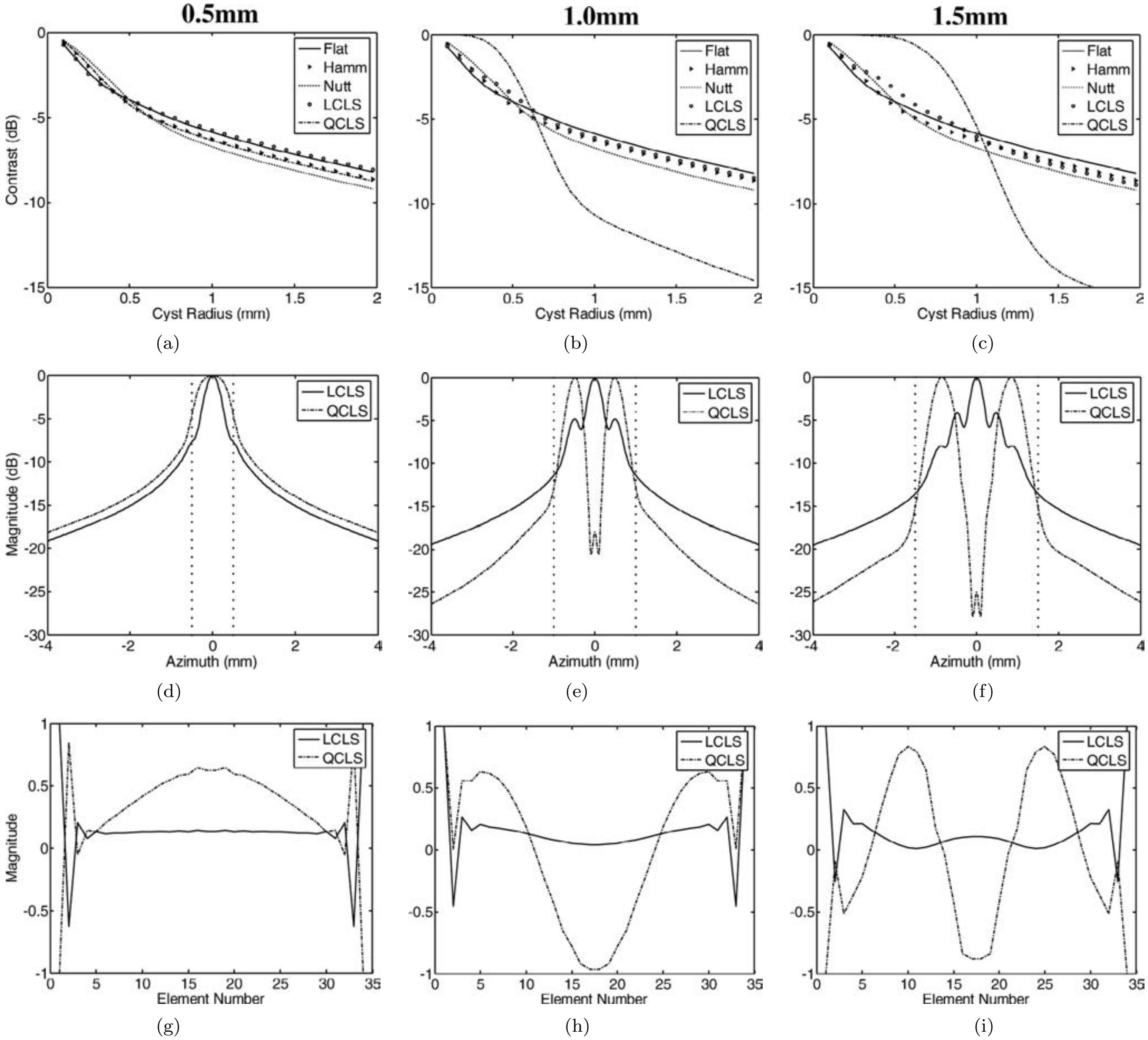

Fig. 3. Comparison of apodization profiles with large design cyst radius. Panels (a)–(c) plot the contrast curves for design radii of 0.5 mm, 1.0 mm, and 1.5 mm, respectively. The second row of plots shows the integrated lateral beamplots. The third row of plots, panels (g)–(i), shows the LCLS and QCLS apodization profiles as a function of element number across the aperture. Note that, for larger design radii, the QCLS algorithm results in PSFs with multiple peaks in the mainlobe region.

observed a peculiar phenomenon for the QCLS algorithm for the larger design cyst radii. Because the algorithm attempts to keep the energy of the PSF inside the cyst boundary constant, when larger design cyst radii are used, the QCLS weights make a PSF with multiple peaks. This is equivalent to the eigenfilter design approach in which the frequency response ripples in the pass band [12], [13]. Fig. 3 plots (e) and (f) accurately depict this phenomenon. These data use the 10 MHz array described in Table II with a dynamic receive focus at 1.0 cm (f/2). The first row of plots in Fig. 3(a)–(c), shows the contrast curves for increasing design radii of 0.5 mm, 1.0 mm, and 1.5 mm, respectively. Note for the larger design radii, the QCLS algorithm results in contrast improvements ranging from 5 dB to 10 dB but poor contrast resolution for smaller cyst sizes. Fig. 3 plots (d)–(f) show the integrated beamplots for the LCLS and QCLS apodization profiles. Here we see how the QCLS algorithm was able to achieve the dramatic contrast improvements for the larger cyst sizes by having multiple mainlobes inside the cyst boundary. Likewise, for large design radii, the LCLS apodization profile results in higher sidelobes inside the boundary in order to achieve lower sidelobes outside the boundary.

The modulation of the mainlobe in the QCLS PSFs would not be an ideal spatial response for general imaging purposes. Notice that the shape of the QCLS apodization profiles that yield multiple mainlobe peaks are approximately sinusoidal [Fig. 3 panels (h) and (i)]. According to the Fraunhoffer approximation, which states that the spatial response of an aperture is the Fourier transform

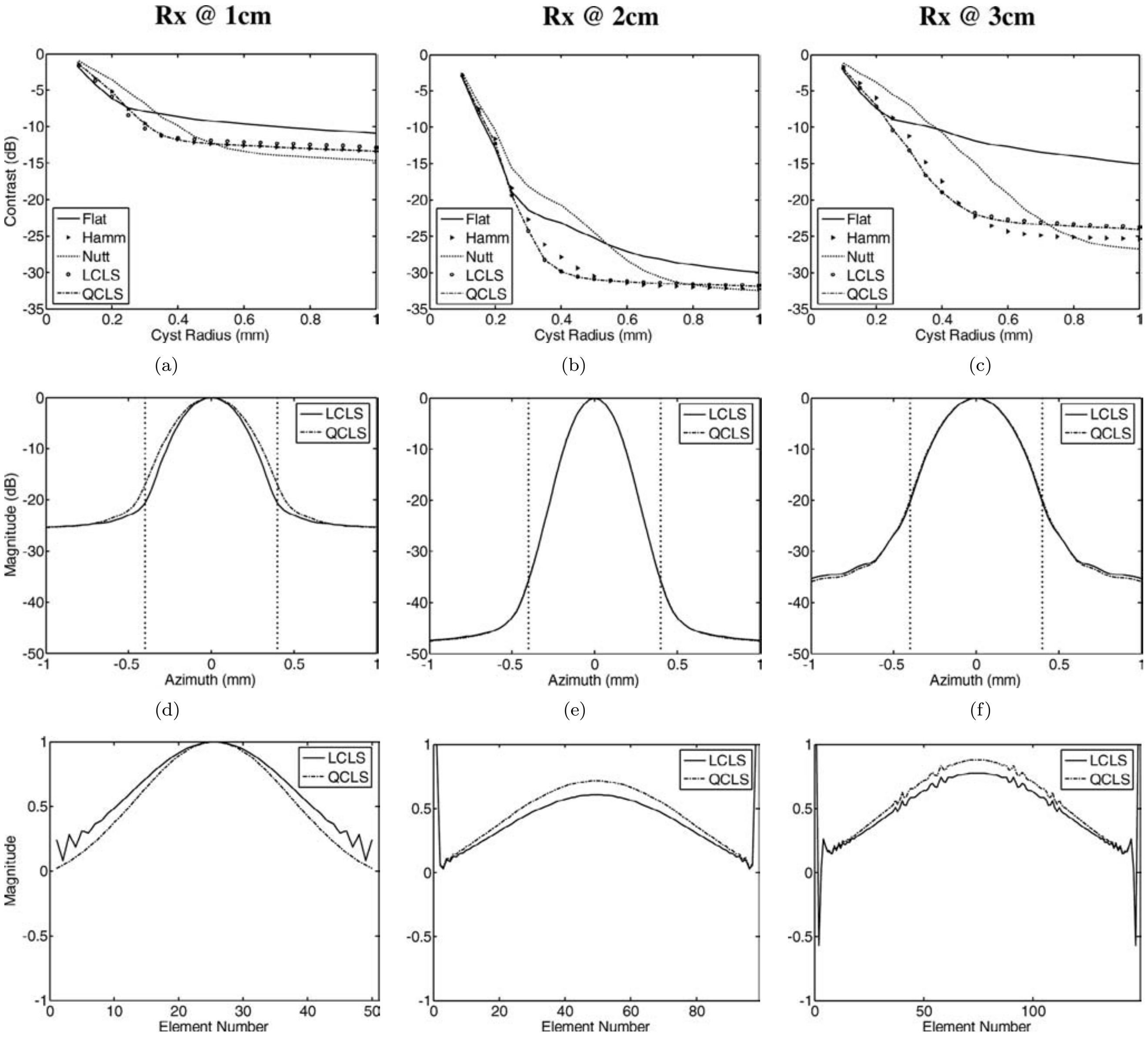

(a) (b) (c)

(d) (e) (f)

(g) (h) (i)

Fig. 4. Comparison of apodization profiles at different dynamic receive foci of 1 cm, 2 cm, and 3 cm and constant f/# (f/1). Panels (a)–(c) show contrast curves for the different apodization schemes (flat, Hamming, Nuttall, LCLS, and QCLS). The second row of plots, (d)–(f), show the integrated beamplots of the CLS profiles in which the dotted line corresponds to the cyst boundary used to design the windows. Plots (g)–(i) show the magnitude of the CLS profiles across the aperture. The CLS profiles improve contrast over a range of smaller cysts at all dynamic receive focal depths.

of the aperture function [2], a rectangular windowed sinusoidal aperture function should result in a lateral spatial response resembling two sinc functions (the convolution between a sinc and two impulses). These two sinc functions correspond to the two mainlobes in the responses seen in Fig. 3 panels (e) and (f). Furthermore, note that, when the frequency of the sinusoid corresponding to the aperture definition is increased [comparing panel (h) to panel (i)], the two mainlobes of the spatial response separate further in azimuth [panel (e) and (f)]. This result is consistent with Fourier transform theory.

Clearly imaging with a PSF that has two mainlobes should not produce an image of a cyst with 10 dB contrast improvement, as the contrast curves of Fig. 3 panels (b) and (c) suggest. However, there are applications in which lateral modulation of the PSF could prove beneficial [14], [15]. For example, such a PSF could be used in Doppler ultrasound for which acquiring the axial as well as lateral component of velocity can lead to more accurate estimation of the velocity vector [16]. Other applications could include designing ultrasound spatial responses for hyperthermia treatments during which control over localized energy delivery is paramount [17]. We also are investigating ways to modify the QCLS apodization design formulation to reduce the modulation/multiple peak effect to an equiripple, similar to finite impulse response (FIR) filter design [18]. One possible method is to use the weighting function discussed and derived in [1]. Applying a weighting function to the mainlobe region of the PSF that emphasizes the focal point compared to the surrounding area would yield a PSF with a single mainlobe. Preliminary results show that the weighting can be applied to the QCLS algorithm to mitigate the multiple mainlobe effect. The resulting QCLS weights produce PSFs whose lateral beamplots are similar to the LCLS beamplots in Fig. 3 panels (e) and (f) with slightly higher sidelobes inside the cyst boundary.

B. Effects of Dynamic Receive Focusing on the CLS Apodization Algorithms

In our simulations, we also investigated the effects of dynamic receive focusing on the performance of the CLS algorithms. Conventional systems typically maintain a constant beamwidth over a large range by transmitting on a higher f/# and dynamically receiving with a constant, lower f/#. Because our apodization design schemes effectively control mainlobe size, we expect to see improvements in DOF. For these simulations, we used the 6.5 MHz linear array setup with the fixed transmit focus at 2 cm (f/2), then we dynamically received focused data at 1 cm, 1.5 cm, 2 cm, 2.5 cm, and 3 cm with an f/1 aperture. CLS apodization profiles were designed with an aggressive cyst radius of 0.4 mm for the PSFs at each range. Fig. 4 shows the results from these dynamic receive focused and apodized simulations. We show only data from dynamic receive depths of 1 cm, 2 cm, and 3 cm because the data at the other two depths showed similar trends. Fig. 4 panels (a)–(c) show the contrast curves for the different apodization schemes across cyst radii. The LCLS and QCLS contrast curves for all three ranges are very similar, hence why the QCLS curve is difficult to distinguish. The reduced contrast at the 1 cm and 3 cm depths can be attributed to the spreading of the mainlobe away from the transmit focus. At all three ranges, the CLS apodization schemes show marked contrast improvements over the flat and Nuttall apodization schemes across a large range of cyst sizes and reasonable improvements over the Hamming window at smaller cyst radii. Both the Hamming and the Nuttall window outperform the CLS apodization profiles for cyst radii greater than 0.5 mm when receiving at 1 cm, but these improvements are a modest gain of about 2 dB. Panels (d)–(f) of Fig. 4 show the mainlobe characteristics of integrated lateral beamplots using the CLS apodization profiles. The dotted vertical lines on these images correspond to the cyst boundary used to design the windows. Mainlobes for the LCLS and QCLS windows are quite similar for the three different ranges. The third row of plots in Fig. 3 shows the designed apodization weights for the LCLS and QCLS profiles across the aperture. Note that the aperture size increases with range to maintain a constant f/# on receive. These profiles show discontinuities of the weighting function at the edges of the aperture.

In order to investigate the improvements in DOF for the CLS algorithms compared to the conventional windows, we looked at the beamwidths of the integrated beamplots at −6 dB (FWHM) and −20 dB. We also show images of the 2-D PSFs for the 6.5 MHz array at each range superimposed to qualitatively depict the constant mainlobe size with range. In Fig. 5 we show images of the 2-D PSFs at each range for flat, Hamming, Nuttall, LCLS, and QCLS apodization profiles. The CLS profiles were designed using a cyst radius of 0.4 mm. The images are 1 cm in azimuth and extend from 0.8 cm to 3.2 cm in range. Each image was normalized and log compressed to −60 dB. The CLS apodization profiles maintain a relatively constant mainlobe size through range compared to the mainlobe spreading seen in the Hamming and Nuttall windows. The sidelobes of the CLS profiles are higher than the Hamming and Nuttall windows at the 2.5 and 3 cm depths but lower than the large sidelobes evident in the flat apodization PSFs. Fig. 6 plots the −6 dB (FWHM) and −20 dB beamwidths of the PSFs for the different apodizations at all five ranges. In Fig. 6 we see that the CLS apodization profiles maintain a relatively constant beamwidth with range compared with the Nuttall and Hamming windows. The flat apodization profile maintains a somewhat constant FWHM level across range but deviates greatly with range at the −20 dB level; whereas the CLS profiles remain relatively constant.

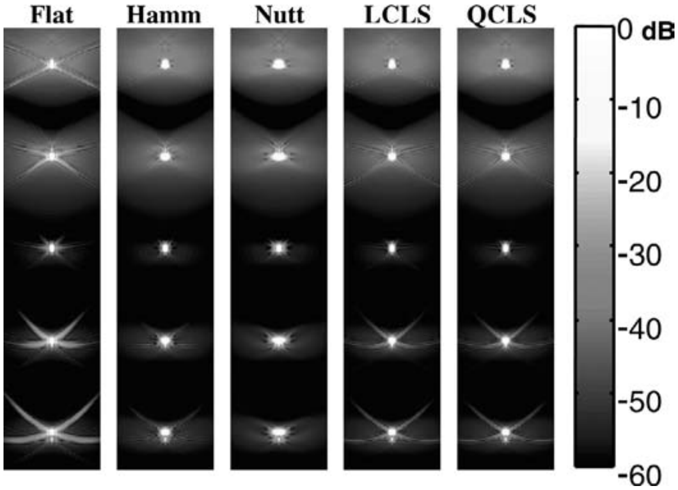

Fig. 5. Comparison of 2-D PSFs of different apodization profiles with range on dynamic receive. The CLS profiles were designed using a cyst radius of 0.4 mm. The system had a transmit focus at 2 cm (f/2), then was dynamically focused and apodized at ranges of 1 cm, 1.5 cm, 2 cm, 2.5 cm, and 3 cm (f/1). Each image was normalized and log compressed to −60 dB. Note the spreading of the mainlobe in the conventional windows PSFs away from the transmit focus and the relatively constant mainlobe of the CLS apodized PSFs.

We also produced similar images for the CLS apodization profiles using a design cyst radius of 0.6 mm in Fig. 7. Again, the CLS apodization profiles maintain a relatively constant mainlobe size across ranges compared to the mainlobe spreading evident with the Hamming and Nuttall windows. The sidelobes of the CLS profiles are suppressed at the 2.5 and 3 cm depths compared to Fig. 5. The QCLS PSF exhibits a larger mainlobe with higher sidelobes at 1 cm dynamic receive, a phenomenon due to the algorithm maintaining constant energy of the PSF inside the cyst boundary. This effect is quantified in Fig. 8, in which the QCLS profile exhibits the largest FWHM

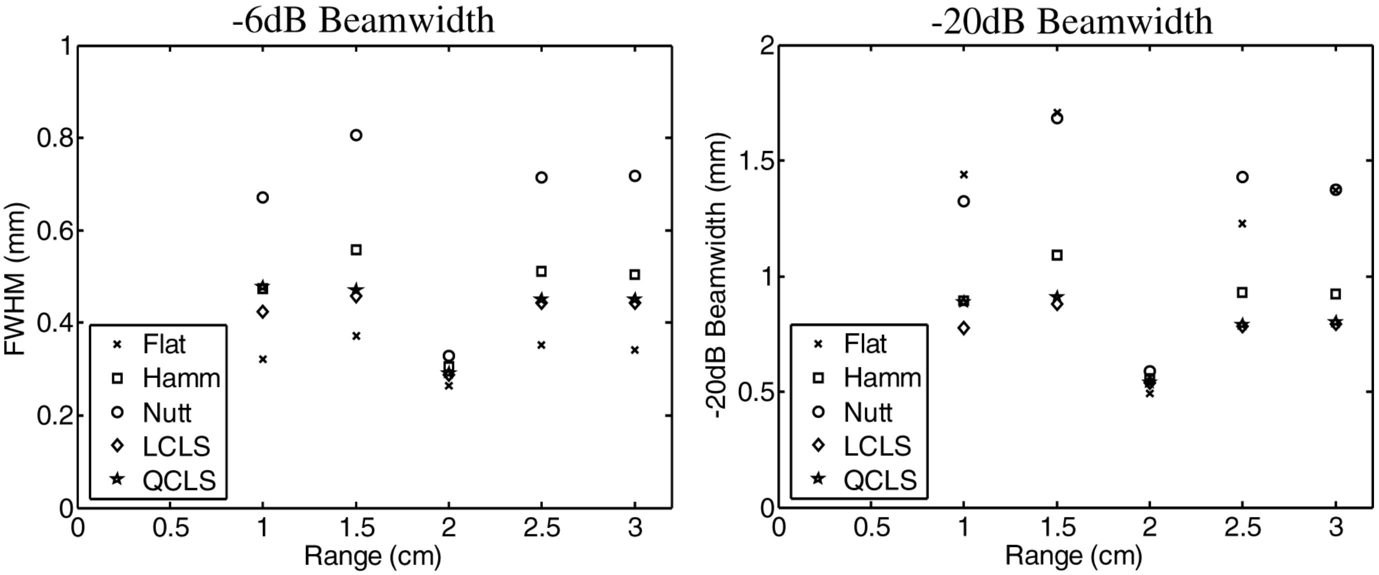

Fig. 6. Comparison of the −6 dB (FWHM) and −20 dB beamwidths of the PSFs for different apodization profiles with range on dynamic receive. The CLS apodization profiles were designed using a cyst radius of 0.4 mm. The system had a transmit focus at 2 cm (f/2), then was dynamically focused and apodized at ranges of 1 cm, 1.5 cm, 2 cm, 2.5 cm, and 3 cm (f/1). The FWHM and the −20 dB beamwidths of the CLS PSFs remain stable in range. They also achieve the narrowest −20 dB beamwidths away from the transmit focus.

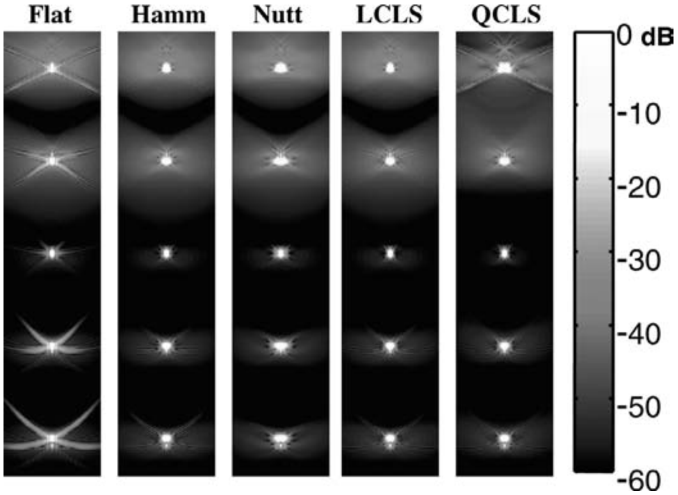

Fig. 7. Comparison of 2-D PSFs of different apodization profiles with range on dynamic receive. The CLS profiles were designed using a cyst radius of 0.6 mm. The system had a transmit focus at 2 cm (f/2), then was dynamically focused and apodized at ranges of 1 cm, 1.5 cm, 2 cm, 2.5 cm, and 3 cm (f/1). Each image was normalized and log compressed to −60 dB. Notice the greater sidelobe suppression of the CLS profiles in the deeper ranges compared to Fig. 5.

at a range of 1 cm. Other than this anomaly, the CLS apodization profiles exhibit a relatively constant FWHM and −20 dB beamwidth across range.

C. Effects of Receive F/# on the CLS Apodization Algorithms

The effect of f/# on receive was investigated to test the robustness of the CLS apodization design algorithms. For these simulations, we used the more aggressive 10 MHz array using a fixed transmit focus at 2 cm (f/4) and dynamic receive focusing and apodization. F/#'s ranging from f/0.5 to f/4 were used on receive, which varied the size of the receive aperture. Therefore, CLS apodization profiles were calculated for each receive aperture using a 0.6 mm design cyst radius. Fig. 9 shows the results of these simulations. The data show three different f/#'s used (f/0.5, f/2, and f/4) while dynamically receiving at 2.0 cm in range. We also analyzed the CLS algorithms at 1.0 cm and 3.0 cm in range, and they gave similar results. Panels (a)–(c) in Fig. 9 show the contrast curves for the different apodization profiles across a range of cyst radii. In general, contrast improves for all windows with smaller f/#'s. The CLS apodization profiles show modest contrast gains (1 dB to 3 dB) relative to the flat, Hamming, and Nuttall windows. The contrast improvements of the CLS windows over the conventional windows increase with increasing f/#. It is interesting to note that the Hamming and Nuttall windows have worse cystic resolution than the flat, LCLS, and QCLS windows at f/2 and f/4 across the entire range of cyst radii. This is a phenomenon we did not observe in the previous 6.5 MHz array simulations. The Hamming and Nuttall windows increase the size of the mainlobe in order to achieve sidelobe suppression. Furthermore, when analyzed with the cystic resolution metric, the decrease in sidelobe energy of the Hamming and Nuttall PSFs does not outweigh their relative increase in mainlobe width. The CLS apodization profiles, on the other hand, are able to maintain a narrow mainlobe width while decreasing the energy in the sidelobe region. Hence, improving cystic contrast. The second row of plots, (d)–(f), in Fig. 9 show the mainlobe region of the CLS integrated beamplots. The dotted line is the boundary of the design cyst radius of 0.6 mm. We see very little difference be-

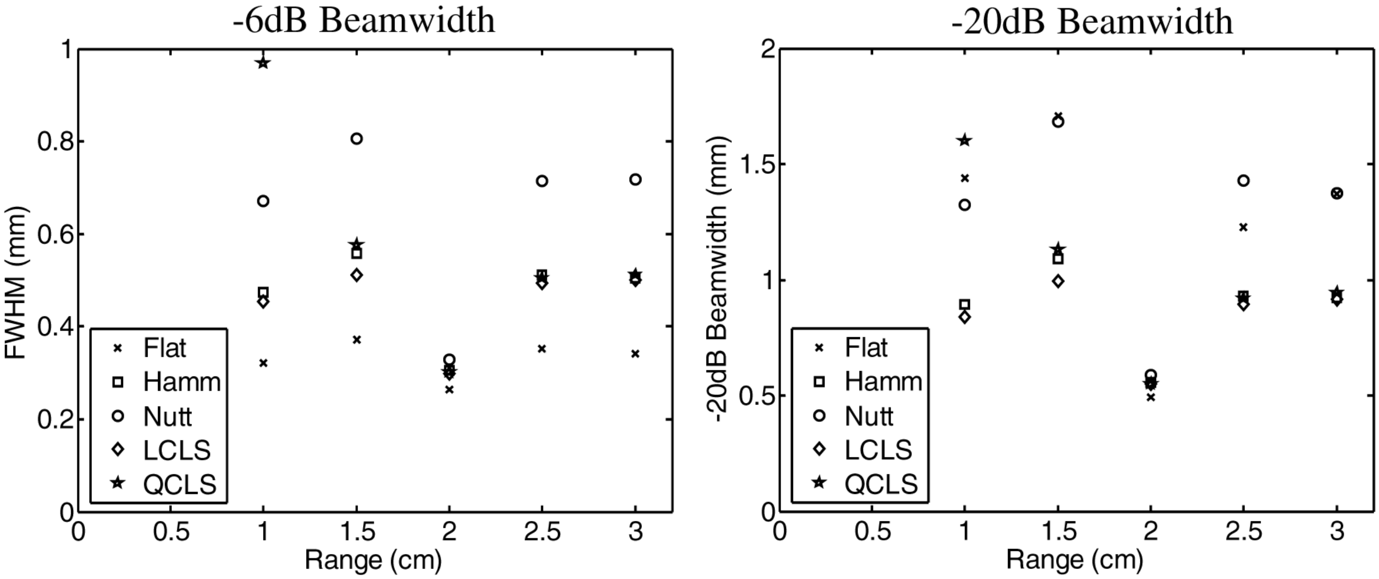

Fig. 8. Comparison of the −6 dB (FWHM) and −20 dB beamwidths of the PSFs for different apodization profiles with range on dynamic receive. The CLS apodization profiles were designed using a cyst radius of 0.6 mm. The system had a transmit focus at 2 cm (f/2), then was dynamically focused and apodized at ranges of 1 cm, 1.5 cm, 2 cm, 2.5 cm, and 3 cm (f/1). Notice the large FWHM of the QCLS algorithm compared to Fig. 6 at a range of 1 cm, a phenomenon due to the algorithm's attempt to maintain constant energy of the PSF inside the mainlobe region.

tween the two mainlobes, with the QCLS mainlobe a bit wider than the LCLS mainlobe. The third row of plots in Fig. 9 shows the weights of the CLS apodizations across the aperture. For the lower f/#'s, the difference between the CLS windows are greater.

Changing the f/# on receive did not produce results that we intuitively expected. We assumed that operating the CLS algorithms with smaller f/#'s or larger apertures would yield markedly better contrast curves than the conventional windows. Even though the CLS algorithms had more information to use in potentially achieving smaller sidelobe levels, the synthetic responses simply could not be summed together at that instant in time in order to destructively interfere. Ultimately, the algorithms still are governed by diffraction. Although large gains in contrast were not achieved with smaller f/#'s, the LCLS and QCLS profiles did achieve improved contrast (2 dB to 4 dB) compared to the conventional windows at the f/#'s investigated. Note that increasing the receive aperture size with range, a method typically used to maintain a constant f/# and improve DOF, is not entirely necessary with the CLS algorithms. It may be possible to use a fixed number of elements in the receive aperture at all ranges and let the algorithms control beam size. This is a method we are currently investigating.

D. Effects of Sound Speed Errors on the CLS Apodization Algorithms

In our final set of simulations, we investigated the sensitivity of the CLS apodization design algorithms to errors in the assumed speed of acoustic wave propagation. We performed these simulations using the 6.5 MHz array with a transmit focus at 2.0 cm (f/2) and a receive focus at 2.0 cm (f/1). For these simulations, the system always assumed a sound speed of 1545 m/s. Therefore, even when the propagation speed varied, the system never changed the transmit and receive focal delays. For all the simulations, the receive apodization applied was always the CLS apodization profile computed for the 1545 m/s PSF dynamically focused at 2.0 cm and with a design cyst radius of 0.6 mm. Fig. 10 shows the contrast curves (left) and integrated lateral beamplots (right) for the CLS apodizations with the correct sound speed in the medium of 1545 m/s. Fig. 10 should be used as a reference for the simulation results presented in Figs. 11 and 12. We obtained PSFs when the speed of sound was overestimated by 1%, 3%, and 5%, then underestimated by 1%, 3%, and 5%. Because the system always assumed a sound speed of 1545 m/s, the different propagation speeds shifted the PSFs in range. In order to be consistent when applying the cystic resolution metric, the cyst was shifted in range so that it was always centered on the degraded PSF. Fig. 11 shows the results for the simulations when the assumed speed of sound was overestimated, meaning that the true propagation speed through the medium was less than 1545 m/s. The first row of plots, (a)–(c), in Fig. 11 shows the contrast curves that were computed with the cyst centered on the shifted PSF. The Hamming, LCLS, and QCLS curves are similar for the 5%, 3%, and 1% overestimation. The Nuttall window interestingly achieves the best contrast at all cyst radii for the 5% overestimation simulation, but it is the worst in the 0.1–0.5 mm cyst radii range in the 1% overestimation. The second row of plots in Fig. 11 shows the mainlobe region of the integrated lateral beamplots for the CLS apodized PSFs. Panels (g)–(i) in Fig. 11 show the entire lateral extent of the integrated beamplots in which differences in the grating lobes for the CLS apodized PSFs can be seen.

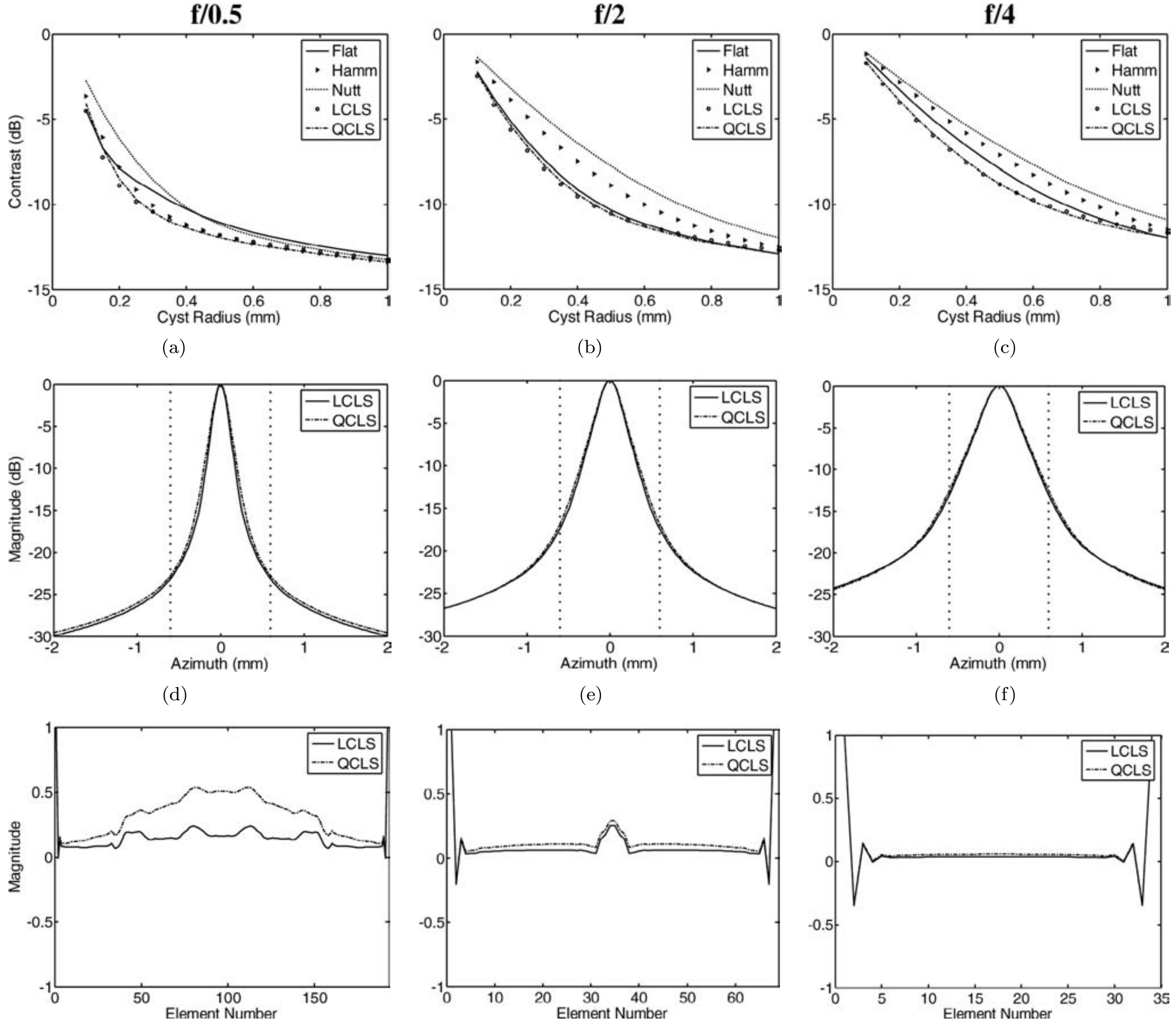

(a) (b) (c)

(d) (e) (f)

(g) (h) (i)

Fig. 9. Comparison of apodization profiles at different f/#'s on receive (f/0.5, f/2, and f/4). These simulations use the 10 MHz linear array with fixed transmit focus at 2 cm (f/4) and dynamic receive at 2 cm. Panels (a)–(c) show contrast curves for the different apodization schemes (flat, Hamming, Nuttall, LCLS, and QCLS). Panels (d)–(f) show the integrated beamplots of the CLS profiles in which the dotted line corresponds to the cyst boundary used to design the windows. Panels (g)–(i) show the magnitude of the CLS profiles across the aperture. The CLS algorithms produce better contrast at every cyst size than the Hamming and Nuttall windows for the f/2 and f/4 apertures.

We also investigated the effect of underestimating the sound speed by 1%, 3%, and 5%, meaning that the true propagation speed through the medium was greater than 1545 m/s. These results are shown in Fig. 12. Plots (a)–(c) in Fig. 12 show the contrast curves computed with the cyst centered on the shifted PSF. The Hamming, LCLS, and QCLS curves are similar for the 5%, 3%, and 1% underestimation. The Nuttall window again achieves the best contrast for all cyst sizes in the 5% underestimation simulation. The second row of plots in Fig. 12 shows the mainlobe region of the integrated lateral beamplots for the CLS apodized PSFs. Plots (g)–(i) in Fig. 12 show the entire lateral extent of the integrated beamplots in which differences in the grating lobes for the CLS apodized PSFs can be seen. These results closely match those from the overestimated speed of sound simulations in Fig. 11.

The design radius for the speed of sound simulations was 0.6 mm. In order to be thorough, we present results showing how the contrast curves change when we apply CLS apodizations designed over a range of cyst radii (0.4 mm–1.0 mm). We show results for two simulations, one in which the sound speed was underestimated by 1% and another in which we have grossly overestimated the sound speed by 5%.

The contrast curves for the underestimated sound speed are shown in Fig. 13. The effects of design radius for the LCLS profiles are shown in the left panel of Fig. 13. The corresponding QCLS profiles are plotted on the right. The

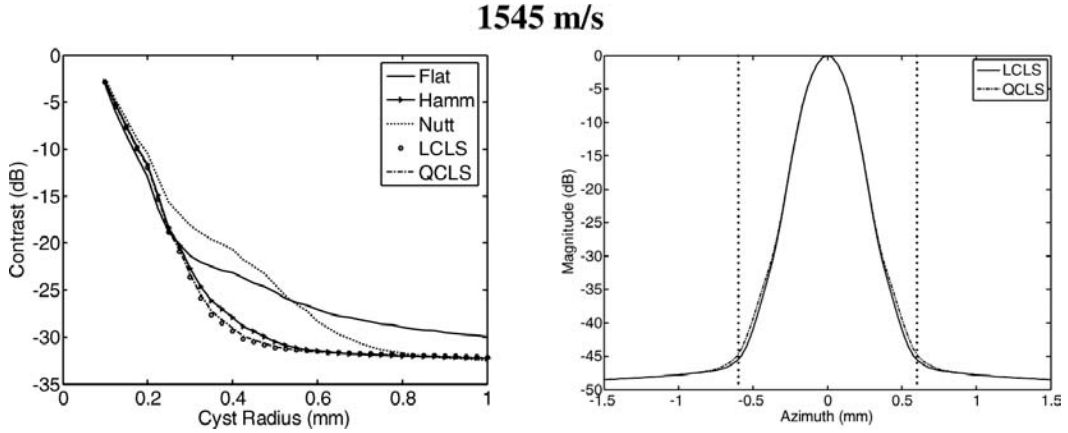

Fig. 10. Contrast curves (left) and integrated lateral beamplots (right) for the CLS apodizations designed assuming the correct speed of sound (1545 m/s). The dotted vertical lines delineate the design cyst radius of 0.6 mm. The LCLS and QCLS windows produced similar beamplots.

flat apodization contrast curve is plotted for reference in both plots. The QCLS contrast curves show more variability with design radius in which larger design radii achieve better contrast for larger cysts; but smaller design radii achieve better contrast for smaller cysts. The contrast curves corresponding to changing design radii with a 5% overestimation in speed of sound are shown in Fig. 14. The LCLS curves are shown on the left and QCLS curves are shown on the right. Both plots depict the flat apodization contrast curve for reference. In general, the curves designed with the smaller radii result in worse cystic contrast. The QCLS algorithm has a greater variability in achieved contrast than the LCLS algorithm. It should be noted that the CLS apodization profiles achieve better contrast at all cyst sizes compared with the flat apodization contrast curve.

These simulations address the concerns that the variation of sound speed in human tissues will degrade the CLS profiles. We have shown that the CLS algorithms remain relatively stable in the presence of wave propagation speed errors, but ultimately these results must be tested experimentally.

IV. Discussion

Our simulations demonstrate the use of our novel strategies for designing optimal apodization profiles. In our methods, we collect spatial impulse responses at the instant in time corresponding to the dynamic receive focus. We produce weights that minimize the energy of the spatial point spread function outside a selected radius from the mainlobe peak. This minimization is subject to a constraint that either forces unity amplitude gain at the peak of the response (LCLS method) or maintains constant energy of the PSF inside the circular region defined by the selected radius (QCLS method). The LCLS approach in general yields a narrow mainlobe and low sidelobe levels. Although such narrow mainlobes are attractive for point imaging, they may not be optimal for imaging diffuse legions and low echogenicity cysts. In these cases, the QCLS approach that yields a slightly broader mainlobe and slightly higher sidelobe levels may be desirable.

Although the LCLS and QCLS apodization design methods have been validated theoretically and through computer simulations, we must begin to assess their performance experimentally. Initial results are positive and suggest that the technique is quite robust; however, full assessment with an experimental scanner will be necessary to fully prove their efficacy. We are currently designing such experiments, and collecting the entire data set of single channel receive spatial impulse responses is a challenging task. We will need to account for spatial variance of the PSF in the lateral dimension as well as in range. Once we have fully characterized the spatial impulse response of the system, we will be able to produce CLS apodization profiles for each output image pixel, make data reconstruction seamless and rapid, and assess the performance of our algorithms to produce optimal contrast.

Obviously, the CLS apodization design algorithms can be realistically used only in a conventional system by choosing a specific design radius. Although the cystic resolution metric can be used to decide which profile can achieve the best contrast for a given application (i.e., imaging a cyst with a 0.4 mm radius or achieving −15 dB contrast for cysts ranging from 0.2 mm to 2.0 mm), the definitive optimal CLS profile is difficult to determine. We have found empirically that choosing the profile around the point at which the contrast curve begins to level off results in the best contrast for the entire range of cyst sizes. Typically, the apodization profiles at the extreme ends of the design cyst radius range exhibit more erratic behavior, like the multiple mainlobe phenomenon in the QCLS case with the large design cyst radii or the large sidelobes in the minimum beamwidth LCLS case in Fig. 1. Ideally, a library of CLS profiles could be constructed and specific profiles applied, depending on the imaging application. A peripheral vasculature exam in which contrast for larger voids would be important might use a profile designed for larger cysts while breast imaging, in which finer detail is critical might use a profile designed for a smaller cyst.

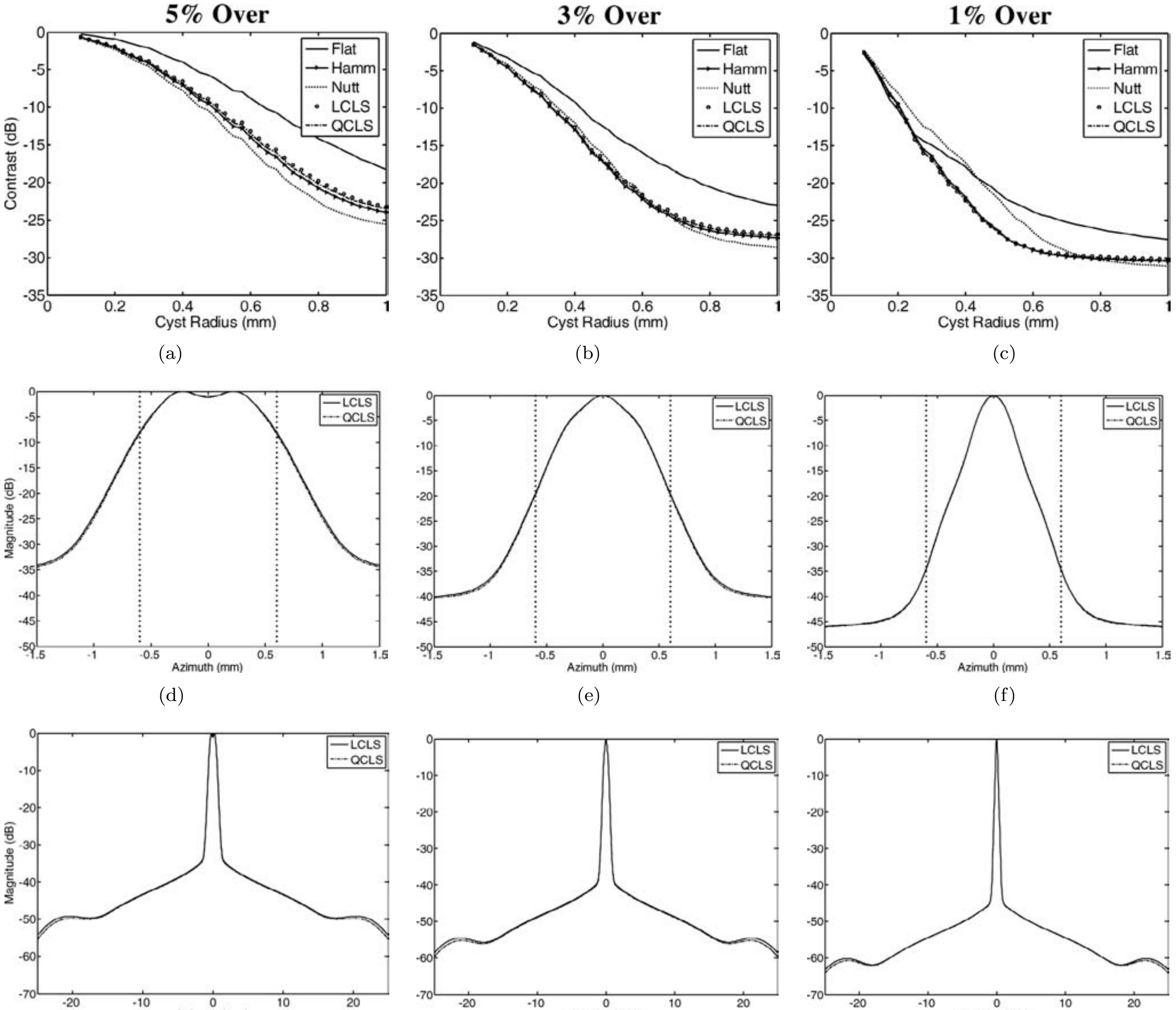

(a) (b) (c)

(d) (e) (f)

(g) (h) (i)

Fig. 11. Effect of assumed sound speed on the CLS algorithm. For these simulations, the wave propagation speed was overestimated by 1%, 3%, and 5%. The CLS profiles computed for 1545 m/s were applied to the degraded PSFs. Panels (a)–(c) show the resulting contrast curves. The Hamming, LCLS, and QCLS contrast curves are similar at the different sound speeds. Panels (d)–(f) plot the mainlobe region of the CLS apodized PSFs in which the dotted line delineates the design radius of 0.6 mm. The entire lateral extent of the integrated beamplots for the CLS apodized PSFs are shown in (g)–(i). The CLS algorithms remain quite stable for the sound speed errors investigated, in which the worst cystic contrast is for the simulation corresponding to the grossest sound speed error of 5%. It is interesting to note that the Nuttall window, which performs the worst at the correct speed of sound (Fig. 10), outperforms all other windows for the 5% overestimation simulation.

It is important to note that our contrast analysis is for a specific instant in time, when the PSF is centered directly in the middle of the cyst. For the speed of sound simulations in which errors in the assumed wave propagation speed shift the PSF in range, we still calculate contrast with the PSF centered on the cyst. Furthermore, the contrast resolution metric describes the point contrast of an image, not the overall contrast of the cyst. Overall cystic contrast analysis requires taking a B-mode image of a cyst, integrating the intensities over the lesion, and comparing this to the integrated intensity over a region of background speckle of the same size at the same depth [19], [20]. Extending the contrast resolution metric to incorporate overall cystic contrast is an area of ongoing research.

Results presented in this paper show that the CLS algorithms for apodization design outperform conventional windows such as the Hamming, Nuttall, and flat apodizations across a range of imaging scenarios and system parameters. The contrast curve results must be interpreted with caution because the resolution metric used to compute the cystic contrast is a point contrast value not the contrast of the overall anechoic region compared to the background speckle. We intend to perform human observer studies that will further investigate the use of the CLS

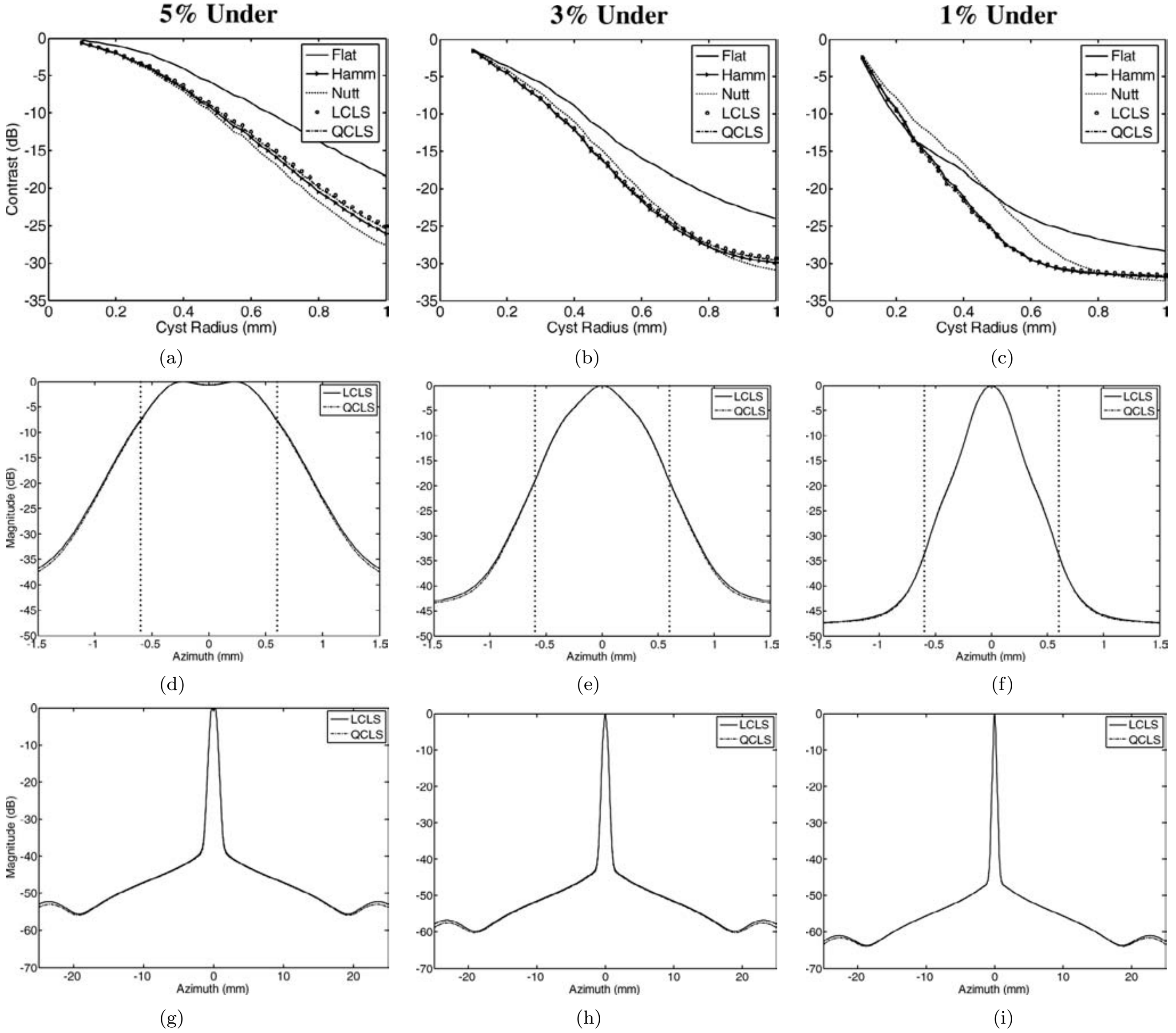

(a) (b) (c)

(d) (e) (f)

(g) (h) (i)

Fig. 12. Effect of assumed sound speed on the CLS algorithm. For these simulations, the wave propagation speed was underestimated by 1%, 3%, and 5%. The CLS profiles computed for 1545 m/s were applied to the degraded PSFs. Panels (a)–(c) show the resulting contrast curves. The Hamming, LCLS, and QCLS contrast curves are similar at the different sound speeds. Panels (d)–(f) show the mainlobe region of the CLS apodized PSFs in which the dotted line delineates the design radius of 0.6 mm. The entire lateral extent of the integrated beamplots for the CLS apodized PSFs is shown in (g)–(i). The CLS algorithms remain quite stable for the sound speed errors investigated. These results closely resemble those seen for the overestimated sound speeds in Fig. 11.

apodization profiles for optimal cystic contrast and, based on the simulation results presented, we believe that the CLS windows will meet our expectations. Overall the CLS apodization design technique has the potential to improve contrast of anechoic legions but also improve beamforming in general due to the formation of PSFs that have narrower mainlobes and lower sidelobes than the conventional windows. There also exists the potential for the technique to aid in the design of system responses used for hyperthermia applications and Doppler signal processing. In order for our technique to be implemented on a clinical system, adequate characterization of the system is required, including the shift variance of the PSF. However, once the system has been characterized, our algorithms save a great deal of time by obviating iterative design.

V. Conclusions

The CLS array pattern synthesis technique presented in this paper has been shown to be effective in designing apodization profiles that can improve contrast in ultrasound images. The LCLS approach achieved a 2-D spatial impulse response with a narrower mainlobe and lower sidelobes than conventional windows currently used to reduce clutter. In cases in which imaging cysts or anechoic regions are of importance and a wider mainlobe may improve cystic resolution, the QCLS technique can be used for improved contrast. We have shown that our algorithms are stable across imaging scenarios such as dynamic receive focusing, varying f/#, and different transmit frequencies. The LCLS and QCLS algorithms also improved DOF

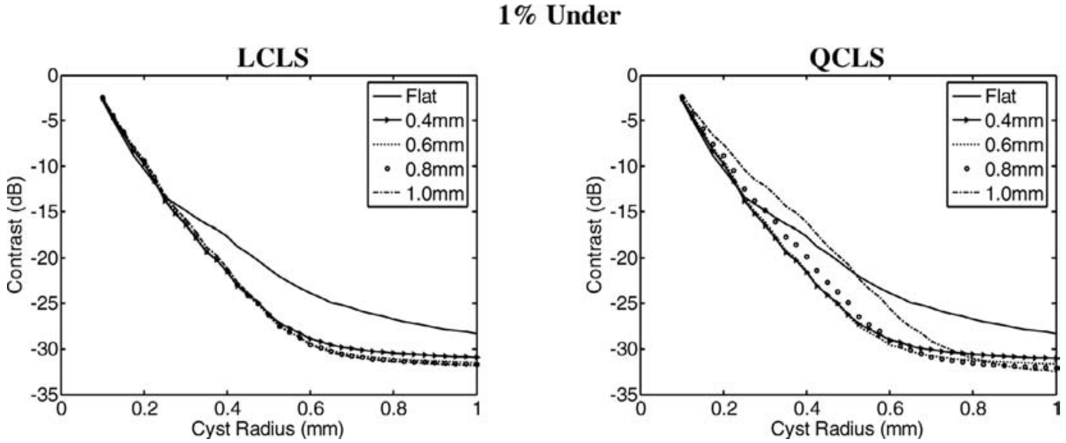

Fig. 13. Effect of design cyst radius when the assumed sound speed has been underestimated by 1%. The LCLS (left) and QCLS (right) apodization profiles were designed for 0.4 mm, 0.6 mm, 0.8 mm, and 1.0 mm cyst radii. The flat apodization contrast curve is shown for reference. The CLS profiles achieve better contrast than flat apodization across a wide range of cyst sizes. The LCLS and QCLS contrast curves remain stable in the presence of sound speed errors. The QCLS curves in general decrease contrast for the smaller cyst sizes as the design cyst radius increases.

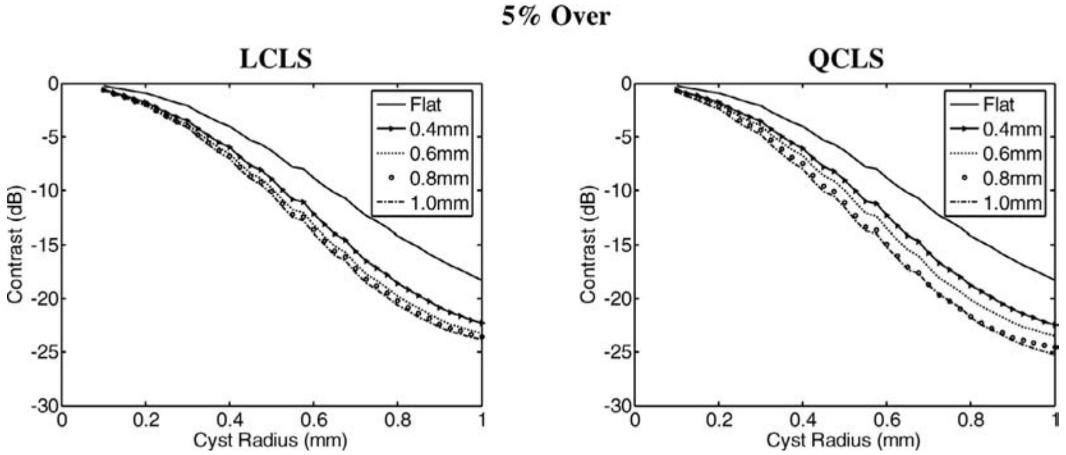

Fig. 14. Effect of design cyst radius when the assumed sound speed has been grossly overestimated by 5%. The LCLS (left) and QCLS (right) apodization profiles were designed for 0.4 mm, 0.6 mm, 0.8 mm, and 1.0 mm cyst radii. The flat apodization contrast curve is shown for reference. The LCLS and QCLS contrast curves produce better contrast than the flat apodization at all cyst sizes. In general, contrast improves for larger design cyst radii.

by maintaining relatively constant beamwidths through range. In cases in which the wave propagation speed is different than the assumed sound speed, the algorithms remain stable and still can improve contrast. Simulation results obtained by implementing the CLS algorithms demonstrate the success of the technique in solving common problems associated with ultrasound imaging, such as a restricted depth of field.

The CLS apodization design algorithms have significant potential to improve ultrasound beamforming and can be applied in any ultrasound application in which the system response is well characterized. There is no iteration involved in producing the apodization profiles; therefore, design time is considerably reduced as compared to other optimal apodization design techniques. Further investigation is required to examine the effects of phase aberration, blocked elements, shift variance of the system response, and overall cystic contrast. However, our simulations indicate that the CLS techniques improve cystic resolution and consistently outperform current conventional apodization profiles.

References

[1] D. A. Guenther and W. F. Walker, "Optimal apodization design for medical ultrasound using constrained least squares. Part I: Theory," *IEEE Trans. Ultrason., Ferroelect., Freq. Contr.*, vol. 54, no. 2, pp. 332–342, 2007.

[2] J. W. Goodman, *Introduction to Fourier Optics*. 3rd ed. Englewood, CO: Roberts, 2005.

[3] A. R. Selfridge, G. S. Kino, and B. T. Khuri-Yakub, "A theory for the radiation pattern of a narrow-strip acoustic transducer," *Appl. Phys. Lett.*, vol. 37, no. 1, pp. 35–36, 1980.

[4] L. L. Scharf, *Statistical Signal Processing: Detection, Estimation, and Time Series Analysis*. Reading, MA: Addison-Wesley, 1991.

[5] S. Docolo and M. Moonen, "Design of far-field and near-field broadband beamformers using eigenfilters," *Signal Process.*, vol. 83, pp. 2641–2673, 2003.

[6] W. H. Gander, "Least squares with a quadratic constraint," *Numerische Mathematik*, vol. 36, pp. 291–307, 1981.

[7] M. Ellis, D. A. Guenther, and W. F. Walker, "A spline based approach for computing spatial impulse responses," *IEEE Trans. Ultrason., Ferroelect., Freq. Contr.*, submitted for publication.

[8] K. Ranganathan and W. F. Walker, "A general cystic resolution metric for medical ultrasound," *IEEE Trans. Ultrason., Ferroelect., Freq. Contr.*, submitted for publication.

[9] M. E. Anderson, "The impact of sound speed errors on medical ultrasound imaging," *J. Acoust. Soc. Amer.*, vol. 107, no. 6, pp. 3540–3548, 1997.

[10] J. T. Bushberg, J. A. Seibert, E. M. Leidholt, Jr., and J. M. Boone, *The Essential Physics of Medical Imaging.* 2nd ed. New York: Lippincott, Williams, and Wilkins, 2002.

[11] W. F. Walker and G. E. Trahey, "The application of k-space in pulse echo ultrasound," *IEEE Trans. Ultrason., Ferroelect., Freq. Contr.*, vol. 45, pp. 541–558, 1998.

[12] Y.-M. Law and C.-W. Kok, "Constrained eigenfilter design without specified transition bands," *IEEE Trans. Circuits Syst. II*, vol. 52, no. 1, pp. 14–21, 2005.

[13] S.-C. Pei and J.-J. Shyu, "2-D FIR eigenfilters: A least-squares approach," *IEEE Trans. Circuits Syst.*, vol. 37, no. 1, pp. 24–43, 1990.

[14] J. A. Jensen and P. Munk, "A new method for estimation of velocity vectors," *IEEE Trans. Ultrason., Ferroelect., Freq. Contr.*, vol. 45, pp. 837–851, 1998.

[15] M. E. Anderson, "Spatial quadrature: A novel technique for multidimensional velocity estimation," in *Proc. IEEE Ultrason. Symp.*, 1997, pp. 1233–1238.

[16] W. F. Walker and G. E. Trahey, "A fundamental limit on delay estimation using partially correlated speckle signals," *IEEE Trans. Ultrason., Ferroelect., Freq. Contr.*, vol. 42, pp. 301–308, 1995.

[17] E. S. Ebbini and C. Cain, "Multiple-focus ultrasound phased-array pattern synthesis: Optimal driving-signal distributions for hyperthermia," *IEEE Trans. Ultrason., Ferroelect., Freq. Contr.*, vol. 36, no. 5, pp. 540–548, 1989.

[18] I. W. Selesnick, M. Lang, and C. S. Burrus, "Constrained least square design of FIR filters without specified transition bands," *IEEE Trans. Signal Processing*, vol. 44, no. 8, pp. 1879–1892, 1996.

[19] S. W. Smith, R. F. Wagner, J. M. Sandrik, and H. Lopez, "Low contrast detectability and contrast/detail analysis in medical ultrasound," *IEEE Trans. Sonics Ultrason.*, vol. 30, no. 3, pp. 164–173, 1983.

[20] S. W. Smith and H. Lopez, "A contrast-detail analysis of diagnostic ultrasound imaging," *Med. Phys.*, vol. 9, no. 1, pp. 4–12, 1982.

[21] A. H. Nuttall, "Some windows with very good sidelobe behavior," *IEEE Trans. Acoust. Speech Signal Processing*, vol. 29, no. 1, pp. 84–91, 1981.

Drake A. Guenther received his B.S.E. degree in biomedical engineering in 2003 from Duke University, Durham, NC. His undergraduate research as a Pratt Fellow explored adaptive beamforming and spatial compounding in ultrasound.

After completing his B.S.E., he joined the Department of Biomedical Engineering at the University of Virginia, Charlottesville, VA, where he is currently pursuing his Ph.D. degree. His research interests include ultrasound beamforming, signal processing, and angular scatter imaging.

William F. Walker (S'95–M'96) received the B.S.E. and Ph.D. degrees in 1990 and 1995 from Duke University, Durham, NC. His dissertation explored fundamental limits on the accuracy of adaptive ultrasound imaging.

After completing his doctoral work, he stayed at Duke as an assistant research professor in the Department of Biomedical Engineering. At the same time, he served as a Senior Scientist and President of NovaSon Corporation located in Durham, NC. In 1997 he joined the faculty of the Department of Biomedical Engineering at the University of Virginia, Charlottesville, VA, being promoted to associate professor in 2003. He is an active founder in two ultrasound-based startup companies, PocketSonics Inc., Charlottesville, VA, and HemoSonics LLC, Charlottesville, VA.

His research interests include aperture domain processing, beamforming, angular scatter imaging, tissue elasticity imaging, low-cost system architectures, and time-delay and motion estimation.

A Novel Method for Designing and Fabricating Single Piston Transducers with Extended Depth of Field.

K. Owen, W. F. Walker;
University of Virginia, Charlottesville, VA.

Abstract: Motivation/Background:
Gabor zone plate lenses offer adequate focusing performance at a lower cost, and also have the potential to operate successfully beyond the upper frequency range of current annular arrays and single piston transducers. Zone plates achieve a focus varying the transmittance across a flat lens. Although it is difficult to apply a continuously varying transmittance across a transducer, it is possible to mimic this using a high-resolution binary micropattern for easier manufacturing. We propose that binary micropatterning one of the electrodes on a PVDF transducer can be used to produce low-cost focused transducers capable of operating up to very high frequencies.

Statement of the Contribution/Methods:
These lenses suffer from two main limitations. Firstly focusing is based on single-frequency excitation, and so varies with frequency. Secondly, for a real and non-negative transmittance, the ideal focused image must be accompanied by a conjugate phase (virtual) image, and the image of a plane wave at the transducer face. Interference between the three images seriously degrades focusing. To lessen this effect we have developed an alternating projection algorithm whereby the desired radiation pattern is projected onto a feasible transducer pattern, and then in turn this pattern is projected onto a new radiation pattern, which is restricted to meet a set of predefined response magnitude constraints before continuing. This method iteratively modifies the transducer pattern so that the sum of the three images tries to meet the constraints, which can include both frequency and spatial responses.

Results/Discussion:
The described algorithm consistently improves zone plate lens results. In the simplest case of a simulated linear patterned transducer (figure), where the desired radiation pattern is uniform in a central region and zero outside, the algorithm gives ~14dB less energy in the stopband compared to a non-optimized zone plate, and ~10dB less when compared to an apodized zone plate. Further results show that when more than one frequency or focal distance is given in the constraints, the method continues to perform well. We make micropatterned transducers using a PCB as one electrode, and half-metallized PVDF. Beamplots and details of higher resolution patterning to follow at the conference.

Diffuse Targets for Improved Contrast in Beamforming Adapted to Target

Michael A. Ellis, Francesco Viola, William F. Walker
Department of Biomedical Engineering, University of Virginia, Charlottesville VA 22908.

I. Motivation

In medical ultrasound, bright off-axis targets can introduce broad image clutter, which reduces the both image contrast and resolution. Such image degradation can make clinical diagnoses of small features, such as breast calcifications, very difficult. Recently, we have developed an adaptive beamforming (BF) algorithm, entitled TONE, that significantly increases both image contrast and resolution by conducting a global optimization based on a sparse set of hypothetical source locations. Based on the electronic signal to noise ratio and the location of the targets with respect to the hypothetical sources, this optimization can often creates clouds around the target in the final image, reducing the effective image contrast. Here we have developed a method to reduce the appearance of the clouds and further enhance the image contrast and resolution with no change in the time required to beamform.

II. Methods

In this paper, we alter the system model from a grid of single hypothetical source locations to a grid in which each hypothetical location is the weighted sum of many sources in the surrounding region. This diffuse grid encourages TONE to place hypothetical sources in the immediate vicinity of the true source, rather than in a large cloud around that source. The result is a reduction in the appearance of such clouds, further increasing image contrast and resolution. Because the grid of hypothetical sources has not changed in size, there is no change in the computation time, making this system model even more attractive.

We have performed a series of simulations using FIELD II to test the performance of this modification as compared to the original TONE and conventional BF. Two point targets were placed with a 100um lateral separation. Data was simulated for a 33 element aperture with a 300um pitch, transmitting at 5MHz with 80% bandwidth. Hypothetical sources were placed every 40um laterally and every 20um axially. All BFs were evaluated for both noise-free data and data with 15dB per-channel-SNR.

We have also performed a series of experiments using a Philips SONOS 5500 (6MHz with 80% bandwidth) to further test the performance of this modification. Conventional BF was applied using the default parameters of the Philips scanner, whereas SPOC was applied on single-channel, unfocused data with plane wave transmit. Hypothetical sources were placed every 67um laterally and 20um axially. Five 20um wires were imaged in a water tank and the result are shown in Fig. 1.

III. Results and Discussion

The results of both the simulations and experiments show a significant reduction in the image clouds in the case of the diffuse target model.

Supported by the US Army CDMRP in Breast Cancer grant No. W81XWH-04-1-0590.

Optimal Contrast Resolution Beamforming

Drake A. Guenther[1] and William F. Walker[1, 2]

[1]*Biomedical Engineering, University of Virginia, Charlottesville, VA 22908*
[2] *Electrical and Computer Engineering, University of Virginia, Charlottesville, VA 22904*

ABSTRACT

I. Motivation and Background

The delay-and-sum (DAS) beamformer, utilized in current state of the art ultrasound imaging systems, delays each receive channel to focus the returning echoes and weights each receive channel prior to beam summation. Delays and apodization are applied dynamically to focus and maintain a constant f/# with range. Apodization functions like the Hamming window shape the overall system impulse response (PSF) by altering the sidelobe levels and mainlobe width. As a result, apodization greatly impacts the contrast and resolution of the final output image. Adding to the rich history of array pattern synthesis, we describe an optimal contrast resolution beamformer for broadband imaging systems.

II. Statement of Contribution/Methods

This paper describes a novel receive beamformer architecture that replaces the weight on each channel of the DAS beamformer with channel-unique finite impulse response (FIR) filters. Our proposed FIR beamformer passes the focused receive signals through multi-tap FIR filters on each receive channel prior to summation. The FIR filters are constructed to maximize the contrast resolution of the system's PSF using an array pattern synthesis technique that utilizes *a priori* knowledge about the imaging system. We thoroughly investigate the contrast resolution performance of the DAS and FIR beamformers through simulations and phantom experiments.

III. Results/Discussion

We present simulation results showing that FIR filters of modest tap lengths (3-7) can yield marked improvement in image contrast and point resolution. Specifically we show that 7-tap FIR filters can reduce sidelobe and grating lobe energy by 30dB and improve contrast resolution by as much as 20dB compared to the DAS beamformer. We investigate the potential effects of phase aberration on the FIR beamformer by simulating a nearfield thin phase screen aberrator. In the presence of aberrators characterized by a root-mean-square strength of 28 ns and a full-width at half-maximum correlation length of 3.6 mm the FIR beamformer still outperforms the conventional DAS beamformer's contrast resolution by as much as 15 dB.

We show experimental results wherein FIR filters are used to synthesize 2D spatial PSFs on an Ultrasonix Sonix RP scanner (Ultrasonix Medical Corp., Richmond, BC, Canada). The resulting 2D PSFs have low sidelobes while achieving a narrow mainlobe. Using these experimental PSFs we present results where the FIR beamformer improves the contrast to noise ratio in simulated B-mode cyst images by more than 4 dB.

Our array pattern synthesis algorithm and novel FIR beamformer have the potential to significantly improve broadband imaging systems in any application where

the system response is well characterized. The FIR beamformer improves the contrast resolution of ultrasound images and initial results suggest that the beamformer is robust to phase aberration. Therefore, we believe the FIR beamformer will considerably enhance diagnostic ultrasound.

Receive Channel FIR Filters for Enhanced Contrast in Medical Ultrasound

Drake A. Guenther and William F. Walker
Dept. of Biomedical Engineering, University of Virginia
dag2m@virginia.edu

ABSTRACT

Aperture weighting functions are critical design parameters in the development of ultrasound systems because beam characteristics determine the contrast and point resolution of the final image. In previous work by our group, we developed a general apodization design method that optimizes a broadband imaging system's contrast resolution performance [1, 2]. In that algorithm we used constrained least squares (CLS) techniques and a linear algebra formulation of the system point spread function (PSF) as a function of the scalar aperture weights. In this work we replace the receive aperture weights with individual channel finite impulse response (FIR) filters to produce PSFs with narrower mainlobe widths and lower sidelobe levels compared to PSFs produced with conventional apodization functions. Our approach minimizes the energy of the PSF outside a defined boundary while imposing a quadratic constraint on the energy of the PSF inside the boundary.

We present simulation results showing that FIR filters of modest tap lengths (3-7) can yield marked improvement in image contrast and point resolution. Specifically we show results that 7-tap FIR filters can reduce sidelobe and grating lobe energy by 30dB and improve cystic contrast [3] by as much as 20dB compared to conventional apodization profiles. We also show experimental results where multi-tap FIR filters decrease sidelobe energy in the resulting 2D PSF and maintain a narrow mainlobe. Our algorithm has the potential to significantly improve ultrasound beamforming in any application where the system response is well characterized. Furthermore, this algorithm can be used to increase contrast and resolution in novel receive only beamforming systems [4, 5].

Keywords – beamforming, contrast resolution, constrained least squares

I. INTRODUCTION

In conventional ultrasound systems, apodization is applied to individual receive channels after dynamic focusing but before channel summation. These weights can be applied dynamically to control f/# with range and to suppress edge effects resulting from a finite aperture size. Conventional apodization functions, like the rectangular, Hamming, or Nuttall [6] window, typically offer a tradeoff between the system spatial impulse response's mainlobe width and sidelobe level. Thus, apodization greatly affects the contrast and resolution of the final image. In previous work by our group we proposed an apodization design algorithm that optimized the system's contrast resolution [1, 2]. Performance was quantified using a "cystic resolution" metric where contrast is measured as a function of cyst size. Although other resolution metrics exist, like the full width at half maximum (FWHM) of the system's beamplot, we consider cystic resolution a more appropriate performance metric for ultrasound systems [3]. Our previous apodization design algorithm, formulated using constrained least squares, produced PSFs with narrower mainlobes and smaller sidelobes than the PSFs formed using conventional apodization profiles. According to the cystic resolution metric, the least squares apodization profiles improved contrast resolution by 2-3dB.

In this paper we investigate applying dynamic receive apodization with individual receive channel multi-tap FIR filters. A simplified depiction of a conventional receive beamformer and the proposed FIR beamformer is shown in figure 1. Note that apodization is applied in both architectures after the dynamic focal delays have been applied. The proposed FIR filter beamformer increases system complexity, but should be relatively easy and inexpensive to implement using modern hardware. Some novel ultrasound systems employ receive only beamforming. For example the system described in [4] focuses only on receive to maintain high frame rates for elasticity imaging, and opto-acoustic imaging devices use the ultrasound transducer purely as a receiver [5]. Our beamforming algorithm can be readily applied to these systems, and offers the potential to significantly improve point resolution and contrast of the output images. Our previous design method optimized the apodization weights of the conventional beamformer to maximize contrast resolution. In this paper we extend that algorithm to calculate the optimal weights for the FIR beamformer utilizing the same performance metric.

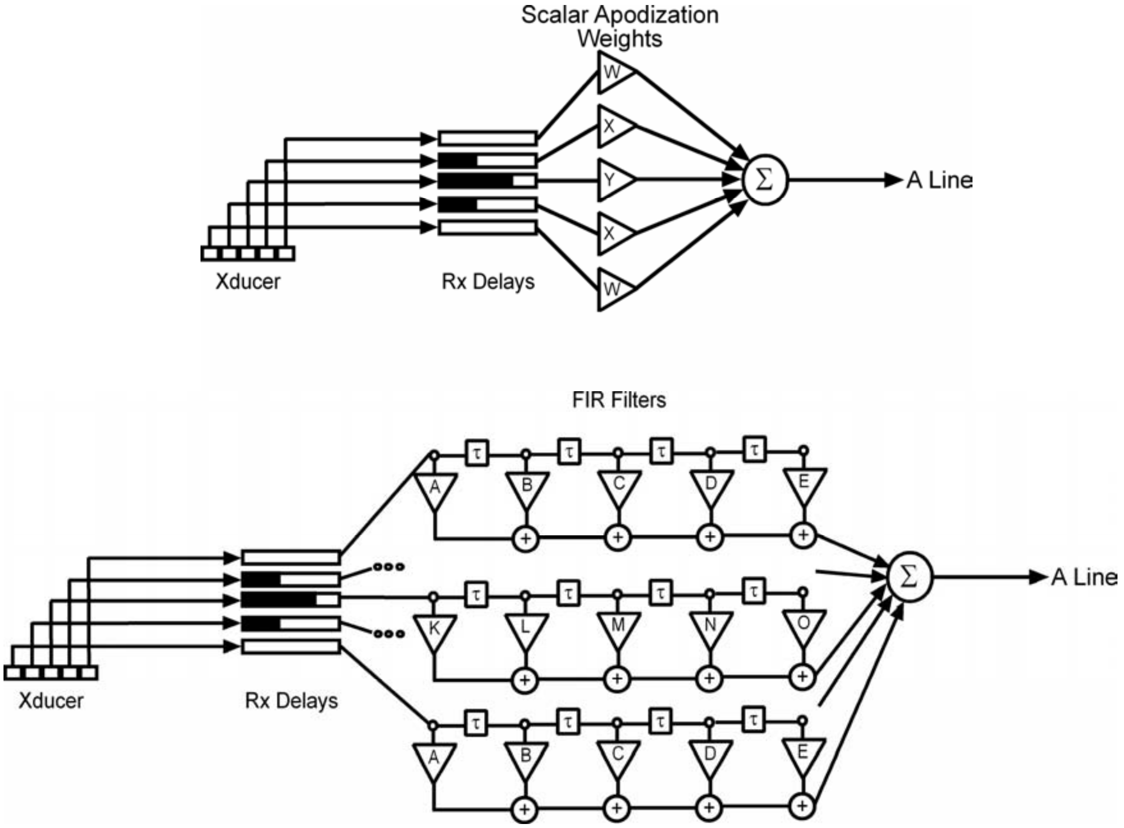

Fig. 1. Receive beamformer architectures: (top) Conventional (bottom) Proposed. The architecture depicted on the bottom shows the proposed beamformer with 5-tap FIR filters. Note that apodization is applied after dynamic receive focusing in both architectures.

II. THEORY

A. Linear algebra formulation of the spatial point spread function

The sensitivity field for a transducer during pulse-echo imaging can be expressed as the product of a propagation matrix, *S*, and a set of aperture weightings, *w*. The propagation matrix uses superposition to describe the contribution of each transducer element at each field point at an instant in time. For our formulation, *S* is a function of the transmit aperture weights, the excitation pulse, and the individual element impulse responses of the transmit and receive apertures. We also apply dynamic receive focusing in our formulation by adjusting the receive delays of each individual element.

The two way pulse echo propagation matrix, *S*, for a fixed transmit aperture and a *n* element dynamically focused receive aperture at a total number of *p* points in three dimensional space is:

$$S = \begin{bmatrix} s_{1,1} & s_{1,2} & \cdots & s_{1,n} \\ s_{2,1} & . & \cdots & . \\ \vdots & \vdots & \ddots & \vdots \\ s_{p,1} & . & \cdots & s_{p,n} \end{bmatrix}, \tag{1}$$

where $s_{i,j}$ is the contribution of the *j*th receive element at the *i*th point in space. The receive aperture weighting function, w, for each of the *n* elements used on receive can be written in vector form as:

$$w = \begin{bmatrix} w_1 & w_2 & w_3 & \cdots & w_n \end{bmatrix}^T \ , \tag{2}$$

where T denotes the vector transpose operation. Using (1) and (2), we can now write the complete two-way pulse echo system PSF, P, as follows:

$$P = Sw \ , \tag{3}$$

the propagation matrix multiplied by the receive weighting vector. Note that this results in the one dimensional column vector, P, of length p the total number of points in three dimensional space where the system PSF is measured.

To expand our formulation to include receive channel FIR filters, we recognize that the final spatial PSF is a linear superposition of multiple dynamically focused 2-way PSFs. We create a new propagation matrix, S_{FIR}, which is a simple combination of the propagation matrices associated with each dynamic receive focus. The number of propagation matrices included corresponds to number of FIR filter taps, k.

$$S_{FIR} = \left[S_{z1}\,,\, S_{z2}\,,\, S_{z3}\,,\ldots\, S_{zk}\right] = \begin{bmatrix} s_{z1,1,1} & s_{z1,1,2} & \cdots & s_{z1,1,n} & \cdots & s_{zk,1,1} & s_{zk,1,2} & \cdots & s_{zk,1,n} \\ s_{z1,2,1} & \cdot & \cdots & \cdot & \cdots & s_{zk,2,1} & \cdot & \cdots & \cdot \\ \vdots & \vdots & \ddots & \vdots & \cdots & \vdots & \vdots & \ddots & \vdots \\ s_{z1,p,1} & \cdot & \cdots & s_{z1,p,n} & \cdots & s_{zk,p,1} & \cdot & \cdots & s_{zk,p,n} \end{bmatrix} , \tag{4}$$

where $s_{zk,i,j}$ is the contribution of the jth element at the ith point in space for the kth receive focus. Adequate spatial and temporal sampling of the three dimensional PSF yields huge propagation matrices, and therefore for this paper we have limited our analysis to two spatial dimensions, azimuth and range, and assume a temporal sampling rate of 40MHz for the FIR filters. The receive FIR filter taps, w_{FIR}, can also be written in vector form as:

$$w_{FIR} = \begin{bmatrix} w_{z1,1} & w_{z1,2} & w_{z1,3} & \cdots & w_{z1,n} \cdots & w_{zk,1} & w_{zk,2} & w_{zk,3} & \cdots & w_{zk,n} \end{bmatrix}^T , \tag{5}$$

where $w_{zk,j}$ is the weight applied for the kth receive focus on the jth receive element. Using (4) and (5), the complete two-way pulse echo system PSF for the receive channel FIR beamformer using k-taps on each channel is written as follows:

$$P_{FIR} = S_{FIR} w_{FIR} \ . \tag{6}$$

B. Algorithm for computing the FIR filter taps

The cystic resolution metric described in [7] quantifies the contrast at the center of an anechoic cyst embedded in a speckle generating background. Note that this metric measures contrast at a specific point in space (the center of the cyst) at an instant in time. This is a different parameter than overall cystic contrast that is typically computed from a B-mode image [8]. We refer to the cystic resolution metric's result as a "point contrast" to avoid this confusion. From [7] the point contrast of the center of a cyst relative to the background neglecting electronic noise is defined as:

$$C = \sqrt{\frac{E_{out}}{E_{tot}}} \ , \tag{7}$$

where E_{out} is the PSF energy outside the cyst and E_{tot} is the total PSF energy. The contrast resolution metric identifies the contribution of specific points in the PSF to the overall contrast. Note that if all of the PSF energy lay within the cyst, C would be 0, indicating the best possible contrast. On the other hand, if most of the PSF energy lies outside the cyst, C approaches a value of 1. Therefore, when we present contrast curves as a function of cyst radius, a more negative dB value indicates better performance.

The apodization design algorithm uses the above cystic resolution metric to formulate a least squares minimization problem with a quadratic constraint. We call the resulting weights quadratically constrained least squares (QCLS) apodization profiles. Our algorithm utilizes the linear algebraic representation of the PSF presented above. If we describe the PSF for all spatial points in the final image, we can develop a full set of optimal dynamic receive aperture weights for the FIR receive beamformer in figure 1.

We can optimize contrast according to (7) by minimizing the ratio of PSF energy outside a specified cyst boundary to the total PSF energy. This is equivalent to minimizing the ratio of PSF energy outside the cyst to PSF energy inside the cyst:

$$\min_{w} \left\| S_{out} w \right\|^2 \quad \text{subject to the quadratic constraint} \quad \left\| S_{in} w \right\|^2 = 1 \ , \tag{8}$$

where $\left\| \bullet \right\|^2$ denotes the square of the ℓ^2-norm, S_{out} is the propagation matrix for all the spatial points of the PSF lying outside the cyst boundary, and S_{in} is the propagation matrix for all the spatial points of the PSF lying inside the cyst boundary. Note that the quadratic constraint minimizes the ratio of PSF energy outside the cyst to PSF energy inside the cyst. Drawing upon [9], the optimal receive aperture weightings satisfying the quadratic constraint is the generalized eigenvector, w_{eig}, corresponding to the minimum generalized eigenvalue resulting from the generalized eigenvalue decomposition problem of $S_{out}^T S_{out}$ and $S_{in}^T S_{in}$. One of the main advantages of the QCLS technique is that no matrix inversion is required to solve for the optimal apodization profile.

III. SIMULATION RESULTS

We simulated a 64 element 1D linear array operating at 6.5MHz and 75% fractional bandwidth in DELFI [10], a custom ultrasound simulation tool. Spatial PSFs were calculated in a 2D plane, azimuth and range, at different instances in time corresponding to particular dynamic receive foci. We investigated the ability of our algorithm to produce optimal PSFs when using different size receive apertures, different FIR filter lengths, and different dynamic receive focal depths. We investigated FIR tap lengths ranging from 1-tap to 7-taps. We find that excellent performance can be achieved with a modest tap length. In figure 2 we show results corresponding to a 64 element receive aperture dynamically focused at 1.0cm, 2.0cm (transmit focus), and 3.0cm. The top figures plot the integrated lateral beamplots when using different apodization windows. The beamplots were calculated by integrating the energy of the different spatial PSFs in range. We compare our FIR-QCLS windows against conventional windows such as the rectangular, the Hamming, and the Nuttall windows. We only show results comparing the QCLS windows with the rectangular window since the results for the other conventional windows were similar. We calculated FIR-QCLS windows using a design cyst radius of 0.4mm with 1-tap, 3-taps, 5-taps, and 7-taps per channel. Notice the marked reduction of the sidelobe levels for the higher tap FIR-QCLS weights. Some lateral beamplots show sidelobe level reduction of 30dB compared to the rectangular beamplot. The second row of plots in figure 2 show the contrast curves computed from (7) as a function of cyst radius (from 0.1mm to 1.0mm) with the PSF centered in the middle of the cyst. In general contrast improves when increasing the number of taps on each receive channel, however the biggest contrast improvement occurs between using 3-taps versus 1-tap. The FIR-QCLS windows show cystic resolution improvements greater than 10dB for a wide range of cyst sizes. The FIR-QCLS weights computed for the 1.0cm dynamically focused data actually show contrast improvements of 15dB over the conventional windows for cysts larger than 0.4mm. In general we see similar trends at all three dynamic receive focal depths. The gains in contrast improvement decrease at ranges deeper than the transmit focus.

Figure 3 shows the calculated FIR-QCLS weights for the data dynamically focused at 2.0cm. These weights were computed for a design cyst radius of 0.4mm. The 1-tap and 3-tap FIR-QCLS weights are mostly smooth Gaussian like functions across the aperture, except at the endpoints where discontinuities appear. The 5-tap and 7-tap weights are much more variant and discontinuous. It is interesting to note that the FIR-QCLS weights take on negative values, a phenomenon never seen in conventional windows like the Hamming or Nuttall window. In general, the results using smaller receive apertures (48 and 32 elements) showed similar trends to the 64 element aperture and are not included.

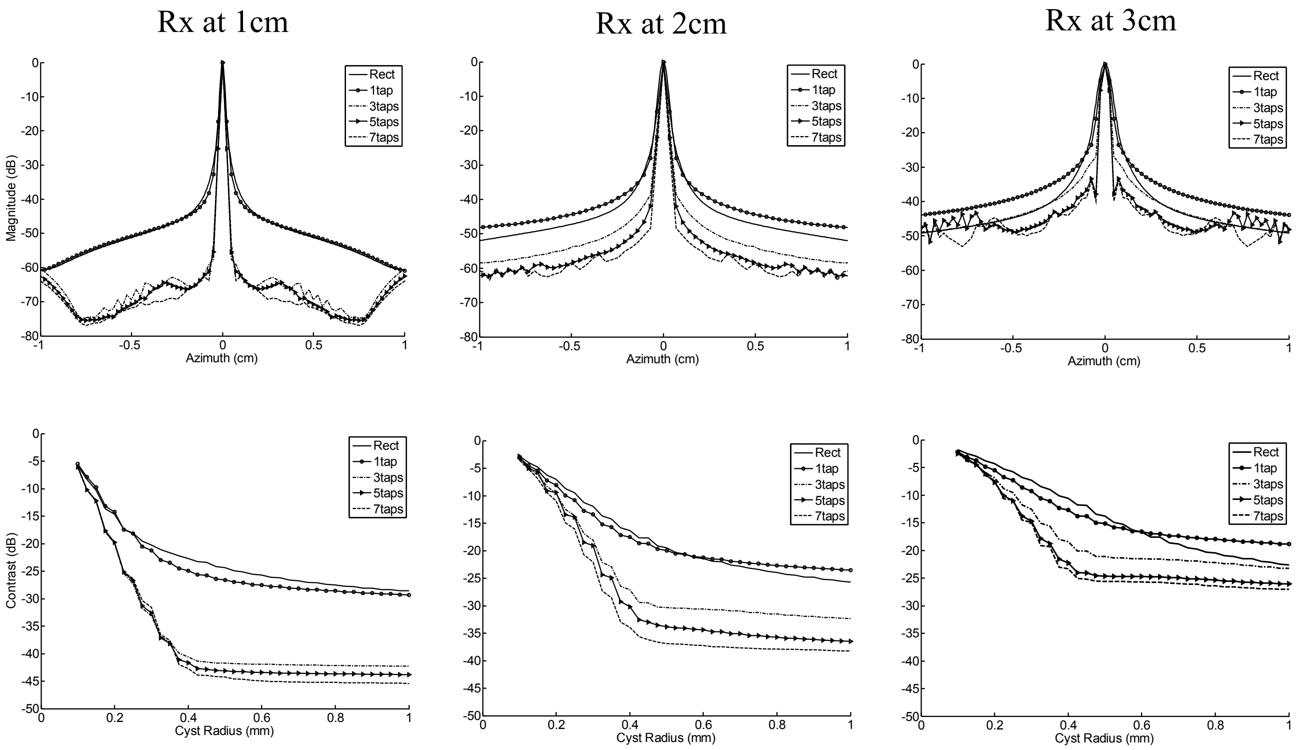

Fig. 2. Integrated lateral beamplots and cystic contrast curves comparing different apodization functions at different dynamic receive depths (Tx focus at 2.0cm). FIR-QCLS weights were calculated for 1-tap, 3-tap, 5-tap, and 7-tap FIR filters with a design cyst radius of 0.4mm. Notice the large reduction in sidelobe and grating lobe levels for the higher tap filters. The bottom row of plots shows cystic contrast curves as a function of cyst radius for the same apodization functions. Cystic contrast is improved by more than -20dB for the higher tap FIR filters at dynamic receive depths of 1.0 and 2.0cm. In general longer tap filters improve contrast resolution.

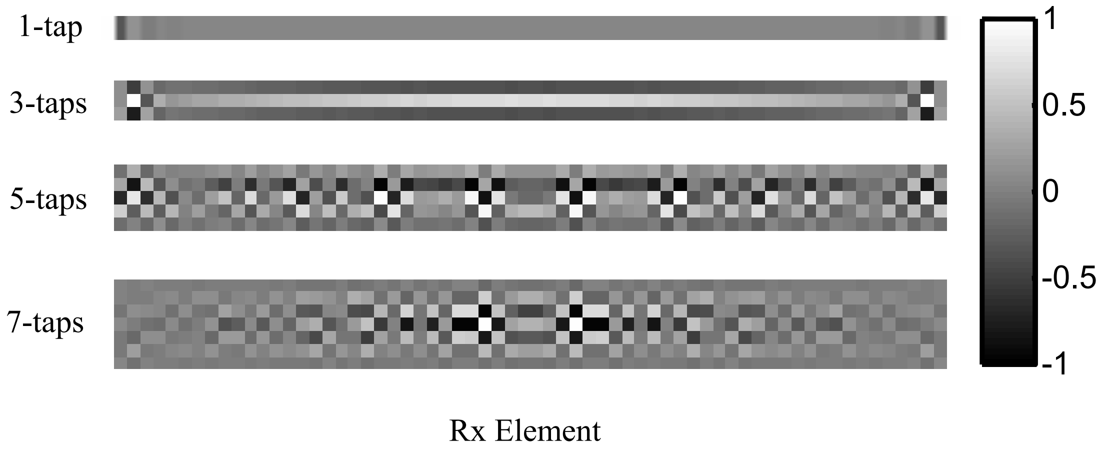

Fig. 3. FIR-QCLS weights for the multi-tap filters. These weights correspond to the dynamic receive at 2.0cm results in figure 2. The 1-tap and 3-tap weights are smooth across the receive aperture, showing some discontinuities at the edges. The 5-tap and 7-tap filters are more variant across the receive aperture. Notice that some weights take on negative amplitudes.

IV. EXPERIMENTAL RESULTS

We investigated the ability of our algorithm and novel receive beamformer architecture to improve the spatial PSF characteristics of an Ultrasonix Sonix RP ultrasound scanner (Ultrasonix Medical Corp., Burnaby, BC, Canada).

The Sonix RP system has a software development kit (SDK) named TEXO that enables low level scanner control with the ability to acquire single channel RF data sampled at 40MHz with 12bit precision. We have also created a Python™ programming language interface to the TEXO SDK that allows us to create customized pulse sequences without the need to recompile the system C code. Utilizing our Python™ interface with the TEXO SDK we can acquire a full set of synthetic receive aperture data from a 64 element transmit aperture and 64 element receive aperture in fractions of a second. In order to generate the 2D PSF required for our algorithm, we imaged a 20μm steel wire in a tank full of deionized water. We electronically scanned the transmit aperture across the array as well as mechanically moved the array using a 3-axis positioning system (Newport Motion Controller MM3000, Newport Co., Irvine, CA) in order to achieve azimuth spatial sampling of 75μm and axial spatial sampling of 50μm. We acquired a 1.95cm (azimuth) by 0.2cm (range) by 3000 time samples dataset to characterize the 3D spatio-temporal PSF. The entire experiment required 29 hours to execute, resulting in over 10Gbytes of raw, averaged RF data. The water temperature remained relatively constant over the course of the experiment between 21.6-22.4^{o}C.

We used the L14-5 128 element linear probe excited with a 1 cycle 6.67MHz pulse for the experiment. The transmit aperture consisted of 64 elements focused at 4.0cm in range (f/2). We acquired 64 receive elements synthetically and averaged each receive signal 100 times to improve electronic SNR. The receive data was also digitally bandpass filtered in MATLAB (The Mathworks, Inc., Natick, MA) with a 101st order bandpass filter with cutoff frequencies at 4 and 8MHz. An experimental 2D spatial PSF was made by sampling the 3D spatio-temporal PSF for each receive element according to a dynamic receive profile for a particular receive focus.

The log compressed envelope detected experimental 2D PSFs dynamically focused at 2.0cm using different conventional receive apodization functions are shown in figure 4. Also shown are experimental 2D PSFs computed using 1-tap, 3-tap, 5-tap and 7-tap FIR-QCLS windows designed for a cyst radius of 0.35mm. All images are log compressed to 60dB. Notice the progressive reduction of PSF energy in the sidelobe regions when using the multi-tap FIR-QCLS design. Figure 5 shows the integrated lateral beamplots and contrast curves for the experimental results. The FIR-QCLS weights reduce sidelobe levels, lower the total PSF energy outside the mainlobe, as well as decrease mainlobe width. Only the 1-tap and 7-tap QCLS plots are shown for clarity. The contrast curves for the rectangular, Hamming, Nuttall, 1-tap QCLS and 7-tap QCLS experimental PSFs are shown in the right hand plot of figure 5. The FIR-QCLS PSFs show increases in cystic resolution compared to the conventional windows. Specifically, the 7-tap apodization profile improved contrast by 7dB compared to the Hamming window, by 10dB compared to the rectangular window, and by 12dB compared to the Nuttall window over a range of cyst sizes.

V. DISCUSSUION

This paper demonstrates a novel receive beamformer with multi-tap FIR filters on each receive channel; a system architecture not currently employed in medical ultrasound. Schwann *et al.* suggested a similar type of architecture using linear phase FIR filters and also discussed the calculation of frequency dependent optimal receive apodization profiles. Their simulation results showed contrast improvements, however, their multiple objective formulation required iterative procedures and made it difficult to determine an "optimal" apodization profile [11]. Our formulation on the other hand requires no iterations and produces optimal apodization profiles in a least squares sense that maximize cystic resolution. Furthermore, the improvements in system performance using the FIR-QCLS windows are easily quantified using the contrast resolution metric.

The frequency response of the individual channel FIR filters is a concern because it could reduce SNR, negating the improvements in contrast resolution. However, the results from our simulations and experiments do not indicate that the FIR-QCLS filters drastically change the spectra of the receive data. If future results show that SNR is severely decreased, it may be possible to include an SNR constraint in our formulation, perform subband processing, or constrain the weights to be linear phase. This is an area of future research.

Although we were able to produce successful experimental results to show the use of our novel beamforming strategy, they do not show the same large gains in contrast (15-20dB) and point resolution observed in the simulations. Possible causes for these shortcomings include: a limited element angular response on the array, poor single channel SNR, element nonuniformity, and hysteresis in our experimental setup. All of these effects are detrimental to the FIR-QCLS algorithm. It would be nearly impossible to acquire the full spatio-temporal dataset needed to produce dynamic receive FIR-QCLS filters for every output image pixel with our given experimental setup. Indeed, the QCLS apodization design algorithm requires thorough characterization of the system's PSF. We are currently researching methods to improve our characterization of the system without the need to physically acquire the full 4D spatio-temporal

PSF. If these solutions prove successful, we will be able to calculate the full set of receive filters, make data reconstruction seamless and rapid, and further assess the performance of our algorithm to produce optimal contrast.

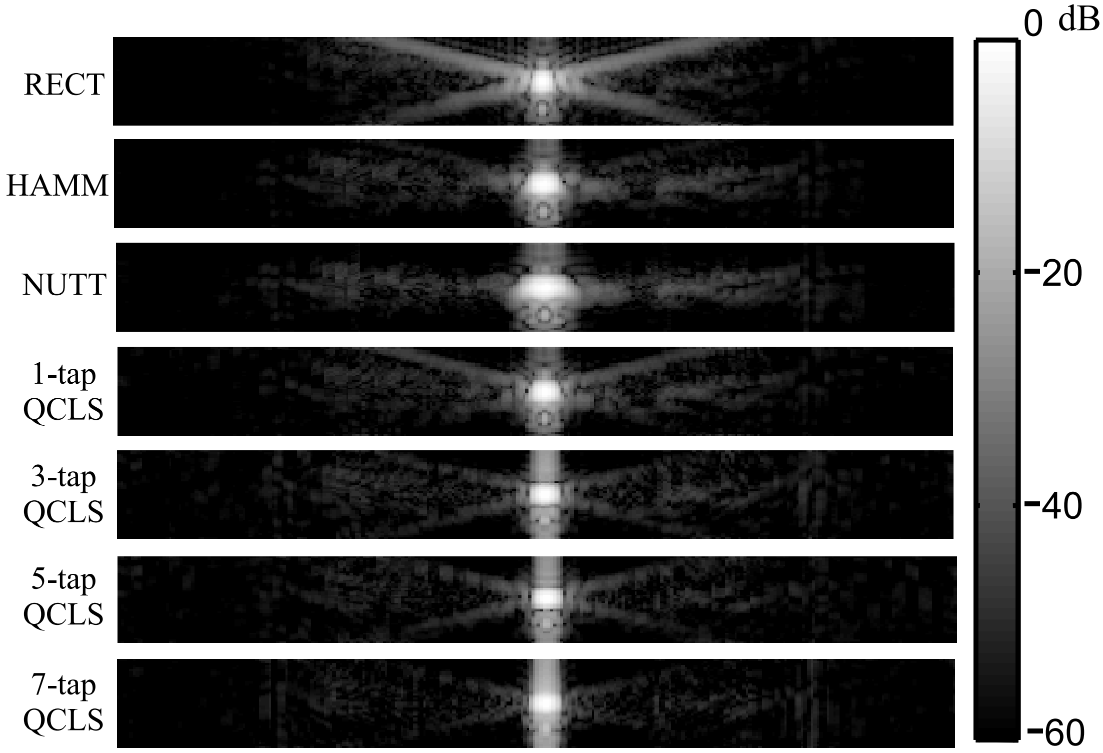

Fig. 4. Experimental 2D PSFs with different receive apodization functions applied. Each image is 0.2cm axially by 1.95cm laterally. All images were envelope detected and log compressed to 60dB. The multi-tap FIR-QCLS apodization functions progressively reduce the total sidelobe energy while maintaining a tight mainlobe.

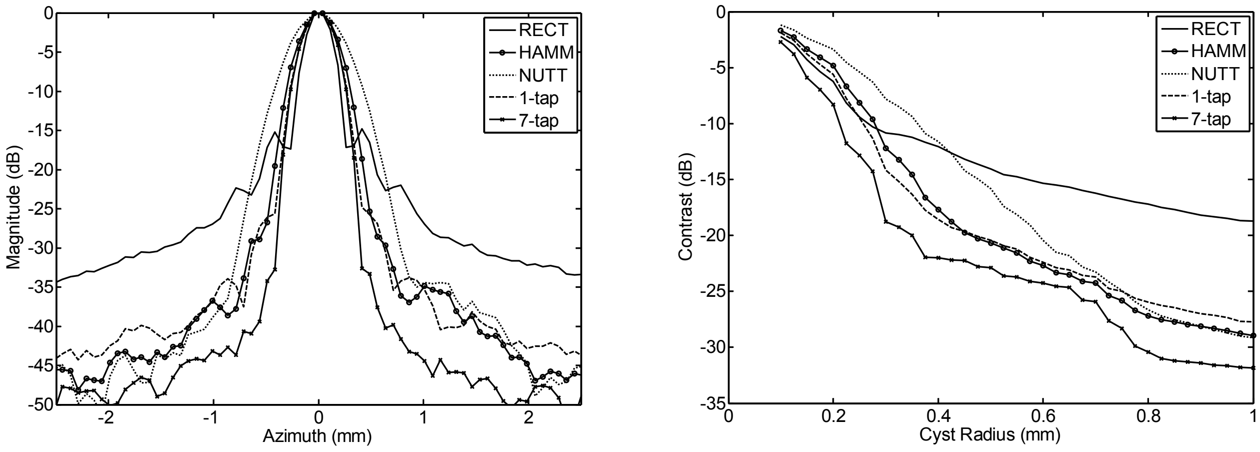

Fig. 5. Experimental integrated lateral beamplots (left) and contrast curves (right) with different receive apodization functions applied. The Hamming and Nuttall windows achieve lower sidelobes than the rectangular apodization function but have a larger mainlobe. The 1-tap QCLS apodization function achieves a tight mainlobe, but has a significant amount of energy in the sidelobe region. The 7-tap QCLS apodization function achieves a tight mainlobe and dramatically reduces the amount of sidelobe energy. The Hamming, Nuttall and 1-tap QCLS functions achieve worse contrast than the rectangular apodization function for small cyst sizes due to their mainlobe widths. The 1-tap QCLS apodization function is outperformed by the Hamming and Nuttall windows at larger cyst sizes. The 7-tap FIR-QCLS apodization function improves cystic resolution by more than 7dB for a range of cyst sizes and achieves the best contrast at every cyst size investigated.

VI. CONCLUSION

The FIR-QCLS receive beamformer presented in this paper enhances the contrast resolution of ultrasound images. The 2D spatial PSFs produced in experiments and simulations show lower sidelobe levels and narrower mainlobes than PSFs produced with conventional apodization functions. The algorithm appears stable across dynamic receive focal ranges and aperture sizes. Further investigation is required to examine the effects of phase aberration, shift variance of the system response, varying frequency response of the individual channel filters, and determine implementation in a real system. Results suggest that filters with as few as 7 taps can still offer large contrast improvements. Furthermore the FIR-QCLS apodization profiles consistently outperform conventional apodization windows and offer significant gains in image quality with a modest increase in system complexity.

ACKNOWLEDGEMENTS

The authors would like to thank Kevin Owen for his assistance in developing the experimental control software. We thank Kris Dickie and Ultrasonix Medical Corporation for technical support. This work was supported by US Army Congressionally Directed Research Program Grant No. W81XWH-04-1-0590.

REFERENCES

[1] D. A. Guenther and W. F. Walker, "Optimal Apodization Design for Medical Ultrasound using Constrained Least Squares. Part I: Theory," *IEEE Transactions on Ultrasonics, Ferroelectrics, and Frequency Control*, vol. 54, no. 2, pp. 332-342.

[2] D. A. Guenther and W. F. Walker, "Optimal Apodization Design for Medical Ultrasound using Constrained Least Squares. Part II: Simulation Results," *IEEE Transactions on Ultrasonics, Ferroelectrics, and Frequency Control*, vol. 54, no. 2, pp. 343-358.

[3] D. Vilkomerson, J. Greenleaf, and V. Dutt, "Towards a resolution metric for medical ultrasonic imaging," *Proc. IEEE Ultrason. Symp.*, vol. 2, pp. 1405-1410, 1995.

[4] M. Fink, L. Sandrin, M. Tanter, S. Catheline, S. Chaffai, J. Bercoff, and J.-L. Gennisson, "Ultra High Speed Imaging of Elasticity," *Proc. of the 2002 IEEE International Ultrasonics Symposium*, vol. 2, pp. 1811-1820, 2002.

[5] S. Emelianov, *et al.* "Combined ultrasound, optoacoustic, and elasticity imaging, "*Proc. of the 2004 International Biomedical Optics Symposium*, vol. 5320, pp. 101-112, 2004.

[6] A. H. Nuttall, "Some Windows with Very Good Sidelobe Behavior." *IEEE Trans. Acoust., Speech, and Signal Process.*, vol. 29, no. 1, pp. 84-91, 1981.

[7] K. Ranganthan and W. F. Walker, "A General Cystic Resolution Metric for Medical Ultrasound," accepted for publication in *IEEE Transactions on Ultrasonics, Ferroelectrics, and Frequency Control.*

[8] S. W. Smith and H. Lopez, "A contrast-detail analysis of diagnostic ultrasound imaging," *Med. Phys.*, vol. 9, no. 1, pp. 4-12, 1982.

[9] W. H. Gander, "Least Squares with a Quadratic Constraint," Numerische Mathematik, vol. 36, pp. 291-307, 1981.

[10] M. Ellis, D. A. Guenther, and W. F. Walker, "A Spline Based Approach for Computing Spatial Impulse Responses," accepted for publication in *IEEE Transactions on Ultrasonics, Ferroelectrics, and Frequency Control.*

[11] R. Schwann, N. Stache, and T. G. Noll, "Optimization of Frequency Dependent Receive Apodization," *Proc. of the 2005 IEEE International Ultrasonics Symposium*, vol. 4, pp. 1988-1991, 2005.

Near-Field, Broadband Adaptive Beamforming for Ultrasound Imaging

Francesco Viola[1], Michael A. Ellis, and William F. Walker[1,2]
[1]Department of Biomedical Engineering
[2]Department of Electrical and Computer Engineering
University of Virginia
Charlottesville, VA 22908

Abstract— **For over fifty years adaptive beamforming (ABF) algorithms have been applied in RADAR and SONAR signal processing. These algorithms reduce the contribution of undesired off-axis signals while maintaining a desired response along a specific look direction. Typically, ABF achieves higher resolution and contrast than conventional beamforming (CBF), at the price of an increased computational load. In this paper we describe a novel ABF designed for medical ultrasound, named the Time-domain Optimized Near-field Estimator, or TONE. We performed a series of simulations using ultrasound data to test the performance of this algorithm and compare it to conventional, data independent, delay and sum beamforming. We also performed experiments using a Philips SONOS 5500. CBF was applied using the default parameters of the Philips scanner, whereas TONE was applied on single-channel, unfocused data with plane wave transmit. TONE images were reconstructed at a sampling of 67μm laterally and 19μm axially. The results obtained for a series of 5 20μm wires in a water tank show a significant improvement in spatial resolution when compared to CBF. We also analyzed the performance of TONE as a function of speed of sound errors and array sparsity, finding TONE robust to both.**

I. INTRODUCTION

Sensor arrays are used in many application fields including RADAR, SONAR, geophysics, and medical imaging. For these applications, the received data is often processed using the conventional "delay-and-sum" beamforming. While this approach is straightforward and easy to implement, off-axis scatterers can introduce clutter, reducing the overall quality of the beamformer output. The contribution of such clutter is shown in figure 1. In panel A, an array of sensors is focused along the dotted line and a single point target is placed in the look direction, or on-axis, at a fixed distance from the array. As energy is reflected toward the array, a signal is received by each of the individual sensors. Focal delays are applied to each signal to generate the sensor/range data set shown in the figure. Summation across sensors to form an image line will amplify the signal coming from the look direction. However, when a secondary target is placed off-axis, as shown in panel B of figure 1, it may lie within the array's beam and thus corrupt the desired information. This is represented by the tilted waveforms visible in the sensor/range data set. Although summation across sensors amplifies the signal coming from directly in front of the array, it does not entirely eliminate the contribution of the off-axis target. Finally, panel C of figure 1 depicts single channel echo data obtained from the thyroid of a human subject at Duke University. At least three clear waveforms are visible in this sensors/range data set. These non-focal targets would appear in this image line as clutter, reducing image contrast.

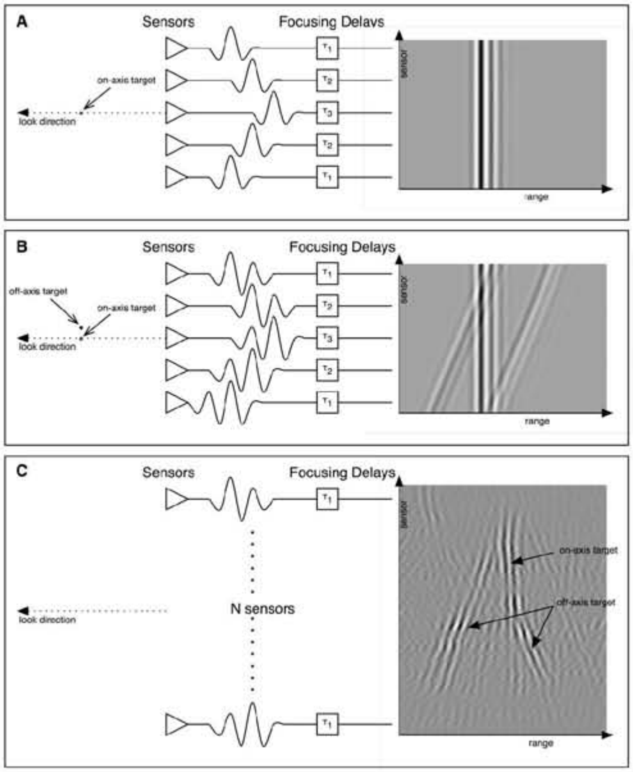

Figure 1. Panel A and B: schematic representation of the interference problem with conventional beamforming. Panel C: *in vivo* single channel thyroid data. The data clearly show the presence of bright off-axis scatterers as evidenced by the tilted plane wave. Courtesy of G. E. Trahey.

The problem of nulling the contribution of off-axis targets was first investigated for RADAR and SONAR systems by extending the pioneering work of Norbert Wiener. The

---

This work was supported by the US Army Congressionally Directed Medical Research Program in Breast Cancer grant No.W81XWH-04-1-0590

1-4244-0785-0/06/$20.00

application of Wiener filter theory to array signal processing led to the initial development of adaptive beamforming [1-3]. In adaptive beamforming, the information associated with the data received by an array of sensors is used to determine a set of filter weights that optimize the beamformer output. In the past fifty years, a plethora of algorithms have been developed, each exploiting specific properties of the received data [2-3]. These algorithms are able to achieve resolution far superior to that predicted by diffraction theory, while attaining excellent side lobe reduction.

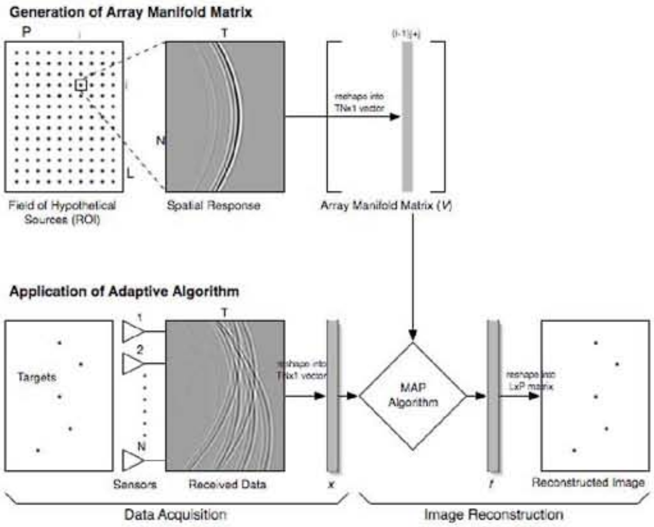

Figure 2. Schematic representation of TONE beamforming.

While adaptive beamforming is often used in applications involving narrowband signals in the far-field, current techniques have not been proven successful in the case of broadband signals originating in the near-field of the array. This is the case of medical ultrasound. In this paper we present an algorithm that is well suited for broadband signals generated in the near-field. This algorithm is developed from the Spatial Processing: Optimized and Constrained (SPOC) technique originally described by Van Trees *et al.* for applications in passive SONAR [4]. We term it Time-domain, Optimized, Near-field Estimator, or TONE. TONE is particularly useful since it does not require knowledge of second order statistics and is therefore suitable to use with only a single realization of data. Furthermore, it does not require any additional pre-processing technique to be applied.

II. TONE BEAMFORMING

The imaging region, referred to as the region of interest (ROI), is first subdivided into a collection of hypothetical sources at arbitrary positions, as shown schematically in the top panel of figure 2. Finer grid sampling yields finer final image resolution but entails higher computational costs. For each hypothetical source in the ROI, we determine (through experiments, simulation, or theory) the signal received by the array from target at that specific point (i.e., the spatial responses). For every hypothetical source, the spatial response is a matrix of dimensions TxN, where T is the number of samples in the axial, or temporal, dimension and N is the number of elements in the array. After the spatial responses for all the hypothetical sources have been determined, these responses are reshaped to form an array manifold matrix V of dimensions NTxLP, where L and P are the numbers of hypothetical sources in the range and lateral dimensions, respectively. The observation model becomes:

$$x = Vf \tag{1}$$

where $x=[x_1\ x_2\ \dots\ x_N]^T$ is the data received by the N-element array and f is the LPx1 signal vector, whose elements are the amplitudes of the hypothetical sources located in the ROI. x is a NTx1 vector that is obtained by concatenating the Tx1 channel data x_i. Given x and V, TONE operates on the received data x and the array manifold matrix V to solve for the position and intensity of the real sources (i.e., the vector f). For this purpose we consider the joint probability density function (PDF) $p(x,f)$. The maximum likelihood estimate of f is given by [5]:

$$\hat{f} = \arg\max_f p(x,f) = \arg\max_f (p(x/f)p(f)) \tag{2}$$

We assume that the marginal PDF $p(f)$ is known *a priori* and mathematically expressed as a zero-mean Gaussian distribution. Furthermore, since (1) needs to be satisfied, equation (2) reduces to the following [4]:

$$\hat{f} = \arg\max_f p(f) \tag{3}$$

which is referred to as maximum a posteriori (MAP) estimate of f. By substituting the marginal PDF $p(f)$ in (3) and rearranging terms, the MAP problem becomes:

$$\arg\max_f \sum_{l=1}^{LP} -|f_l|^2 \ \textit{subject to}\ x = Vf \tag{4}$$

where f_l are elements of f. A solution for (4) is found using the iterative procedure described in [4].

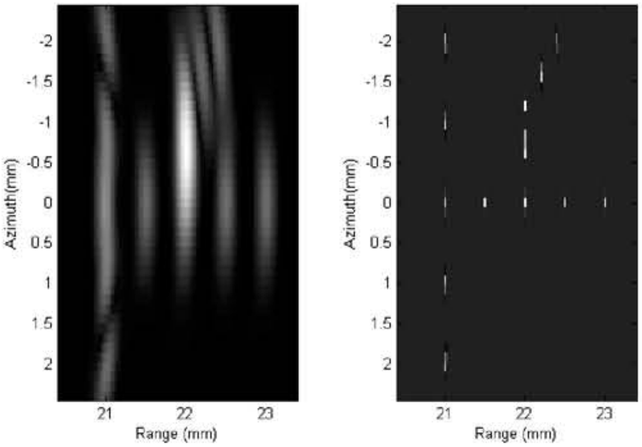

Figure 3. Conventional delay-and-sum beamforming (left) and TONE beamformed (right) of simulated point targets.

III. SIMULATION METHODS AND RESULTS

A series of computer simulations were performed to compare the performance of TONE to conventional delay-and-sum beamforming. All calculations were performed in MATLAB and utilized synthetic ultrasound signals. Furthermore, for all the simulations presented here, the array manifold matrix was obtained using the following procedure. First, the response to a reference point was obtained. For every hypothetical source, the reference response was then delayed and re-interpolated (via cubic splines) according to the geometrical delay profile corresponding to that specific source.

A. Point Targets

A series of point targets were distributed within a 4x5mm region in range and azimuth, respectively. In this case, we simulated a 33 element linear array operating at 5 Mhz with 150μm element pitch. The final sampling frequency was set at 40 MHz. A plane wave was used on transmit for both the conventional beamforming and TONE. Conventional beamforming was applied on the received RF data using Hann apodization and dynamic receive focusing. For TONE, we discretized the image region in a series of hypothetical targets separated 20μm in range and 120μm in azimuth. The positions of the points were chosen so that some, but not all coincide with the positions of the hypothetical targets. The results of this set of simulations are presented in figure 3.

B. Anechoic Cyst

A 1mm radius anechoic cyst was placed in front of the array and surrounded by roughly 4,000 scatterers randomly distributed within the image region. Scatterers' amplitudes followed a Gaussian distribution with zero mean and standard deviation of one. Simulation methods are the same of those described in the previous section, except that the hypothetical source sampling was reduced to 100μm in azimuth. Again, the positions of the scatterers do not necessarily coincide with the position of the hypothetical sources. The results are shown in figure 4.

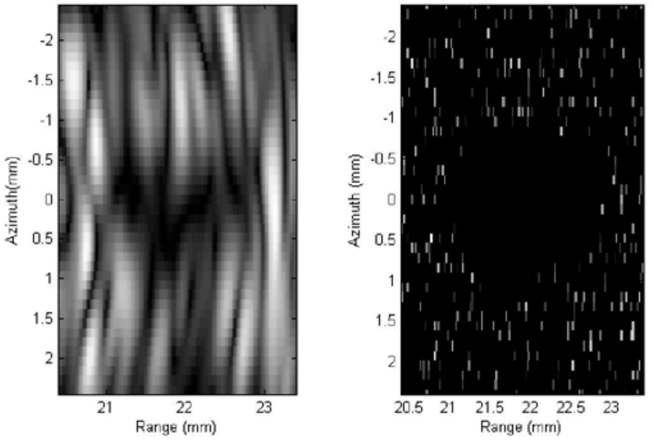

Figure 4. Conventional delay-and-sum beamforming (left) and TONE beamformed (right) of a simulated anechoic cyst.

IV. EXPERIMENTAL METHODS AND RESULTS

Experiments were also performed using a Philips SONOS 5500 imaging system employing a 6MHz linear array. The system was programmed to transmit on all elements simultaneously as to mimic a plane wave. The received data was obtained by stepping sequentially through the 128 receive channels. Received data was filtered using a 100 taps FIR filter with pass-band between 3 and 11Mhz. TONE was then applied on a 32-processor SGI Altix server with the aid of the Star-P parallel computing platform (Interactive Supercomputing, Inc.) The array manifold matrix was constructed using a procedure similar to that used for the computer simulations. In this case, however, the reference response was provided by a 20μm stainless steel wire suspended in a water tank.

A. Wire Targets

5 stainless steel wires (20μm diameter) were suspended in a water tank kept at room temperature. The wires were placed at a depth of roughly 2.2cm from the transducer's face. The top panel of figure 5 shows the image outputted by the SONOS, whereas the bottom panel shows the TONE image of the 5 wires. In the case of TONE, hypothetical sources were placed every 19μm axially and every 67μm laterally.

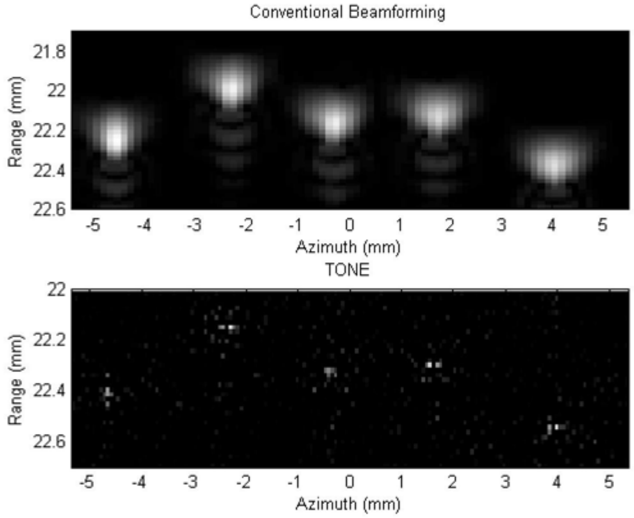

Figure 5. Conventional beamforming (top) and TONE beamforming (bottom) images of a set of 5 wires in water.

We have also analyzed the performance of TONE as a function of mismatched speed of sound. In this case the array manifold matrix was constructed using a speed of sound that differs from the true value. Results obtained for a 15m/s and 30m/s error are shown in the top and bottom panels of figure 6, respectively.

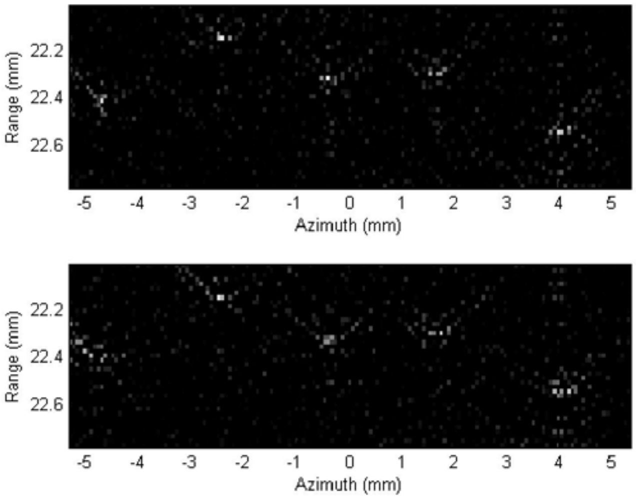

Figure 6. TONE beamformed images of the 5 steel wires with 15m/s (top) and 30m/s (bottom) mismatch in speed of sound.

We also analyzed the performance of TONE as a function of missing receive channels. While the images shown in figures 5 and 6 were generated using the full 128 channels provided by the SONOS (135μm pitch), figure 7 shows results obtained when the number of channels is reduced to 64, 32, and finally to 16. The corresponding pitches are 270μm, 540μm, and 1080μm, respectively.

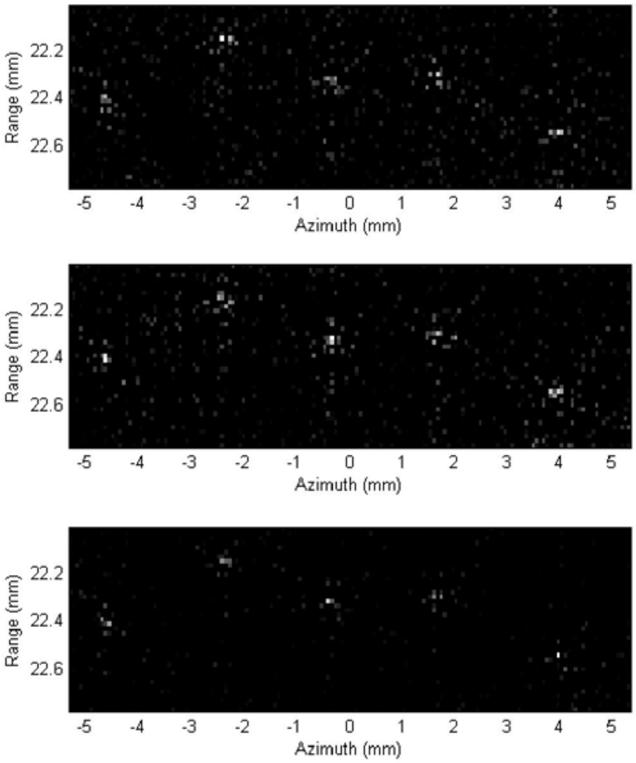

Figure 7. TONE beamforming with 64 (top), 32 (middle), and 16 (bottom), receive channels.

V. DISCUSSION

In medical ultrasound, bright off-axis targets can seriously degrade image quality by introducing broad image clutter. The application of ABF could reduce the effects of these targets, thus improving the overall image quality. However, the unique characteristics of ultrasound data make blind application of existing adaptive beamforming algorithms unlikely to be successful. In this paper a new beamforming technique, termed (TONE), has been presented and its performance has been evaluated both through simulations and experiments.

Figures 3 and 4 compare the TONE algorithm with the conventional delay and sum beamforming on synthetic data depicting wires and anechoic cyst phantoms. The superiority of TONE is clearly evident from those figures. Although not presented, we have performed additional simulations analyzing the stability of TONE with respect to additive noise. We have found that down to a 10 dB/channel SNR the performance of TONE remains excellent.

Figures 5-7 analyze the performance of TONE on experimental data. Hypothetical sources were placed every 19μm axially and every 67μm laterally. Similar results to those obtained in simulations are observed in figure 5. Although the five wires are clearly resolved, a small cloud of scatterers is visible around them. This is most likely due to noise and imperfection of the manifold matrix used. As stated above, the manifold matrix was generated by simply delaying and re-interpolating the response obtained from a single steel wire. More sophisticated models could be generated which would include for example the effects of element angular sensitivity. Furthermore, the current formulation of TONE is derived for a plane wave transmission. This was approximated by transmitting simultaneously on all the elements of the array.

The results of figure 6 show the stability of TONE with respect to aberration errors. The performance remains acceptable for a mismatch in speed of sound of 15m/sec and 30m/sec. These results are significant since most adaptive beamforming algorithm rapidly degrade when ideal conditions are not met.

Finally, figure 7 shows that TONE performance is independent on variations in channel number/pitch dimensions. While applying conventional beamforming on a 16 channel systems with 1.1mm pitch would result in massive grating lobes, the bottom panel of this figure shows that TONE remains almost unaffected.

Currently, the main limitation of this algorithm is represented by its high computational complexity. While higher spatial resolution is achieved using finer sampling of the ROI, this also incurs in higher complexity. The generation of the manifold matrix and the iterative procedure to estimate f represents the most costly steps. For an image region of 1cm by 1cm and assuming a sampling grid of hypothetical sources of 20μm by 70μm, V is on the order of 64K by 71K elements. However, for a given ROI and a desired sampling grid, the manifold matrix can be calculated in advance and stored for later application. Furthermore, TONE may also be applied to a given receive data set using a variety of iterative approaches to reduce the required computational complexity and data storage size. In one such approach the complete received data set is subdivided into multiple data segments that may or may not be uniformly sampled and may or may not overlap. For each received data segment, a distinct array manifold matrix is formed to represent the responses from hypothetical sources which could contribute to the specific data segment. TONE could then be applied separately to each of the data segments and their matched array manifold matrices. We are currently investigating this and other approaches.

VI. CONCLUSIONS

A new beamforming approach has been presented in this paper. Simulation and experimental results clearly suggest the advantages of this algorithm over conventional beamforming.

VII. ACKNOWLEDGMENT

We acknowledge technical support from Interactive Supercomputing Inc. and Philips Medical Systems.

REFERENCES

[1] S. Haykin, “Adaptive Filter Theory,” 4th ed., Prentice-Hall, Upper Saddle River, New Jersey, 2002.

[2] B. D. Van Veen and K. M. Buckley, “Beamforming: A Versatile Approach to Spatial Filtering,” *IEEE ASSP Magazine*, pp. 4-24, 1988.

[3] W. F. Gabriel, “Adaptive Processing Array Systems,” *Proc. IEEE*, vol. 80, no. 1, pp. 152-162, 1992.

[4] R. Bethel, B. Shapo, and H. L. Van Trees, “Single Snapshot Spatial Processing: Optimized and Constrained,” *Sensor Array and Multichannel Signal Processing Workshop Proceedings*, pp. 508-512, 2002.

[5] L. L. Sharf, “Statistical Signal Processing: Detection, Estimation, and Time Series Analysis,” Addison Wesley, 1991.

Piecewise-Linear Approximation for Improved Accuracy in Near-Field Ultrasound Simulation

Michael A. Ellis and William F. Walker
Department of Biomedical Engineering
University of Virginia
Charlottesville, VA 22908

Abstract— **Computer simulation is an important tool for the design of phased array ultrasonic systems. FIELD II, which determines the two-way temporal response of a transducer at a point in space, is the current *de facto* standard for ultrasound simulation tools [1]. However, our laboratory has recently described [2] a complementary tool, entitled DELFI, which is optimized for prediction of spatial responses at a single instant in time. This tool makes use of an analytical approach by defining the impulse response as delta functions or sums of unit step or unit ramp functions. Here we have modified this original DELFI tool, removing any far-field assumptions, to achieve a significant increase in accuracy for near-field applications, with only a slight loss in computational efficiency. For applications requiring a spatial response at a single instant in time, new DELFI is roughly 110 times faster than FIELD-triangles for similar amounts of error and 9 times more accurate than original DELFI at a computational cost factor of 1.3. For spatio-temporal applications, new DELFI has about the same computational efficiency as FIELD-triangles for similar amounts of error and is 9.3 times more accurate than original DELFI at a computational cost factor of 1.5.**

I. INTRODUCTION

Due to the broadband, near-field characteristics of typical clinical ultrasound applications, simple mathematical models to predict the ensuing pressure field of a system, such as the Fraunhofer approximation, are of limited use. Consequently, the design of modern ultrasound systems is highly dependent on the use of computer simulation tools. It is important for these tools to be both accurate and computationally efficient so that the designer can use them for high level system optimization without too great a time requirement.

Our laboratory has recently described such a simulation tool, entitled DELFI, which utilizes a signal model similar to that of FIELD II, the *de facto* standard for system simulation in ultrasound. This tool determines the system response as the sum of polynomial functions and is optimized for computing spatial responses at a single instant in time.

Here, we describe a modification to DELFI that allows for increased accuracy in near-field simulations with little added computation time. Using a combination of superposition and a piecewise-linear approximation to the true analytical response, this new tool makes use of the pre-existing, optimized DELFI architecture, leading to only small increases in computational cost.

II. ORIGINAL DELFI

The original DELFI simulation tool is optimized to determine the spatial response of a system at a single instant in time, thus making it complementary to the well known FIELD II program. Both tools make use of the same far-field approximation originally described by Stepanishen [3], only DELFI computes an analytical response as opposed to the sampled, numerical response determined by FIELD II.

Drawing upon the methodology of FIELD, DELFI describes the one-way spatial impulse response as one of three functions, depending on the location of the field point with respect to the computational element. If the field point lies on a line perpendicular to the element face and passing through its center then the spatial impulse response as a function of time is simply a delta function. If, instead, the field point lies upon one of two planes passing through the element center and perpendicular to the element face then the spatial impulse response in time is a rectangle function. Otherwise, if the field point fulfills neither of the above conditions then the spatial impulse response in time is a trapezoid function. The latter two can be described analytically as the sum of unit step or ramp functions.

$$h_0(x,y,z,t) = A_0(x,y,z)\delta(t-t_0) \tag{1}$$

$$h_1(x,y,z,t) = A_1(x,y,z)u(t-t_{1,0}) - A_1(x,y,z)u(t-t_{1,1}) \tag{2}$$

$$\begin{aligned} h_2(x,y,z,t) = {} & (t-t_{2,0})A_2(x,y,z)u(t-t_{2,0}) - (t-t_{2,1})A_2(x,y,z)u(t-t_{2,1}) \\ & -(t-t_{2,2})A_2(x,y,z)u(t-t_{2,2}) + (t-t_{2,3})A_2(x,y,z)u(t-t_{2,3}) \end{aligned} \tag{3}$$

where h_0, h_1, and h_2 represent the delta, rectangle, and trapezoid spatial impulse responses respectively and $u(t)$ is the unit step function. The scaling functions $A_0(x,y,z)$, $A_1(x,y,z)$, and $A_2(x,y,z)$ are constant at any specific spatial location and include $1/r$ spreading, scaling to account for the element size, and an obliquity factor to account for a soft transducer baffle [4], if desired. The time delay t_0 present in (1) is determined by the speed of sound and the distance from the element center to the field point. Similarly, the delays present in (2) and (3) are determined from the speed of sound and distances between the field point and the element edges and corners, respectively.

This work was supported by the US Army Congressionally Directed Medical Research Program in Breast Cancer grant No.W81XWH-04-1-0590 and NIH NIBIB grant RO1 EB0023489

Analytical equations for the resulting two-way responses can then be obtained by convolving the appropriate one-way response for the transmit element with that of the receive element. The result is six possible two-way impulse responses.

$$h_{0_a} \underset{t}{*} h_{0_b} = A_{0_a} A_{0_b} \delta\left(t - t_{0_a} - t_{0_b}\right) \tag{4}$$

$$h_0 \underset{t}{*} h_1 = A_0 A_1 \sum_{j=0}^{1} (-1)^j u\left(t - t_0 - t_{1,j}\right) \tag{5}$$

$$h_0 \underset{t}{*} h_2 = A_0 A_2 \sum_{j=0}^{3} c_j \left(t - t_0 - t_{2,j}\right) u\left(t - t_0 - t_{2,j}\right) \tag{6}$$

$$h_{1_a} \underset{t}{*} h_{1_b} = A_{1_a} A_{1_b} \sum_{j=0}^{1} \sum_{k=0}^{1} (-1)^j (-1)^k \left(t - t_{1_a,j} - t_{1_b,k}\right) u\left(t - t_{1_a,j} - t_{1_b,k}\right) \tag{7}$$

$$h_1 \underset{t}{*} h_2 = A_1 A_2 \sum_{j=0}^{1} \sum_{k=0}^{3} (-1)^j c_k \left(t - t_{1,j} - t_{2,k}\right)^2 u\left(t - t_{1,j} - t_{2,k}\right) \tag{8}$$

$$h_{2_a} \underset{t}{*} h_{2_b} = A_{2_a} A_{2_b} \sum_{j=0}^{3} \sum_{k=0}^{3} c_j c_k \left(t - t_{2_a,j} - t_{2_b,k}\right)^3 u\left(t - t_{2_a,j} - t_{2_b,k}\right) \tag{9}$$

Using cubic splines, the excitation function can also be described analytically. The system response can then be computed as the summation of the convolution of cubic spline segments with delta, unit step, or unit ramp functions.

III. NEW DELFI

New DELFI was designed to achieve increased accuracy in near-field simulations with only a small increase in computation time. By simply adjusting the slopes of the ramp functions used to describe the spatial impulse responses, we can make a piece-wise linear analytical approximation of the true impulse response, thereby removing any far-field assumptions. The result is a more accurate representation of the spatial impulse response that can still be described as a sum of ramp functions. Because original DELFI is already optimized to model the spatial impulse responses as sums of ramp functions, new DELFI is only slightly more computationally costly. Figure 2 shows an example of how the piece-wise linear approximations compare to the true impulse responses.

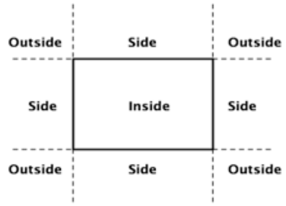

Figure 1. Map showing the three spatial regions used to determine element subdivision.

This approximation was further improved upon by utilizing superposition in regions where the field point is directly above the element or off to one side. By actively dividing the element such that the field point is always in the outside region of the sub-elements, as described by Figure 1, the response can always be approximated by the sum of four ramp functions of varying slopes. So, if the field point is in the side region, the element will be divided into two sub-divisions. If the element is in the inside region, the element is divided into four sub-divisions. Otherwise, the field point is already in the outside region and the element is not sub-divided.

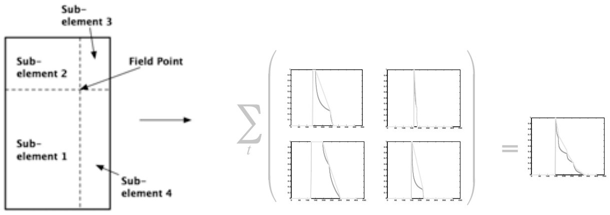

Figure 2. The element is subdivided so that the field point is always in the outside region of each of the sub-elements. The responses of each sub-element are summed to get the total element response.

IV. VALIDATION

The accuracy of the proposed algorithm was tested by comparing the one-way spatio-temporal response of a single 2D array element as predicted by both the new and original DELFI with that of FIELD II using triangles, sampled at 10GHz temporally. At such a sampling rate, FIELD-triangles offers a very good model of the true system response, thus making it a good choice for a gold standard. The array element was modeled using a single 300 x 300 µm computational element. All responses assumed a combined excitation and transmit electromechanical impulse response equal to a 5 MHz sine multiplied by an 8-cycle Nuttall window.

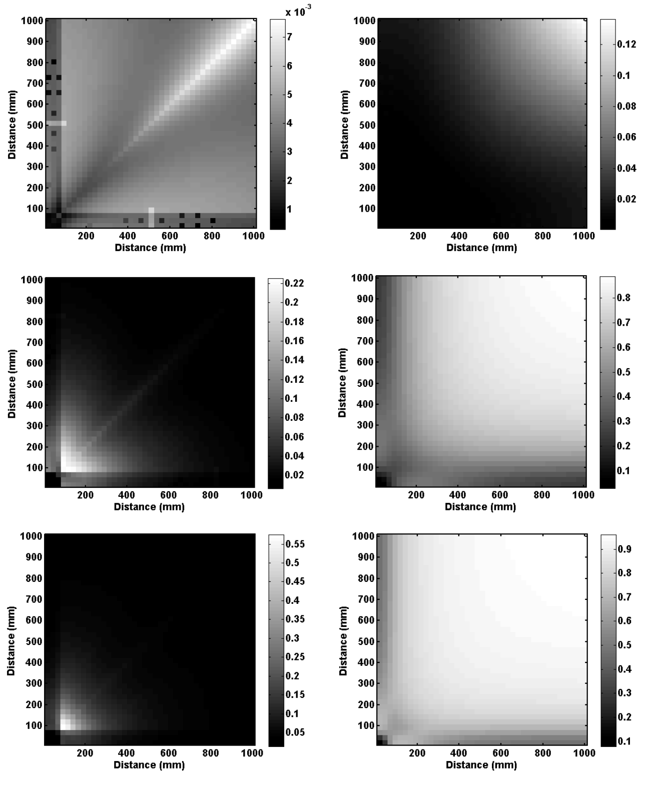

Figure 3. Normalized sum squared errors for new DELFI and original DELFI as compared to FIELD-triangles sampled at 10GHz temporally. Error was computed on the temporal response at each spatial location in a square extending 2 mm from the center of the element in azimuth and elevation, sampled every 50 µm. The left column shows the errors for new DELFI and the right column shows those for original DELFI. From the top row to bottom are the errors at ranges of 2mm, 200 µm, and 100 µm, respectively.

The system response was determined in a square region extending 2mm from the center of the element in both azimuth and elevation, sampled every 50 µm. This space-space-time data set was determined for a total of three different ranges, as shown in Figure 3. The space-space-time datasets were normalized by the peak amplitude of the temporal response for the spatial point directly above the center of the element. The datasets were also sub-sample shifted temporally to provide maximal alignment for the spatial point directly above the element center. Sum squared errors were computed for the temporal response at each spatial location.

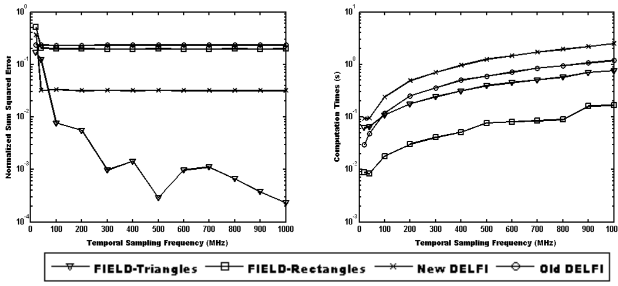

Figure 4. Comparison of new DELFI, original DELFI, FIELD-rectangles, and FIELD-triangles with respect to temporal sampling frequency for spatio-temporal responses. The left panel shows normalized sum squared error with respect to FIELD-triangles sampled at 10 GHz. The right panel shows computation times as determined by the `tic` and `toc` commands in MATLAB.

Sum squared error and computation times for new DELFI, original DELFI, FIELD-rectangles and FIELD-triangles were determined as a function of temporal sampling frequency. The same simulation parameters used above, only now fixed at a range of 200 µm, were repeated for temporal sampling rates between 20 MHz and 1 GHz. Sum squared errors, as shown in the left panel of Figure 4, were again computed for the temporal response at each spatial location and then averaged over the entire spatial region, yielding a single mean error value over the region at the given sampling rate. Computation times, as shown in the right panel of Figure 4, were determined using the `tic` and `toc` commands within MATLAB (The Mathworks, Inc. Natick, MA).

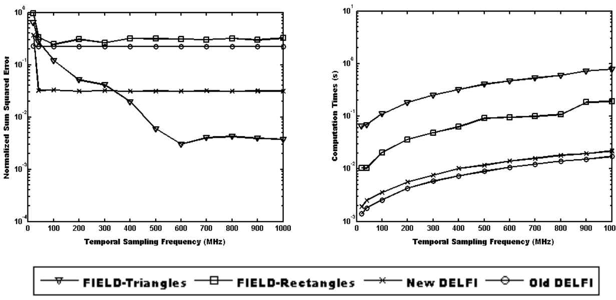

Figure 5. Comparison of new DELFI, original DELFI, FIELD-rectangles, and FIELD-triangles with respect to temporal sampling frequency for space-space responses. The left panel shows normalized sum squared error with respect to FIELD-triangles sampled at 10 GHz. The right panel shows computation times as determined by the `tic` and `toc` commands in MATLAB.

The same set of comparisons was repeated for the same spatial region, only now at a single instant in time, yielding a space-space response rather than a space-time response. The responses were normalized to the amplitude of the spatial point directly above the element center and were bulk shifted spatially so as to provide maximal alignment of the region. Again, the normalized sum squared error was computed with respect to FIELD-triangles sampled at 10 GHz. However, for this dataset, errors were computed on the amplitude of the response at each spatial location in the region examined, as there was not a full time course to compare. Results from this comparison are shown in Figure 5.

V. DISCUSSION

The proposed algorithm is intended to offer increased accuracy for only a slight sacrifice in computational efficiency as compared to the original DELFI. Examining the scales of the colorbars in Figure 3, we can see that new DELFI has a lower maximum error in each of the spatial regions examined, showing that it is indeed a closer approximation to the true response. This result is to be expected, as new DELFI offers a closer approximation to the true impulse response.

Examining the images in Figure 3, we see that the error of new DELFI occurs in a specific spatial pattern. The peak errors in new DELFI occur along the diagonal from the center of the element. This is due to the true response along this line having a highly curved shape that is difficult to model using piece-wise linear approximations. It can also be seen that new DELFI produces smaller errors in the region directly above and directly to the sides of the element. This is due to a subdivision of the element in these regions and the application of superposition. The result is an element response that more accurately models the true response in these regions, leading to smaller errors. By that same token, the errors within the inside region are the smallest because they result from a superposition of four sub-elements rather than the one or two used in the outside and side regions, respectively.

Looking at the plots in Figure 4, we see that, for spatio-temporal responses, new DELFI achieves a similar amount of error sampled at 40 MHz as FIELD-triangles achieves sampled at around 80 MHz. Comparing the computation times of the two methods at these respective temporal sampling frequencies, we see that they both require about the same amount of time to achieve similar errors. For spatio-temporal responses, new DELFI is also roughly 9.3 times more accurate that original DELFI while taking roughly 1.5 times longer to calculate.

Looking at the plots in Figure 5, we see that, for space-space responses, new DELFI achieves a similar amount of error sampled at 40 MHz as FIELD-triangles achieves sampled at around 350 MHz. Again comparing the computation times of the two methods at these respective temporal sampling rates, we see that new DELFI is roughly 110 times faster than FIELD-triangles for similar amounts of error. For space-space responses, new DELFI is also about 9 times more accurate than original DELFI while taking 1.3 times longer to compute.

Although new DELFI performs quite well with respect to FIELD-triangles in both space-space and space-time applications, there are several modifications that could be made to make it an even more appealing simulation tool. For example, a significant portion of the error generated by new DELFI comes from a shifting of the energy in the impulse responses due to superposition of the linear approximations. By calculating the center of mass of the responses and taking the difference, we can determine the necessary time shift to minimize this source of error.

VI. CONCLUSIONS

New DELFI has proven to be an attractive complement to both FIELD and the original DELFI simulation tool. It provides an increase in accuracy for a small sacrifice in computational cost, making it an ideal applicant for near-field simulations of the system spatial response at a single instant in time. When used to determine spatial responses at a single instant in time, new DELFI proves to be roughly two orders of magnitude faster than FIELD-triangles to achieve similar error. FIELD-rectangles and original DELFI do not achieve similar errors in the frequency range examined. When used to determine spatio-temporal responses, new DELFI achieves similar error to FIELD-triangles, but at a slightly longer computation time. However, several modifications could be made to new DELFI to decrease its error even further, making it as appealing in spatio-temporal applications as it is in spatial applications.

REFERENCES

[1] J. A. Jensen and N. B. Svendsen, "Calculation of pressure fields from arbitrarily shaped, apodized, and excited ultrasound transducers," *Ultrasonics, Ferroelectrics and Frequency Control, IEEE Transactions on*, vol. 39, pp. 262-267, 1992.

[2] M.A. Ellis, D.A. Guenther, and W.F. Walker. "A Spline Based Approach for Computing Spatial Impulse Responses," *Ultrasonics, Ferroelectrics and Frequency Control, IEEE Transactions on*, submitted for peer review August 11, 2006.

[3] P. R. Stepanishen, "Transient Radiation from Pistons in an Infinite Baffle," *Journal of the Acoustical Society of America*, vol. 49, pp. 1629-1638, 1970.

[4] A. R. Selfridge, G. S. Kino, and B. T. Khuri-Yahub, "A theory for the radiation pattern of a narrow strip acoustic transducer," *Applied Physics Letters*, vol. 37, pp. 35-6, 1980.

Ultrasound Imaging with Beamforming Adapted to Target

Francesco Viola[1], Michael A. Ellis[1], and William F. Walker[1,2]
[1]Department of Biomedical Engineering
[2]Department of Electrical and Computer Engineering
University of Virginia
Charlottesville, VA 22908

Abstract— **For over fifty years adaptive beamforming (ABF) algorithms have been applied in RADAR and SONAR signal processing. These algorithms reduce the contribution of undesired off-axis signals while maintaining a desired response along a specific look direction. Typically, ABF achieves higher resolution and contrast than conventional beamforming (CBF), at the price of an increased computational load. In this paper we develop a novel ABF that can be applied to medical ultrasound, named the Time-domain Optimized Near-field Estimator, or TONE. We performed a series of simulations using ultrasound data to test the performance of this algorithm and compare it to conventional, data independent, delay and sum beamforming. We also performed experiments using a Philips SONOS 5500. CBF was applied using the default parameters of the Philips scanner, whereas TONE was applied on single-channel, unfocused data with plane wave transmit. TONE images were reconstructed at a sampling of 67µm laterally and 19µm axially. The results obtained for a series of 5 20µm wires in a water tank show a significant improvement in spatial resolution when compared to CBF. We also analyzed the performance of TONE as a function of speed of sound errors and array sparsity, finding TONE robust to both.**

I. INTRODUCTION

Sensor arrays are used in many application fields including RADAR, SONAR, geophysics, and medical imaging. For these applications, the received data is often processed using the so-called conventional "delay-and-sum" beamforming. While this approach is straightforward and easy to implement, off-axis scatterers can introduce clutter, reducing the overall quality of the beamformer output. The contribution of such clutter is shown in figure 1. In panel A, an array of sensors is focused along the dotted line and a single point target is placed along the look direction, or on-axis, at a fixed distance from the array. As energy is reflected toward the array, a signal is received by each of the individual sensors. Focal delays are applied to each signal to generate the sensor/range set of data shown in the figure. Summation across sensors to form an image line will amplify the signal coming from the look direction. However, when a secondary target is placed off-axis, as shown in panel B of figure 1, it may lie within the array's beam and thus corrupt the desired information. This is represented by the tilted waveforms visible in the sensor/range data set. Although summation across sensors would amplify the signal coming from directly in front of the array, it would not entirely eliminate the contribution of the off-axis target. Finally, panel C of figure 1 depicts single channel echo data obtained from the thyroid of a human subject at Duke University. At least three clear waveforms are visible in this sensors/range data set. These non-focal targets would appear in this image line as clutter, reducing image contrast.

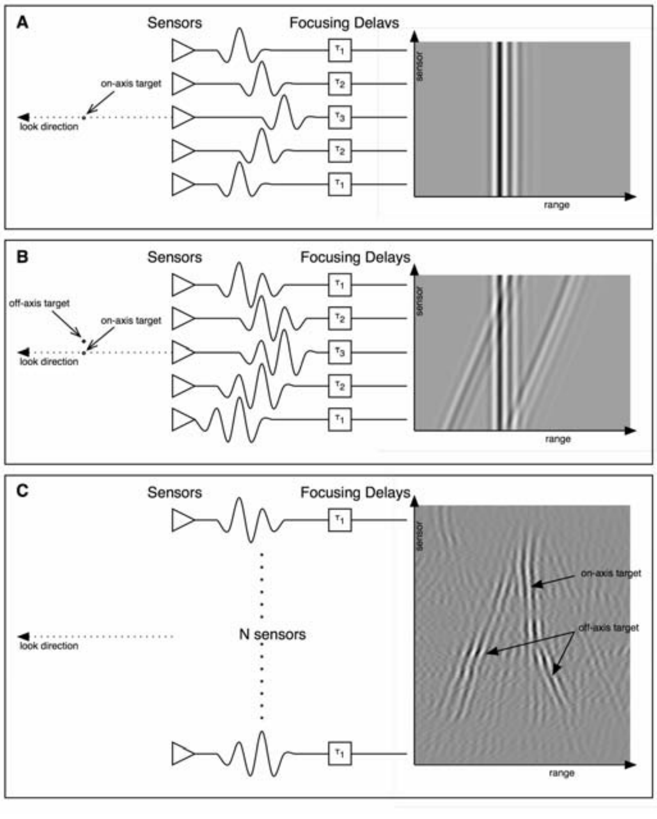

Figure 1. Panel A and B: schematic representation of the interference problem with conventional beamforming. Panel C: *in vivo* single channel thyroid data. The data clearly show the presence of bright off-axis scatterers as evidenced by the tilted plane wave. Courtesy of G. E. Trahey.

The problem of nulling the contribution of off-axis targets was first investigated for RADAR and SONAR systems by extending the pioneering work of Norbert Wiener. The

---

This work was supported by the US Army Congressionally Directed Medical Research Program in Breast Cancer grant No.W81XWH-04-1-0590

application of Wiener filter theory to array signal processing led to the initial development of adaptive beamforming [1-3]. In adaptive beamforming, the information associated with the data received by an array of sensors is used to determine a set of filter weights that optimize the beamformer output. In the past fifty years, a plethora of algorithms have been developed, each exploiting specific properties of the received data [2-3]. These algorithms are able to achieve resolution far superior to that predicted by diffraction theory, while attaining excellent side lobe reduction.

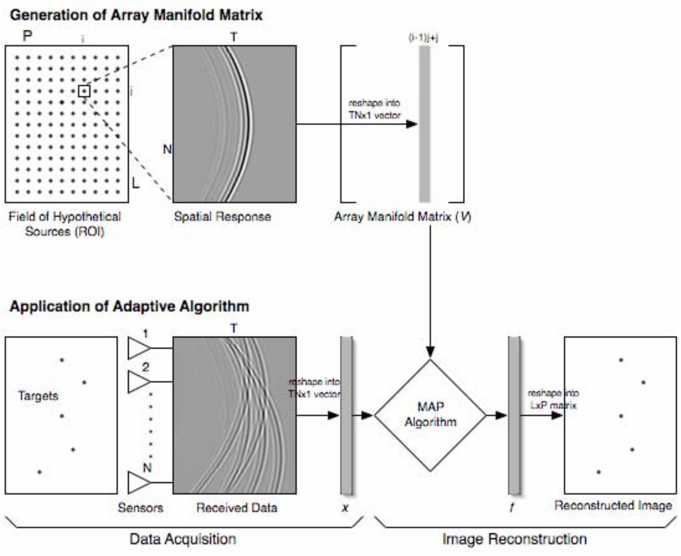

Figure 2. Schematic representation of TONE beamforming.

While adaptive beamforming is often used in applications involving narrowband signals in the far-field, current techniques have not been proven successful in the case of broadband signals originating in the near-field of the array. This is the case of medical ultrasound. In this paper we present an algorithm that is well suited for broadband signals generated in the near-field. This algorithm is built upon the Spatial Processing: Optimized and Constrained (SPOC) technique originally described by Van Trees *et al.* for applications in passive SONAR [4]. We term it Time-domain, Optimized, Near-field Estimator, or TONE. TONE is particularly useful since it does not require knowledge of second order statistics and is therefore suitable to use with only a single realization of data. Furthermore, it does not require any additional pre-processing technique to be applied.

II. TONE BEAMFORMING

The imaging region, named here the region of interest (ROI), is first subdivided into a collection of hypothetical sources at arbitrary positions, as shown schematically in the top panel of figure 2. Finer grid sampling yields finer final resolution but entails higher computational costs. For each hypothetical source in the ROI, we calculate the hypothetical signal received by the array for that specific point (i.e., the spatial responses). For every hypothetical source, the spatial response is a matrix of dimensions TxN, where T is the number of samples in the axial, or temporal, dimension and N is the number of elements in the array. After the spatial responses for all the hypothetical sources have been calculated, these responses are reshaped to form an array manifold matrix *V* of dimensions NTxLP, where L and P are the numbers of hypothetical sources in the range and lateral dimensions, respectively. The observation model becomes:

$$x = Vf \qquad (1)$$

where $x=[x_1\ x_2\ \dots\ x_N]^T$ is the data received by the N-element array and f is the LPx1 signal vector, whose elements are the amplitudes of the hypothetical sources located in the ROI. x is a NTx1 vector that is obtained by concatenating the Tx1 channel data x_i. We wish to estimate the signal vector f, given x and V. For this purpose we consider the joint probability density function (PDF) $p(x,f)$. The maximum likelihood estimate of f is given by [5]:

$$\hat{f} = \arg\max_f\ p(x,f) = \arg\max_f\,(p(x/f)p(f)) \qquad (2)$$

We assume that the marginal PDF $p(f)$ is known *a priori* and mathematically expressed as a zero-mean Gaussian function. Furthermore, since (1) needs to be satisfied, equation (2) reduces to the following [4]:

$$\hat{f} = \arg\max_f\ p(f) \qquad (3)$$

which is referred to as maximum a posteriori (MAP) estimate of f. By substituting the marginal PDF $p(f)$ in (3) and rearranging terms, the MAP problem becomes:

$$\arg\max_f \sum_{l=1}^{LP} -|f_l|^2 \ \ subject\ to\ x = Vf \qquad (4)$$

where f_l are elements of f. A solution for (4) is found using the iterative procedure described in [4].

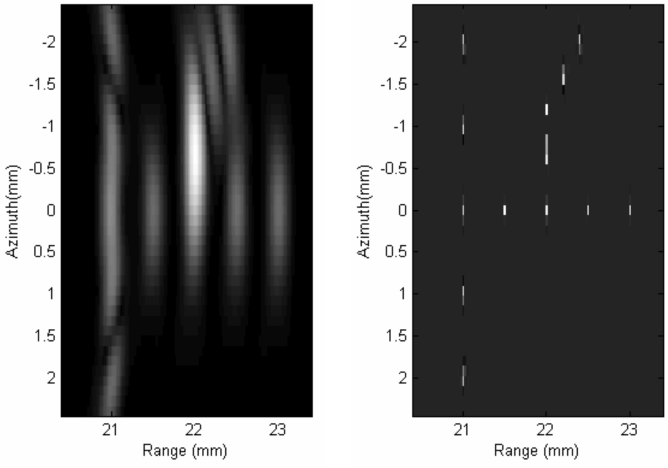

Figure 3. Conventional delay-and-sum beamforming (left) and TONE beamformed (right) of simulated point targets.

III. SIMULATION METHODS AND RESULTS

A series of computer simulations were performed to compare the performance of TONE to conventional delay-and-sum beamforming. All calculations were performed in MATLAB and utilized synthetic ultrasound signals.

A. *Point Targets*

A series of point targets were distributed within a 4x5mm region in range and azimuth, respectively. In this case, we simulated a 33 element linear array operating at 5 MHz. The final sampling frequency was set at 40 MHz. A plane wave was used on transmit for both the conventional beamforming and TONE. Conventional beamforming was applied on the received RF data using Hann apodization and dynamic receive focusing. For TONE, we discretized the image region in a series of hypothetical targets separated 20µm in range and 120µm in azimuth. The positions of the points were chosen so that some, but not all coincide with the positions of the hypothetical targets. The results of this set of simulations are presented in figure 3.

B. *Anechoic Cyst*

A 1mm radius anechoic cyst was placed in front of the array and surrounded by roughly 4,000 scatterers uniformly distributed within the image region. Scatterers' amplitudes followed a Gaussian distribution with zero mean and standard deviation equal to one. Simulation methods are the same of those described in the previous section, except that the hypothetical source sampling was reduced to 100µm in azimuth. Again, the positions of the scatterers do not necessarily coincide with the position of the hypothetical sources. The results are shown in figure 4.

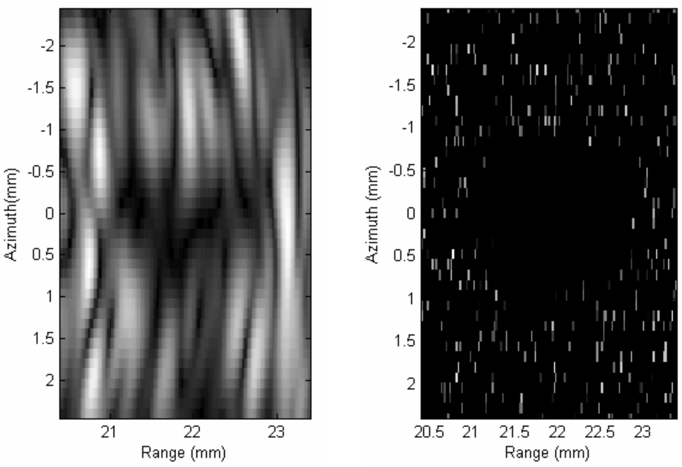

Figure 4. Conventional delay-and-sum beamforming (left) and TONE beamformed (right) of a simulated anechoic cyst.

IV. EXPERIMENTAL METHODS AND RESULTS

Experiments were also performed using a modified Philips SONOS 5500 imaging system employing a 6MHz linear array. The system was programmed to transmit a plane wave and to obtain data from individual channels. Received data was filtered using a 100 taps FIR filter. The array manifold matrix was constructed by warping and shifting the spatial response obtained from a 20µm stainless steel wire suspended in a water tank.

A. *Wire Targets*

5 stainless steel wires (20µm diameter) were suspended in a water tank kept at room temperature. The wires were placed at a depth of roughly 2.2cm from the transducer's face. The top panel of figure 5 shows the image outputted by the SONOS, whereas the bottom panel shows the TONE image of the 5 wires. In the case of TONE, hypothetical sources were placed every 19µm axially and every 67µm laterally.

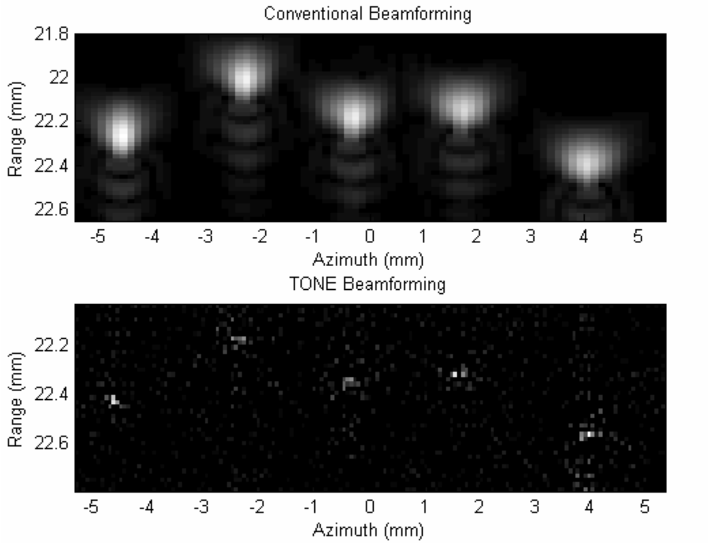

Figure 5. Conventional beamforming (top) and TONE beamforming (bottom) images of a set of 5 wires in water.

We have also analyzed the performance of TONE as a function of mismatched speed of sound. In this case the array manifold matrix was constructed using a speed of sound that differs from the true value. Results obtained for a 15m/s and 30m/s error are shown in the top and bottom panels of figure 6, respectively.

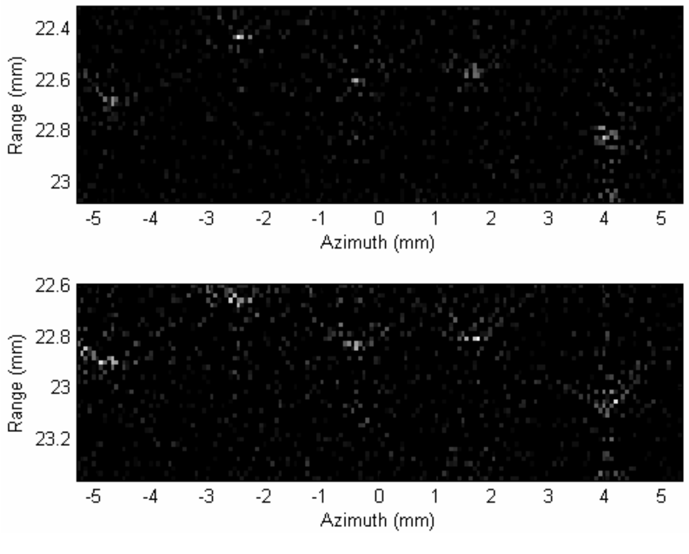

Figure 6. TONE beamformed images of the 5 steel wires with 15m/s (top) and 30m/s (bottom) mismatch in speed of sound.

We also analyzed the performance of TONE as a function of missing receive channels. While the images shown in figures 5 and 6 were generated using the full 128 channels provided by the SONOS (135μm pitch), figure 7 shows results obtained when the number of channels is reduced to 64, 32, and finally to 16. The corresponding pitches are 270μm, 540μm, and 1080μm, respectively.

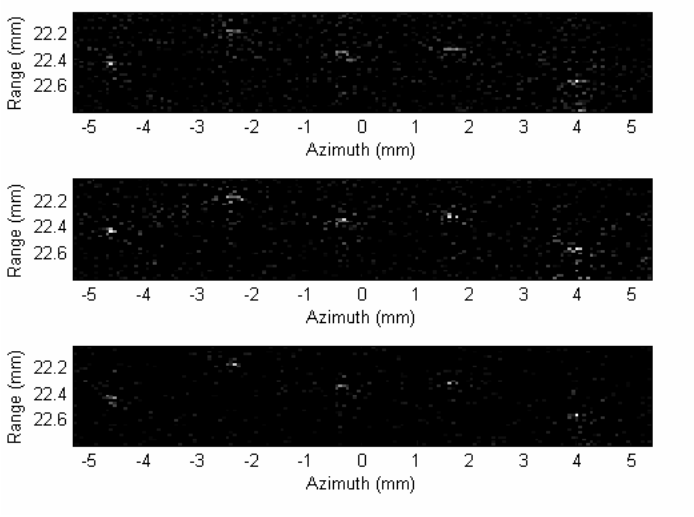

Figure 7. TONE beamforming with 64 (top), 32 (middle), and 16 (bottom), receive channels.

V. DISCUSSION

In medical ultrasound, bright off-axis targets can seriously degrade image quality by introducing broad image clutter. The application of ABF could reduce the effects of these targets, thus improving the overall image quality. However, the unique characteristics of ultrasound data make blind application of existing adaptive beamforming algorithms unlikely to be successful. In this paper a new beamforming technique, termed (TONE), has been presented and its performance has been evaluated both in simulations and experiments.

Figures 3 and 4 compare the TONE algorithm with the conventional delay and sum beamforming on synthetic data depicting wires and anechoic cyst phantoms. The superiority of TONE is clearly evident from those figures. Although not presented, we have performed additional simulations analyzing the stability of TONE with respect to additive noise. We have found that down to a 10 dB/channel SNR the performance of TONE remains excellent.

Figures 5-7 analyze the performance of TONE on experimental data. Hypothetical sources were placed every 19μm axially and every 67μm laterally. Similar results to those obtained in simulations are observed in figure 5. Although the five wires are clearly resolved, a small cloud of scatterers is visible around them. This is most likely due to noise and imperfection of the manifold matrix used. As stated above, the manifold matrix was generated by simply warping and shifting the response obtained from a single steel wire. More sophisticated model could be generated which would include for example the effects of element angular sensitivity.

The results of figure 6 show the stability of TONE with respect to aberration errors. The performance remains acceptable for a mismatch in speed of sound of 15m/sec and 30m/sec. These results are significant since most adaptive beamforming algorithm rapidly degrade when ideal conditions are not met.

Finally, figure 7 shows that TONE performance is independent on variations in channel number/pitch dimensions. While applying conventional beamforming on a 16 channel systems with 1.1mm pitch would result in massive grating lobes, the bottom panel of this figure shows that TONE remains almost unaffected.

Currently, the main limitation of this algorithm is represented by its high computational complexity. While higher spatial resolution is achieved using finer sampling of the ROI, this also incurs in higher complexity. The generation of the manifold matrix and the iterative procedure to estimate f represents the most costly steps. For an image region of 1cm by 1cm and assuming a sampling grid of hypothetical sources of 20μm by 70μm, V is on the order of 64K by 71K elements. However, for a given ROI and a desired sampling grid, the manifold matrix can be calculated in advance and stored for later application. Furthermore, TONE may also be applied to a given receive data set using a variety of iterative approaches to reduce the required computational complexity and data storage size. In one such approach the complete received data set is subdivided into multiple data segments that may or may not be uniformly sampled and may or may not overlap. For each received data segment, a distinct array manifold matrix is formed to represent the responses from hypothetical sources which could contribute to the specific data segment. TONE could then be applied separately to each of the data segments and their matched array manifold matrices. We are currently investigating this and other approaches.

VI. CONCLUSIONS

A new beamforming approach has been presented in this paper. Simulation and experimental results clearly suggest the advantages of this algorithm over conventional beamforming.

VII. ACKNOWLEDGMENT

We acknowledge technical support from Interactive Supercomputing Inc. and Philips Medical Systems.

REFERENCES

[1] S. Haykin, “Adaptive Filter Theory,” 4th ed., Prentice-Hall, Upper Saddle River, New Jersey, 2002.

[2] B. D. Van Veen and K. M. Buckley, “Beamforming: A Versatile Approach to Spatial Filtering,” *IEEE ASSP Magazine*, pp. 4-24, 1988.

[3] W. F. Gabriel, “Adaptive Processing Array Systems,” *Proc. IEEE*, vol. 80, no. 1, pp. 152-162, 1992.

[4] R. Bethel, B. Shapo, and H. L. Van Trees, “Single Snapshot Spatial Processing: Optimized and Constrained,” *Sensor Array and Multichannel Signal Processing Workshop Proceedings*, pp. 508-512, 2002.

[5] L. L. Sharf, “Statistical Signal Processing: Detection, Estimation, and Time Series Analysis,” Addison Wesley, 1991.

Design of Apodization Profiles Using a Cystic Resolution Metric for Ultrasound

K. Ranganathan, D. A. Guenther, and W. F. Walker
Department of Biomedical Engineering
University of Virginia
Charlottesville, VA 22908
dag2m@virginia.edu

Abstract*—We have previously described a metric that characterizes the 3D resolution of broadband ultrasound systems [1]. Resolution is expressed as the size of a spherical anechoic cyst, embedded in a speckle generating background, that is required to generate a specific contrast. The contrast of the cyst relative to the background depends on the ratio of the system point spread function (psf) energy outside the cyst to the total psf energy. In this work, we apply our formulation to guide the design of a low-cost, C-scan system being developed at the University of Virginia, demonstrating the utility of our metric in the optimization of system parameters. We simulated the impact of f/# and show that higher f/#'s yield better cystic contrast for larger cysts, but lower contrast for smaller cysts. We also applied a constrained least squares (CLS) approach to design receive apodization profiles to optimize cystic contrast. We use a linear algebra formulation of the psf and minimize the psf's energy in regions outside a specified boundary. We show results that the CLS apodization profiles improve contrast around -10 dB compared to a flat apodization profile at a range of cyst sizes. Our results highlight the metric's utility in designing system parameters and our CLS apodization profiles improve cystic contrast.

I. INTRODUCTION

The ability to reliably estimate the imaging performance of ultrasound systems is critical, both to characterize the fundamental imaging limits of the system, and to optimize image quality. It is possible to estimate the performance of existing systems by imaging phantoms or human subjects, but it is necessary during system design to be able to determine imaging performance prior to system construction. The ability to accurately predict performance enables system optimization and quantitative consideration of engineering tradeoffs early in the design process and significantly reduces the time and cost investment in system development.

The most common metric used to estimate scanner performance is the beamplot [2], the use of which has been adapted from RADAR. The -6 dB beamwidth of the beamplot, the full width at half maximum (FWHM), and the beamwidth at other levels are used to estimate scanner resolution. Sidelobe and grating lobe levels are used to estimate eventual image contrast. Although widely used, there are disadvantages to using the beamplot to estimate the performance of ultrasound systems. Targets in medical ultrasound are usually weakly reflecting tissues in a scattering medium, unlike RADAR targets that are more often highly reflective and in a non-scattering background. There may be scenarios in which the FWHM criterion indicates excellent performance, but actual images of tissue do not reveal important details. Vilkomerson *et al.* [3] demonstrated that the FWHM criterion sometimes provides misleading information about resolution in ultrasound systems. It is, in addition, difficult to decide whether to optimize the mainlobe width or sidelobe and grating lobe levels for an overall increase in image quality. Although imaging phantoms and repeated simulations may determine imaging performance, such approaches are time consuming and do not offer a simple method to guide system design. A theoretical metric that combines resolution and contrast in a relevant way to diagnostic ultrasound imaging is therefore required.

Vilkomerson *et al.* addressed the limitations of the beamplot and proposed the concept of "cystic resolution" [3] in which performance was quantified as the size of a void that produced a given contrast. The analysis, while novel and useful, was limited to narrowband circular apertures and neglected the axial dimension. Üstüner *et al.* [4] extended cystic resolution to a 3D broadband model that addressed the above problems, but did not describe its theoretical foundation, resulting in a limited understanding of the formulation and its utility and drawbacks. A general cystic resolution metric was previously derived by our group [1]; the metric accounts for the effect of electronic noise and, under certain assumptions, reduces to that described in [4].

This paper demonstrates the utility of the resolution metric to optimize system parameters. We have applied it to guide the design of a low-cost, C-scan system being developed at the University of Virginia. We also apply the metric in designing apodization windows for optimal cystic resolution on a 1D linear array. Using this metric, parameter optimization reduces to the straightforward task of picking the value that yields the maximum contrast at the cyst size of interest, or alternatively picking the value that yields the required contrast with the smallest cyst.

II. THEORY

A. Cystic Resolution Metric

The goal of the metric, as stated above, is to quantify the contrast resolution of an arbitrary broadband ultrasound system. We refer the reader to [1] for a more detailed

---

This work was supported by NIH NIBIB grant EB002349 and by award W81XWH-04-1-0590 from the US Army CDMRP.

discussion of the derivation of the metric and provide a brief synopsis here. Let the point spread function (psf) of the ultrasound system be defined as $P(\vec{x},t)$, a function of three-dimensional (3D) space ($\vec{x}$) and time (t). The medium scattering function is modeled as a zero-mean stochastic process $N(\vec{x})$ undergoing negligible tissue motion during reception of an individual echo line and therefore is constant with time. The effect of electronic noise during transmit is assumed to be negligible due to the high signal to noise ratio (SNR) on transmit, and the electronic noise on receive is modeled as another zero-mean stochastic process $E(t)$ which is purely additive. We define a mask that describes the location and size of a spherical anechoic void (cyst):

$$\begin{aligned} M(\vec{x}) &= 0,\ |\vec{x}| \le R \\ &= 1,\ |\vec{x}| > R, \end{aligned} \tag{1}$$

where R is the radius of the cyst and the cyst center is at the origin of the coordinate system. $M(\vec{x})$ is also independent of time since tissue motion during the acquisition is assumed to be negligible. The cyst embedded in a scattering background is therefore represented as $N(\vec{x})M(\vec{x})$. The received signal energy is expected to be at a minimum when the beam axis coincides with the center of the void. The received signal in this circumstance can be written as:

$$S_c(t) = \int_{-\infty}^{\infty} P(\vec{x},t)N(\vec{x})M(\vec{x})d\vec{x} + E(t) \tag{2}$$

The electronic SNR can be defined as a function of time:

$$SNR(t) = \frac{\sigma_{signal}(t)}{\sigma_{noise}(t)} = \sqrt{\frac{a\int_{-\infty}^{\infty} P^2(\vec{x},t)d\vec{x}}{\langle E^2(t)\rangle}} \tag{3}$$

where $c_{signal}(t)$ and $\sigma_{noise}(t)$ are the standard deviations of the signal and noise components respectively and a is a scaling factor. Note that the standard deviations are defined over an ensemble of signal and noise realizations and not over time.

While the metric can completely characterize system performance for a given cyst, analysis at the instant in time when the received signal is minimum (i.e. when as much of the psf energy as possible lies within the cyst) is usually sufficient. At this single instant in time t_o, the psf can be expressed as a function of only 3D space at the time of interest $P_{t_o}(\vec{x})$, and the SNR is also defined at the time of interest SNR_{t_o}. The contrast of the cyst relative to the background is defined as the ratio of the rms signal received with the cyst to the rms signal received from the background [1]:

$$C_{t_0} = \sqrt{\frac{1 + SNR_{t_o}^2 \frac{E_{t_o}^{out}}{E_{t_o}^{tot}}}{1 + SNR_{t_o}^2}} \tag{4}$$

where $E_{t_o}^{out}$ is the psf energy outside the cyst and $E_{t_o}^{tot}$ is the total psf energy, both at time t_o. Equation (4) describes the contrast of an anechoic cyst, whose size and location are described by the mask $M(\vec{x})$, relative to background speckle obtained by an imaging system with the psf $P(\vec{x})$ and electronic SNR defined statistically by SNR_{t_o}. Neglecting electronic noise, SNR_{t_o} becomes infinite and (4) can be modified to the equation for contrast presented in [4], which is simply the square root of the ratio of the psf energy outside the cyst and the total psf energy:

$$C_{t_o} = \sqrt{\frac{E_{t_o}^{out}}{E_{t_o}^{tot}}} \tag{5}$$

The contrast for cysts of different sizes can be computed using the above expressions for cystic contrast, and system performance can be characterized as a function of cyst size as in [3] and [4]. This metric can be used for 4D spatiotemporal analysis of broadband ultrasound systems, but 3D spatial analysis using (4) or (5) is adequate to characterize scanner performance as temporal analysis does not provide critical information. Note that in certain cases, it is valuable to compute the metric with cysts at different locations to quantify the depth of field, the effect of dynamic focusing, and other factors pertaining to the shift variance of the imaging system. Note also that while the metric can be used to determine cystic resolution, it can also be used to optimize system parameters by computing contrast as a function of cyst size and determining parameter values that maximize the contrast at the cyst sizes of interest.

B. *Constrained Least Squares (CLS) Apodization Design*

One conspicuous result of the above metric is that cystic contrast is a function of the spatiotemporal psf energy. In fact, contrast would be maximum if all the energy of the psf lies inside the void of the cyst. Whereas the beamplot can be misleading about overall image quality, our new metric specifically defines the portions of the psf that affect cystic contrast most dramatically. Contrast will improve when any region of the psf outside the cyst boundary contains less energy or there is more energy of the psf inside the cyst.

Cystic contrast is degraded due to psf energy outside the cyst. We minimize this energy by solving for the set of receive aperture weights that, when applied to the synthetic receive element responses, will yield a psf with minimum energy outside the cyst boundary. The acoustic field during pulse echo propagation at a point in space at a single time point can be expressed as a function of a propagation matrix, *S*, and a set of aperture weightings, *w*. The propagation matrix uses superposition to describe the contribution of each element at each field point as a function of time. *S* is a function of the transmit aperture weights, the excitation pulse, and the individual element impulse responses of the transmit and receive apertures [5].

The two way pulse echo propagation matrix, S, for a fixed transmit aperture and n element receive aperture at a total number of p points in three dimensional space is:

$$S = \begin{bmatrix} s_{1,1} & s_{1,2} & \cdots & s_{1,n} \\ s_{2,1} & \cdot & \cdots & \cdot \\ \vdots & \vdots & \ddots & \vdots \\ s_{p,1} & \cdot & \cdots & s_{p,n} \end{bmatrix}, \tag{6}$$

where $S_{i,j}$ is the contribution of the jth element at the ith point in space. The receive aperture weighting function, w_i^T, for each of the n elements used on receive can be written in vector form as:

$$w_i^T = [w_1 \quad w_2 \quad w_3 \quad \cdots \quad w_n]^T, \tag{7}$$

where T denotes the vector transpose operation. Using (6) and (7), we can now write the complete two-way pulse echo system psf, P_z, as follows:

$$P_z = Sw^T \tag{8}$$

the propagation matrix multiplied by the receive weighting vector. Note that this results in the one dimensional column vector, P_z, where z = [1, 2, …. p] the total number of points where the system psf is measured in three dimensional space.

Adequate spatial sampling of the three dimensional psf yields huge propagation matrices, and therefore for this paper we have limited our analysis to two dimensions, azimuth and range. Clearly the elevation dimension matters in planar ultrasonic B-mode images, even with acoustic lenses on linear arrays. However, restricting our analysis to two dimensions eases visualization of the algorithm while still providing meaningful results.

Assuming the psf is focused at the center of the cyst, our problem becomes minimizing the energy outside the cyst boundary. The algorithm is initialized by selecting the spatial points of the psf which lie outside the cyst. We form the associated propagation matrix, S, which has as many rows as the number of points outside the cyst region and as many columns as elements in the active receive aperture. The algorithm calculates the weights which minimize the energy in the sidelobe regions while simultaneously maintaining a peak gain at the center of the cyst. These weights are determined from the constrained least squares problem:

$$\min_{w^T} \left\| Sw^T \right\|^2 \quad \text{subject to the linear constraint } Cw^T = 1 \tag{9}$$

In this expression $\|\bullet\|^2$ denotes the square of the ℓ^2-norm and the row vector C has elements corresponding to the amplitude of each synthetic receive response at the center of the cyst. The equation in (9) is common in the signal processing literature and drawing upon [6] the optimal receive aperture weightings are given by:

$$w_{opt}^T = \frac{\left(S^T S\right)^{-1} C}{C^T \left(S^T S\right)^{-1} C} \tag{10}$$

where $(\bullet)^{-1}$ denotes the matrix inverse operation. Equation (10) provides a simple method to calculate the receive weightings that will minimize the energy in the psf outside a specified mainlobe region while simultaneously achieving peak gain inside the mainlobe region. The optimal receive weights minimize $E_{t_o}^{out}$ in (5) above, so we expect to see improved cystic contrast using the CLS apodization windows over commonly used windows such as the flat, Hamming and the Nuttall [7] window.

III. SIMULATIONS

The cystic resolution metric is useful in guiding the design and optimization of ultrasound systems. In our group's efforts to develop a low cost, handheld, C-scan ultrasound system, the metric was used to quantify the impact of system parameters such as f/#, electronic noise, quantization in the analog to digital converter, crosstalk, and apodization. The new system utilizes a fully sampled 2D array interfaced to a custom integrated circuit [8]. Our beamforming strategy, direct sampled IQ (DSIQ) beamforming [9], reduces system complexity and cost but suffers from poorer image quality than might be obtained using time delays. The system transmits an unfocused plane wave and apodizes and focuses on receive.

We simulated our system using DELFI [10], a custom ultrasound simulation package that efficiently calculates the spatial response of a given aperture. Spatial pulse-echo responses were computed by transmitting a plane wave on all elements and synthetically receiving on each individual element. The psfs were computed in a 3D cylindrical volume, focused using DSIQ beamforming and apodized with a 2D Nuttall [7] window on receive.

One of the system parameters investigated was the choice of f/# during reception. This is an important design parameter for our system because the DSIQ focusing scheme is limited by larger apertures [9]. In addition the elements in the 2D array are highly directive due to a large pitch (635 µm) and thus larger apertures will suffer from higher grating lobes. We explored the impact of f/# by computing cystic contrast curves as a function of cyst radius for varying f/#'s.

Another system parameter investigated was receive apodization profiles. We calculated receive weights for a linear array operating at 6.5 MHz and a 50% fractional bandwidth with a fixed transmit focus at 2cm. Using DELFI [10] 2D spatial psfs were computed for the linear array by synthetically receiving on each element at the transmit focus. The 2D psfs were then used to calculate the optimal receive weights according to the CLS approach outlined above. Corresponding cystic contrast curves as a function of cyst radius were calculated for the CLS windows and compared to the flat, Hamming and the Nuttall [7] window.

IV. RESULTS AND DISCUSSION

Figure 1 below shows the cystic contrast curves for the f/# simulations.

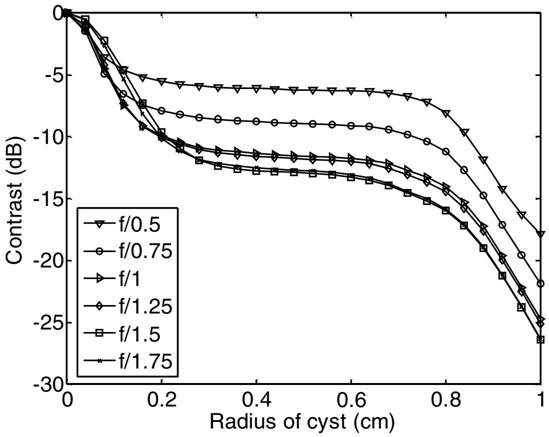

Figure 1. Effect of receive f/#. Contrasts were computed using equation (6) and are plotted as a function of cyst size for varying f/#'s.

It is apparent that contrast increases with increasing f/# for large cysts. This is due to highly directive elements that generate large grating lobes when larger apertures are used. However, higher f/#s (>f/1.5) result in a broad mainlobe and reduce contrast when imaging small cysts. Figure 1 suggests that an f/1 for the low cost system would be a good compromise for imaging cysts of all sizes. This analysis ignores the effect of aperture size on system sensitivity. Sensitivity increases with increasing aperture size. Considering the impact of SNR and f/# simultaneously may be necessary.

Optimal receive apodization profiles were computed for a linear 1D array according to the CLS formulation discussed above. For every cyst radius from 0.1mm to 2cm the CLS apodization profiles resulted in psfs that had the lowest energy in the sidelobe region compared to other windows. In conventional systems, scanning through apodization profiles for each cyst radii would be unrealistic. Therefore, it is interesting to see how a profile designed for a specific cyst size performs across a range of sizes. We chose the profile corresponding to a cyst radius of 0.4mm and then computed the cystic contrast curve. Figure 2 shows the contrast curves for this particular CLS profile compared to the flat, Hamming, and Nuttall windows. Although the CLS window does not produce the best contrasts for smaller cysts (<0.2mm) or for larger cysts (>0.8mm), it performs well over the entire range, with -10dB improvement in contrast over the flat apodization and -2dB improvement over the Hamming profile for cysts around 0.4mm in radius. The Nuttall window does a poor job for the small cysts due to a relatively large mainlobe. All the curves plateau as the cyst encompasses more of the psf energy.

We attempted to maximize cystic contrast through our least squares formulation by minimizing the energy in the psf outside the cyst region. Although the apodization profiles did minimize this energy they also reduced sensitivity in the mainlobe region. For larger cyst sizes the CLS apodization profiles do not produce "optimal" cystic contrast due to decreased psf energy inside the cyst compared to the other apodization windows. We are currently addressing this shortcoming by adjusting the constraints. It may be necessary to consider the impact of SNR and apodization simultaneously.

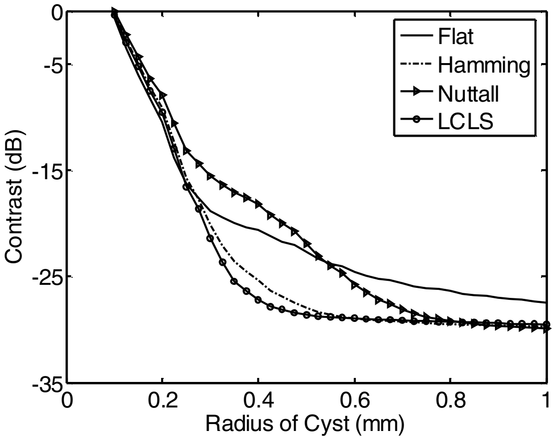

Figure 2. Effect of apodization. The CLS window performs well across the range of cyst sizes.

V. CONCLUSIONS

Our cystic contrast resolution metric is extremely useful in guiding system design of 3D broadband coherent imaging systems including the effects of electronic noise. The metric was used in the design of a portable, low cost ultrasound system currently under development. The metric also stimulated the design of optimal apodization profiles to maximize cystic contrast for a 1D linear array. The results presented in this paper demonstrate the utility of the metric in designing ultrasound systems and show that it enables optimization of any parameter that affects image quality.

REFERENCES

[1] K. Ranganathan and W. F. Walker, "A General Cystic Resolution Metric for Medical Ultrasound," submitted to the IEEE Transactions on Ultrasonics, Ferroelectrics, and Frequency Control.

[2] B. D. Steinberg, *Principles of Aperture and Array System Design*, John Wiley & Sons, 1976, pp. 40-52.

[3] D. Vilkomerson, J. Greenleaf, and V. Dutt, "Towards a resolution metric for medical ultrasonic imaging," Proc. IEEE Ultrason. Symp., vol. 2, pp. 1405-1410, 1995.

[4] K. F. Üstüner and G. L. Holley, "Ultrasound Imaging System Performance Assessment," presented at the 2003 AAPM Annual Meeting.

[5] K. Ranganathan and W. F. Walker, "A novel beamformer design method for medical ultrasound. Part I: Theory," *IEEE Trans. Ultrason., Ferroelect., and Freq. Contr.*, vol. 50, no. 1, pp. 15-24, 2003.

[6] L. L. Scharf, Statistical Signal Processing: Detection, Estimation, and Time Series Analysis, Addison-Wesley Publishing Company, 1991, p.365.

[7] A. H. Nuttall, "Some Windows with Very Good Sidelobe Behavior." IEEE Trans. Acoust. Speech Signal Process., vol. 29, no. 1, pp. 84-91, 1981.

[8] M. Fuller, T. Blalock, W. Walker, and J. Hossack, "A Portable, Low-cost, Highly Integrated 3D Medical Ultrasound System," Proc. IEEE Ultrason. Symp., pp. 38-41, 2003.

[9] K. Ranganathan, M. K. Santy, T. N. Blalock, J. A. Hossack., and W. F. Walker, "Direct Sampled I/Q Beamforming for Compact and Very Low Cost Ultrasound Imaging," IEEE Trans. Ultrason. Ferroelectr., Freq. Contr., vol. 51, no. 9, pp. 1082-1094, 2004.

[10] W. F. Walker, "A Spline Based Approach for Computing Spatial Impulse Responses," submitted to the IEEE Transactions on Ultrasonics, Ferroelectrics, and Frequency Control.

Adaptive Signal Processing in Medical Ultrasound Beamforming

Francesco Viola and William F. Walker
Department of Biomedical Engineering
University of Virginia
Charlottesville, VA 22908

Abstract— **For over thirty years adaptive beamforming (AB) algorithms have been applied in RADAR and SONAR signal processing. Higher resolution and contrast is attainable using those algorithms at the price of an increased computational load. In this paper we consider four beamformers (BFs): Frost BF, Duvall BF, SSB, and SPOC. These algorithms are well know in the RADAR/SONAR literature. We have performed a series of simulations using ultrasound data to test the performance of those algorithms and compare them to the conventional, data independent, beamforming. Every algorithm was applied on single channel ultrasonic data that was generated using Field II. For a 32 element linear array operating at 5 MHz, beamplot results show that while the Duvall and SSB beamformers reduce sidelobes by roughly 20 dB, the sidelobes using the Frost algorithm rise by 23dB. The –6dB resolution is improved by 38%, 83%, and 43% in the case of Duvall, Frost, and SSB algorithms, respectively. In the case of SPOC, the beamplot shows a super-resolution peak with noise floor at –110 dB. Similar results were obtained for an array consisting of 64 elements.**

I. INTRODUCTION

The application of Wiener filter theory to RADAR and SONAR signal processing led to the development of adaptive beamforming (AB) [1, 2]. In AB, the information associated with the data received by an array of sensors is used to determine a set of weights that optimize the beamformer output [2]. The weights are determined by minimizing the energy in the beamsum signal, subject to the constraint that the beamformer must exhibit a given response in the look-direction. The second order statistics of the data are used to generate the weights. These algorithms are able to achieve resolutions far superior to those predicted by diffraction theory, while attaining excellent side lobe reduction. In parallel, a series of adaptive algorithms has also been developed which do not rely on statistical properties of the data and thus can be used on a single realization (or snapshot). In the past fifty years a plethora of algorithms have been developed, each exploiting specific properties of the received data.

In medical ultrasound, bright off-axis targets can seriously degrade image quality by introducing broad image clutter, which reduces image contrast and resolution. Figure 1 shows single channel radio frequency (RF) echo data obtained from calcifications in the thyroid of a human subject at Duke University. At least three clear waveforms are visible in this data set. Although summation across channels to form an RF image line would amplify the echo coming from directly in front of the array, it would not entirely eliminate the two other visible targets. These non-focal targets would appear in this image line as clutter, reducing image contrast.

The application of AB can reduce the effects of bright off-axis targets, thus improving the overall image quality. In our laboratory we are exploring the application of these AB algorithms to medical ultrasonic imaging. We have examined statistical AB algorithms such as the Duvall and Frost beamformers [3,4], as well as deterministic AB algorithms such as the Adaptive Single Snapshot Beamformer (SSB) and the Spatial Processing Optimized and Constrained (SPOC) algorithm [5,6]. These algorithms are well known and recognized in the RADAR/SONAR literature.

We briefly describe some AB algorithms and present simulation results obtained applying the algorithms to medical ultrasound data.

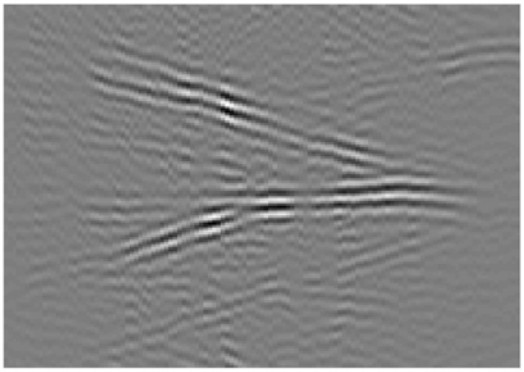

Figure 1. *In vivo* single channel thyroid data. The data clearly show the presence of bright off-axis scatterers as evidenced by the tilted plane wave visible in the top half of the image. Courtesy of G. E. Trahey.

II. ADAPTIVE BEAMFORMING ALGORITHMS

Adaptive beamformers can be divided in two broad categories: statistical and deterministic. While many algorithms have been developed in the past years, we consider two statistical and two deterministic beamformers (BF).

This work was supported by the US Army Congressionally Directed Medical Research Program in Breast Cancer grant No.W81XWH-04-1-0590

A. Statistical Beamformers

1) Frost Beamformer [3]

A weight vector is chosen to minimize the output energy given a linear constraint on the weights. Mathematically:

$$\min_{w} w^T R w \quad subject\ \ to\ \ C^T w = f$$
$$w_{opt} = \frac{R^{-1}C}{C^T R^{-1} C} f, \ \ y_{opt} = w_{opt}^T x \qquad (1)$$

where R is the covariance matrix, C is the constraint matrix, and f is the desired frequency response. w_{opt} in (1) represents the optimal weight solution. The Frost BF uses K taps in time, therefore allowing the use of broadband signals. This algorithm requires knowledge of the second order statistics of the signal of interest and interference. Significant problems occur if the signal of interest and noise (off-axis signal) are correlated (i.e., they have the same spectral response). A schematic representation of the Frost BF is shown in figure 2.

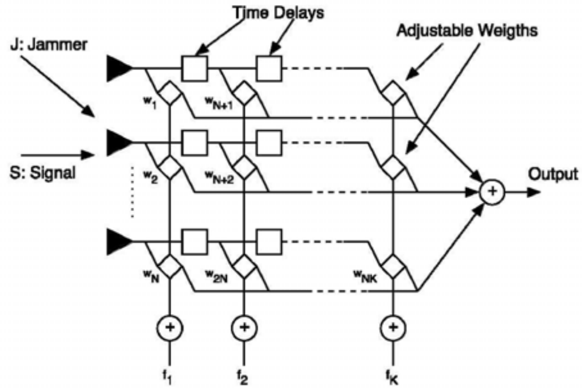

Figure 2. Schematic representation of the Frost beamformer.

2) Duvall Beamformer [4]

The Duvall BF is equivalent to the Frost BF in its formulation and assumptions. This algorithm, however, is designed to get around the problem arising when signal and noise are correlated. It uses two BFs; the first one is a slave BF, whereas the second is connected to the array elements through a subtractive process. The weights calculated in the latter BF are then copied in the slave BF to generate an output. A schematic representation of the Duvall BF is shown in figure 3.

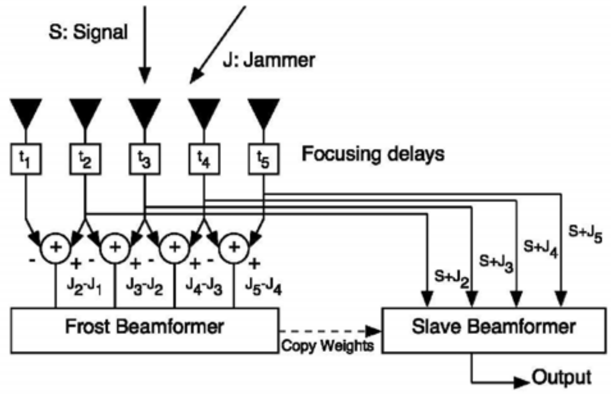

Figure 3. Schematic representation of the Duvall beamformer.

B. Deterministic Beamformers

The following BFs do not make use of any statistics, therefore are suitable to use with only a single snapshot of data.

1) Adaptive Single Snapshot Beamformer (SSB) [5]

This algorithm subdivides the array into G groups of K elements (the groups can overlap), and rearranges the data into a GxK matrix X. For every steering direction, this beamforming scheme solves the right- and left-hand side generalized eigenvalue problem given by:

$$(X-(a_1 g_1^T)y)v = 0, \quad u^T(X-(a_1 g_1^T)y) = 0^T$$
$$u^T = \frac{g_1^T X^{-1}}{g_1^T X^{-1} a_1}, \quad v = \frac{X^{-1} a_1}{g_1^T X^{-1} a_1}, \quad y_{opt} = u^T X v \qquad (2)$$

where a_1 and g_1 are the group and sub-group (respectively) on-axis steering vector, whereas u and v are the beamforming weights. The SSB BF is designed for narrowband, far field signals. However, it can also be implemented in the frequency domain for broadband data. A schematic representation of the SSB BF is given in figure 4.

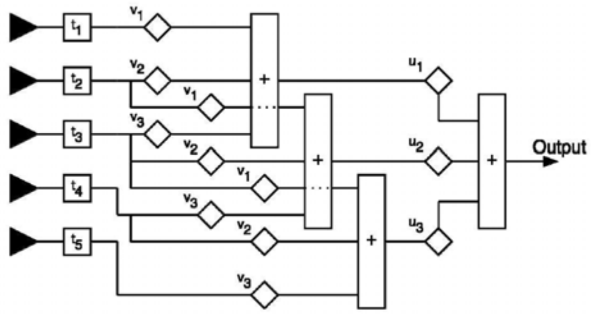

Figure 4. Schematic representation of the SSB beamformer.

2) SPOC [6]

This algorithm takes a completely different approach. A signal model is first generated of the field produced by a series of hypothetical sources. The sensors' output is matched to the signal model to solve for the position and intensity of the real sources. Statistics are not required and both near-field/far-field and broad/narrow band cases can be modeled.

The algorithm:

- The region of interest (ROI) is subdivided in a grid of hypothetical sources at arbitrary positions, as shown in figure 5. Finer grid sampling yields finer final resolution.
- For each point in the ROI, we calculate the hypothetical field received by the array for that specific point. These responses are included into the array manifold matrix V of dimensions LxP, where L and P are the numbers of hypothetical sources in the range and lateral dimensions, respectively.
- The data vector $x = [x_1\ x_2\ \ldots\ x_N]$ is received by the N-element linear array. This vector can be modeled as $x = V{*}f$. In this expression, f is the LPx1 signal vector,

whose elements are the amplitudes of sources located in the ROI.

- Given *x* and *V*, SPOC recursively estimates the signal vector *f*.

The main problems with this algorithm are the high computational cost, and the derivation of an accurate signal model. SPOC is shown schematically in figure 5.

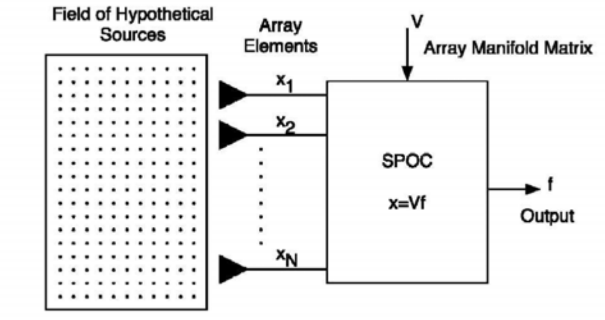

Figure 5. Schematic representation of SPOC.

III. SIMULATION METHODS AND RESULTS

A. *Beamplots*

For this and the successive section, single channel data was generated with Field II. We modeled a linear array operating at 5MHz with roughly 70% fractional bandwidth (BW). The final sampling rate was 40MHz. While the Frost, Duvall, and SSB BFs were applied on RF data, SPOC was applied on complex demodulated IQ data. Another important difference is that with SPOC the transmit pulse is a plane wave. This allows a more efficient and compact description of the ROI.

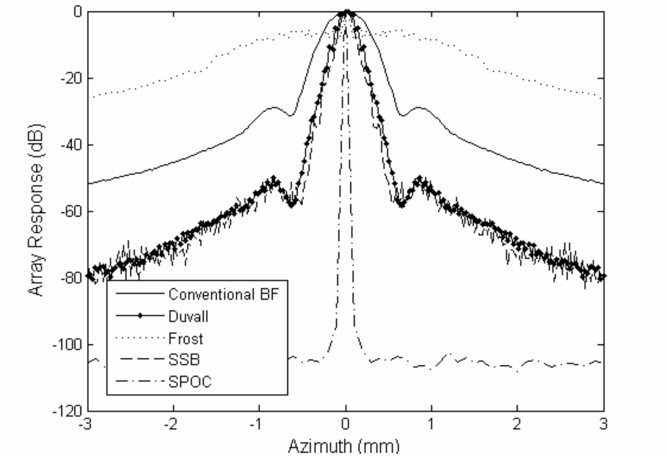

Figure 6. Beamplots for a 32 element linear array operating at 5MHz with 70% bandwidth. No apodization was used for the conventional BF.

Figure 6 shows beamplots obtained from a 32 element linear array. The four adaptive BFs are compared to the conventional, data independent BF. No apodization was used in the conventional BF. In the case of Frost and Duvall BFs, the constraint vector *f* is chosen to match the signal BW. For the SSB BF, the array is divided in sub-apertures of 16 elements each. Finally, in the case of SPOC, hypothetical sources are placed every 20μm in range and every 100μm in azimuth.

The results presented in figure 6 clearly show that SPOC outperform other adaptive BFs both in terms of resolution and contrast. For this reason and because of limited space, in the following sections we present simulation results that compare only conventional BF and SPOC.

B. *Wire Targets*

In this case, we simulated a 33 element linear array. A plane wave was used in transmit. A series of wire targets were distributed within a 4x5mm region in range and azimuth, respectively. The receive data was sampled at 40MHz and the conventional BF was applied on RF data using dynamic focusing. In the case of SPOC, we discretized the image region in a series of hypothetical sources separated 20μm in range and 120μm in azimuth. As before, complex demodulated IQ signals were used with SPOC. The results of this set of simulations are presented in figure 7 and 8. The figures are in linear scale. Note that the wires are placed in spatial positions which do not correspond to the positions of hypothetical sources.

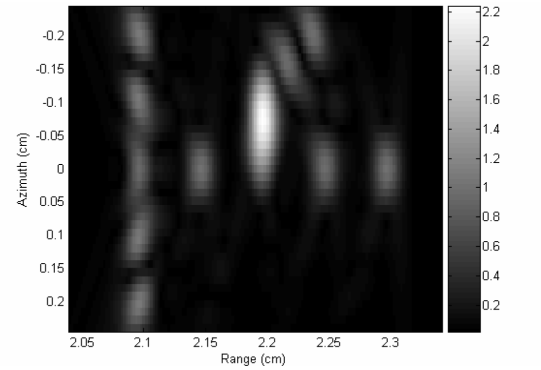

Figure 7. Conventional delay-and-sum beamforming. No apodization.

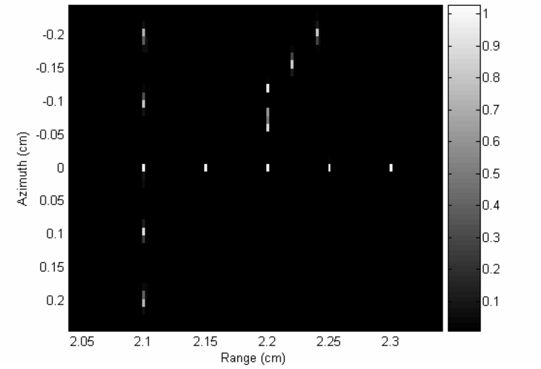

Figure 8. SPOC beamformer ouput.

C. *Anechoic Cyst*

An anechoic cyst was placed in front of the array and surrounded by ultrasonic scatterers. The cyst is round with a 1mm radius. Simulation methods are the same of those described in the previous section, except that the hypothetical source sampling was now reduced to 100μm in azimuth. The results of this set of simulations are presented in figure 9 and 10. The figures are in linear scale. The scatterers are placed in random positions within the image region.

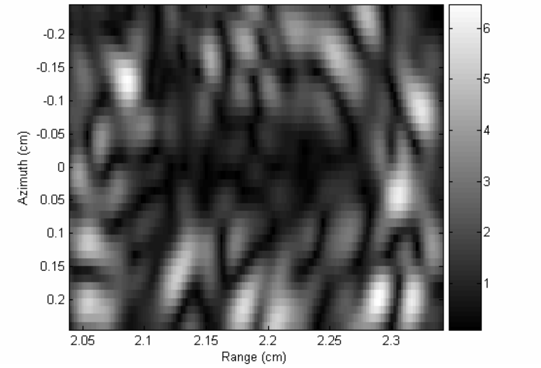

Figure 9. Conventional delay-and-sum beamforming. No apodization.

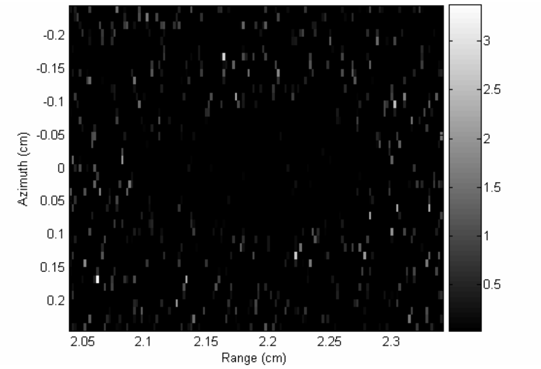

Figure 10. SPOC beamformer output.

IV. DISCUSSION

A series of AB algorithms have been presented in this paper and their performances were compared to the conventional, data independent beamforming technique.

As shown in figure 6, all the adaptive BFs achieve resolutions that are significantly better than that obtained by conventional BF. Furthermore, except for the Frost BF, we can observe a significant reduction in side lobe level. This figure also reveals that the SPOC significantly outperforms every other algorithms with a noise floor level of roughly –110dB. Also note that the super-resolution peak obtained with SPOC is a function of the hypothetical sources sampling; the finer the sources' grid, the better the final resolution. The performance of the Frost algorithm is significantly limited in medical ultrasound. Unlike SONAR and RADAR, we operate in a limited statistics scenario where on-axis and off-axis signals are highly correlated. These factors conspire to reduce the performance of this algorithm. The Duvall BF, instead, takes into account the correlation between signal of interest and off-axis signals using a subtractive process, as shown schematically in figure 3. From figure 6 it can be observed that the Duvall BF performs significantly better than the Frost BF, with a reduction of side lobe levels of roughly 20dB when compared to conventional BF. Finally, figure 6 shows that the SSB BF has similar performance to that of the Duvall BF. The main limitation of this algorithm is that narrow-band signals are originated from far-field. Obviously this is not a good assumption for medical ultrasound. Note that we have also performed additional simulations using a 64 elements array and found similar trends to those presented in figure 6.

It is clear at this point that most of the AB algorithms previously described, tend to fail when applied to medical ultrasound data. This can be attributed to some or all of the following factors: we are operating in a near-field scenario, our signals are broadband, and we have limited statistical information available. However, SPOC is well suited for medical ultrasound since it requires neither a far-field/narrow-band assumption nor second order statistics of the signals. Figures 7-10 compare the SPOC algorithm with the conventional BF on synthetic data depicting wires and anechoic cyst phantoms. The superiority of SPOC is clearly evident from those figures. Although not presented, we have performed additional simulations analyzing the stability of SPOC with respect to additive noise. We have found that down to a 10 dB/channel SNR the performance of SPOC remains excellent. The main limitation of this algorithm is the high computational complexity associated with it. We are currently investigating how to maintain the same performance with more efficient implementation.

V. CONCLUSIONS

Adaptive beamforming could help reduce clutter and yield super-resolution in medical ultrasound imaging. Simulation results show that SPOC significantly outperforms other AB algorithms. Additional work is required, however, to reduce the computational costs associated with SPOC.

REFERENCES

[1] S. Haykin, "Adaptive Filter Theory," 4th ed., Prentice-Hall, Upper Saddle River, New Jersey, 2002.

[2] B. D. Van Veen and K. M. Buckley, "Beamforming: A Versatile Approach to Spatial Filtering," *IEEE ASSP Magazine*, pp. 4-24, 1988.

[3] O. L. Frost III, "An Algorithm for Linearly Constrained Adaptive Array Processing," *Proc. IEEE*, vol. 60, no. 8, pp. 926-935, 1972.

[4] B. Widrow, K. M. Duvall, R. P. Gooch, and W. C. Newman, "Signal Cancellation Phenomena in Adaptive Antennas: Causes and Cures," *IEEE Trans. Antennas Propagat.*, vol. AP-30, no. 3, pp. 469-478, 1982.

[5] M. E. Ali and F. Schreib, "Adaptive Single Snapshot Beamforming: A New Concept for the Rejection of Nonstationary and Coherent Interferers," *IEEE Trans, Signal Processing*, vol. 40, no. 12, pp. 3055-3058, 1992.

[6] R. Bethel, B. Shapo, and H. L. Van Trees, "Single Snapshot Spatial Processing: Optimized and Constrained," *Sensor Array and Multichannel Signal Processing Workshop Proceedings*, pp. 508-512, 2002.